OEB Univ. Publish. Co.

Larbi Ben M'hidi University
Oum El-Bouaghi (Algeria)

Journal of New Technology and Materials
JNTM

ISSN : 2170-161X

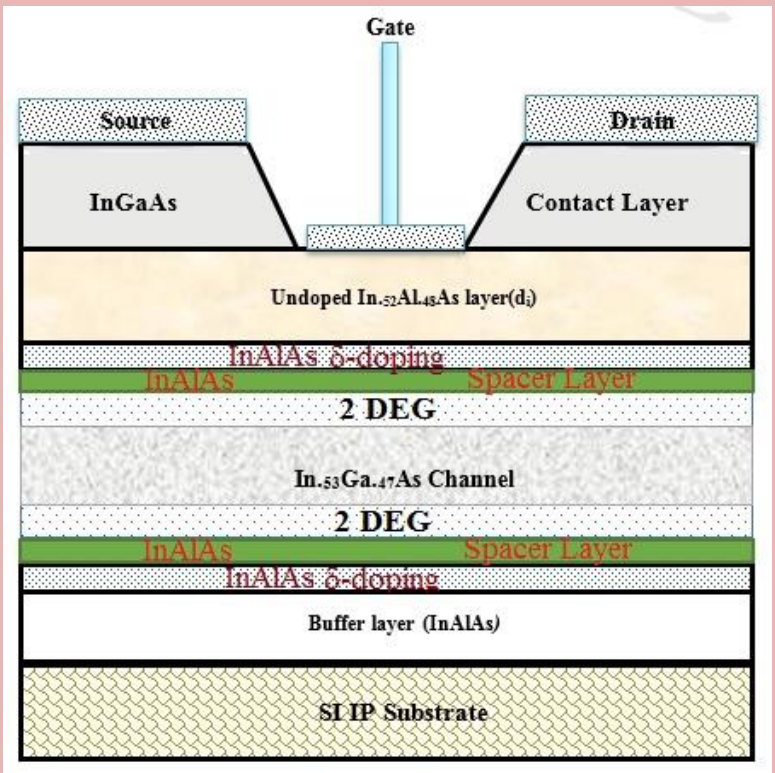

Volume: 07 **Issue: 01** **Year: 2017**

Address: University of Oum El-Bouaghi, 04000 Algeria
Fax: 00213(0)32563565, Email: jntm@univ-oeb.dz & jntm11@yahoo.fr
Website: http://sites.google.com/sites/jntmjournal

Table of contents

مجلة التكنولوجيا الجديدة والمواد

Journal of New Technology and Materials "JNTM"

Print ISSN : 2170-161X

Edition: University of Oum El-Bouaghi, Algeria
Address: Oum El-Bouaghi, 04000 Algeria

Impression: SARL DAR El-HOUDA
Address: B.P. 193, Ain Mlila 04300 Algeria

http://sites.google.com/site/jntmjournal
Email1: jntm11@yahoo.fr
Email2 : jntm@univ-oeb.dz
Phone/Fax: +213(0)32563565

Advisory Editors

Guidelines for Authors

"Journal of New technology and Materials"(JNTM) is an international peer-reviewed journal that publishes high quality original works on the Material sciences (physics, chemistry and life sciences) and engineering. It covers the aspect of materials science and engineering in all forms, particularly materials associated with new technologies (nanoscience and nanotechnology). The journal has an editorial board and international advisory editors, covering the majority areas of materials and engineering research. Coverage is broad and includes the design and synthesis of materials, their characterization, processing, modelling, properties and applications in the fields of theoretical physics, applied physics, metallurgy, chemistry, theoretical chemistry, nuclear physics, ceramics, semiconductors, electronic devices, spintronics, spectroscopy and life sciences. Papers covering interdisciplinary research and papers from related disciplines are encouraged, in particular those addressing emerging and quickly developing fields.

To establish the suitability of the articles for *JNTM* they must highlight the novel properties or applications (or potential properties/applications) of the materials studied. Papers that report primarily structural studies will be considered for publication only where the materials have interesting properties or are of potential interest for the materials and technology communities.

- New Authors: If you are submitting for the first time, you will first be required to send some information (name, title, fax, phone, ...).
- Manuscripts are to be prepared according to the instructions provided (see below). They should preferably be prepared using MS Word file. Authors are expected to check their proofs before publication.
- Once a paper is accepted, authors are assumed to cede copyrights of the paper over to *OEB Univ. Publish. Co.*
- All papers will be acknowledged and refereed. They will not be returned.
- Submission of a manuscript indicates a tacit understanding that the paper is not under consideration for publication with other journals.
- There is no page charge for the journal.
- All authors for the regular issues will be provided with a free pdf file of the final paper. As for the special issues, only the lead authors or the corresponding authors will be provided with a free pdf.

Authors should note that the following practices are likely grounds for rejection of a manuscript, or acceptance only after substantial revision.

1. Papers must be written in English.
2. Papers must be written in MS-Word format and sent by email as an attached file to jntm11@yahoo.fr, or jntm@univ-oeb.dz or online via the web site.
3. **Title.** A paper should have a short, straightforward title directed at the general reader. Lengthy systematic names and complicated and numerous chemical formulae should therefore be avoided where possible. The use of non-standard abbreviations and symbols in a title is not encouraged. The title should be in Baskerville Old Face (18 pts).
4. **Authors name should be in** Baskerville Old Face (12pts).
5. **Affiliations should be in** Baskerville Old Face (10pts) italic.
6. **Abstract.** Every paper must be accompanied by an abstract (70–200 words) setting out briefly and clearly the main results of the work; it should give the reader a clear idea of what has been achieved. The text of abstract should be in Baskerville Old Face (10pts) italic and it must be followed by three or five keywords.
7. **Introduction.** This should give clearly and briefly, with relevant references, both the nature of the problem under investigation and its background. The text of introduction should be in Baskerville Old Face (10pts).
8. **Main text.** Only strictly relevant results should be presented and figures, tables, and equations should be used for purposes of clarity and brevity. The use of flow diagrams and reaction schemes is encouraged. Data must not be reproduced in more than one form, *e.g.* in both figures and tables, without good reason. The text should be in Baskerville Old Face (10pts).
9. **Conclusion.** This is for interpretation and to highlight the novelty and significance of the work. The conclusions should *not* summarize information already present in the text or abstract. The text of the conclusion should be in Baskerville Old Face (10pts).
10. **References.** The reference numbers should be cited between brackets [...] in the correct sequence through the text (including those in tables and figure captions, numbered according to where the table or figure is designated to appear). The references themselves are given at the end of the final printed text along with any Notes.
    - **Journals**. For example: A. Nouiri, R. Aouati, *Physica E* 40 (2008) 1751-1753
    - **Books.** For example: A. Nouiri, S. Chaguetmi, A. Djemel, and R-J. Tarento in Science, Technology and Education of Microscopy : an Overview, Ed. A. Mendez-Vilas, FORMATEX, Madrid (Spain), 99(2003)
    - **Material presented at meetings**. For example: A. Nouiri, Proceedings of the Third Symposium on Scientific Research and Technological Devlopment Outlook in the Arab Word (SROIII), April 11-14, 2004 Riyadh, Kingdom of Saudi Arabia
    - **Theses.** For example: A. Nouiri, Doctorate Thesis, 2000, University of Constantine (Algeria)
11. Color figures are not accepted (for the time being)
12. Authors must split the contents of a text field (Introduction, main text, conclusion and references) into two columns.

Detailed instructions for preparation of manuscripts are available in:
http://sites.google.com/site/jntmjournal/paper-submission

Abbreviation: J. New. Technol. Mater.

Indexing

Journal of New Technology and Materials (JNTM) is indexed in:

- Emerging Sources Citation Index
- Chemical Abstracts Service (CAS)
- The Directory of Open Access Journals (DOAJ)
- Google Scholar
- Journal Seek
- SerialsSolution
- German Institute of Global and Area studies
- Social Science Research Center Berlin (WZB)
- Research Center Petra Christian University
- ProQuest
- InnoSpace - SJIF Scientific Journal Impact Factor
- Webreview CERIST (Algeria)
- E-Marefa database
- Al Manhal Database
- WorldCat Database
- InfoBase Index

Publication Ethics and Malpractice Statement

Publication and authorship :

1. All manuscripts will be evaluated basing on content without regard to ethnic origin, gender, sexual orientation, citizenship, religious belief or political philosophy of the authors
2. All submitted papers are subject to double peer-review process by at least one international and one local reviewer and that are experts in the area of the particular paper.
3. The factors that are taken into account in review are significance, originality, readability and language.
4. The possible decisions include acceptance, acceptance with major/minor revisions, or rejection.
5. If authors are encouraged to resubmit a paper after major revisions, there is no guarantee that the revised submission will be accepted.
6. Rejected articles will not be re-reviewed, but it can be resubmitted in other format.
7. The paper acceptance is constrained by such legal requirements as shall then be in force regarding libel, copyright infringement and plagiarism.

Duties of Authors :

1. Authors must certify that the manuscript has not previously been published elsewhere.
2. Authors must certify that the manuscript is not currently being considered for publication elsewhere
3. Authors must certify that their manuscripts are their original work.
4. Authors are obliged to provide retractions or corrections of mistakes.
5. All Authors mentioned in the paper must be informed about the submission of paper.
6. Authors must state that all data in the paper are real and authentic.
7. Authors must notify the Editor-in-chief of any conflicts of interest.
8. Authors must identify all sources used in the creation of their manuscript.
9. Authors must report any errors they discover in their published paper to the Editor-in-chief.
10. Author and co-authors should sign the copyright transfer agreement after the acceptation of paper.
11. Authors should read and agree the Publication Ethics and Malpractice Statement and guidlines for authors before the submission of paper

Duties of Reviewers：

1. Reviewers should keep all information regarding papers confidential and treat them as privileged information.
2. Reviews should be conducted objectively, with no personal criticism of the author
3. Reviewers should express their views clearly with supporting arguments
4. Reviewers also check the manuscript for plagiarism, research fabrication, falsification and improper use of humans or animals in research
5. Reviewers should also call to the Editor-in-chief attention any substantial similarity or overlap between the manuscript under consideration and any other published paper of which they have personal knowledge.
6. Reviewers should not review manuscripts in which they have conflicts of interest resulting from competitive, collaborative, or other relationships or connections with any of the authors, companies, or institutions connected to the papers.

Duties of Editor :

1. JNTM Editor has complete responsibility and authority to reject/accept an article.
2. JNTM Editor is responsible for the contents and overall quality of the publication.
3. JNTM Editor should always consider the needs of the authors and the readers when attempting to improve the publication.
4. JNTM Editor should guarantee the quality of the papers and the integrity of the academic record.
5. JNTM Editor should publish errata pages or make corrections when needed.
6. JNTM Editor should base their decisions solely one the papers' importance, originality, clarity and relevance to publication's scope.
7. JNTM Editor should not reverse their decisions nor overturn the ones of previous editors without serious reason.
8. JNTM Editor should preserve the anonymity of reviewers.
9. JNTM Editor should ensure that all research material they publish conforms to internationally accepted ethical guidelines.
10. JNTM Editor should act if they suspect misconduct, whether a paper is published or unpublished, and make all reasonable attempts to persist in obtaining a resolution to the problem.
11. JNTM Editor should not reject papers based on suspicions, they should have proof of misconduct.
12. JNTM Editor should not allow any conflicts of interest between staff, authors, reviewers and board members.
13. JNTM Editor verify the plagiarism
14. In the case of plagiarism, JNTM Editor can forbid all future publications from the same authors

Journal of New Technology and Materials
JNTM
Vol. 07, N°01 (2017)09-17

OEB Univ. Publish. Co.

Analysis of impurities of Nd-Fe-B Magnet by nuclear method and recovery by precipitation chemical of Nd and Pr rare earths

K. Cheraitia[a], A. Lounis[a] and M. Mehenni[a]

[a]*Laboratory of Sciences and Material Engineering, University of Sciences and Technology, Houari Boumediene, BP32 El Alia. 16111 Algiers, Algeria.*

Corresponding author: email: cheraitiak@yahoo.fr
Received date: January 08, 2017; revised date: April 10, 2017; accepted date: May 23, 2017

Abstract

The products of the new information and communication technologies (NTIC), whose life often not exceed three years, became consumables to the computer image and other waste that contains neodymium and praseodymium (rare earths). In this field of analysis of impurities, treatment and recycling of waste, we propose the recovery of elements such as neodymium and praseodymium, from the super-magnet Nd-Fe-B, Our study provides a simple process and inexpensive. The implementation scheme of our project consists in a first step in developing a plan of experience that has been made specifically to perform the optimization of operating conditions of the precipitation process. This experimental design was inspired by a statistical technique advanced design of experiments known factorial design. The flow sheet processing of recovery begins by embrittlement in liquid nitrogen (-196°C) followed by dissolution in an acidic solution and precipitation of Nd as neodymium oxalate. For characterization we used the following techniques: The neutron radiography, the neutron activation analysis (NAA), the scanning electron microscope coupled with EDX and XRD. The counting of γ spectrum shows that the purity of the precipitate is higher than 99%. Then, the thermal decomposition transforms this powder to neodymium oxide. After the reduction we obtain pure neodymium

Keywords: Magnet analysis; rare earths; neutron activation analysis; neutron radiography; precipitation chemical; separation by solvent extraction;

1. Introduction

The development of the nuclear industry and the development of new separation techniques (ion exchange, solvent extraction) lanthanides compounds have become more common chemicals. The Lanthanides are considered important industrial materials by their specific characteristics. The specificity of rare earth is mainly due to the f electrons which gives them two essential properties: optical and magnetic. The rare earths are used to make magnetic alloys (neodymium-doped dysprosium) which play an important role in advanced technologies used in particular for wind turbines. Their magnetic properties, which depend on quantum characteristics, are exceptional: the f electrons are not involved in chemical bonds; they are free to participate in magnetism. The rare earth having these f electrons are difficult to separate because their numbers of electrons also affect their physical properties, which has an impact on their industrial interest [1, 2]. The rare earths have exceptional magnetic properties, their saturation magnetization is much higher than the iron one [3].

From raw material the composition is very complex. The steps that achieve different lanthanides as pure products are long, difficult and expensive [4-7]. The dissolved lanthanides are separated from impurities by various reactions as the insolubility hydroxides, fluorides, oxalates, phosphates or alkali double sulfates [8-10]. In this context we would like to assess the degree of contamination of the magnet Nd-Fe-B, they have the highest magnetic field intensity. The demand for rare earth elements increases wish 9-15% per year [11, 12]. The production of neodymium (Nd) has considerably increased since the development of neodymium-iron-boron (Nd-Fe-B) permanent magnet [13-14]. These magnets are found in almost all the NTIC products (New Technologies of Information and Communication). NTIC products whose life cycle does not usually exceed three years have become consumables. Just like the hard disks drive (HDD) in a personal computer, which contain neodymium and praseodymium [15]. The concept of sustainable development is invoked as a necessity for recycling materials. The waste from NTIC products has nevertheless a residual material value, compromised by the disassembly cost in the developed countries, but economic in developing or third world countries.

Our work has two stages. The first step is to determine the content of neodymium and the impurities of a magnet Nd-Fe-B. To do this we used the following techniques: The neutron radiography, the neutron activation analysis

(NAA) and the scanning electron microscope (SEM) coupled with EDX. Few studies mention the analysis of impurities in the magnets marketed. In a second step the powder (Nd-Fe-B magnet) is dissolved in hydrochloric acid solution. We add an oxalic acid solution to precipitate Nd as neodymium oxalate [4, 16]. The powder was analyzed by SEM/EDX and X-ray diffraction. The gamma (γ) counting allows the determination of the content of neodymium, after oxalate precipitation and production of the Nd2O3 powder [17].

2. Materials and methods

2.1. Neutron activation analysis

The neutron activation analysis is a method of making a sample radioactive by irradiation in a neutron field and thereafter one proceeds to identification via the energy emitted by the corresponding isotopes and their half life [18]. Samples of the Nd-Fe-B matrix and the standard were weighed, packaged, and irradiated simultaneously in the thermal reactor column under a neutron flux magnitude of $5.4x10^{12}n/cm^2/s$. The long irradiation was made in thermal column, with a magnitude of $2.1x10^{11}n/cm^2/s$ for a time of 10 hours. At the end of the long irradiation, the samples were transferred directly to a shielded cell for 10 days decay time. The radioactivity of the samples was measured using a γ spectrometric chain which is composed of the following elements: germanium high purity detector (Hp/Ge) having a efficiency ε = 1.2%, and resolution of 1.80 keV. The ratio Pic/Compton is 40. These characteristics are measured for γ line at 1.33 MeV 60Co. A preamplifier and an analyzer 8192 ORTEC channels incorporating an amplifier samples and standard were measured in the same counting geometries.

2.2. Neutron radiography

This technique is non-destructive analysis for the control and structural characterization of opaque or solid materials at the micrometer scale. In this work, we will apply the so-called transfer technique to obtain radiographs of super magnet, thereafter we will use digital processing techniques of the images obtained for qualitative operation to access information structures. In the transfer method only the converter is exposed to neutron beams and becomes radioactive. The intensity of the secondary radiation is proportional to the spatial neutron intensities. The converter is transferred after irradiation in the darkroom and placed in contact with a radiographic film. In this technique the gamma flux present in the beam does not interfere with the method.

2.3. Mass spectrometry

A small portion of the sample is transformed into ions. These ions are then subjected to electric and possibly magnetic fields and their path will depend on the m/z ratio. After separation, the ions finish their path in a detector sensor. An analysis of the chemical composition of the samples was performed using a mass spectrometer SPECTRO MaxX.

2.4. Precipitation of neodymium

As extraction method we increased our choice of precipitation. We note in passing that the solubility of a metal (Neodymium), that is to say the neodymium concentration present in all its forms in the leaching solution, highly dependent on pH. Note also that the pH of maximum precipitation of metals does not coincide. It is therefore necessary to seek an optimum pH range to optimize removal of the desired metal. A wise choice provides a precipitate uncontaminated. Faced with changing regulations which requires severe concentration thresholds before discharge of the effluent, we must optimize returns from precipitation. The precipitation process is also influenced by other factors: choice of reagent, concentration of the precipitating agent, valence of the cation to eliminate proportion of cations, temperature, stirring speed. The optimum parameters are impossible to predict without resorting to preliminary tests. Subsequently mathematical modeling established between precipitation returns and levels of selected factor, the precipitation tests were performed according to a planning of experiments at three levels three (3^3 or 27 experiments).

2.4.1 Optimization of operating conditions

The goal is to have a minimum number of experiments to obtain the necessary information; this method reduces the confusion between the effects of different parameters. In addition, this method allows the simultaneous variation, systematic and effective in several settings at once. The aim of this experimental plan is to measure the causal relationships effect between the operating conditions and answers 'y' through the construction of an empirical model. This model can then be used to determine the minimum response "y" within the experimental range under observation, and the operating conditions to achieve it. After these experiments, it is possible to obtain a precipitation pattern of response to be optimized. This linear model has three settings and three variables each (3^3) : the influence of the three unit parameters , the three interactions of three factors lead to a total of 27 experiments. The three variables are: the concentration of Nd (0.001M, 0.003M, and 0.009M), the oxalic acid concentration of 0.5M, 1M and 0.75M and the pH of the solution 2.5, 3 and 3.5. Each parameter has three levels. Every time, it will be necessary, we adjust the pH with a sodium hydroxide solution. Depending on the experimental design, the mass balance of Nd -Fe-B powders 27 manipulation is performed. For this step we have plate and agitation motors, three Erlenmeyer flasks,

three beakers and three funnels and filter paper to perform the filtration.

An oven for drying and analytical balance for weighing the precipitate and calculate the returns of each precipitation assay. The addition of oxalic acid is carried out under stirring. Precise amounts of reagents are based on theoretical calculations in line with the following reaction:

$2Nd^{3+}+3(H_2C_2O_4.2H_2O)+4H_2O \rightarrow Nd_2(C_2O_4)_3.10H_2O+6H^+$

To ensure the total recovery of Nd, is added drip to slightly exceed the theoretical amount calculated, After filtering the solution a drying to 70°C. This is done for 24 hours. The precipitate is weighed and stored.

2.5. Characterization

The resultant powder was characterized by using X-ray diffractometer carried out with X'Pert Pro MPD under Cu-Kα radiation (λ=0.154 nm). Microstructure and chemical composition of the samples were investigated by JSM-6360, JEOL scanning electron microscope (SEM) equipped with an energy dispersive X-ray (EDX) analyser at an accelerating voltage of 10-20 kV.

3. Results and discussion

The results of neutron activation are presented as intensity spectra of γ radiation as a function of energy. The methodology adopted in this work is to identify all the elements present in the sample. This step is very important because it allows us to identify short period elements. These elements become saturated quickly and therefore they require very short irradiation time. The long-period elements slowly reach saturation, they require higher fluence neutron irradiation. The qualitative analysis of elements is performed by short periods γ spectrometry. Induced activity in the sample is due to radioisotope production. When N_1 stable atoms of a material are irradiated by a neutron flux φ (n/cm²/s) for a time *dt*, the number of radioactive atoms N_1 formed is given by the equation (1). At the same time begin the disappearance decay of radioisotopes formed. The system of evolution equations is obtained by producing the balance production – disappearance in equation (2).

$$dN_1/dt = \sigma_1.\varphi.N_1 \quad (1)$$

$$dN_2/dt = \sigma_1.\varphi.N_1 - \sigma_2.\varphi.N_2 - \lambda_2 N_2 \quad (2)$$

Where:

- σ_i (cm²) the capture cross section of the radioisotope i
- N_1 et N_2 (at/cm³): density numbers respectively of the isotopes X_1 and X_2
- λ_i (s⁻¹): constant of radioactive decay of the radioisotope i
- φ(n/cm²/s): neutron flux
- *t* (s): neutron irradiation time

With the following conditions at t=0, $N_1(0)= N_1^0$ and $N_2(0)=0$, the solution of the system of equations (1) and (2) is written:

$$N_1(t) = N_1^0 e^{-\sigma_1\varphi.t} \quad (3)$$

$$N_1^0 = \frac{m.\xi.N}{M_A} \quad (4)$$

Where:

- m: mass of the sample
- N: Avogadro's number
- M_A: atomic mass,
- ξ: isotopic enrichment

$$N_2(t) = \frac{\sigma_1.\varphi.N_1^0}{\lambda_2 + (\sigma_1 - \sigma_2)\varphi}(e^{-\sigma_1.\varphi.t} - e^{-(\lambda_2+\sigma_2.\varphi)t}) \quad (5)$$

The activity $A_2(t)$ is written:

$$A_2(t) = \lambda_2.N_2(t) \quad (6)$$

Asking $\lambda^* = \lambda_2.N_2.\sigma_2.\varphi$ equation (6) is written:

$$A_2(t_i) = \frac{\lambda_2\sigma_1.\varphi.N_1^0}{\lambda^* - \sigma_1.\varphi}(e^{-\sigma_1.\varphi.t_i} - e^{-\lambda^* t_i}) \quad (7)$$

This relation is valid in most cases. However when it comes to a long irradiation for the elements with a large cross sections of absorption (high neutron flux), then take into account the consumption of target (burn-up).

For items with a large full resonance, consideration should account the fraction of the neutron spectrum located beyond the thermal field. The term $\sigma_1\varphi$ will be replaced by $(\sigma_1\varphi + I_0.\varphi_{epi})$

Where:

- φ_{epi} is the epi-thermal neutron flux and I_0, the resonance integral (in barns).

The sample activity at the end of irradiation (at time t = t_i) and after a time decrease t_d is given by equation (8).

$$A_2(t_i, t_d) = A_2(t_i)e^{-\lambda_2 t_d} \quad (8)$$

The cumulative activity of the sample after a time t_c count is:

$$A_2(t_i, t_d, t_c) = \int_0^{t_c} A_2(t_i, t_d)e^{-\lambda_2 t_c} dt \quad (9)$$

$$A_2(t_i, t_d, t_c) = \frac{\sigma_1.\varphi.N_1^0}{\lambda_2}(1 - e^{-\lambda_2 t_i})(1 - e^{-\lambda_2 t_c})e^{-\lambda_2 t_d} \quad (10)$$

Determining the individual half-life of each radioelement is made by following the decrease of this one at constant time intervals. Table 1 provides the nuclear reactions used for sample analysis. The presence of specific radioisotopes is demonstrated in the γ spectra in Figure2-5.

Table1. Nuclear reactions for sample analysis

Element	Target isotopes	Nuclear reactions	product	ε (%)	λ (s^{-1})	γ peak (KeV)
Nd	^{146}Nd	^{146}Nd (n, γ) ^{147}Nd	^{147}Nd	17.2	7.30E-07	531
Fe	^{58}Fe	^{58}Fe (n, γ) ^{59}Fe	^{59}Fe	0.28	1.68E-07	1099
Co	^{59}Co	^{59}Co (n, γ) ^{60}Co ^{61}Ni (n, p) ^{60}Co	^{60}Co	100	3.79E-09	1173
Al	^{28}Al	^{28}Al (n, γ) ^{29}Al	^{29}Al	100	4.68E-03	1780
V	^{51}V	^{51}V (n, γ) ^{52}V	^{52}V	99.75	2.8E-03	1435
Cu	^{63}Cu	^{63}Cu (n, γ) ^{64}Cu	^{64}Cu	69.15	1.36E-05	511

For the three energy intervals, Figure 2 we can clearly infer the existence of elements that accompany Fe and Nd, these are: Al28, V52, Mn56, Cu66, Ge66, Ag108, Cs 136, Lu177m, Tb160, Re224, Bk246. Note also the presence of rare earth elements such as Dy160 and its isotope Dy165.

The elements of long period require very large irradiation time and do not appear on these spectra. The time counting of the vanadium element is taken as the reference time. The time decay of the respective elements will be determined from time decay vanadium which is given in table 2.

The energy measured by the neutron activation technique is confirmed by tables and energy isotopes. Tables 3 and 4 show the ratios of the matrix Nd-Fe-B obtained by neutron activation analysis, where all the elements short and long periods present appeared.

Table2. Reference time of the elements analyzed by NAA

Element	Decay time (s)
Vanadium	0
Cooper/Manganese	9035
Neodymium	18585
Iron	91534
Nickel	100219
Nd-Fe-B Matrix	169477
Cobalt	176891

Table3. Elements present in the Nd-Fe-B matrix after 2Min of a decay time

Probable radioisotope	Energy measured	Probable radioisotope	Energy measured
Ti-51	242	Lu-177m	54.07
Ni-65	55	Sm-153	69.67
Ni-65	181	J-131	80.18
In-116m	92	Eu-155	86.54
Ni-65	39	Cd-109	88.03
Cu-64	274	Nd-147	91.11
Ti-51	14	Np-239	99.55
Ni-65	24	Ta-182	100.11
In-116m	818.70	Sm-153	103.18
Mg-27	843.76	Gd-153	103.18
Mn-56	846.77	Np-239	103.76
Ni-65	852.70	Eu-155	105.31
Ti-51	928.63	Lu-177m	105.36
Ni-65	952.99	Np-239	106.12
In-116m	1096	Lu-177m	112.95
Cu-64	1346.55	Np-239	117
V-52	1434	Se-75	121.12
K-42	1523	Eu-152	121.78
Al-28	1778	Eu-154	123.07
Mn-56	1810.67	Ba-131	123.84

Table4. Elements present in the Nd-Fe-B matrix after 10 days of a decay time

Probable radioisotope	Energy measured	Probable radioisotope	Energy measured
Lu-177m	54.07	Ba-131	123.84
Sm-153	69.67	Yb-175	282.52
J-131	80.18	Pa-233	300.04
Eu-155	86.54	Se-75	303.92
Cd-109	88.03	Nd-147	319.41
Nd-147	91.11	La-140	432.49
Np-239	99.55	Nd-147	439.88
Ta-182	100.11	Hf-181	482.18
Sm-153	103.18	Ru-103	497.33
Gd-153	103.18	Cs-134	561.76
Np-239	103.76	Ga-72	600.95
Eu-155	105.31	Sc-46	889
Lu-177m	105.36	Tb-160	966.44
Np-239	106.12	Rb-86	1078
Yb-169	109.78	Ta-182	1121

The images obtained by neutron radiography are presented below in Figure1. The difference in contrast is due to the presence of the elements in the matrix Fe-Nd-B that does not absorb neutrons. We note that there are two colors, a dark which represents the clear film and the other representing the Fe-Nd-B matrix. The distribution of the components of the matrix is said to be homogeneous because the light portion of image shows that there is no chaotic distribution of these elements.

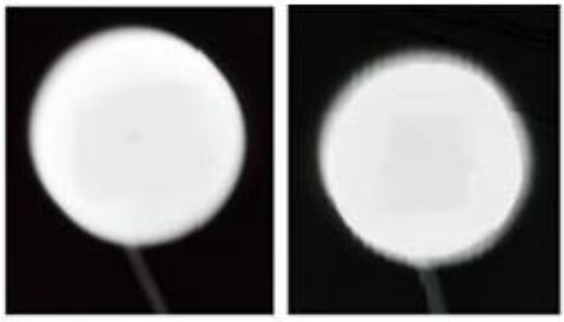

Figure1. Neutron radiography image of the Nd-Fe-B Matrix

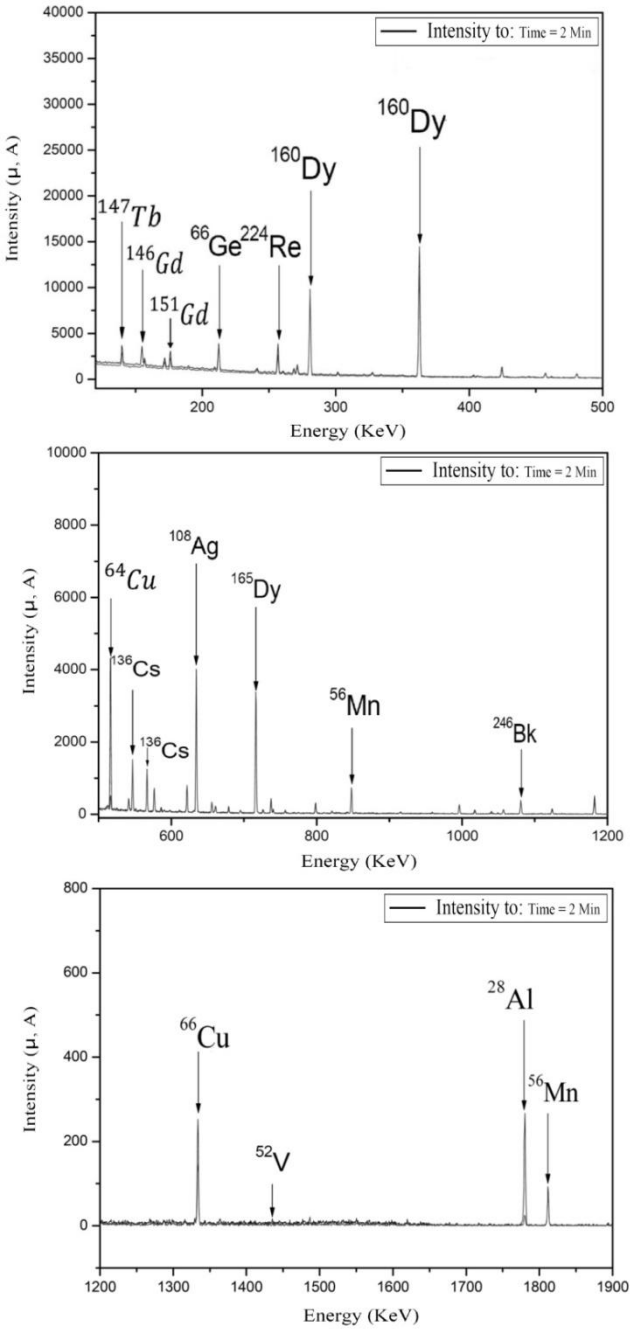

Figure2. Gamma specta of the Nd-Fe-B Matrix: (a)100-500Kev.(b)500-1200Kev.(c)1200-1900Kev.

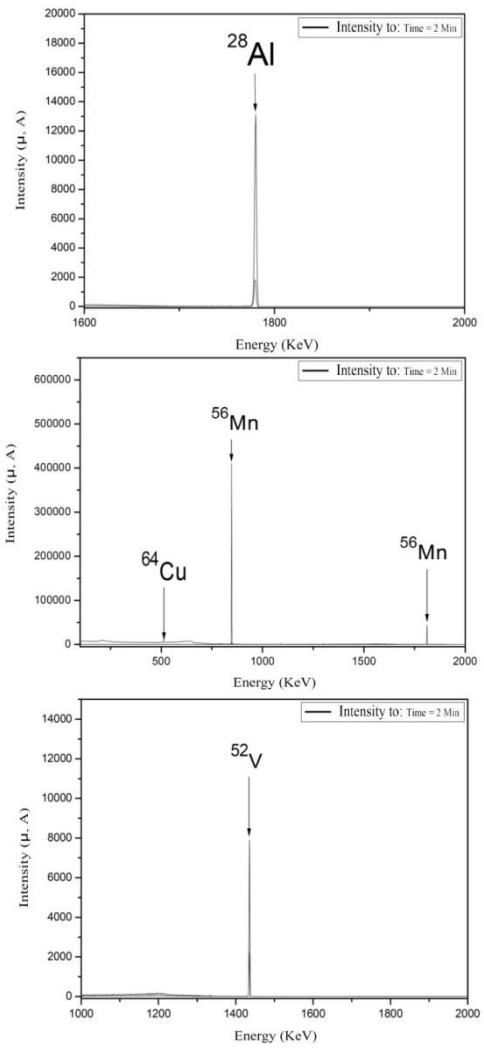

Figure3. Gamma specta of the Standard sample:(a)1600-2000Kev. (b)120-2000Kev.(c)1000-2000Kev.

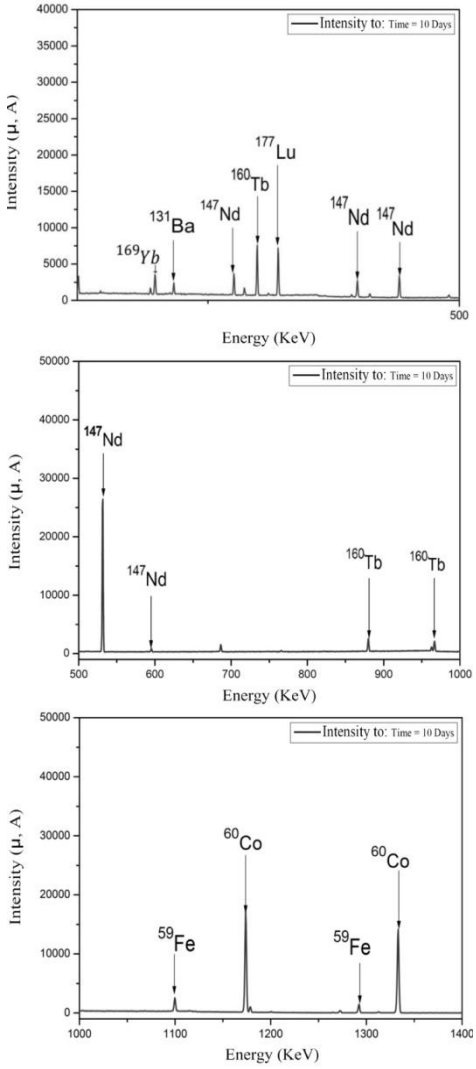

Figure4. Gamma specta of the Nd-Fe-B Matrix: (a)100-500Kev. (b)500-1000Kev. (c)1000-1400Kev.

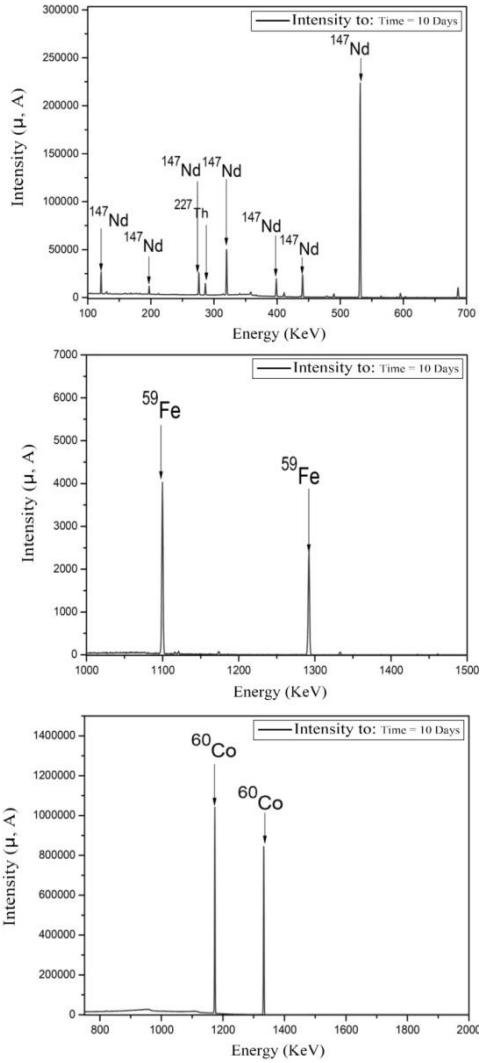

Figure5. Gamma specta of the standard sample: (a)100-700Kev. (b)100-1500Kev. (c)750-2000Kev.

The micrographs (Fig. 6), shows the microstructure of Fe-Nd-B matrix, we can see the distribution of three different phases of contrast clear, gray, and black representing the iron, the neodymium and the boron. It is observed that the distribution of components is typical of a matrix of sintering materials. Neodymium grains are distributed between iron particle interstices. The particle distribution is uniform over the entire sample surface

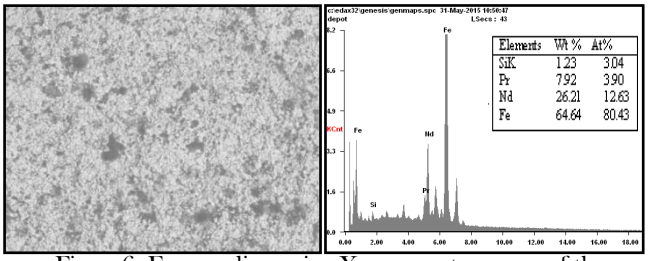

Figure6. Energy dispersive X-ray spectroscopy of the Nd-Fe-B Matrix

On the results of the precipitation tests: the best yield, 99% was obtained for [Nd]=0.003M, pH=3 and an oxalic acid concentration of 0.75M.

The obtained precipitate (neodymium oxalate) is analyzed: Identification of the three intense peaks of spectrum XRD (Fig.7) with cards ICDD, shows that three compounds are envisaged: the hydrated neodymium oxalate of $Nd_2C_6H_{20}O_{22}$ chemical formula, praseodymium hydrate ($FeO_3Pr_{0.51}$), and iron-praseodymium oxide ($Pr_5O_{30}.25H_20$).The NAA shows that the precipitate contains 86.27% of neodymium and 13.72% of praseodymium and impurities. The thermal decomposition of this precipitate is carried out in a furnace (900°C, 1H) according to the reaction (a):

$$Nd_2(C_2O_4)_3 10H_2O + 3/2\ O_2 \rightarrow Nd_2O_3 + 6CO_2 + 10H_2O \quad (a)$$

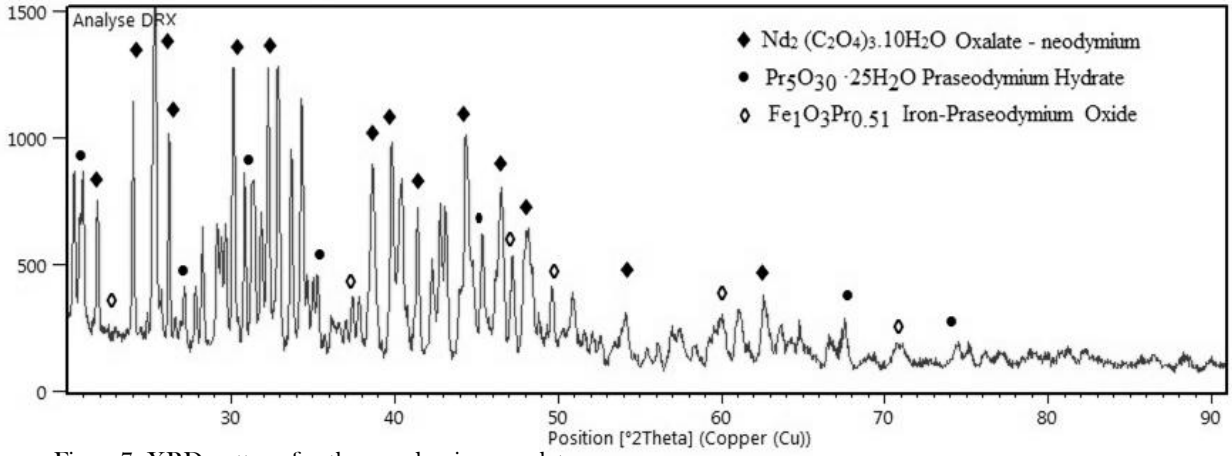

Figure7. XRD pattern for the neodymium oxalate

The result of chemical composition analysis for Nd2O3 is in accord with XRD pattern (Fig.8) and micrographs SEM/EDX (Fig.9), in which the oxide of neodymium phase (hexagonal) is observed. The spectrum shows three intense peaks corresponding to the diffraction of the plans (110), (102) and (103). The presence of PrNdO4 was also confirmed.

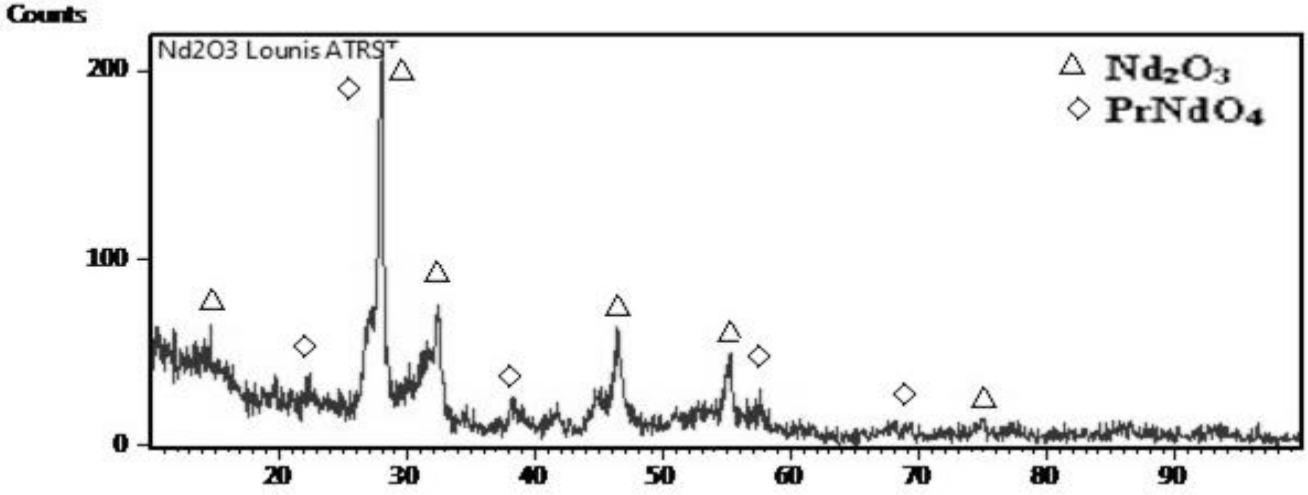

Figure 8. XRD pattern for the neodymium oxide

The last step is the reduction at 750°C of both oxides obtained previously. The choice of a reducer is conditioned initially by thermodynamic considerations resulting from the diagram of Ellingham, but also for kinetic and economic considerations. We chose CaCl2 in the presence of sodium according to reaction (b) and (c):

$Nd_2O_3+3CaCl_2+6Na \rightarrow 3CaO+2Nd+6NaCl$ (b)

$PrNdO_4+4CaCl_2+8Na \rightarrow 4CaO+PrNd+8NaCl$ (c)

The consideration of the diagrams of Ellingham is by the way when the difficulty of the reduction of oxides arises and in particular of metallic oxides in order to extract the elements. By taking into account the number of components, phases and equilibrium relations, the use of Gibbs phase rule gives a variance v =1, therefore we have an invariant system. The control of the temperature is sufficient. After reduction the product obtained is analyzed by XRD. The results are given in Figure 10. The XRD spectrum of the obtained product shows the presence of CaO, Nd, NdPr and NaCl. Three intense peaks of neodymium, assigned to the diffraction of the planes (111), (200) and (220), corresponding to cubic structure and a lattice parameter of 0.48 nm.

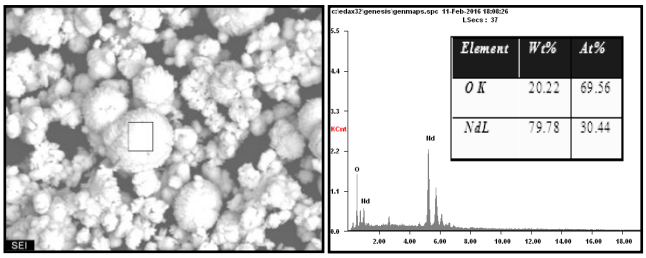

Figure9. Energy dispersive X-ray spectroscopy of the Nd_2O_3

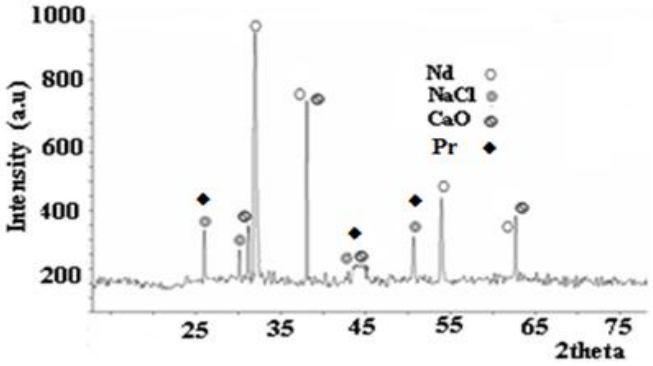

Figure10. XRD pattern reduction of neodymium oxide

4. Conclusion

Our study concerns the recovery and analysis of rare earths from the electronic waste: this work has two stages. The implementation scheme of our project in particular has embrittlement in liquid nitrogen (-196°C), a dissolving in an acid and a recovery solution by unit operation of chemical engineering that will be followed by purification of neodymium and praseodymium. The first step is to determine the content of neodymium and the impurities of a magnet Nd-Fe-B. In a second step we add an oxalic acid to precipitate Nd as neodymium oxalate after dissolved the powder (Nd-Fe-B) in hydrochloric acid. For the determination of impurities in trace, neutron activation analysis is one of the few methods that achieves its theoretical limits of detection. His response times are dependent on the decay period of radioisotopes used and can reach several days. We have shown that this method can analyze trace and ultra-trace. From the same sample NAA gives us the ability to assay simultaneously a large number of elements present in the Nd-Fe-B alloy used as a super magnet. We can clearly infer the existence of elements that accompany Fe and Nd, these are: Al28, V52, Mn56, Cu66, Ge66, Ag108, Cs 136, Lu177m, Tb160, Re224, Bk246. On the results of the precipitation tests: the best yield, 99% was obtained for [Nd]=0.003M, pH=3 and an oxalic acid concentration of 0.75M. Another step of reduction at also been used with the Ellingham diagram, is to extractive metallurgy of reducing Nd_2O_3 and $PrNdO_4$ so as to recover the metals namely Nd and Pr. The identification of the most intense peaks in the XRD spectrum shows the presence of a single compound which hydrated neodymium oxalate chemical formula $Nd_2(C_2O_4)_3.10H_2O$. Its purity is measured by neutron activation analysis. The presence of $PrNdO_4$ was also confirmed. The result of chemical composition analysis for Nd_2O_3 is in accord with XRD pattern and MEB/EDS in which the oxide of neodymium phase (hexagonal) is observed.

The processes of chemical precipitation, so the results that we found provide of real prospects for the recovery of rare earths from electronic waste

Acknowledgment

We acknowledge financial support from the Research Thematic Agency in Science and Technology. The authors are grateful for ATRST Algiers, Algeria.

References

[1] M. Zakotnik, I.R. Harris, A.J. Williams. Multiple recycling of NdFeB-type sintered magnets, Journal of Alloys and Compounds 469 (2008) 314–321

[2] C.Milmo. Concern as China clamps down on rare earth exports, 318, China 2010.

[3] S. Ruoho. Modeling Demagnetization of Sintered NdFeB Magnet Material in Time-Discretized Finite Element Analysis, Department of Electrical Engineering, New York, USA, 2011.

[4] B. Mokili, C. Potrenaud. Modelling of the extraction of Nd and Pr nitrates from aqueous solutions containing a salting-out agent or nitric acid by tri-n-butyl phosphate, Journal of Solvent Extraction and Ion Exchange. 14(4) (1996) 617.

[5] T. Saito, H. Sato, T. Motegi. Recovery of rare earths from sludges containing rare-earth elements, Journal of Alloys and Compounds, 425 (2006) 145–147.

[6] Y. Kanazawa, M. Kamitani. Rare earth minerals and resources in the world, Journal of Alloys and Compounds 408–412 (2006) 1339–1343.

[7] S. Lalleman, M. Bertrand, E. Plasari. Physical simulation of precipitation of radioactive element oxalates by using the harmless neodymium oxalate for studying the agglomeration phenomena, Journal of Crystal Growth. 342 (2011) 42–49.

[8] W. Yantasee, G.E. Fryxell, R.S. Addleman, R.J. Wiacek, V. Koonsiripaiboon, K. Pattamakomsan, V. Sukwarotwat, J. Xu, K.N. Raymond. Selective removal of lanthanides from natural waters, acidic streams and dialysate. Journal of Hazard Mater. 168 (2009) 1233–1238.

[9] W H. Duan, P J.Cao, Y J.Zhu. Extraction of rare earth elements from their oxides using organophosphorus reagent complexes with HNO_3 and H_2O in supercritical CO_2, Journal of Rare Earths. 28(2) (2010) 221.

[10] G.A. Moldoveanu, V.G. Papangelakis. Recovery of rare earth elements adsorbedon clay minerals. I. Desorption mechanism, journal of Hydrometallurgy. 117–118 (2012) 71–78.168.

[11] M. Zakotnik, I.R. Harris, A.J. Williams. Possible methods of recycling NdFeB-type sintered magnets using the HD/degassing process, Department of Metallurgy and Materials, University of Birmingham 450 (2007) 525–53.

[12] T.Itakura, R. Sasai, H. Itoh. Resource recovery from Nd–Fe–B sintered magnet by hydrothermal treatment, Journal of Alloys and Compounds, 408–412 (2005) 1382–1385.

[13] X Y.Du, T E.Graedel. Global rare earth in-use stocks in NdFeB permanent magnets, Journal of. Ind. Ecol, 15 (2011) 836.

[14] J.H. Rademaker, R. Kleijn, Y.X. Yang. Recycling as a strategy against rare earth element criticality: a systemic evaluation of the potential yield of NdFeB magnet recycling, journal of Environ. Sci. Technol. 47 (2013) 10129–10136.

[15] T.H. Okabe, O. Takeda, K. Fukuda, Y. Umetsu. Direct extraction and recovery of neodymium metal from magnet scrap, journal of Materials Transactions 44(4) (2003) 798.

[16] T. Kobayashi, Y. Morita, M. Kubota. Development of Partitioning Method:Method of Precipitation Transuranium Elements with Oxalic acid", JAERI-M88 (1988) 026.

[17] J.W. Lyman, G.R. Palmer. Recycling of rare earths and iron from NdFeB magnet scrap, Journal of High Temperature Materials and Processes. 11(1–4) (2011) 175.

[18] C. DE Wispelaere, J. P. OP DE Beeck, J. Hoste. Non-destructive determination of trace impurities in iron by thermal neutron activation analysis with long – LIVED ISOTOPES, Institute of Nuclear Sciences, Ghent University, Ghent, Journal of Analytica ChiraicaActa. 64 (1973) 321-332.

Journal of New Technology and Materials
JNTM
Vol. 07, N°01 (2017)18-26

OEB Univ. Publish. Co.

Assessing Vulnerability of groundwater with GOD model: a case study in Oran Sebkha basin - Algeria

N. Boualla[1]*, A. Benziane[1] and A. Ait-Mokhtar[2]

[1] *Université des Sciences et de la Technologie d'Oran Mohamed Boudiaf, USTO-MB, BP 1505, El M'naouer, 31000 Oran Algérie.*
[2]*Université de La Rochelle, LaSIE UMR CNRS 7356, Avenue Michel Crépeau – 17042 La Rochelle cedex 1, France.*
Corresponding author: professional Email: nabilaboualla@univ-usto.dz, nibrasnabila@yahoo.fr

Received date: September 12, 2016; revised date: May 15, 2017; accepted date: May 23, 2017

Abstract

The vulnerability of groundwater is a relative, non-measurable and dimensionless property, which is based on the concept that some land areas are more vulnerable to groundwater contamination than others. Most groundwater vulnerability modeling has been based on current hydrogeology and land use conditions. However, groundwater vulnerability is strongly dependent on factors such as depth to water, recharge and land use conditions that may change in response to future changes in climate and/or socio-economic conditions. The evaluation of the aquifer vulnerability is one of the tools supporting decision making related to aquifer protection.

This study is a help approach to protect and prevent pollution of the Oran Sebkha basin. It discusses the creation of a groundwater vulnerability map. This area of the aquifer is essentially occupied by agricultural areas characterized by an important use of chemical fertilizers, which are in addition to the discharge of industrial zones. The water resources are becoming increasingly scarce, over-exploited, poorly distributed and most especially polluted.

Information on the hydraulic confinement, overlying strata in terms of their lithological character and depth to groundwater table that is affect and control groundwater contamination were incorporated into the GOD model, to produce groundwater vulnerability maps.

The final map shows interesting results and stresses the need for the GIS to test and improve on the groundwater contamination risk assessment method. It was found that the studied water is characterized by a low to very high degree of vulnerability. A moderate vulnerability in area covering 71.5% of the extension of the shallow aquifer.

Keywords: Vulnerability, GOD, Nitrate, GIS, ARCGIS 10.

1. Introduction

Nowadays, groundwater resources play an important role in meeting demands on water supply because of regional climate change and scanty surface water source or their unsuitability (Alwathaf and El Mansouri 2011).

Pollution of groundwater is a major issue because aquifers and the contained groundwater are inherently susceptible to contamination from land use and other anthropogenic impacts (Thirumalaivasan et al. 2003), but because of the self purification function of the reservoir, groundwater is protected to the contamination. The infiltration and subsurface storage of rain and river water can reduce water stress. Artificial groundwater recharge, possibly combined with bank filtration, plant purification and/or the use of subsurface dams and artificial aquifers, is especially advantageous in areas where layers of gravel and sand exist below the earth's surface. Artificial infiltration of surface water into the uppermost aquifer has qualitative and quantitative advantages. The contamination of infiltrated river water will be reduced by natural attenuation. Clay minerals, iron hydroxide and humic matter as well as microorganisms located in the subsurface have high decontamination capacities (Balke and Zhu 2008).

Nevertheless, if the water resource is contaminated, it is not easy to modify its quality. Moreover, the groundwater quality is closely related to the lithology and the thickness of the vadose zone and the geometry of the reservoir.

All the hydrogeological aspects of the aquifer system such as recharge zone, groundwater flow and land use must be involved in the evaluation of the water resource quality.

Assessing the vulnerability of groundwater resource is a preventive tool for controlling groundwater contamination (Farjad et al. 2012). Aquifer system protection is necessary for a sustainable use and protection of the groundwater resources (Demiroglu and Dowd 2014; Gogu et al. 2003; Liggett and Talwar 2009).

In arid regions, over-exploitation of groundwater induced alarming declines in water levels (Edoulati 2013).

Generally, quality of water in arid regions is always changing due excessively factors: low rainfall, high evapotranspiration, structural and soil condition. Increasing populations and high living standards in most arid countries causes excessive water demands used in industries and urban needs (Ruopu and Merchant 2013).

Since detection, monitoring and treatment of groundwater pollution are relatively cost-prohibited;

management of groundwater quality has emphasized protection of the resource (i.e., prevention of contamination).

Protection strategies, however, need to be targeted so that staff, funds and technology can be focused upon those areas that are most threatened (Merchant 1994).

The concept of vulnerability of groundwater to contamination was introduced in the 1960s in France by Margat (1968). He used the term "vulnerability" to mean the degree of protection that the natural environment provides against the ingress of pollutants to groundwater. Since then, several definitions of vulnerability have been proposed. Groundwater vulnerability to contamination can be defined as the propensity or likelihood for contaminants to reach some specific position in the groundwater system after their introduction at some point above the top of the uppermost aquifer (Rao and Alley 1993). Generally speaking, the level of groundwater contamination is determined by the natural attenuation processes occurring within the zone between the pollution source and the aquifer (Fig. 1).

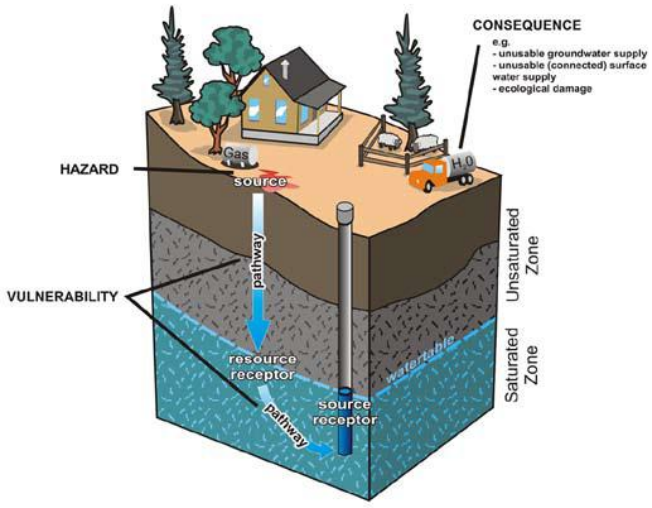

Figure 1: Source–pathway–receptor model for contaminants (Jessica and Talwar 2009).

The vulnerability is also identified as the hazard of the groundwater linked to the vadose zone lithology and the properties of the contaminant (Babiker et al. 2005; Demiroglu and Dowd 2014; Musekiwa and Majola 2013). The vulnerability of an aquifer to the pollution is related to many parameters such as lithology of the aquifer, geometry of the reservoir and hydrogeology (Varol and Davraz 2010; Moratalla et al. 2011).

Remediation of contaminated aquifers is expensive. To recognize the need to an efficient method to protect groundwater resources from contamination, scientists and managers develop aquifer vulnerability techniques to define, which areas are the most vulnerable (Pervinquere 1903).

The assessment of groundwater vulnerability to pollution has been the subject to intensive research during the past years and a variety of methods have been developed.

The available models for the assessment of the groundwater vulnerability are based on the combination of several hydrogeological parameters involved in the contamination process of groundwater.

The vulnerability concept was described based on the effect of the vadose zone to protect the groundwater quality. In fact, the vadose zone can play a key role to eliminate some pollutants infiltrated from surface water.

From 1980s, various models and approaches for the vulnerability assessment and mapping have been developed and tested all over the world (Haertle 1983; Aller et al.1987; Foster 1987; Foster and Hirata 1988). The process of groundwater vulnerability mapping combines hydrogeological parameters of the aquifer to establish a map with a zoning related to the susceptibility of groundwater contamination by pollutant (Foster et al. 2002).

Many approaches have been developed to evaluate aquifer vulnerability. They include process based methods, statistical methods, and overlay and index methods.

Then, there were several approaches for developing aquifer vulnerability assessment maps. Conventional methods (i.e. DRASTIC, AVI, GOD, SINTACS) are able to distinguish degrees of vulnerability at regional scales where different lithologies exist (Vias et al. 2005).

From the evidence available, GOD approach was used to creating a vulnerability map (Groundwater hydraulic confinement/Overlaying strata/Depth to groundwater table) (Foster 1987). The objective of this study is to assess the vulnerability of groundwater to contamination in Oran Sebkha basin area using a GOD model combined with a Geographic Information System (GIS). This method considers the soil and unsaturated zone without taking into account the transport processes in the saturated zone.

2. Morphological and structural presentation

The zone of study covers: the great Oran Sebkha basin (with an area of 1,878 km^2); the Sebkha itself (with an area of 298 km^2) and the stretches (over 40 km long and 6–13 km wide). The zone is located in the Central Coastal Oran basin and is bound by: the Djebel Murdjadjo (530 m) in the north, the Mount Tessala (1,061 m) in the south, the plain oued Tlelat in the east, and oued Mellah in the west (Fig.2) (Boualla et al. 2013).

The basin of the Great Sebkha of Oran extends over an estimated area of about 1890 km^2. According to Petroleum Geologists (Perrodon 1957), it would be part of the western extremity of the Neogene basin of Lower Cheliff. This area subsided with a sedimentation load rate (largely exceeding 300 meter/million years) (Thomas 1985), presumably presents a major continental alluvial

sedimentation in the axial area. It is also asymmetrical due to the difference in dip of the outcrops (gentle in the North, steep in South). The basin is delimited by faults, especially to the South, similar to a "collapsing rift". The basin is this composed of three main areas: the southern slopes of Jebel Murdjadjo in the north, the northern slops of Tessala Mounts in the south and the Sabkha Mlèta in the central area of the basin, where are accumulated soluble and insoluble products that come from reliefs (Fig.3).

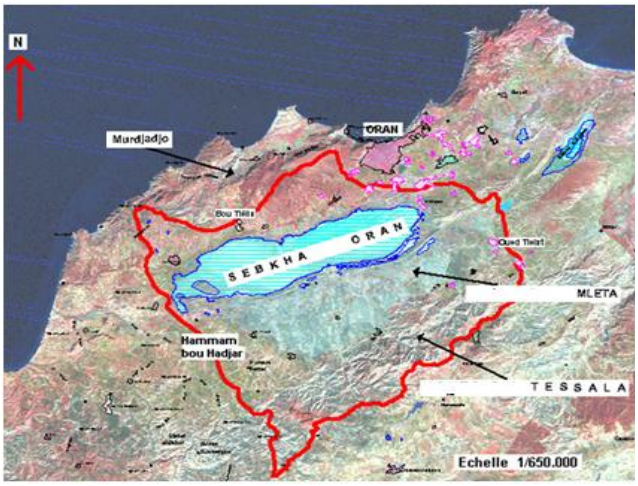

Figure 2: Location map of the great Sebkha basin of Oran.

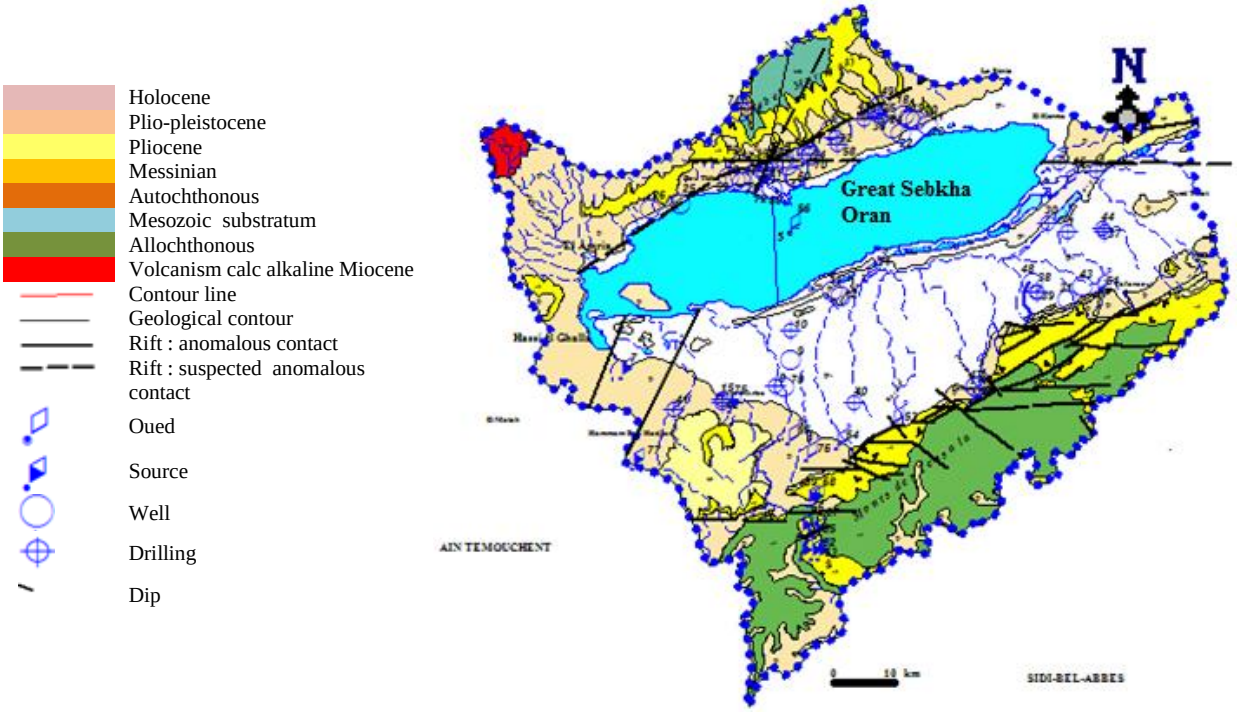

Figure 3: Aquifer system map of the Great Sebkha of Oran (Benziane 2013).

The Neogene basin of the Great Sebkha of Oran is characterized by a stack of two or three aquifers layers at the central area. The bedrock formations are characterized by water circulation of minor importance in some permeable layers, or in fracture networks. Neogene formations constitute the best groundwater reservoirs of the basin.

The Messenian consists of algae limestone outcropping on the southern slopes of Jebel Murdjadjo and on northern slopes of the Tessala Mountains.

These reef limestones are developed on both sides of the Sabkha-Mlèta area and constitute the peak of Jebel Tessala. Their extension underneath the lake remains hypothetic. The Pliocene outcrops in the El Kerma area and in the south of Aïn El Arba. These Outcrops are formed of sandstone hills characterized by a good infiltration capacity, easily absorbing rainfalls. The infiltrated water is not drained by water springs, but has to flow northward underneath the Figuier Plaine, and southward in the M'lèta Plaine. In depth, the Pliocene

sandstones contain abundant ascending water-table, of which the quality varies depending to the geographical areas. At the south of the M'lèta Plain, the Pliocene outcrops form, along the rupture line of the slope of Tessala Mountains, a more or less narrow band underneath carbonate facies. Under the plains of M'lèta and Maflak, the Pliocene sandstone, associated with the Miocene, form an aquifer complex recognized and captured by deep drilling (300–500 m); this relatively powerful set (150 m) lies locally on impermeable allochthonous formations. The Quaternary consists of alluvium extended in plains of the periphery of the Great Sebkha of Oran. They contain a groundwater table fed by its own catchment and infiltration of runoffs issued from the reliefs. Water from this aquifer generally has a high concentration of solutes and its mineralization increases gradually, when we get close to salt lake. This groundwater layer, which flows generally towards the Sebkha, is captured by farmer wells used for irrigation (Benziane 2013).

3. Methodology

Many approaches have been developed to assess groundwater vulnerability and it can be divided into three major categories: overlay and index methods, process based methods, and statistical methods. The method chosen for vulnerability assessment will depend on factors such as the scale of the study area, data availability, and the specific results desired (Tesoriero et al. 1998). In this work the GOD method was used to assess the Oran Sebkha basin vulnerability. This is an easy and quick assessment method to map the groundwater vulnerability for contamination as the classical models assume some generic contaminants. This model has relatively lesser parameters in comparison to pragmatic models such as DRASTIC, SEEPAGE, and SINTACS.

This method has a simple and pragmatic structure. It is a rating system that assesses vulnerability by means of three variables: groundwater occurrence (G), overall lithology of aquifer (O) and depth to groundwater table (D) (Foster 1987).

In developing GOD, the method's authors have given particular consideration to the likelihood of fractures or fracture systems to develop in the soils, overburden, or overlying geologic units of the aquifer. Although this method uses smaller number of parameters than other approaches, this does not imply that it is a less convincing method. It doesn't consider the heterogeneities in the used parameters. The model is described pictorially in figure 4.

The governing equation of the calculation of vulnerability index for the GOD model is given as below:

IGOD= Gr*Or*Dr

Gr is the rating assigned to the groundwater occurrence parameter; Or is the rating assigned to the overlying lithology parameter; and Dr is the rating assigned to the depth to water table parameter (tab.1).

Following the GOD flowchart, the area vulnerability index is computed by choosing first the rating of groundwater occurrence parameter and then multiplying by the overlying lithology rating as well as with the depth to water parameter rating. The overlying lithology parameter contributes to the vulnerability index only in the case of unconfined aquifers. The parameters can only take values from 0 to 1 (tab.2), the computation result is usually a value less than the score assigned to each parameter.

The overlying lithology contributes to the vulnerability index only in the case of unconfined aquifers (in other words, is equal to one for other types of aquifers).

In the particular case where two parameters have a value equal to 1, the vulnerability score is equal to the score of the third parameter (Gogu et al. 2003). For this, geology map 28 boreholes boreholes were considered.

To indexing spatial information a variety of GIS analysis and geo-processing framework has been applied using ArcGIS 10 software.

Table 1: Attribution of notes for GOD model parameters (Khemiri et al. 2013).

Aquifer type Gr	Note	Depth Dr (m)	Note	Lithology Or	Note
None aquifer	0	<2	1	Residual soil	0.4
Artesian	0.1	2-5	0.9	Limon alluvial, loess, shale, fine limestone	0.5
Confined	0.2	5-10	0.8	Acolian sand, siltite, tuf, igneous, rock	0.6
Semi-confined	0.3	10-20	0.7	Sand and gravel, sandstone, tufa	0.7
Free with cover	0.4-0.6	20-50	0.6	Gravel	0.8
Free with cover	0.7-1	50-100	0.5	Limestone	0.9
		>100	0.4	Fracture or karstic limestone	1

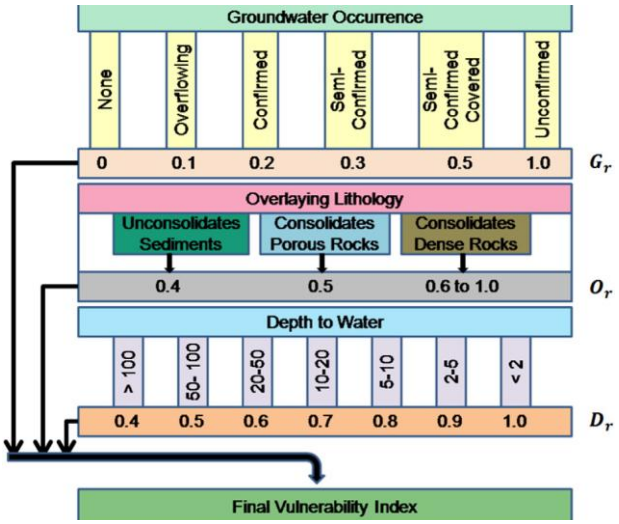

Figure 4: GOD model (Foster 1987).

Table 2 Reclassification of the methods in order to carry out the comparison (Khemiri et al. 2013).

Vulnerability	Class	GOD
Very high	A	0.7-1
High	B	0.5-0.7
Intermediate	C	0.3 – 0.5
Low	D	0.1-0.3

4. Result and discussion

This work can be greatly eased by using a GIS for overlaying the different data sources. GIS allows spatial data gathering, at the same time, gives a means for data processing such as geo-referencing, digitizing and spatial analysis.

Groundwater Contamination Risk Mapping is carried out by overlay of layers representing the different parameters in the par-metrics models.

After mapping all the parameters, the vulnerability maps were obtained by overlaying the individual maps. The spatial mapping in Raster format by interpolation of these parameters is a necessary step in this work. In this case, we obtain the result shown in (Fig.5). The vulnerability index for GOD model is calculated and the final vulnerability map was subdivided into classes related to vulnerability degrees of according to the classification. All the realized maps are projected in "WGS 1984 UTM Zone 32N".

According to the previous discussion Classification of groundwater vulnerability, the study area was divided into four vulnerable classes these classes indicate areas of higher, moderate, and low groundwater vulnerability. Low and moderate vulnerability covers about 7.1 % and 71.5% of the study area. They are essentially due to the deep groundwater, the low permeability and the vadose zone sediments, added to that the low hydraulic conductivity. The recharge and the depth of groundwater are two parameters having an influence on vulnerability degrees to pollution. The groundwater in these areas is most protected from pollutants so these areas are the most suitable areas for sustainable development. High vulnerability assigned to 1.12% of the study area. The north-west part of basin (Amria, Hassi El Ghella, Messerghin and south part of Sebkha) is the most exposed part to contamination with very high vulnerability is assigned 0.56 % . The region is an area of high agricultural activity with an intense use of chemical fertilizers.

The combination of quaternary alluvium, shallow groundwater, high recharge and high hydraulic conductivity. Results in a low capacity to attenuate the contaminants. A high vulnerability is linked with the type of soil, a permeable vadoze zone, and a slight slope.

Coarse texture of the soil zone and high downward flows which permit infiltration of more pollutants from the upper Holocene to the underlying Pleistocene aquifer, the risk of vulnerability of groundwater pollution in that area is high (Feumba and Ngoumou Ngatcha 2014).

In order to investigate the effect of over-farming on groundwater quality and to indentify an appropriate methodology for pollution risk management, we have carried out a comparative study on the potential risk of contamination from nitrate of agricultural origin, combined with the GOD aquifer vulnerability methods. All parameters used in this risk assessment were prepared, classified, weighed, and integrated in a GIS environment. For calibrating the models and optimizing and/or weighing the examined factors, the modeling results were validated by comparing them with groundwater quality data, in particular nitrate content. The criterion for checking this method was the correlation coefficient of each model with the nitrate concentration in the groundwater. A relative coincidence of a high nitrate concentration and risk mapping was observed, this correlation was significant using the GOD method (Pisciotta et al. 2015).

The vulnerability approach is easy to apply and provides a good assessment of groundwater vulnerability to contamination. A great similarity can be observed in the distribution of the vulnerable zones recognized by map of nitrate (fig. 6).

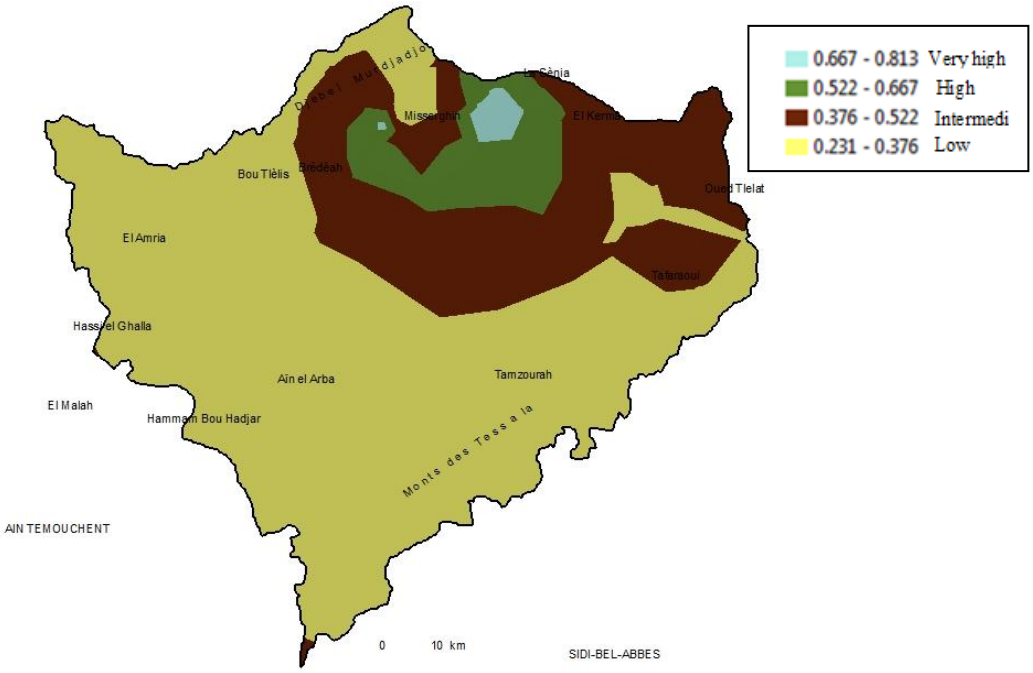

Figure 5: Vulnerability map of Oran Sebkha basin.

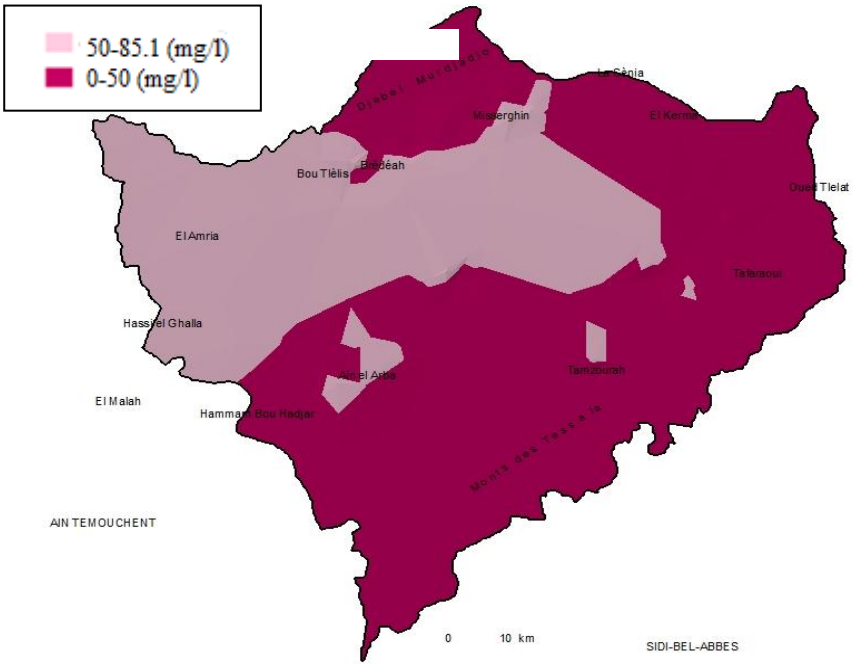

Figure 6: Nitrate pollution map.

Over fifty five water samples collected, eleven exceed the guideline value for nitrate in drinking water of 50 mg/l (WHO 2004), up to levels of about 85.1 mg/l by spectrometry method (Spectrometer Optizen 2120 UV). Highest concentration of nitrate was recorded at Boutlélis, Al Amria and Hassi El Ghalla.The calcareous/gypsum and sandy/marl aquifers are the system with the highest intrinsic vulnerability values. The main groundwater reservoirs are shallow aquifers with the water table being only a few tens of meters deep with overburden permeability on average quite high therefore short travel times for infiltration, this can indicate that the main source of nitrate pollution in the groundwater is due directly to

farming. May be increases in nitrate contents can be also attributed to the recharging pollution of sanitary drainage according to local movement of groundwater. The nitrate pollution map was based on average values for all of the measurements of nitrate concentration recorded for each sampling point (as there were no significant intra-annual variations). ArcGIS 10 was used to interpolate the nitrate concentrations used to generate the nitrate pollution map.

These observations lead to the conclusion that the vulnerability methods underestimate the real distribution of vulnerability to anthropogenic sources and do not take into account the specific properties of particular contaminants and they are inflexible in the assignment of ratings and weights to the model parameters (Sener and Davraz 2013). The methods applied only emphasize the special importance of the lithological nature of the unsaturated zone and of the soil texture for the purposes of vulnerability mapping.

This consideration explains the similarities of the distribution of vulnerability shown by the maps of the GOD method and nitrate. The intrinsic nitrate contamination risk from agricultural sources reflects the probability of groundwater to be actually contaminated by human activities. The potential risk maps show the highest risk of nitrate pollution of groundwater.

The intensive agricultural activities, inappropriate placement of commercial and industrial regions and high intensity residential areas can potentially cause pollution of the groundwater. The main aim of this study was to evaluate two prevalent vulnerability parametric methods.

GOD method developed from the probability estimation of the groundwater contaminant concentrations, hydrogeological approaches, and evaluation of the pollution risk from anthropogenic activities to assess the groundwater quality monitoring network and evaluate the risky zones of the aquifers (Pisciotta et al. 2015). The vulnerability mapping identifies locations which must have a high priority in terms of protection and pollution prevention.

5. Conclusion

The GIS techniques use, to identify contamination risk by mapping, is primarily due to the automatization of certain operations. The database, which is "behind" each layer can any time be updated. In addition, the use of GIS facilitates the rapid visualization of some elements in the map by selecting them from the attribute table. Vulnerability and the land use maps, contamination data and groundwater quality can be used in view of a rapid and correct evaluation of pollution risk. We are assured by using this technology that the information will be used in an efficient manner.

The GIS developed is a good decision tool. It is an efficient method for water resources management to evaluate vulnerability. The results are a way to avoid possible contamination water.

The vulnerability of groundwater to contamination in the study area was quantified by using the GOD model combined with GIS. The models application showed that Oran Sebkha basin was characterized by low to very high vulnerability degrees. The most vulnerable areas to pollution are located in the northwest part.

This disparity may be related to notes assigned to various parameters (Murat eta l. 2003), the groundwater over-exploitation, the high permeability, the lithologic variability that are marked mainly by quaternary alluvium, facilitates the rainwater infiltration and accumulation. Waters are easily accompanied by various geochemical elements coming from toxic pesticides and their extensive use in farmland, and wastewater. In high vulnerability areas, we shouldn't allow additional high risk activities in order to obtain economic advantage and to reduce environmental pollution hazard and temporal scales. The vulnerability methods have to be used as screening tools. The aquifer protection issues are discussed using the groundwater vulnerability concept. Groundwater vulnerability to the pollution is a dimensionless parameter, which is not directly measurable. It cannot replace the professional expertise. In all cases, the limitations of different classes found, are not absolute values, but relative values (Khemiri et al. 2013). These limits can then vary from one study to another.

GOD method can be a good idea to sensitive zone in order to be forecast necessary protection for vulnerable area.

This paper represents a contribution to the problem of groundwater contamination risk assessment, and it shows the need to continue the research in this direction in order to improve and to standardize methods for the construction of the basic thematic maps and the final map.

References

[1] Alwathaf, Y., El Mansouri, B., 2011. Assessment of Aquifer Vulnerability Based on GIS and ARCGIS Methods: A Case Study of the Sana'a Basin (Yemen). Journal of Water Resource and Protection. 3, 845-855 doi:10.4236/jwarp.2011.312094.

[2] Aller, L., Bennet, T., Lehr, J.H., Petty, R.J., 1987. DRASTIC: A Standardized System for Evaluating Ground Water Pollution Potential using Hydro Geologic Settings, U.S. EPA.

[3] Babiker, I.S., Mohamed, A.M., Hiyama, T., Kato, K., 2005. A GIS-based DRASTIC model for assessing aquifer vulnerability in Kakamigahara Heights, Gifu Prefecture, Central Japan. Sci. Total Environ. 345 (1–3), 127–140.

[4] Balke K.D., Zhu, Y., 2008. Natural water purification and water management by artificial groundwater recharge.

J Zhejiang Univ Sci B. 9 (3). 221–226. doi: 10.1631/jzus.B0710635.
[5] Benziane, A., 2013. Le système aquifère de la Grande Sebkha d'Oran : considérations géologiques et hydrogéologiques. Bulletin de l'Institut Scientifique, Rabat, Section Sciences de la Terre, n° 35, 77–92.
[6] Boualla, N., Benziane, A., Moussa, K., 2013. An assessment of the physico-chemical parameters of Oran sebkha basin. Appl Water Sci DOI 10.1007/s13201-013-0149-3.
[7] Demiroglu, M., Dowd, J., 2014. The utility of vulnerability maps and GIS in groundwater management: a case study. Turkish J. Earth. Sci. 23, 80–90.
[8] Edoulati, N., Boutaleb, S., Bettar, I., Ouchbani, A., 2013. Contributions of Chemical and Isotopic Tools for Un- derstanding the Groundwater Modes Recharge and Flow in the Lower Cretaceous Aquifer in the Moroccan Sa- hara," Journal of Water Resource and Protection, Vol. 5, No. 2, 2013, pp. 183-199. doi:10.4236/jwarp. 52020.
[9] Farjad, B., Zulhaidi, H., Mohamed, T.A., Pirasteh, S., Wijesekara, N., 2012. Groundwater intrinsic vulnerability and risk mapping. Water Manage. 165, 441–450.
[10] Feumba, R., Ngoumou Ngatcha, B., 2014. Maps of vulnerability to pollution : a useful tool for sustainable groundwater in Douala, Cameroon. 37th WEDC International Conference, Hanoi, Vietnam.
[11] Foster, S.S.D., 1987. Fundamental concepts in aquifer vulnerability, pollution risk and protection strategy. In: Duijvenbooden W. van and Waegeningh H.G. van (Eds.): NOCommittee on Hydrological Research, The Hague. Vulnerability of soil and groundwater to pollutants, Proceedings and Information, vol. 38, pp.69–86.
[12] Foster, S.S.D., Hirata, R., 1988. Groundwater Pollution Risk Assessment: A Methodology Using Available Data. WHO-PAHO/HPE-CEPIS Technical Manual, Lima, Peru, 78 pp.
[13] Foster, S., Hirata, R., Gomes, D., D'Elia M., Paris, M., 2002. Groundwater Quality Protection. A guide for water utilities, municipal authorities, and environmental agencies. The World Bank. Washington, D.C.
[14] Gogu, R.C., Hallet, V., Dassargues, A., 2003. Comparison of aquifer vulnerability assessment techniques. Application to the Neblon river basin (Belgium). Environ. Geol. 44 (8), 881–892.
[15] Haertle, A., 1983. Method of working and employment of EDP during the preparation of groundwater vulnerability maps. Int. Assoc. Hydrol. Sci. Publ. 142, 1073–1085.
[16] Jessica, E.L., Talwar, S., 2009. Groundwater Vulnerability Assessments and Integrated Water Resource Management. Streamline Watershed Management Bulletin Vol. 13/No. 1Fall.
[17] Khemiri, S., Khnissi, A., Ben Alaya, M., Saidi, S., Zargouni, F., 2013. Using GIS for the Comparison of Intrinsic Parametric Methods Assessment of Groundwater Vulnerability to Pollution in Scenarios of Semi Arid Climate. The Case of Foussana Groundwater in the Central of Tunisia. Journal of Water Resource and Protection, 2013, 5, 835-845 http://dx.doi.org/10.4236/jwarp.2013.58084 Published Online August (http://www.scirp.org/journal/jwarp).
[18] Liggett, J.E., Talwar, S., 2009. Groundwater vulnerability assessments and integrated water resource management. Streamline Watershed Manage. Bull. 13 (1), 18–29.
[19] Margat, J., 1968. Ground water vulnerability to contamination (in French). Bases de al cartographie, (Doc.) BRGM, 68 SGC 198 HYD, Orleans, France.
[20] Merchant, J.M., 1994. GIS-based groundwater pollution hazard assessment: a critical review of the DRASTIC model. Photogramm Eng Remote Sens;60(9):1117–27.
[21] Moratalla, A., Gomez-Alday, J.J., Sanz, D., Castano, S., De Las Heras, J., 2011. Evaluation of a GIS-based integrated vulnerability risk assessment for the Mancha oriental system (SE Spain). Water Resour. Manage. 25, 3677–3697.
[22] Murat, V., Paradsi, D., Savard, M.M., Nastev, M., Bourque, E., Hamel, A., Lefebvre, R., Martel, R., 2003. Vulnérabilité à la nappe des aquifères fracturés du sud-ouest du Québec : évaluation par les méthodes DRASTIC et GOD. Commission géologique du Canad, Recherches en cours 2003 D3, 14p.
[23] Musekiwa, C., Majola, K., 2013. Groundwater vulnerability map for South Africa. South African J. Geomatics 2, 152–163.
[24] Perrodon, A., 1957. Étude géologique des bassins néogènes sublittoraux de l'Algérie occidentale. Publ. Serv. Carte géol. de l'Algérie, 12, 328 p.
[25] Pervinquere, L., 1903. Geological Study of Central Tunisia," Ph.D. Thesis, Es-Sci. University, Paris, 360 pages.
[26] Pisciotta, A., Gioacchino, C., Rocco, F., 2015. Groundwater nitrate risk assessment using intrinsic vulnerability methods: A comparative study of environmental impact by intensive farming in the Mediterranean region of Sicily, Italy. Journal of Geochemical Exploration 156 89–100.
[27] Rao, P.S.C., Alley, W.M., 1993. Pesticides. In: Alley WM (ed) Regional groundwater quality. Van Nostrand Reinhold, New York, pp 345–382.
[28] Ruopu, L., Merchant, J.W., 2013. Modeling vulnerability of groundwater to pollution under future scenarios of climate change and biofuels-related land use change: A case study in North Dakota, USA". Papers in Natural Resources. Paper 368. http://digitalcommons.unl.edu/natrespapers/368.
[29] Sener, E., Davraz, A., 2013. Assessment of groundwater vulnerability based on a modified DRASTIC model, GIS and an analytic hierarchy process (AHP)

method: the case of Egirdir Lake basin (Isparta, Turkey). Hydrogeol. J. 21, 701–714.

[30] Tesoriero, A.J., Inkpen, E.L., Voss, F.D., 1998. Assessing ground-water vulnerability using logisticregression. Proceedings for the Source Water Assessment and Protection 98 Conference, Dallas,TX; p. 157 – 65.

[31] Thomas, G., 1985. Géodynamique d'un bassin intramontagneux : le bassin du Bas Chélif occidental (Algérie) durant le Mio-plioquaternaire. Thèse Doct. es-Sciences, Univ. Pau et Pays de l'Adour, 594 p.

[32] Thirumalaivasan, D., Karmegam, M., Venugopal, K., 2003. AHP-DRASTIC: Software for Specific Aquifer Vulnerability Assessment Using DRASTIC Model and GIS. Environmental Model & Software. 18 (7). 645-656. doi:10.1016/S1364-8152(03)00051-3 .

[33] Varol, S.O., Davraz, A., 2010. Hydrogeological investigation of Sarkikaraagac Basin (Isparta, Turkey) and groundwater vulnerability. Water Int. 35 (2), 177–194.

[34] Vias, J. M., Andreo, B., Perles, M. J., Carrasco, F., 2005. A Comparative Study of Four Schemes for Groundwater Vulnerability Mapping in a Diffuse Flow Carbonate Aquifer Under Mediterranean Climatic Condition. Environmental Geology. 47 (4), 586-595. doi:10.1007/s00254-004-1185-y.

[35] WHO. 2004. [Online] Available: www.who.int/water_sanitationhealth/publications/facts2004/en/index.html. World Health Organization (WHO) (2004) Guidelines for Drinking Water Quality, 1 Recommendations, 3rd edn. WHO, Geneva.

Journal of New Technology and Materials
JNTM
Vol. 07, N°01 (2017)27-32

OEB Univ. Publish. Co.

Breves generator of pulses at different flow rates (40 GHz, 80 GHz and 160 GHz)

Amar Hamouda and Kaddour Saouchi

Laboratory of Study and Research in Instrumentation and Communication of Annaba (LERICA).
Electronics department, Badji Mokhtar university of Annaba, Algeria
Email:amarhamouda23@gmail.com
Received date: April 21, 2016; revised date: April 28, 2017; accepted date: May 23, 2017

Abstract

This work presents the realization by simulation a breves generator of pulse has different flow rates (40 GHz, 80 GHz, 160 GHz). In a first step, we have realized the source of short pulse train at 40 GHz by the non-linear compression of a sinusoidal flapping through a process of mixtures four multi-wave, using the Mach-Zehnder modulator and optic isolator simple. In a second step, the pulse train obtained is then fiberized to reduce the duty ratio of 1/5 to 1/16. In a third step the train obtained encoded then multiplexed to a throughput of 80 Gbit/s. In the last step, we present the re-coding and re-multiplexing again, in order to obtain a rate of 160 Gbit/s, in order to perform simulation a brief pulse generator, simple, easy implementation, is not expensive, in three outputs of different rates, stable and without jigs.
Keywords: optic *isolator, pulse train, Mach-Zehnder modulator, four wave multiplexing, temporal compression.*

1. Introduction

Laser sources emitting ultra-short pulses at very high repetition rates (>10GHz) are increasingly used in many applications such as clock generation, all-optical computers, the spectroscopy or testing components. Many works have been made to design impulse fibered sources that offer a great flexibility in terms of pace and time width [1].

Technically increased flows inevitably require the use of pulses of shorter and shorter, which can propagate in a stable way for high power injected into the fiber. From a fundamental point of view, propagation of ultra-short sets games linear effects and non-linear pulses such that the chromatic dispersion, the four-wave mixing, self phase modulation and the Brillouin and Raman effects [2].

Components such as gain switching laser (gain-switched laser) or of the mode-locked laser diodes (Locked Mode Laser Diode) are the main pulsed sources used for generating the optical pulse train, necessary in systems transmissions OTDM. However, these solutions are laboratory components, and most of them are expensive and not always commercially available [3]. But at least most CW laser fulfills this role easily and commercially available, on the other hand, the association of OTDM and WDM techniques can increase the overall throughput of the transmission systems [3]. Speeds exceeding Tb/s have been achieved. However, the incoherent nature of the pulses optical sources impose significant spectral spacing between channels in wavelength-division multiplexing [2]. These factors are the starting point of this work, the aim is to achieve a simulation of a generator has an optical transmission system in time division multiplexing, optical components based on low cost and commercially available.

The solution chosen for the optical pulse train generation will introduce constraints on its coherent nature. However, eliminating these constraints, the system has the advantage of a very narrow optical spectral efficiency. This allows OTDM techniques, with a much lower spectral channel spacing than those obtained with conventional solutions [1].

The system described here allows the transmission of data to an overall bit rate of 160 Gb/s after multiplexing. The components used are nevertheless suitable for a flow rate of 160 Gb/s, and their commercial availability allow to consider concrete applications and short-term designed system.

2. Theoretical study

2.1. Mounting of the generator

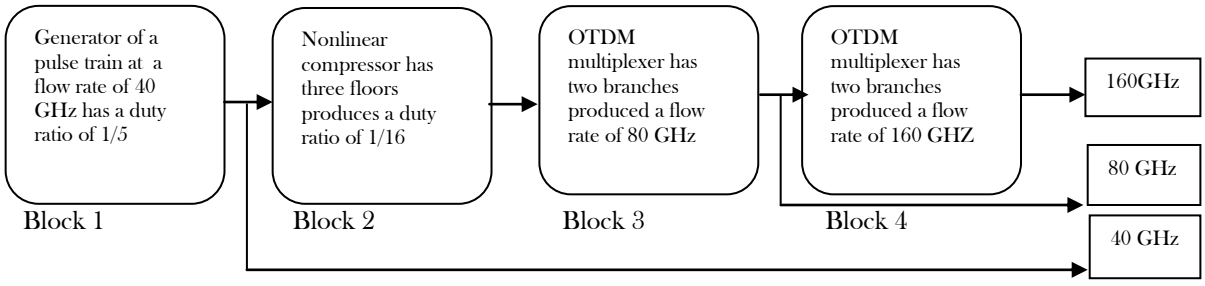

Figure1. Installation of the generator

The installation of the generator is simple, easy implementation is not expensive, consists of four blocks, three different repetition rates of outputs (40 GHz, 80 GHz and 160 GHz) stable and without jigs (see figure 1).

2.1.1. Block 1

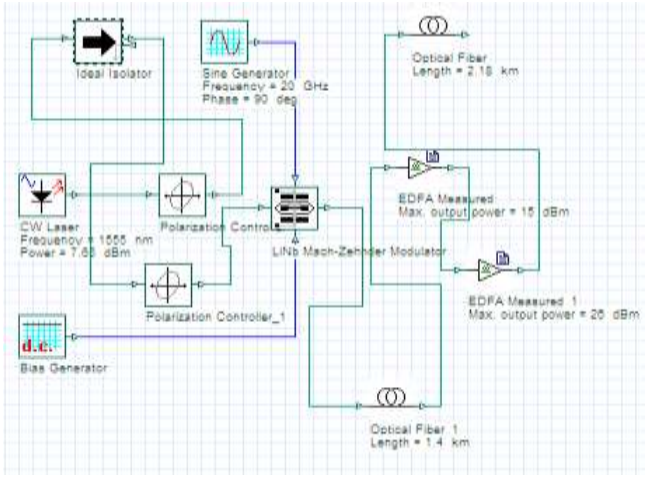

Figure 2. Optical source of breves pulse at 40 GHZ

This block (see figure 2) is a source of breves pulse at a flow rate of 40 GHZ, with a duty ratio of 1/5 (temporal pulse width/pulse period of this), consists of a laser source (CW laser) issued continuous power equal a 7.65 dBm has a wavelength 1555 nm, that power passes through the first polarization controller which optimizes the power level at the output of the isolator, this isolator has the role to completely remove the Brillouin effect, the second polarization controller is used to adjust the bias on the axis of Mach-Zehnder modulator, the latter driving a generator at very high frequencies of 20 GHZ (see figure 6), is obtained at the output of the modulator a pulse train of 40 GHz (see figure 7 and figure 12), was pre-amplified by EDFA1 then amplified by EDFA2, the resulting pulse train is injected into the first fiber, this product a rhythmic pulse train at 40 GHz by nonlinear compression of a sinusoidal flapping through a process mixture of four multi-wave [4],[5],[6], stable and without jigs, has a duty ratio of 1/5 (see figure 8 and figure 13).

2.1.2. Block 2

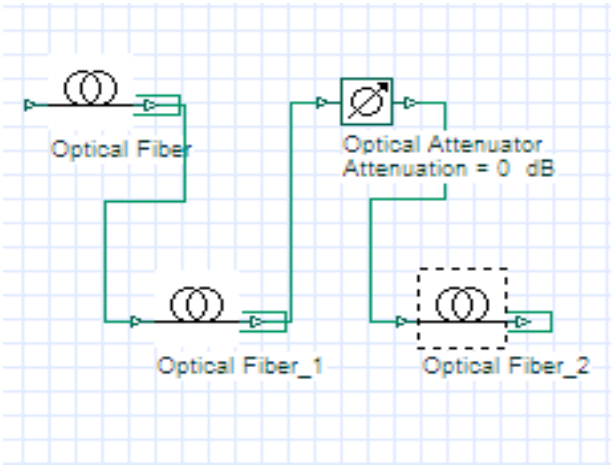

Figure 3. The compressor non-linear

This block (see figure 3) presents a nonlinear compressor, to decrease the duty ratio of 1/5 to 1/16, is composed of three floors, each floor performs a type of fiber to specified parameters (fiber length L, chromatic dispersion D, nonlinear coefficient Kerr γ) (see figure 9 and figure 14).

2.1.3. Block 3

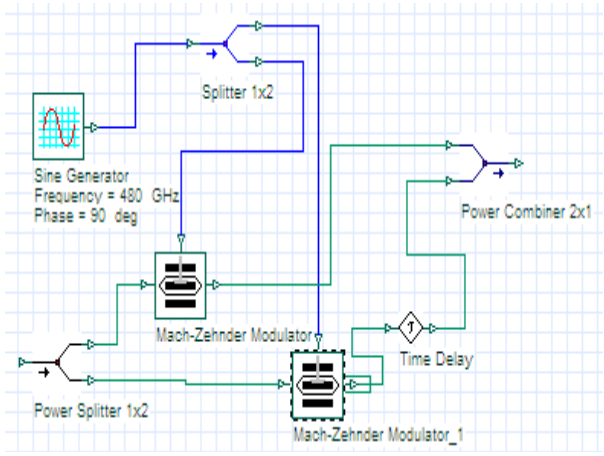

Figure 4. The first OTDM multiplexer

This block (see figure 4) is an OTDM multiplexer [7], rhythmical to the flow of the previous block has 80 GHz repetition of frequencies, consists of two branches, each branch delays the pulse train relative to the previous branch a duration τ well determined (see figure 10).

2.1.4. Block 4

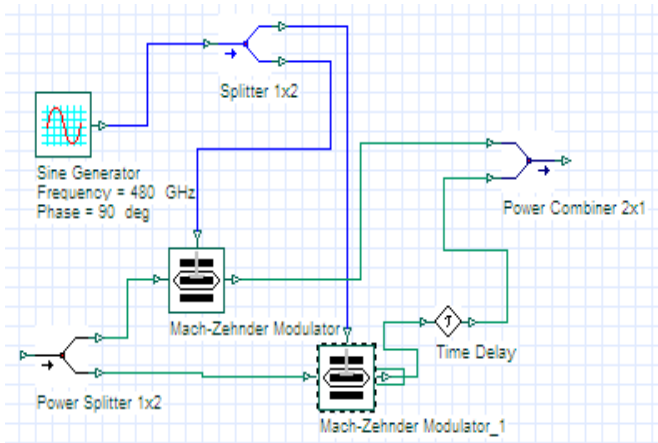

Figure 5. The second OTDM multiplexer

The latter block (see figure 5) is a second multiplexer by the OTDM method, he even flow rate of the previous block a repetition rate of 160 GHz, contains two branches, one of the two branches delays the pulse train

relative to another a duration τ (τ= the period of the pulse/the number of branches), (see figure 11).

2.2. Nonlinear Schrodinger equation

A light pulse of slowly varying envelope A(0,t), which propagates in an optical fiber can be described by the generalized nonlinear Schrödinger equation[8],[9],[10]

$$\underbrace{\frac{\partial A}{\partial z}}_{\text{Propagation}} + \underbrace{i\frac{\beta_2}{2}\frac{\partial^2 A}{\partial t^2} - \frac{\beta_3}{6}\frac{\partial^3 A}{\partial t^3}}_{\text{Chromatic dispersion}} + \underbrace{\frac{\alpha_L}{2}A}_{\text{losses}} - \underbrace{i\gamma|A|^2A}_{\text{Effect of Kerr}} + \underbrace{i\gamma T_r\frac{\partial|A|^2}{\partial t}A}_{\text{effect of Raman}} + \underbrace{\frac{\gamma}{\omega_0}\frac{(\partial|A|^2A)}{\partial t}}_{\text{Stiffening}} = 0 \quad (1)$$

Theoretically, the dispersion effects are expressed by the Taylor expansion in Taylor series of the propagation constant around the carrier frequency of the following:

$$\beta(\omega) = \frac{\omega}{c}n(\omega) = \beta_0 + \beta_1(\omega-\omega_0) + \frac{\beta_2}{2}(\omega-\omega_0)^2 + \frac{\beta_3}{6}(\omega-\omega_0)^3 + \cdots + \frac{\beta_m}{m!}(\omega-\omega_0)^m \quad (2)$$

With $\beta_m = \left(\frac{\partial^m\beta}{\partial t^m}\right)_{(\omega=\omega_0)}$ ou $\beta_3 = \left(\frac{\partial^3\beta}{\partial t^3}\right)_{(\omega=\omega_0)}$ (3)

is the chromatic dispersion of order 3.

While β_2 reflects the fact that two neighboring frequencies see a different group velocity. It is commonly called (dispersion coefficient of group velocity GVD):

$$\beta_2 = \left(\frac{\partial^2\beta}{\partial t^2}\right)_{(\omega=\omega_0)} = \frac{1}{V_g^2}\frac{\partial V_g}{\partial\omega} = \frac{1}{c}\left[2\frac{\partial n}{\partial\omega} + \omega\frac{\partial^2 n}{\partial\omega^2}\right] \quad (4)$$

However, the scientific community telecommunications prefers the use of another parameter D (ps/(nm.km)). The two parameters are related by the following relation ship: $D = -\frac{2\pi c}{\lambda^2}\beta_2$ (5)

The length of the fiber corresponds to the distance at the end of which the initial pulse of a time width 1/e, T_0 has expanded a $\sqrt{2}$ factor is expressed as a result:

$$L_D = \frac{T_0}{|\beta_2|} \quad (6)$$

Electric field incident and modulates around a carrier has ω_0, modifie by his mere presence the index of the medium through which it passes, this change results from the Kerr effect and is dictated by the power profile

$$P(z,t) = |A(z,t)|^2 \quad (7)$$

As indicated by the equation : $n = n_0 + \frac{P(z,t)}{A_{eff}}$ (8)

n_0 : normal refractive index, n_2 is the nonlinear refractive index, A_{eff} is the effective area of the fiber.

The Kerr coefficient γ is expressed by the following equation: $\gamma = \frac{\omega_0 n_2}{cA_{eff}}$ (9)

The phase shift from the self phase modulation given by the following expression:

$$\varphi_{NL} = \gamma|A(0,t)|^2 z \quad (10)$$

This reflects a shift

$$\delta\omega(t) = -\frac{\partial\varphi_{NL}}{\partial t} = -\gamma\frac{\partial|A(0.t)|^2}{\partial t}z \quad (11)$$

Fiber length for which the nonlinear effects become important is expressed by the following equation :

$$L_{NL} = \frac{1}{\gamma P_0} \quad (12)$$

criterion $L_D = L_{NL}$ can describe the soliton pulse [11], proposed in 1973 by Hasegawa and Tapper in the form of a hyperbolic secant as a result :

$$A(z,t) = N\sqrt{P_0}\,\mathrm{sech}\left(\frac{t}{T_0}\right)\exp\left[\frac{iP_0 z}{2\gamma}\right] \quad (13)$$

With N is the order of the soliton, T_0 time width 1/e of the pulse and P_0 the peak power of the soliton connected to the parameter of the optical fiber, gift:

$$P_0 = \frac{\beta_2}{\gamma T_0^2} \quad (14)$$

3. Characteristics and values of components parameters

From the equations (1,..,14), has achieved the following components parameters and values:

Table 1. Fiber parameters and value

fiber	Parameters	Symbol	Value
Fiber 1 DCF (Dispersion compensating Fiber)	Fiber length	L_1	1.4 Km
	Chromatic dispersion	D_1	-100 ps/(nm.Km)
	Nonlinear Kerr coefficient	γ_1	1.3 $W^{-1}.Km^{-1}$
Fiber 2 SMF (Standart Fiber)	Fiber length	L_2	2.18 Km
	Chromatic dispersion	D_2	17 ps/(nm.Km)
	Nonlinear Kerr coefficient	γ_2	1.7 $W^{-1}.Km^{-1}$
Fiber 3 NZ-DSF (Non-Zero Dispersion Shifted Fiber)	Fiber length	L_3	1.29 Km
	Chromatic dispersion	D_3	-1.5 ps/(nm.Km)
	Nonlinear Kerr coefficient	γ_3	1.3 $W^{-1}.Km^{-1}$
Fiber 4 HNLF (High Non-Linear Fiber)	Fiber length	L_4	1 km
	Chromatic dispersion	D_4	-0.45 ps/(nm.Km)
	Nonlinear Kerr coefficient	γ_4	10 $W^{-1}.Km^{-1}$
	Dispersion slope	S	0.01 $ps/(nm^2.Km)$
	Coeffecient losses	α_L	1.64 dB/Km
Fiber 5 SMF 28 (Standard	Fiber length	L_5	0.145 Km
	Chromatic	D_5	17.5

Fiber)	dispersion		ps/(nm.Km)
	Nonlinear Kerr coefficient	γ_5	1.3 $W^{-1}.Km^{-1}$

Table 2. Components parameters and values

Component	Parameter	Symbol	Value
Laser source	Wave length	L	1555 nm
	Power	P	7.65 dBm
Mach-Zehnder Modulator 1	Extinction ratio	U_{ext}	21.5 v
	Bias voltage	V_b	11 v
Mach- Zehnder Modulator 2	Extinction ratio	U_{ext}	33 v
EDFA amplificator 1	Maximum output power	$P_{s,max}$	15 dBm
EDFA amplificator 2	Maximum output power	$P_{s,max}$	26 dBm

4. Simulation and test tools

4.1. Simulation tools OPTISYSTEM

Faced with the growing complexity of developed architectures and systems, the simulation tools have become important. They are increasingly used in order to optimize the parameters involved in the realization of a system. They allow to take a prevision of the expected results experimentally. Also, now they allow to use during a simulation, example OPTISYSTEM [12],[13].

4.2. Results of simulation

From the values and components parameters (see Table 1 and Table 2), has achieved the following results:

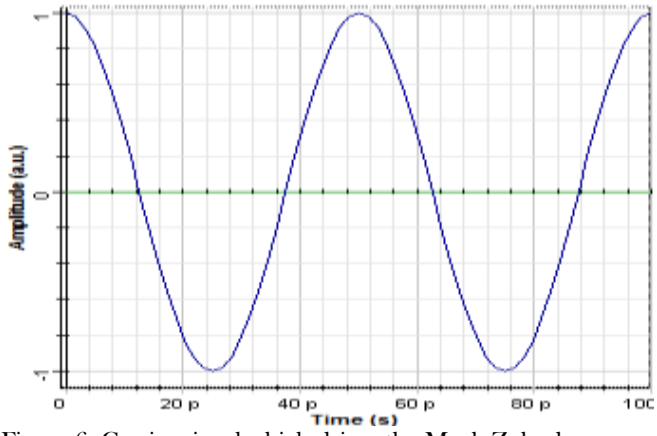

Figure 6. Carrier signal which drives the Mach-Zehnder modulator

.

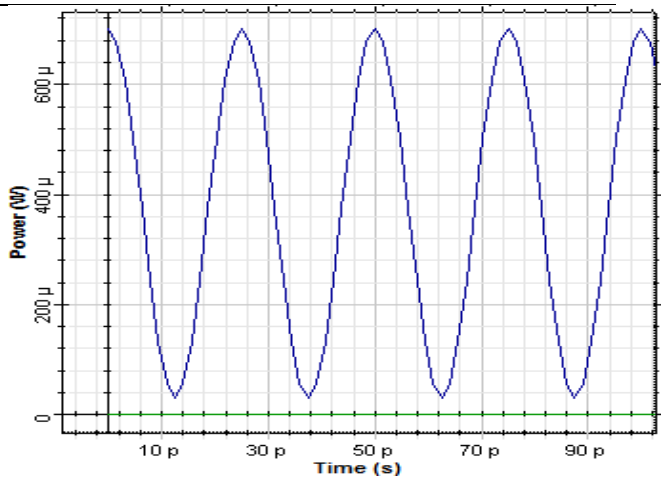

Figure 7. The pulse train at the output of the Mach-Zehnder modulator (the frequency is doubled).

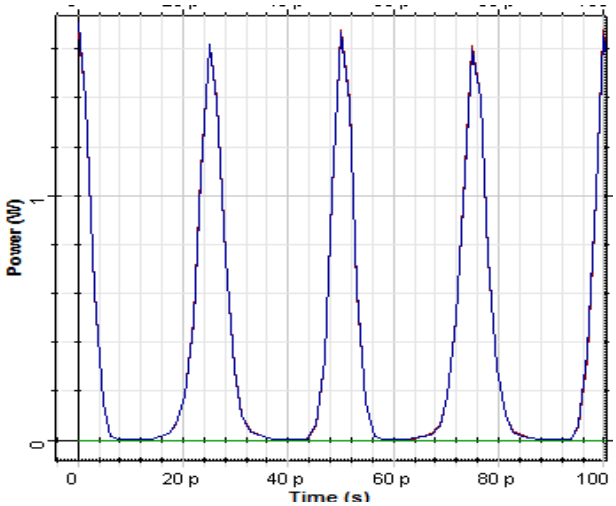

Figure 8. The pulse train at the output of the first block at a rate of 40 GHz has a cyclic ratio of 1/5.

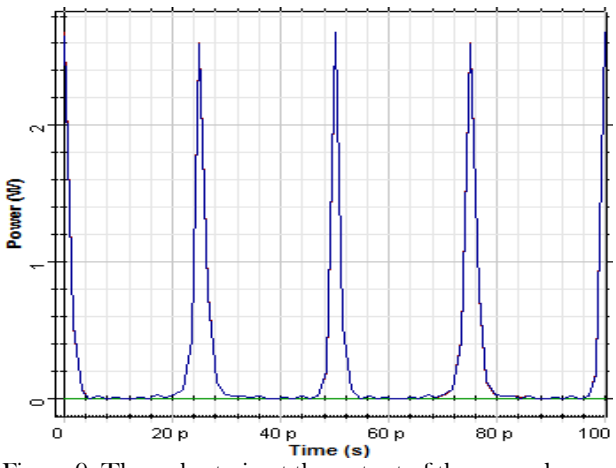

Figure 9. The pulse train at the output of the second block at a rate of 40 GHz has a duty ratio of 1/16.

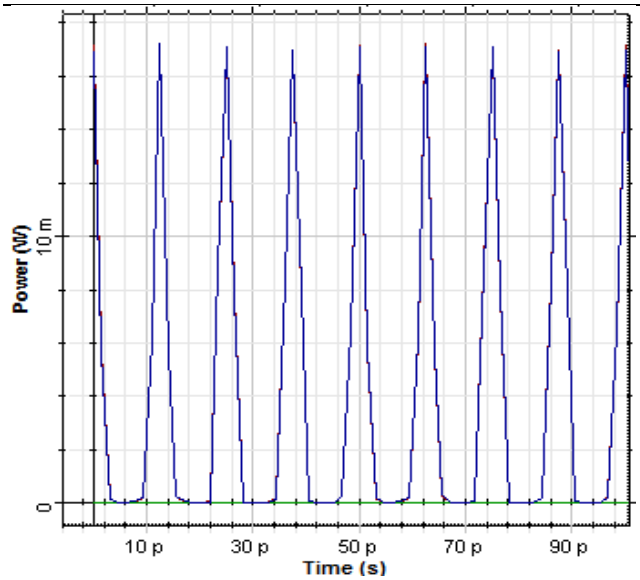

Figure 10. The pulse train output of the third block has a flow rate of 80 GHz, OTDM method is the bitter pre-multiplexing.

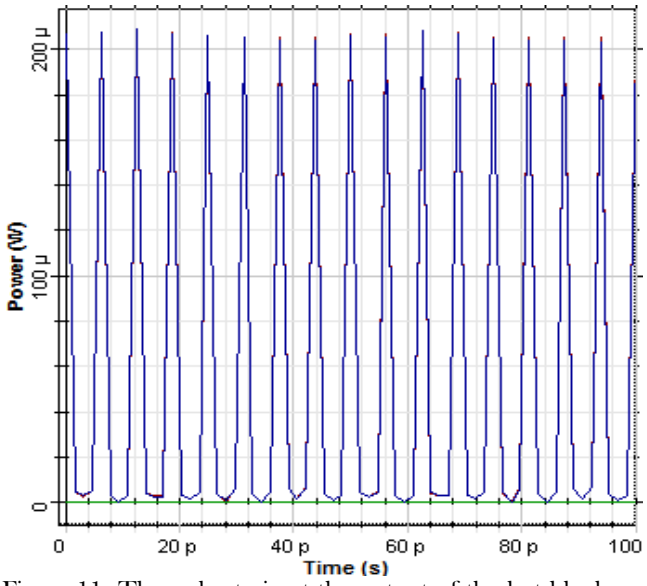

Figure 11. The pulse train at the output of the last block has a flow rate of 160 GHz.

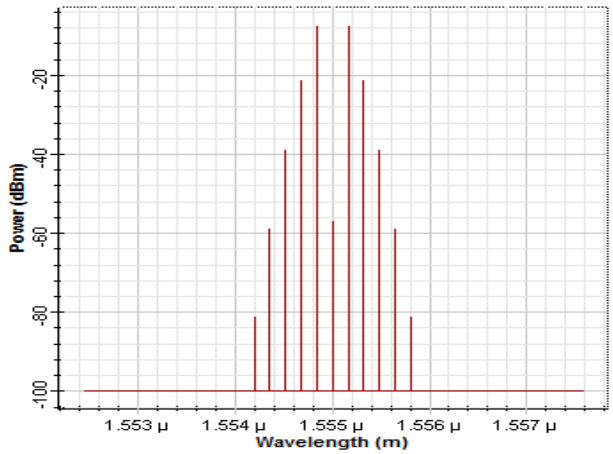

Figure 12. Signal spectrum of the signal at the output of the Mach- Zehnder modulator in the first block.

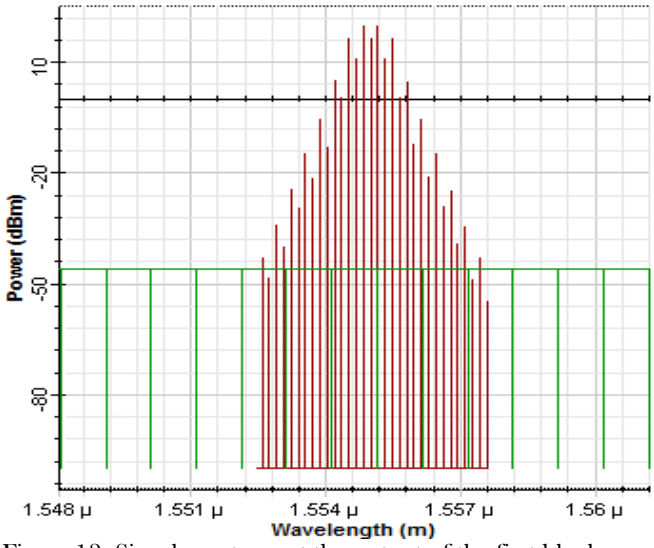

Figure 13. Signal spectrum at the output of the first block, it is noted enrichment of the spectrum by the effect of the curtailment sinusoidal beat by mélange of four-wave process.

.

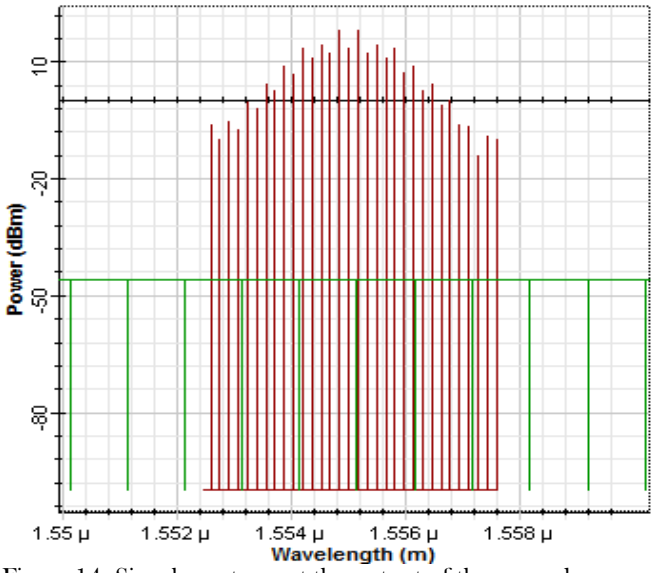

Figure 14. Signal spectrum at the output of the second block.

5. Discussion

Coupling two continuous diodes whose frequency difference is equal to the repetition rate desired, the main advantage of this technique is to achieve repetition rates up to 2 THz [4], [5] which exceeds bandwidth electronic systems (lower 50 GHz). During this, in the absence of special precautions, the spectral instability of the two diodes (line width between 1 and 5 MHz) causes a fluctuation of the repetition rate, and therefore, a significant time jitter on the intensity profile final. The intensity modulation of a single continuous diode then appears as a great alternative to generate a more stable beat (see figure 6 and Table 2). For against, in addition to the limit of bandwidth, this technique is expensive depending on the frequency f of the RF signal which

drives the modulator. To find a compromise between cost and stability of the system, the control of the modulator has its point of zero transmission by the frequency f /2 of the RF, has allowed us to generate a sinusoidal flapping at the rate f qualify (frequency doubling) (see figure 7, figure 12 and Table 2).

The compression of a sinusoidal flapping by mixing four waves is relatively simple to implement for an ultra-short pulse train high speed (see figure 8, figure 13 and Table 1).

To increase flow at very high repetition rate, it has used the OTDM multiplexing method that is quick and simple, it has managed to decrease the duty ratio of 1/5 to 1/16 (see figure 9, figure 14 and Table 1), then multiply by two the resulting flow (see figure 10, Table 1 and Table 2), and late doubling again to get the pace at 160 GHz (see figure 11, Table 1 and Table 2), over the three flows generated mainly in research laboratories at the same time can be used.

6. Conclusion

In this work, and after the theoric study of the generator of a brief pulse train, of three output of flow rates different (40 GHz, 80 GHz, 160 GHz), and introduction of the non linear Schrödinger equation which describes the non linear evolution of the envelop slowly varying of the optical pulse during its propagation along the fiber.

In the first step we have realized by simulation a generator of brief pulse train at the rate of 40 GHz with duty ratio of 1/5, based on non linear compression technique of a sinusoidal flapping through the mixing process of a four multi-wave using Mach-Zehnder and the optic isolator already chosen.

In the second step we succeeded in reducing the duty ratio from 1/5 to 1/16 using the compressor assembling that we realized which is composed by three floors, each floor is a fiber with determined parameters.

In the third step the brief pulse train obtained from the second step coded then multiplied by two, using an assembling of the multiplexer that we realized by simulation, this assembling is composed of of two branches, one branch delays the pulse train of the other branch by a duration τ, we have used the OTDM method to obtain the flow rate at 80 GHz.

In the last step the latter pulse train also multiplied by two, using an assembling of the multiplexer that we realized by simulation, we have used the same OTDM method to obtain th flow rate at 160 GHz, in order to obtain a generator multi-output, sample, easy implantation, is not expensive, used in the C-band Telecommunication

Acknowledgement

We thank the University of Badji Mokhtar Annaba for permission to carry out various researches of LERICA laboratory in good conditions and among them this work.

Author's contributions

Hamouda Amar: Participated in all experiments, coordinated the goal of the work and writing the manuscript.

Kaddour Saouchi: Participated to the design of the research plan and organized the study.

Taybi Mahmoud: Participated to the design of the research plan and organized the study.

Ethics

If there are any ethical issues please send an email to:

E-mail: amarhamouda23@gmail.com.

References

[1] I. El Mansouri, 2013. Sources picosecond pulse all-optical ultra-fast broadband : applications to optical telecommunications, Doctoral dissertation, Dijon, France.

[2] J. Fatome, 2004. Propagation of ultra-short pulses at 160 Gb/s in the lines of optical fiber dispersion-managed, Doctoral dissertation, University of Bourgogne, France

[3] K. Merzouk, 2008. Study of a low cost system optical transmission time multiplexing, Signal and image, National Institute Polytechnic of Grenoble - INPG, France

[4] S. Trillo, S. Wabnitz, and T. A. B. Kennedy, 1994. Nonlinear dynamics of dual-frequency-pumped multiwave mixing in optical fibers, Phys. Rev. A, 50:1732–1747

[5] J. Fatome, S. Pitois, and G. Millot, 2006. 20-GHz-to-1-THz repetition rate pulse sources based on multiple four-wave mixing in optical fibers, Journal of Quantum Electronics, IEEE, 42(10):1038–1046

[6]] C. Chluda, 2006. Bruit basse et moyenne fréquence des amplificateurs optiques distribués à effet Raman, PhD thesis, university Montpellier 2, France

[7] A. D Errico, C. Loiacono, M. Presi, G. Contestabile, and E. Ciaramella, 2003. Widely tunable 40 GHz pulse source for 160 Gbit/s OTDM by simultaneous soliton generation and compression, In ECOC, Italy, page We 2.6.5

[8] G. P. Agrawal, 2006. Nonlinear fiber optics, 4th edition

[9] P. Béjot, B. Kibler, E. Hertz, B. Lavorel, and O. Faucher, 2011. General approach to spatiotemporal modulational instability processes, Physical Review A, 83(1):013830

[10] R. W. Boyd, 2008. Nonlinear optics, Academic press, 3rd edition

[11] A. Hasegawa and F. Tappert, 1973. Transmission of stationary nonlinear optical pulses in dispersive dielectric fibers. I. Anomalous dispersion, Applied Physics Letters, 23:142

[12] S. O. Mohammadi, S. Mozaffari, & M. M. Shahidi, 2011. Simulation of a transmission system to compensate dispersion in an optical fiber by chirp gratings, International journal of the Physical Sciences, 6(32), 7354-7360

[13] N. Nishizawa & T,Goto, 2006. Novel super-continuum fiber lasers and wavelength-tunable soliton pulses, SPIE Newsroom.

Journal of New Technology and Materials
JNTM
Vol. 07, N°01 (2017)33-38

OEB Univ. Publish. Co.

Comparison between the microstructural, morphological, mechanical and tribological characteristics of nanocrystalline Ni and Ni-Co electrodeposited coatings

M. Hamidouche and N. Khennafi-Benghalem

Emerging Materials Research Unit, University of Setif 1, Algeria

Institute of Optics and Precision Mechanic,University of Setif 1, Algeria

Corresponding author: email: hamidouchemohamed@yahoo.fr

Received date: November 22, 2016; revised date: Febrauary 23, 2017; accepted date: May 23, 2017

Abstract

For improving the wear resistance of steel used commonly in industry, nanocrystalline nickel and nickel-cobalt coatings are electrodeposited on A60 steel substrate in a modified Watts bath. The observation of the coatings produced by scanning electron microscopy (SEM) shows that nickel coatings have a smooth morphology whereas Ni-Co alloy deposits have a lens-shaped morphology with a considerable increase in the grains size of Ni-Co alloy deposits. The results of XRD show that nickel coatings having fcc phase structure while Ni-Co coatings have hcp phase structure. The study of coatings micro-hardness indicates that the latter follows Hall Petche effect where nickel deposits which have the smallest grain size show a higher micro-hardness in comparison with Ni-Co coatings. Pin on disk tribometric analysis under unlubricated conditions illustrates a great improvement of the wear resistance by the addition of cobalt on nickel coatings, where the friction coefficient and the wear rates are significantly reduced in Ni-Co coatings compared with nickel coatings.

Keywords: Ni, Ni-Co, Coating, Microstructure, Morphology, Microhardness, Tribological behavior.

1. Introduction

The electrodeposited nickel coatings are used in a large range of applications to improve the hardness [1], corrosion resistance [2], and wear resistance of the coated substrates [3, 4]. In order to improve the performances of nickel coatings, different approaches have been applied such as alloying with other elements [5, 6], crystallites refinement using additives [7, 8], and deposition of composite coatings by dispersing reinforcing particles inside the Ni matrix [9, 10]. The alloying of Ni with cobalt was one of the most commonly techniques used for improve the properties of nanocrystalline nickel coatings [4-6]. Ni-Co alloys have been investigated as important engineering materials for several decades due to their unique properties, such as high resilience [11], good corrosion resistance [12], thermal conductivity [13], electro-catalytic activity [14] and their magnetic properties [15] .In this work, we will try to give more value to these alloys coatings through improving their good tribological properties, In order to show the engineering feasibility of this coating, it is necessary to electrodeposit Ni–Co alloys onto structural materials such as ordinary steel. This will enable us to apply them as anti-wear coatings for increasing lifetime of the components that are subject to friction forces and wear conditions such as engine cylinders, rolling bearings, motion vectors,...etc.

To prove Ni-Co coatings anti-wear resistance, a comparison is made between the microstructural and morphological properties of high cobalt content nanocrystalline Ni-Co alloy coating (87% Co) with a nanocrystalline nickel coating which are produced electrochemically. Thus, a correlation between these properties with mechanical and tribological properties of these deposits is made.

2. Experimental

2.1. Substrate preparation

The nanocrystalline nickel and Ni-Co electrodeposited coatings are electrodeposited on an A60 mild steel substrate with an exposed area of 3,14cm^2. Before electrodeposition, the substrate is subjected to some surface treatment operations, mechanical polishing with Si-C abrasive papers with decreasing grain sizes (80 to 4000), chemical degreasing for 10 min in an alkaline solution of pH=11 by using ultrasonic bath, chemical polishing in a solution of hydrochloric acid (10% by volume) for about 30 s. The chemical composition of A60 mild steel used as substrate is given in Table 1.

Table 1: The chemical composition of A60 mild steel substrate

Element	Fe	P	S	N	Others
Percentage %	99.65	0.028	0.023	0.013	0.286

2.2. Electrodeposition of nanocristallyne Ni and Ni-Co alloy coatings

Two electrolytic baths are used in this work. The first bath contains $NiSO_4$ (200g/l), $NiCl_2$ (20g/l) used for the preparation of nanocrystalline nickel coatings, the second bath contains $NiSO_4$ (200g/l), $NiCl_2$ (20g/l), $CoSO_4$ (200g/l) used for the preparation of Ni-Co alloys coatings with 87% cobalt content. In each bath, boric acid (30g/l) was added as a buffer to fix pH at 4.2±0.05 and to limit the alkalization of the solution around the substrate, saccharine (2g/l) and 2-butyne-1, 4-diol (BD) (0.5g/l) which prove their effect in the grain size reduction and in the improvement of coating properties [16-19] are added as brighteners to refine crystallites size. A pure nickel disc (purity = 99.99%) is used as a soluble anode, the bath temperature is maintained at 318K using a thermostatic bath with water circulation. The solution is continuously stirred by a magnetic stirrer bar (6 mm diameter × 30 mm length) at a speed of 200 rpm. In order to obtain deposits of thicknesses 20±5 µm, the current density is fixed at 4A /dm^2 for a period of 1200 s using 309N Autolab galvanostat-potentiostat.

2.3. Morphological and microstrucural characterization

JEOL JSM-7001F scanning electron microscope (SEM) is used to characterize the morphological and microstructural properties of elaborated deposits. The composition of the deposits is determined using electron scattering spectroscopy (EDS) which is coupled with SEM. The coating thicknesses are measured using Taylor Hobson PGI 1240 mechanical profilometer, three measurements are made on each coating. The crystal structure and grain size are characterized by D8 Avanced Bruker X-ray diffractometer (XRD), while the grain size is calculated according to the Scherrer equation.

2.4. Mechanical and tribological characterization

The microhardness of the deposits is determined by the use of Tukon 2500 Knoop/Vickers hardness tester under a load of 50 g for a 15 second holding time. Five measurements are taken at different places in the coating. The tribological behavior of the coatings is studied using NANOVIA pin on disc tribometer, at room temperature with 28-34% humidity under a load of 3N and with a sliding speed of 5 mm s^{-1} for a total sliding time of 10 min. AISI 1040 hard steel ball (Ø = 6mm, hardness HV=700) is used as a counterpart. The friction coefficient in function of time is automatically calculated during the test. Also, images of wear tracks (50 folds magnification) are taken using Carl Zeiss optical microscope connected with a CCD camera, however, the wear rate is evaluated by the measurement of the mass lost using Sartorius precision balance (Readability $\frac{1}{10}$ mg).

3. Results

3.1. Composition of the coatings

Figure 1 shows the percentage of cobalt $\frac{[Co]}{([Co]+[Ni])}$ in the electrolyte and in the Ni-Co coating. It is clear that the cobalt percentage in the coating (87%) is higher than in the bath (47%), this despite that the concentration of Ni^{2+} ions in the bath is greater than that of Co^{2+} ions. This can be explained by the anomalous co-deposition mechanism of Ni-Co alloys, where the less noble element cobalt is deposited preferentially compared to nickel. A generally accepted explanation for this abnormal phenomenon is the rise of pH at the substrate, this local increase in pH caused by the formation of metal hydroxides Co (OH) and Ni (OH) and their competitive adsorptions [15, 20]. The formation and adsorption of monohydroxides of metal can be expressed as follows [21, 22]:

$2H_2O + 2e^- \leftrightarrow H_2 + 2OH^-$

$M^{2+} + OH^- \leftrightarrow (MOH)^+$

$(MOH)^+ \rightarrow (MOH)^+_{ads}$

$(MOH)^+_{ads} + 2e^- \leftrightarrow M + OH^-$

Where M represents the Ni and Co metal atoms and M_{ads} represents adsorbed metal atoms. The adsorption ability of $Co(OH)^+$ was considered to be higher than $Ni(OH)^+$, this can cause enriching deposits by the less noble metal Co. Several authors working on the co-deposition of Ni-Co alloys noticed the same appearance [15, 20], it is also noted that the thickness of nanocrystalline nickel coatings is about 25 µm, this thickness decreases to about 17 µm in the Ni-Co coatings with 87% cobalt content, which indicates that the deposition rate is reduced by the addition of cobalt in the nickel electrolyte due to the anomalous co-deposition phenomenon.

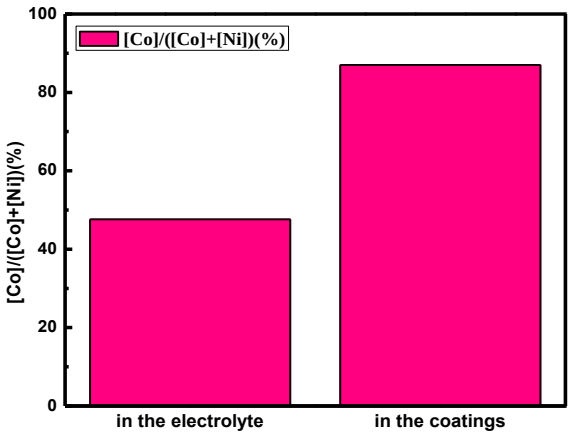

Figure 1: Cobalt proportion in the electrolyte and in the Ni-Co coatings.

3.2. Morphological and microstructural properties of coatings

The SEM observations of the elaborated nanocystalline nickel and Ni-Co deposits are shown in Figure 2a-b, the nanocrystalline nickel is characterized by a smooth surface, while the Ni-Co coatings with high cobalt contents (87% Co) are characterized by a cluster-porous morphology where the appearance of a microscopic porosity in deposits with 87% cobalt content is noticed. The change of the smooth surface to cluster-porous morphology is explained by the change of the crystal structure from fcc to hcp phase when the cobalt is added to the nickel coatings as we see in Figure 3. This indicates that the cobalt addition on the nickel coatings has a significant influence on the surface morphology and structure of deposits.

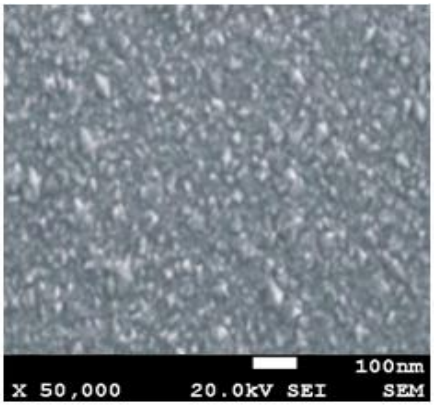

(a)

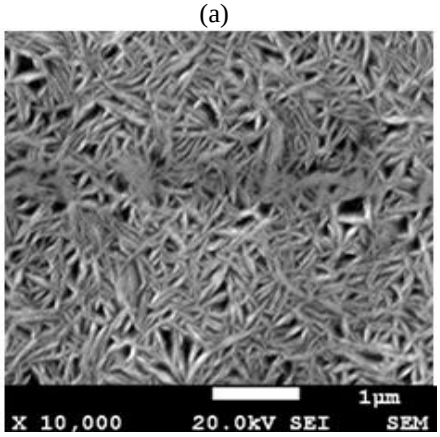

(b)

Figure 2 : SEM observations of nanocrystalline coatings: (a) Pure Ni, (b) Ni-Co with 87% cobalt content.

XRD patterns presented by Figure 3 shows that the cobalt content has a great influence on the coatings crystal structure, where it has been noticed that the pure nickel deposits are characterized by fcc phase structure. But the addition of high cobalt content in the nickel coatings conducted to a complete disappearing of the fcc phase and a new hcp phase which has very good tribological characteristics [23, 24] is appeared. Several authors [25, 26] working on the development of Ni-Co arrive at the same results.

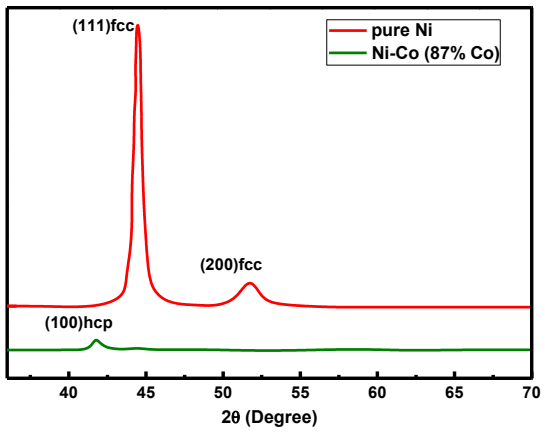

Figure 3: X-ray diffraction spectrum of Ni and Ni-Co nanocrystalline coatings.

3.3. Microhardness of coatings

Figure 4 shows the microhardness of the pure nanocrystalline Ni coating and Ni-Co alloy coating with 87% Co content while Figure 5 shows the grain sizes of the two coatings. The grain size of the deposited coatings is deduced from XRD peak broadening analysis and is calculated using the Scherrer equation [27]:

$$D = k\lambda / (\beta \cos \theta) \qquad (1)$$

where D is the average crystallite size, λ is the X-ray wavelength in nanometer (nm), in our case λ $Cuk\alpha_1$ = 0.15405 nm, β is the peak width of the diffraction peak profile at half maximum height resulting from small crystallite size in radians and k is a constant related to crystallite shape, normally taken as 0.9.

According to Figure 4 the microhardness of pure nickel coatings is about 580 HV0.05, it is reduced by the addition of 87% cobalt in the deposits to about 305 HV0.05, which mainly attributed to the increase of the grains size as shown in Figure 5. This result indicates that the microhardness of coatings follows the classical Hall-Petch relationship [28]:

$$H = H_0 + kd^{-0.5} \qquad (2)$$

Where H_0 is the constant of hardness, k is constant, and d is the grain diameter. The decrease in microhardness of the coatings with the addition of cobalt in nickel coatings can also be attributed to the appearance of porosity due to the addition of cobalt and the formation of the cluster-porous structure as shown in Figure 2b.

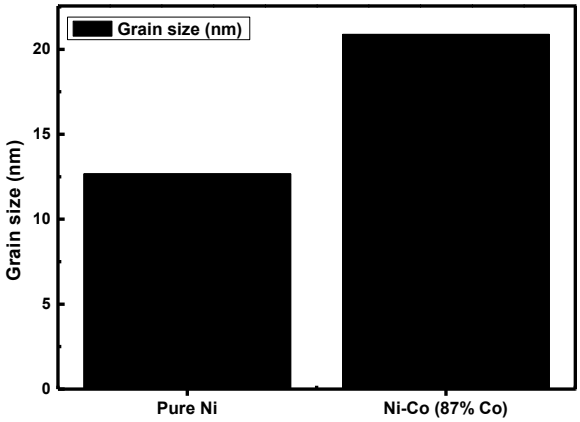

Figure 4: The grain size of Ni and Ni-Co coatings.

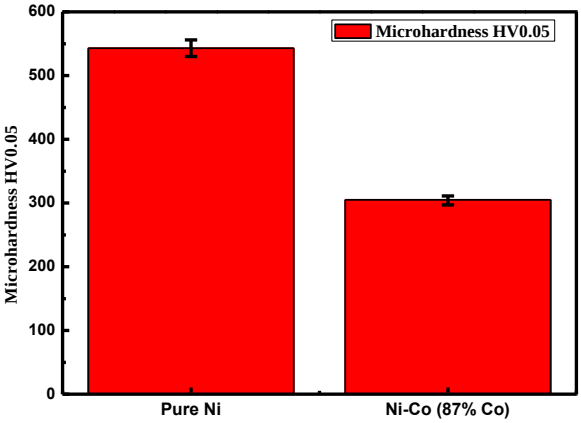

Figure 5: The microhardness of Ni and Ni-Co coatings.

3.4. Tribological properties of the coatings

The friction coefficient of nanocristallyne Ni and Ni-Co coatings is measured using a pin-disc tribometer (without lubrication) is shown in Figure 6. It is clear that the friction coefficient of Ni-Co alloy coatings is lower by about five times than that of pure Ni coatings. In addition, the friction coefficients of Ni-Co alloys are much more stable than that of pure Ni deposits (Figure 6). Combined with the XRD analysis, the excellent friction-reduction behavior can be explained by the change of crystal structure from fcc to hcp crystal phase, this latter has very good tribological properties according to several previous studies [23, 24, 29].

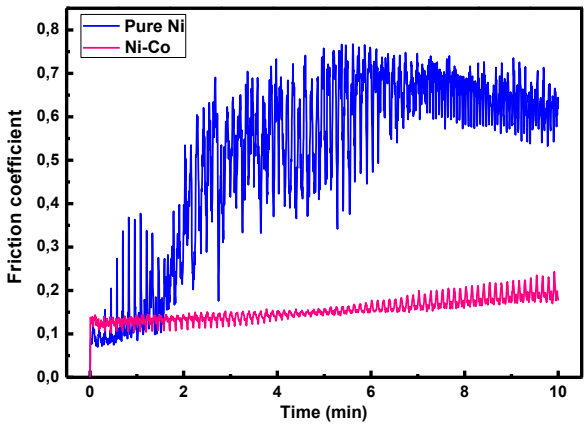

Figure 6: Friction coefficient of Ni and Ni-Co coatings.

In this study, the wear rate is evaluated by the weight loss after pin on disc wear testes for 10 minutes.

$$Weight\ loss\ (\%) = \frac{(mi - mf)}{mi} * 100 \qquad (3)$$

Where m_i and m_f are the initial and the final mass of the sample, respectively. The wear rate of the nanocristallyne Ni and Ni-Co alloy coatings is shown in Figure 7. It is noted in this study that the Ni-Co alloy deposits have the lower wear rate compared to the pure nickel deposits. The pin-disc tribometric analyses without lubrication shows a great improvement of the wear resistance with the addition of 87% Co into the coatings. This despite the decrease in the microhardness of coatings with cobalt addition as we have seen in Figure 5, what contradicts the Archard law [30]:

$$Q = KLN/H \qquad (4)$$

Where Q is the volumic wear rate, L is the total sliding distance; K is the friction coefficient and H the wear surface hardness. This opposite effect to the Archard law is attributed essentially to the formation of the hcp phase in the coatings with high cobalt contents. Also, this effect can be attributed to the wear debris film. A recent study [29] shows the undesirable effect of the formation of tribofilms in the worn surface of pure Ni coatings on the tribological behavior of such coatings, this undesirable film does not appear in the worn surface of Ni-Co coatings with 87% Co as shown Figure 8.

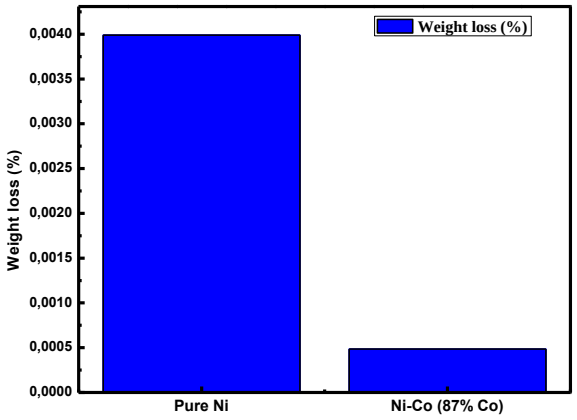

Figure 7: The wear rate of Ni and Ni-Co coatings.

To verify the diversity between the wear behaviour of Ni and Ni–Co coatings, the worn surface morphologies can be used as shown in Figure 8a–b. The appearance of the tribofilms is clearly observed in the worn surface of Ni coatings subjected to the wear constraints which have an fcc crystal structure. The appearance of tribofilms is due to the adhesive wears mechanism of pure nickel coating and the harsh deformation in the sliding track under the compression and shear constraints, which leads to wide wear rate of pure Ni coatings and big tendency for plastic deformation. This led to high formation of asperity spots which guides to high and unstable Ni coatings friction coefficient.

In comparison with pure Ni deposits, there is no tribofilm appearance in the worn surface of Ni-Co coatings with high cobalt contents. When, the worn surface of Ni-Co coatings becomes dense. The worn surface of Ni-Co coating with hcp crystal structure revealed less adhesion wear and smooth surface with smaller smashed spots, just some scars are remarked on the worn surface (Figure 8b). This came out with better wear resistance of Ni-Co alloy coating than Ni coating. That is also the cause behind the friction coefficient of Ni-Co alloy coating that is more stable and about five times lower than of Ni coatings. These results are in good agreement with the study of C. Ma and all [29]. Also, Figure 8a-b shows that the Ni-Co wear scars are much narrower and shallower compared to those of the pure nickel coating, which indicates that the wear rate is lower in the Ni-Co coatings. This observation confirms the obtained results of wear rates verified by the weight loss (Figure 7).

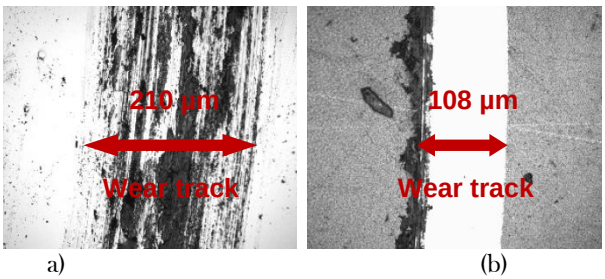

a) (b)

Figure 8: Wear tracks of (a) pure Ni coatings, (b) Ni-Co coatings

4. Conclusion

In this work, the Ni-Co alloys coatings have followed an anomalous codeposition mechanism, where the less noble element cobalt is deposited preferentially compared to nickel.

The addition of high cobalt content in the nickel coatings causes the change of the smooth morphology of nickel coatings to cluster-porous morphology; it also led to the change of the phase crystal structure from fcc to hcp structure.

The microhardness of nanocristallyne nickel coatings is reduced with the increasing in the grain size of coatings caused by the addition of high cobalt content which indicated that the microhardness of deposits follows the Hall-Petch effect.

The Ni-Co alloys deposits have much lower friction coefficient and higher wear resistance than pure Ni coatings. It is concluded that the hcp crystal structure in the Ni-Co alloys coatings contributes to the remarkable effect of reduction of friction and to the very good anti-wear performances.

The Ni-Co coatings with 87% cobalt content have the lowest friction coefficient and the best wear resistance, unfortunately they are characterized by a low microhardness, which requires their hybridization with other components such as hard nano or micro particles of Si-C, Al_2O_3, ZrO_2 etc, or the decrease of their grain sizes by the addition of additives in the bath because their hardness as we demonstrate in this study following the Hall-Petche effect.

Acknowledgements

Several experiments in this work were conducted outside our laboratory for that, the authors would like to thank: LMNM laboratory, LPMM laboratory, LOA laboratory, DAC-HR laboratory (University of Setif 1), LSDM laboratory (USTHB University) and SANIAK-BCR Company (Ain Elkebira-Setif) for helping finishing this work.

References

[1] N.A. Badarulzaman, A.A. Mohamad, S. Puwadaria, Z.A. Ahmad, "The Evaluation of Nickel Deposit Obtained Via Watts Electrolyte at Ambient Temperature."J. Coat. Technol. Res., 7(6), pp. 815-820, 2010.

[2] D.E. Rusu, A. Ispas, A. Bund, C. Gheorghies, G. Carac, "Corrosion tests of nickel coatings prepared from a Watts-type bath," J. Coat. Technol. Res., 9 (1), pp. 87-95, 2012.

[3] D.H. Jeong, F. Gonzalez, G. Palumbo, K.T. Aust and U. Erb, "The effect of grain size on the wear properties of electrodeposited nanocystalline nickel coatings," Scripta mater. , vol. 44, pp. 493-499, 2001.

[4] M. Hamidouche, N. Khennafi-Benghalem, "Microstructural, morphological, mechanical and tribological characterization of nanocrystalline nickel and Ni-Co electrodeposited coatings,"5th International Conference on Welding, Non Destructive Testing and Materials and Alloys Industry, 26-28 November 2016 Oran, Algeria.

[5] C. Ma, S.C. Wang, C. T. J. Low, L. P. Wang and F. C. Walsh, "Effects of additives on microstructure and properties of electrodeposited nanocrystalline Ni–Co alloy coatings of high cobalt content," Transactions of the IMF, vol.92, pp. 191-195, 2014.

[6] Y.F. Yang, B. Deng, Z.H. Wen, "Preparation of Ni-Co Alloy Foils by Electrodeposition," Adv.Chem.Eng.Sci, vol.1, pp.27-32, 2011.

[7] C. Ma, S. C. Wang and F. C. Walsh, "Electrodeposition of nanocrystalline nickel and cobalt coatings," Transactions of the IMF, vol.93, pp.8-17, 2015.

[8] L. Wang, Y. Gao, T. Xu, Q. Xue, "A comparative study on the tribological behavior of nanocrystalline nickeland cobalt coatings correlated with grain size and phase structure," Materials Chemistry and Physics, vol.99, pp.96-103, 2006.

[9] I. Corni, R.J. Chater, A.R. Boccaccini ,M.P. Ryan, "Electro co-deposition of Ni–Al_2O_3 composite coatings," J.Mater.Sci, vol. 47, pp. 5361–5373, 2012.

[10] P. Narasimman, M. Pushpavanama and V.M. Periasamy, "Effect of Surfactants on the Electrodeposition of Ni-SiC Composites," Port. Electrochim. Acta, vol.30, 1-14, 2012.

[11] A.N. Correia, S.A.S .Machado, "Electrodeposition and characterisation of thin layers of Ni-Co alloys obtained from dilute chloride baths," Electrochimica Acta,vol. 45,pp. 1733-1740, 2000.

[12] Z. She, Q. Li, Z. Wang, C. Tan, J. Zhou, L. Li, "Highly anticorrosion, self-cleaning superhydrophobic Ni–Co surface fabricated on AZ91D magnesium alloy," Surface & Coatings Technology,vol.251, pp. 7–14, 2014.

[13] L. Börnstein, "Thermal Conductivity of Pure Metals and Alloys:Ni-Co steels," vol.15C, Springer-Verlag Berlin Heidelberg ,1991.
[14] Z. Wang,Y. Du, F.Zhang, Z. Zheng, Y. Zhang and C. Wang, "High electrocatalytic activity of non-noble Ni-Co/graphene catalyst for direct ethanol fuel cells," J.Solid.State.Electrochem., vol.17, pp. 99-107, 2013.
[15] A. Karpuz, H. Kockar, M. Alper, O. Karaagac, M. Haciismailoglu, "Electrodeposited Ni–Co films from electrolytes with different Co contents," Applied Surface Science, vol.258, pp.4005–4010, 2012.
[16] S. Hassani, K. Raeissi, M.A. Golozar, "Effects of saccharin on the electrodeposition of Ni–Co nanocrystalline coatings," Journal of Applied Electrochemistry, vol.38, pp.689–694, 2008.
[17] B. Bakhit, A. Akbari, "A comparative study of the effects of saccharin and β-SiC nano-particles on the properties of Ni and Ni–Co alloy coatings," Surface & Coatings Technology, vol. 253, pp.76–82, 2014.
[18] S.L. Wang, L.L. Hong, W.W. Yu, "Influence of 2-butyne-1,4-diol on the structure and performance of the Co-Ni alloy plated by electrodeposition," Acta Metallurgica Sinica, vol.21, pp.50-56, 2008.
[19] M.G. Hosseini1, M. Abdolmaleki, H. Ebrahimzadeh, S.A.S. Sadjadi, "Effect of 2-Butyne-1, 4-Diol on the Nanostructure and Corrosion Resistance Properties of Electrodeposited Ni-W-B Coatings," International Journal of Electrochemical Science, vol.6, pp.1189-1205, 2011.
[20] L. Tian, J. Xu, S. Xiao, "The influence of pH and bath composition on the properties of Ni-Co coatings synthesized by electrodeposition," Vacuum, vol.86, pp. 27-33, 2011.
[21] L. Tian, J. Xu, C. Qiang, "The electrodeposition behaviors and magnetic properties of Ni–Co films," Applied Surface Science vol.257, pp.4689–4694, 2011.
[22] R. Orinakova, A. Orinak, G. Vering, I. Talian, R.M. Smith, H.F. Arlinghaus, "Influence of pH on the electrolytic deposition of Ni–Co films," Thin Solid Films, vol.516, pp.3045–3050, 2008.
[23] L. Wang, Y. Gao, Q. Xue, H. Liu, T. Xu, "Microstructure and tribological properties of electrodeposited Ni–Co alloy deposits", Applied Surface Science, vol.242, pp.326-332, 2005.
[24] I. Inman, P. Datta, "Studies of high temperature sliding wear of metallic dissimilar interfaces III: Incoloy MA956 versus Incoloy 800HT," Tribology Internationl, vol.43, pp. 2051–2071, 2010.
[25] I. Kharmachi, L. Dhouibi, P. Berçot, M. Rezrazi, "Co-deposition of Ni-Co alloys on carbon steel and corrosion resistance resistance," J. Mater. Environ. Sci., vol.6, pp. 1807-1812, 2015.
[26] L.D. Rafailovic, H.P. Karnthaler, T. Trisovic, D.M. Minic, "Microstructure and mechanical properties of disperse Ni–Co alloys electrodeposited on Cu substrates," Materials Chemistry and Physics, vol.120, 409-416, 2010.
[27] A. Monshi, M.R. Foroughi, M.R. Monshi, "Modified Scherrer Equation to Estimate More Accurately Nano-Crystallite Size Using XRD," World Journal of Nano Science and Engineering, vol.2, pp.154-160, 2012.
[28] C. Ma, S.C. Wang, R.J. K. Wood, J. Zekonyte, Q. Luo, and F. C. Walsh, "Hardness of Porous Nanocrystalline Co-Ni Electrodeposits," Met. Mater. Int., vol.19, pp. 1187-1192, 2013.
[29] C. Ma, S.C.Wang, L.P. Wang, F.C. Walsh, R.J.K. Wood , The role of a tribofilm and wear debris in the tribological behavior of nanocrystalline Ni-Co electrodeposits, Wear, vol.306, pp.296-303, 2013.
[30] A. Zmitrowicz, "Wear patterns and laws of wear – A review," Journal of theoretical and applied mechanics, vol.44(2), pp.219-253, 2006.

Journal of New Technology and Materials
JNTM
Vol. 07, N°01 (2017)39-46

OEB Univ. Publish.Co.

Electron Transport Properties of Ternary alloysGallium Indium Phosphide

C. Sayah[a], B. Bouazza[b], A. Guen-Bouazza[b] And N. E. Chabane-Sari[b]

[a]*Laboratoire de Structures Intelligentes, Ctr Univ Ain Temouchent, Institut des Sciences et de la Technologie, BP 284- 46000AinTemouchent ،Algerie*
[b]*Unité de recherche des matériaux et des énergies renouvelables,Faculté des sciences de l'ingénieur, Université Abou-BekrBelkaïd de Tlemcen.BP 230, Tlemcen 13000, Algérie.*

Corresponding author: email: *(a) chou28dz@gmail.com, (b) bouaguen@yahoo.fr*

Received date: November 24, 2016; revised date: May 20, 2017; accepted date: May 23, 2017

Abstract

This paper deals with the development and application of Monte Carlo simulations to study electron transport in bulk $Ga_xIn_{1-x}P$ in the zinc blende crystal structure. The simulation model includes three sets of non-parabolic conduction band valleys which can be occupied by electrons during high field transport. The effects on electron transport of impurities and the relevant phonon scattering mechanisms have been considered. The dependence of the transport properties on the material parameters is discussed and also with regard to the temperature, donor concentration. We have introduced and examined the effects of alloy concentration of bulk $Ga_xIn_{1-x}P$, and how this affects the transport properties, especially the average drift velocity, predicted by our Monte-Carlo simulation programs.

Keywords: Monte Carlo method, semiconductor materials, phonon scattering mechanisms, alloys scattering mechanisms, $Ga_xIn_{1-x}P$

1. Introduction

In the development field of new materials, the compound semiconductors continue being an area of great interest and rapid expansion [1-2]. The advantage of alloying is that the alloy properties, such as band gap, can be tuned by varying the alloy composition to meet the specific requirements of modern device applications [3-4]. Indium gallium phosphide (InGaP) is a ternary semiconductor composed of InP and GaP. **Fig. 1** illustrates the band gap energy transition from InP to GaP, where the black solid line shows direct band gap transitions, and the black dashed line describes the indirect band gap transition. Band gap energy and lattice constant values are between the corresponding values of the binary alloys from which it is formed.It is an important alloy for the development of lighting emitting devices, photovoltaic systems, high-power and high-frequency electronics, due to the capacity to control the band gap, which varies according to the indium concentration in a range of energies from 2.26 eV to 1.27 eV [1-5]. Especially the $Ga_{0.5}In_{0.5}P$ is an alloy of significant importance because it can be lattice matched to GaAs. L'InGaP is used mainly in high electron mobility transistor (HEMT) and heterojunction bipolar transistors (HBT) and it has attracted many attentions in high speed and power applications due to the superior transport properties [6], it is also used for the fabrication of high efficiency solar cell used for space applications and, in combination with Alumimium (AlInGaP alloy) to make high brightness laser emission diode with orange-red, orange, yellow, and green colors. $Ga_{0.5}In_{0.5}P$ is used as the high energy junction on double and triple junction photovoltaic cells grown on GaAs [7]. Growth of GaInP by epitaxy can be complicated by the tendency of GaInP to grow as an ordered material, rather than a trulyrandom alloy [8]. The variation of composition for $In_xGa_{1-x}P$ has a marked influence on the splitting of reduction of its energy gap as well as on the splitting of its valence and conduction bands [9].

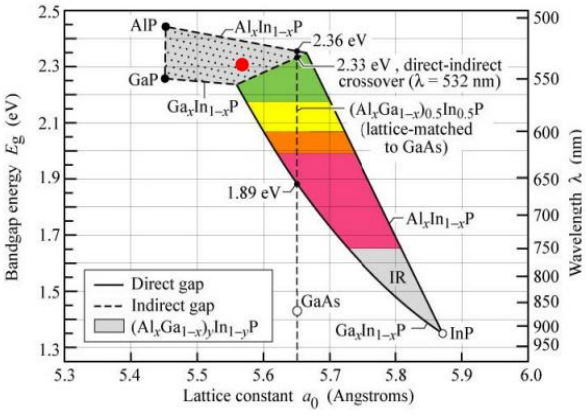

Fig.1. Band gap energy and corresponding wavelength versus lattice constant of $Ga_xIn_{1-x}P$ at 300K [19].

For the purposes of this analysis of the steady-state electron transport within InP, GaP and $Ga_xIn_{1-x}P$. We ployan single semi-classical three-valley Monte Carlo simulation approach. The scattering mechanisms considered are: ionized impurity, polar optical phonon, piezoelectric, acoustic deformation potential and Intervalley scattering. To simulate electron transport in alloys it is necessary to include alloy scattering in the transport model. The alloy scattering is in addition to the scattering mechanisms present in elements and compounds which do not have this chemical disorder. In this model the alloy disorder is considered to be produced by a set of short range scatterers [10-11]. If the A and B atoms are arranged randomly without any correlation the alloy scattering rate, W_{all} is [10-11-12-13]:

$$W_{all}(\varepsilon) = \frac{3.\pi^3}{8.\hbar}.V_0 U_{all}^2.x(1-x).N(\varepsilon)$$

Where V_0 is the volume of the primitive cell, U_{all} is random alloy potential, $x$is Al mole fraction and $N(\varepsilon)$) is the density of states. Different interpretations for the choice of the random alloy potential have been given in the past. Littlejohn et al. [14] have used the conduction band offset to represent the random scattering potential, whilst another is to use the differences in their electron affinities [10-11]. Other workers have fitted values to experimental transport data to obtain a value of 0.42e V [15-16]. Chin et al. [17] have determined the random potential from band gap bowing parameters and applying Phillips' theory of electro negativity differences [18]. Because of the large number of alloys available, each with a continuous range of compositions, the band structure and related parameters are generally not available from experiment. Interpolation between the end point binary materials is normally used to obtain band structure and scattering parameters [10-11-15-20-21].

The values of most interest are the conduction band valley separations and their effective masses. We have used linear interpolation for these parameters. Indium gallium phosphide (InGaP) is a semiconductor composed of indium, gallium and phosphorus. Alloy scattering for $Ga_xIn_{1-x}P$ are simulated using alloy potentials expressed as and where:

$$\Delta U^2 = x(1-x)\left|\varepsilon_{gInP} - \varepsilon_{gGaP}\right|^2$$

ε_{gInP} , ε_{gGaP} are the band gaps for InP and GaP, respectively. For our simulations, the crystal temperature is set to 300 K and the doping concentration is set to $10^{17}cm^{-3}$ for all cases. The influence of holes in the valence band is completely neglected. The conduction band is approximated by the Γ valley centered at (0,0,0), four equivalent L valleys along (1,1,1) and three equivalent X valleys along (1,0,0).

2. Material parameter

For a ternary alloy $A_xB_{1-x}N$ the dependence of a parameter $y$on the mole fraction $x$is usually approximated as:

$$y_{A_xB_{1-x}N} = x.y_{AN} + (1-x)y_{BN} - b.x(1-x)$$

Where the deviation from linear behavior is considered using the bowing factor b.The band gap is one of the most important semiconductor parameters. The Varshni equation has been used until now to describe the band gap dependence on the temperature for almost all the III–V semiconductors [22]. The band gap of InP, GaP [23] and $In_{0.5}Ga_{0.5}P$ [24] can be given by:

$$E_g(T) = 1{,}421 - 4{,}9.10^{-4}\frac{T^2}{T+327}$$
$$E_g(T) = 2{,}34 - 6{,}2.10^{-4}\frac{T^2}{T+460}$$
$$E_g(T) = 1{,}937 - 6{,}12.10^{-4}\frac{T^2}{T+204}$$

The band gap is then calculated depending on the material composition. This is important to assure consistency between the values for alloy materials at x=0 and x=1 and the values for the respective basic materials. In **Fig. 2** the material composition dependence of the Γ, L, and X band gaps in $Ga_xIn_{1-x}P$ at 300 K is shown. Energy separations between Γ, L and X conduction band minima and top of the valence band:

At 10 K [25]

$$E_a^{\Gamma} = 1{,}418 + 0{,}77x + 0{,}648x^2$$
$$E_g^{X} = 2{,}369 - 0{,}152x + 0{,}147x^2$$

At 77 K [26]

$$E_g^{\Gamma} = 1{,}405 + 0{,}702x + 0{,}764x^2$$
$$E_g^{X} = 2{,}248 + 0{,}072x$$

At 300 K [26, 27]

$$E_a^{\Gamma} = 1{,}349 + 0{,}668x + 0{,}76x^2$$
$$E_g^{X} = 1{,}85 - 0{,}06x + 0{,}71x^2$$

Energy gap for direct gap composition ($\mathbf{0} < x \leq 0{,}63$) at 300 K:

$$E_g = 1{,}34 + 0{,}69x + 0{,}48x^2$$

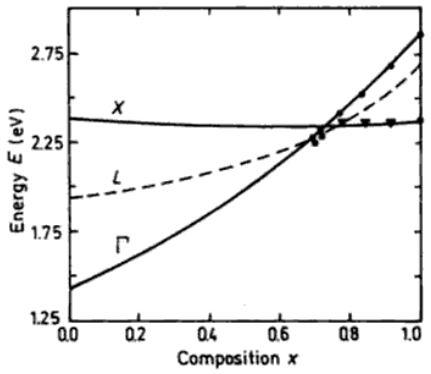

Fig.2: Material composition dependence of the Γ, L, and X-band gaps $Ga_xIn_{1-x}P$ at 10 K[25].

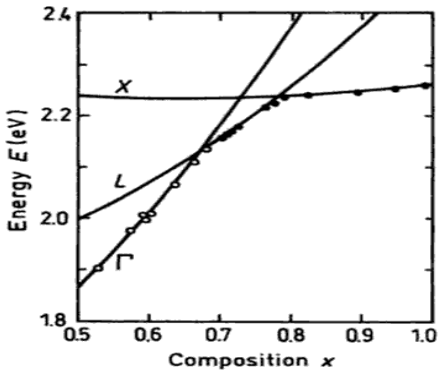

Fig.3: Material composition dependence of the Γ, L, and X-band gaps $Ga_xIn_{1-x}P$ at 300 K[27].

For materials where the band gap changes between direct and indirect the relative electron mass of the lowest band is considered. Then a quadratic interpolation of the masses is used as a function of the material composition of an alloy $Ga_xIn_{1-x}P$[28-29]:

$$m_\Gamma^* = 0.17 - 0.172x + 0.084x^2$$
$$m_L^* = 0{,}63 + 0.13x$$
$$m_X^* = 0{,}667 + 0.13x$$

For materials where the band gap changes between direct and indirect the relative electron mass of the lowest band is considered. Then a quadratic interpolation of the masses is used as a function of the material composition of an alloy $Ga_xIn_{1-x}P$[28-29]:

$$m_\Gamma^* = 0.17 - 0.172x + 0.084x^2$$
$$m_L^* = 0{,}63 + 0.13x$$
$$m_X^* = 0{,}667 + 0.13x$$

For the case of InP, it is found that $m_\Gamma = 0.082$, and $m_X = 0.418$, while for the case of GaP, it is found that $m_\Gamma = 0.15$, and $m_X = 0.5$. The dielectric constant or relative permittivity $\boldsymbol{\varepsilon_r}$ is one of the basic properties of semiconductor. The permittivity's of alloy materials $Ga_xIn_{1-x}P$ are interpolated from the values of the *basic materials* as a linear function of x [28]:

$$\varepsilon_0 = 1.29x + 11.11$$
$$\varepsilon_\infty = 0.44x + 9.113$$

The values of the mass densities of the basic materials are well-known, and are used to model the values for alloy materials. A linear change between the values of basic materials is used [28]:

$$\rho = (0.652x + 4.14).10^3$$

The lattice constant of a ternary alloy $GaxIn1_{-x}P$ can be expressed as a linear combination of the lattice constants of the two forming binary alloys [28]:

$$a = 5.4505 - 0.4182x$$

3. Results

Fig. 3 shows the electron drift velocity versus the electric field simulated for the bulk InP. We note that initially the electron drift velocity monotonically increases with the applied electric field strength, reaching a maximum of about 2.5×10^7 $cm.s^{-1}$when the applied electric field strength is around 10 kV/cm.

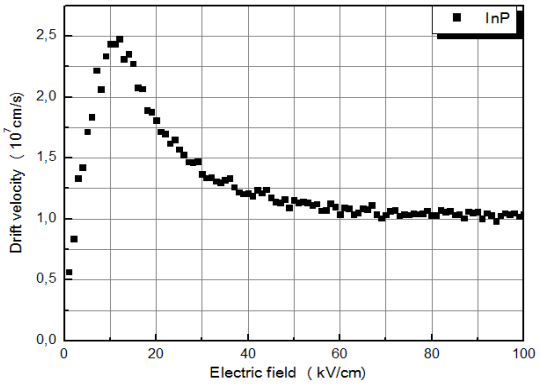

Fig. 3: The velocity-field characteristic associated with bulk InP.

For applied electric fields strengths in excess of ≈10 kV/cm, the electron drift velocity decreases in response to further increases in the applied electric field strength, i.e., a region of negative differential mobility is observed, the electron drift velocity eventually saturating at about 1×10^7 $cm.s^{-1}$ for sufficiently high applied electric field strengths.

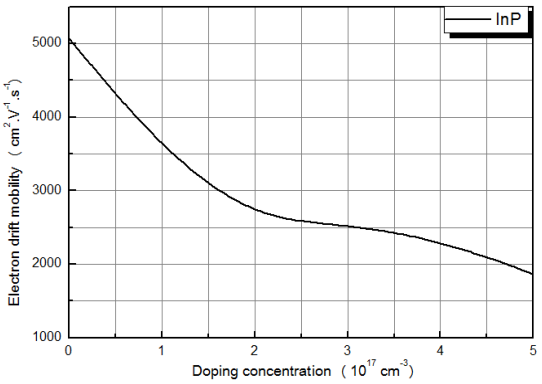

Fig. 4: Mobility of electrons as a function of the electric field in the InP

If we examine the average electron energy as a function of the applied electric field strength, shown in **Fig. 5**, we see that there is a sudden increase at around 6 kV/cm; this result was obtained from the same steady-state InP Monte Carlo simulation of electron transport as that used to determine **Fig. 5**.

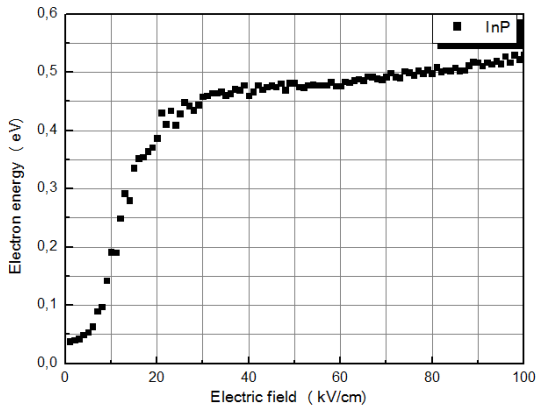

Fig.5: The average electron energy as a function of the applied electric field for bulk InP.

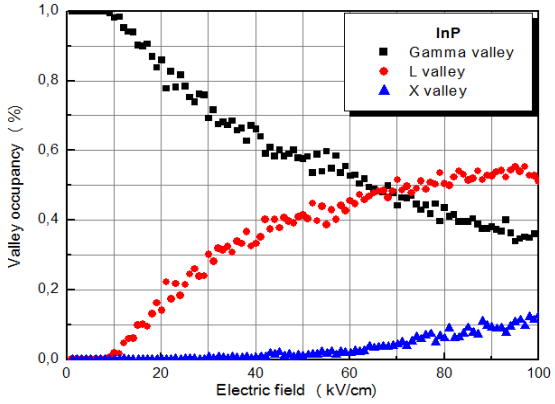

Fig.6: The valley occupancy as a function of the applied electric field for the case of bulk InP.

In order to understand why this increase occurs, we note that the dominant energy loss mechanism for many of the III–V compound semiconductors, including bulk InP, is polar optical phonon scattering. When the applied electric field strength is less than 6 kV/cm, all of the energy that the electrons gain from the applied electric field is lost through polar optical phonon scattering.The other scattering mechanisms, i.e., ionized impurity scattering, piezoelectric scattering, and acoustic deformation potential scattering, do not remove energy from the electron ensemble, i.e., they are elastic scattering mechanisms. Beyond certain critical applied electric field strength, however, the polar optical phonon scattering mechanism can no longer remove all of the energy gained from the applied electric field. Other scattering mechanisms must start to play a role if the electron ensemble is to remain in equilibrium. The average electron energy increases until inter-valley scattering begins and an energy balance is re-established.

In**Fig. 6**, we also plot the fractional electron occupancy of the central conduction band valley as a function of the applied field for zinc blend InP at 300 K, these results being from Monte Carlo simulations of electron transport in this material. We see that intervalley transitions, as indicated by a decrease in the occupancy of the central valley, do indeed begin in the neighborhood of 10 kV/cm. As the applied electric field is increased, the average electron energy increases until a substantial fraction of the electrons have acquired enough energy in order to transfer into the upper valleys. As the effective mass of the electrons in the upper valleys is greater than that in the lowest valley, the electrons in the upper valleys will be slower. As more electrons transfer to the upper valleys, the electron drift velocity decreases. This accounts for the negative differential mobility observed in the velocity–field characteristic depicted in **Fig. 4**.

In **Fig. 7**, the simulated electron drift velocity is plotted as function of applied electric field in Zinc blend GaP, these results being obtained from Monte Carlo simulations of electron transport at 300 K and electron concentration is equal to $10^{14} cm^{-3}$. Gallium Phosphide "GaP" has an indirect band gap and at lower electric fields, so electrons occupied X satellite valley at first; so it is expected that its velocity-field curves does not have a peak. At higher electric field, inter-valley optical phonon emission dominates causing the drift velocity to saturate at around 0.8×10^7 cm.s^{-1}.

In **Fig. 8**, we also plot the average energy of electrons in Zinc blend GaP as a function of the applied field. It is clearly see that energy curves demonstrate a higher monotonic increasing with increasing of external field at first. This increase in the average energy continues until the intervalley energy separation is achieved, at which point many of the electrons will have transferred from the central valley to the upper valleys.

The valley occupancies for the X, Γ and L valleys as a function of the applied field for Zinc blend GaP at 300 K are illustrated in **Fig. 9**.We see that intervalley transitions, as indicated by a decrease in the occupancy of the central valley X. As the applied electric field is increased, the average electron energy increases until a substantial fraction of the electrons have acquired enough energy in order to transfer into the upper valleys L and Γ. As the effective mass of the electrons in the upper valleys is greater than that in the lowest valley, the electrons in the upper valleys will be slower. As more electrons transfer to the upper valleys, the electron drift velocity decreases.

The drift velocity is plotted in **Fig. 10** function of applied electric field in InP and GaP with temperature as a parameter. For the calculations a fixed doping concentration of 1 x 10^{17} cm^{-3} was used. It is well known that temperature plays a decisive role in influencing the velocity-field characteristics of semiconductors occur.We note that the form of the velocity-field characteristic changes substantially as the temperature is increased. In particular, the peak drift velocity and the saturation drift velocity are found to decrease substantially with increased temperatures.

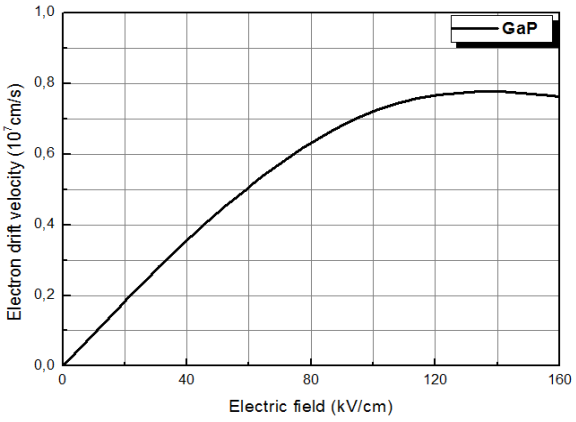

Fig. 7: The velocity-field characteristic associated with bulk GaP.

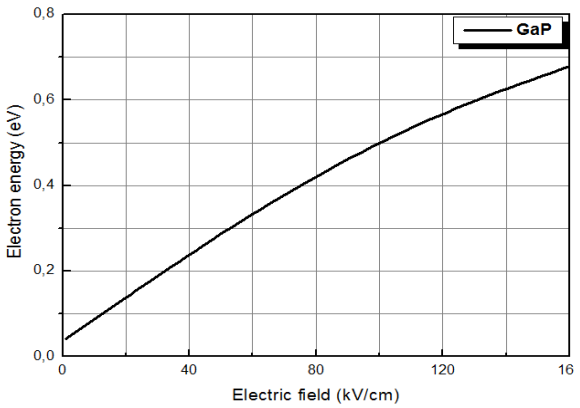

Fig.8: The average electron energy as a function of the applied electric field for bulk GaP

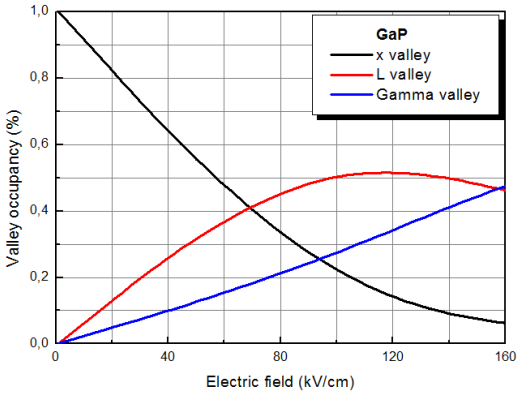

Fig.9: The valley occupancy as a function of the applied electric field for the case of bulk GaP.

It is interesting to note that the low field mobility increases as the temperature is lowered, whereas, the saturation velocity shows a less pronounced temperature dependence. This can be explained by noting that under low field conditions, scattering is dominated by acoustic phonons, ionized impurity, and polar optical phonon absorption which are all suppressed at lower temperatures leading to the improvement in mobility.At low fields for temperatures up to 300 K the hump in the velocity field characteristics is due to impurity scattering. At elevated temperatures the hump disappears due to the dominance of polar optical phonon scattering along with a drastic reduction in impurity scattering. the peak drift velocity decreases from about 2.76 x 10^{7} $cm.s^{-1}$cm s^{-1} at 77 K to about 2.10 x10^{7}cm s^{-1} at 500 K for InP and 0.9x10^{7} $cm.s^{-1}$at 77 K to about 0.6 x10^{7} $cm.s^{-1}$at 500 K forGaP.

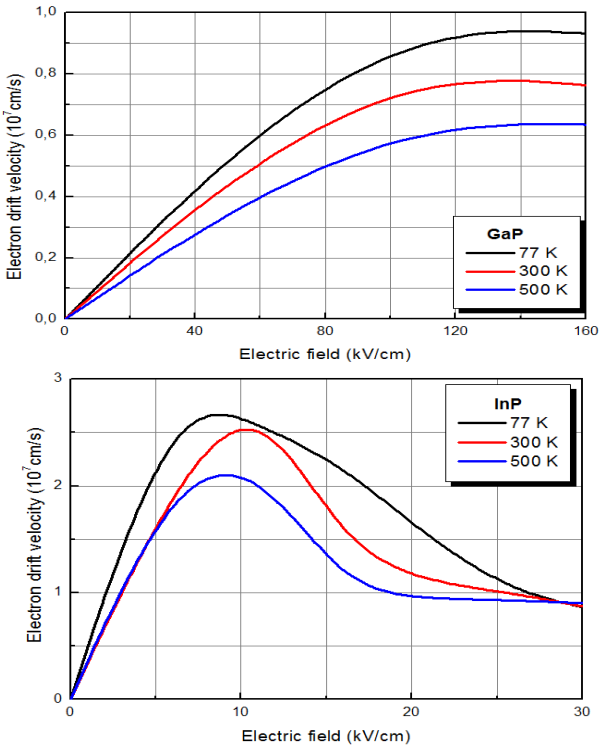

Fig. 10: Electron steady-state drift velocity in bulk InP and GaP as a function of applied electric field at various lattice

temperatures **Fig.11** shows the variation of the steady-state drift velocity as a function of the applied electric field for three different ionized impurity concentrations at room temperature for InP and GaP. The influence of doping becomes particularly noticeable for doping concentrations 1 x10^{18} cm^{-3}; the peak drift velocity decreasing markedly with further doping. the position of the peak velocity moves and decreases from about 2.5 x 10^{7} cm s^{-1} at 1 x 10^{14} cm^{-3} to about 1.72X 10^{7} cm s^{-1} at 1 x 10^{18} cm^{-3} for InP and 0.76x 10^{7} cm s^{-1} at 1 x 10^{14} cm^{-3} to about 0.63x 10^{7} cm s^{-1} at 1 x 10^{18} cm^{-3} for GaP.

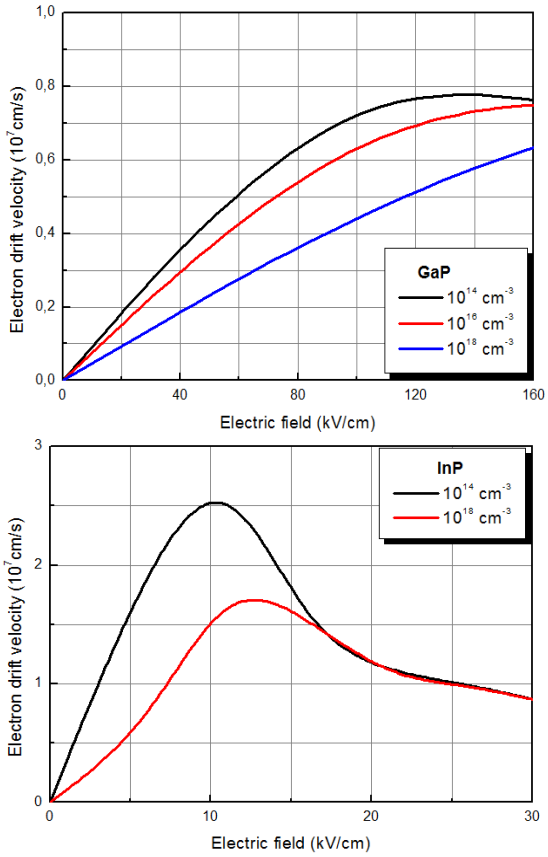

Fig. 11: Electron steady-state drift velocity in bulk InP and GaP as a function of applied electric field at various donor concentration.

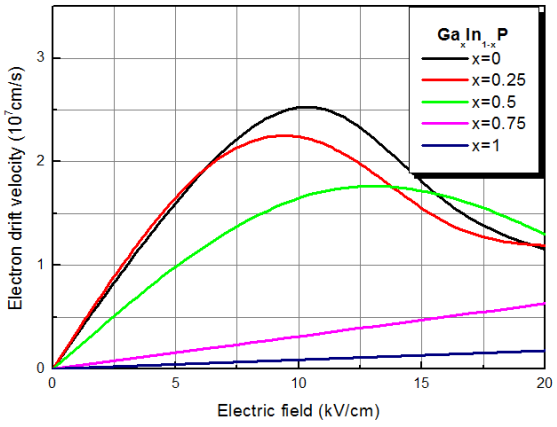

Fig. 12: The velocity-field characteristic associated with bulk $Ga_xIn_{1-x}P$.

The steady-state electron velocity-field for $Ga_xIn_{1-x}P$ doped to 10^{16} cm-3, at 300 K is presented in **Fig. 12**.

The dependence of the velocity-field relationship on increasing Ga mole fraction in $Ga_xIn_{1-x}P$ arises mainly from increases in the band-gap, the separation and the effective mass. The increasing electron effective mass, in the central valley, with increasing Ga mole fraction results in decreasing low field mobility. With increasing Ga mole fraction the valley separation increases with a consequent increase in the critical electric field, defined as the electric field where the velocity peaks. The increase in separation with increasing Ga mole fraction also results in a reduction in the intervalley scattering rate with a consequent decrease in the population in the upper valley and higher drift velocity at high fields. Especially under low fields, The steady-state electron velocity in $Al_xGa_{1-x}As$ is significantly degraded when x is increased to 0.3. Therefore, steady-state electron velocity in $Ga_{0.51}In_{0.49}P$ is higher than that of $Al_{0.3}Ga_{0.7}As$ under moderately high field strengths.

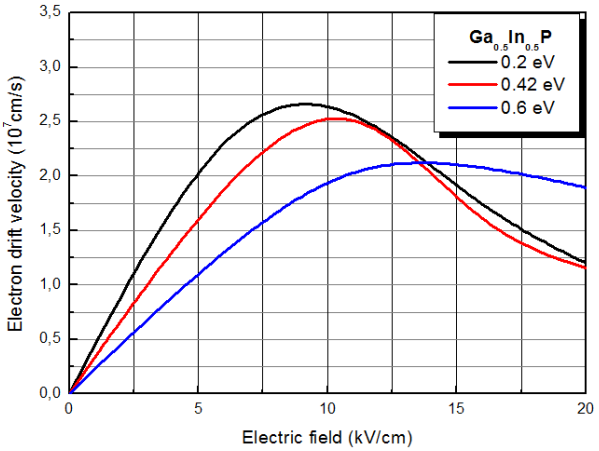

Fig. 13: Electron drift velocity versus electric field for different alloy scattering potentials in bulk $Ga_xIn_{1-x}P$.

The effects of different values of ΔU on the transport of electrons in bulk $Ga_xIn_{1-x}P$ using the single particle Monte-Carlo program have been compared. The results of the transport simulations are shown in **Fig. 13**. The general trend in the velocity-field curves is a reduction of the drift velocity with increased alloy scattering potential. This is expected as an increase in alloy potential increases the total scattering rate and decreases the electron free flight time. so, if the alloy potential is increased, a larger field is needed to achieve a given level of L valley population. This can also be explained by the reduction of the time between collisions. As the free flight time falls the energy gained in this time decreases, and so a higher field is needed for the electron to attain the energy at which scattering to the L valleys becomes possible. A direct consequence of this is that the electron population in the Γ valley at any given field increases with alloy scattering strength and results in the shift of the peak velocity to higher fields seen in **Fig. 13**. If we compare the transport

results for GaP with those for $Ga_xIn_{1-x}P$ with $\Delta U = 0$ eV, we see the effect due to the changes in band structure and material parameters from alloying alone. As expected, the alloy has a greater low field mobility and higher peak velocity which is in turn because it has a lower Γ valley effective mass and a larger $\Delta_{\Gamma L}$ The alloy also has a lower saturation velocity due to its larger satellite valley effective masses.

Conclusions:

In conclusion, we have presented low-field electron transport properties of $Ga_xIn_{1-x}P$. Under moderately high field strengths, average electron velocity in $Ga_xIn_{1-x}P$ has been found to be higher than that of $Al_xGa_{1-x}As$ at the most widely used AI mole fraction of 0.3.In this paper we have introduced and examined the effects of alloy concentration of bulk $Ga_xIn_{1-x}P$, and how this affects the transport properties, especially the average drift velocity, predicted by our Monte-Carlo simulation programs. We found that, for $x = 0.5$, the alloy scattering potential ΔU had an important effect on the carrier velocity, as ΔU increased the scattering rate increased and the carrier velocity was reduced. However, for the most of the range of ΔU considered and especially' the value fitted to experimental results $\Delta U = 0.42$ we found a higher low field mobility and increased peak velocity over that for GaP, due to the smaller Γ valley effective mass and larger $\Delta E_{\Gamma L}$ in the alloy. We have found that (with $\Delta U = 0.42$) increasing Gallium concentration:

- Generally improved low field mobility, due to the smaller Γ valley effective mass,
- Increased the peak velocity, because of the larger value of $\Delta E_{\Gamma L}$,
- Reduced the saturation velocity, which we attributed to the larger satellite valley effective masses.

References

[1] Vedam Ramamurthy, AllaSrivani et G Veeraraghavaiah, "Investigation in Nano III-V ternary InxGa1-x P semiconductor materials by chemical vapor deposition", International Journal of Physical Research, 2 (2) (2014) 37-39.

[2]Ariza C. H, Rev. Acad. Colomb. Cienc., 27 104, (2003), pp. 357-369.

[3] S. Dissanayake, S. X. Huang, H. X. Jiang and J. Y. Lin, "Charge Storage and Persistent Photoconductivity in a CdS0.5Se0.5 Semiconductor Alloym," Physical Review B, Vol. 44, No. 24, 1991, pp. 13343-13348. doi:10.1103/PhysRevB.44.13343.

[4] S. Krishnamurthy, A. Sher, M. Madou and A.-B. Chen, "Semiconductor Alloys for Fast Thermal Sensors," Journal of Applied Physics, Vol. 64, No. 3, 1988, pp. 1530- 1532. doi:10.1063/1.341828.

[5] S. Strite and H. Morkoc, American Vaccum Society, B10 4, (1992), pp. 1237-1266.

[6] Y.H. Wang and K.W. Lee, "Liqiud Phase Oxidation on InGaP and its Applications", Adv. In solid state circuits technologies, ISBN 978-953, pp.446, (2010).

[7] M.J. Mon and E. A. Fitzgerald, J. of Appl. Phys. 105 013107, (2009).

[8]G.R.Moriarty, M.Kildemo, J.T.Beechinor, M.Murtagh, P.V.Kelly, G.M.Crean and S.W.Bland, "Optical and structural properties of InGaPheterostructures" , Thin Solid Films, 364 244-248 (2000).

[9]P.Emst,C.Geng, G.Hahn, F.Scholz, H.Schweizer, F.Philip , and A. Mascarehas, J.Appl. Phys. 79, 2633(1996).

[10]Harrison J. W. and Hauser J. R. 1976 J. Appl. Phys. 47 292.

[11]Harrison J. W. and Hauser J. R. 1976 Phys. Rev. B. 13 5347.

[12]Asch A. E. and Hall G. L. 1963 Phys. Rev. 132 1047.

[13]Littlejohn M. A., Hauser J. R., Glisson T. H., Ferry D. K., and Harrison J. W. 1978 Solid State Electron. 21 107.

[14] M. A. Littlejohn et al., "Alloy scattering and high field transport in ternary and quaternary III-V semiconductors (FET model)," Solid-State Electron., vol. 21, pp. 107–114, Jan. 1978.

[15]Marsh J. H., Houston P. A., and Robson P. N. 1981 Proceedings of the 17th International Symposium on Gallium Arsenide and Related Compounds, Vienna 1980 Institute of Physics, London. p621.

[16]Basu P. K. and Nag B. R. 1983 Appl. Phys. Lett. 43 689.

[17] V. W. L. Chin, B. Zhou, T. L. Tansley, and X. Li, "Alloy-scattering de pendence of electron mobility in the ternary gallium, indium, and aluminum nitrides," J. Appl. Phys., vol. 77, pp. 6064–6066, 1995.

[18] J. C. Phillips, "Ionicity of the chemical bond in crystals," Rev. Mod.*Phys., vol. 42, pp. 317–354, 1970.*

[19] Schubert, E. Fred, Thomas Gessmann, and Jong Kyu Kim. Light emitting diodes. John Wiley & Sons, Inc., 2005.

[20]Adachi S. 1982 J. Appl. Phys. 53 8775.

[21]Adachi S. 1985 J. Appl. Phys. 58 R1.

[22]Varshni Y P. Temperature dependence of the energy gap in semiconductors. Physica, 1967, 34(6): 149.

[23]Pansh, M. B. and H. C.Casey Jr., J. App. Phys. 40, 1 (1969) 163-167.

[24]t'Hooft, G. W. C. J. B. Riviere, M. P. C. Krijn, C. T. H. F. Liedenbaum, and A. Valster, Appl. Phys. Lett. 61, 26 (1992) 3169-3171.

[25] Auvergne, D., Merle, and H. Mathieu, Solid State Commun. 21, 5 (1977) 437-439.

[26] Lange, H., Donecker, and H. Friedrich, Phys. Stat. Solidi (b) 73, 2(1976) 633-639.

[27]Krutogolov, Yu. K., S. v. Dovzhenko, S. a. Diordiev, L. I. Krutogolova, Yu. I. Kunakin, and S. A. Ryzhikh, Sov. Phys. Semicond. 23, 5 (557)-558.

[28]Dessenne, F., "Etude théorique et optimisation de transistors à effet de champ de la filière InP et de la filière GaN", Doctorat Thesis, USTL Lille, 1998.
[29]M. Levinshtein, S. Rumyantsev, "Handbook Series on Semiconductor Parameters", volume 2 ternary and quaternary III-V Compounds, 1999 by world Scientific Publishing Co. Pte.Ltd.

Journal of New Technology and Materials
JNTM
Vol. 07, N°01 (2017)47-52

OEB Univ. Publish. Co.

The heterostructure ZnO/Al/SiO2/Si fabrication for Piezoelectric SAW and BAW Transducers and Sensors

R. Serhane [a], F. Hadj-Larbi [a], S. Lafane [b], S. Abdelli-Messaci [b] and T. Boutkedjirt [c]

[a] *Division Microélectronique et Nanotechnologie, Centre de Développement des Technologies Avancées (CDTA). Cité 20 Août 1956, Baba Hassen, BP: 17, DZ-16303, Algiers Algeria, E-mail : rafik_serhane@hotmail.com*

[b] *Division Milieux Ionisés et Laser, Centre de Développement des Technologies Avancées (CDTA). 20 Août 1956, Baba Hassen, BP: 17, DZ-16303, Algiers, Algeria.*

[c] *Equipe de Recherche Physique des Ultrasons, Faculté de Physique, Université des Sciences et de la Technologie Houari Boumediene (USTHB), BP 32, El-Alia, Bab-Ezzouar, DZ-16111 Algiers, Algeria.*

Corresponding author: email: rafik_serhane@hotmail.com, rserhane@cdta.dz

Received date: March 23, 2017; revised date: May 11, 2017; accepted date: May 23, 2017

Abstract

Zinc oxide (ZnO) thin films were deposited by pulsed laser deposition technique for making ZnO/Al/SiO_2/Si Bulk and Surface Acoustic Wave (BAW and SAW) transducers. The aim is to improve the piezoelectric properties of the ZnO films, which are strongly linked to their texture and microstructure. ZnO films with a wurtzite structure were deposited on the Al electrode layer, at different substrate temperatures, within the 100-500°C range. The characterization by X-ray diffraction showed that the deposited Al electrode was (111) oriented and that the ZnO film has a c-axis (002) preferential orientation. The scanning electron microscopy of the ZnO films on Al/SiO_2/Si substrate showed an evidence of compact grains with a honeycomb-like structure on surface and a columnar structure on cross-section appeared after a sequential transition of amorphous to non-oriented to crystalline phase. The results indicated that the optimum substrate temperature is of 300°C and the electrical input impedance measurement on the Al/ZnO/Al BAW structure showed a piezoelectric response, where the fundamental resonance mode was located at 160 MHz, with an electromechanical coupling coefficient K_{eff}^2 equal to 3.2%. The best piezoelectric response is obtained at the fourth (4th) thickness mode vibration, located at the frequency of 636.3 MHz and having K_{eff}^2 of 9.10%.

Keywords: ZnO, Pulsed laser deposition, Piezoelectricity, BAW and SAW, Thin films ;

1. Introduction

In the past 10 years, Zinc oxide (ZnO) become a very popular material for its large use in thin films [1]. Due to its physical properties of semiconductor, electromechanical transducer and nanocrystalline thin film [2], ZnO has a potential application as schottky diode and solar cell application [3], It is alsoo very interesting for several Micro and Nano-Electro Mechanical Systems (MEMS [4] and NEMS [5]) applications. The high electromechanical coupling coefficient makes ZnO extremely promising as a piezoelectric element for sensors and actuators [6] and for many piezoelectric applications like Surface Acoustic Wave (SAW) [7] and Bulk Acoustic Wave (BAW) [8] transducers. ZnO thin films can be fabricated using phase Spray pyrolysis [9] sol-gel process [10], RF magnetron sputtering [11] and laser ablation [12-14], etc.

In this work, a polycrystalline ZnO was prepared by the Pulsed Laser Deposition (PLD) technique, at different substrate temperatures, ranging from 100 to 500 °C, on multilayer Al(111)/SiO_2/Si substrate. The Al film (with a thickness of 250 nm) considered as the bottom electrode for BAW transducers was prepared, by Electron Beam Evaporation (EBE) technique and deposited, at room temperature, on a 2µm-SiO_2 layer. The SiO_2 film was performed by Silicon wet oxidation step. The BAW transducer was used to study the piezoelectric properties of the deposited ZnO, which could be used in transducers and sensors applications, or

2. Experimental procedures

2.1. Thermal Oxidation of Silicon

The electrical isolation of the device from the Si (100) p-type substrate was performed by using an intermediate SiO_2 layer, this former was grown by a thermal oxidation step of Silicon, according to a dry-wet-dry process, as follows:

- **Furnace load step:** from T=800 °C to 1100 °C, with a heating rate of 5 °C/min, under a gas flow of O_2=500 sccm and N_2=6000 sccm.
- **Dry oxidation step: during t=10 min at T=1100 °C, with O_2=6000 sccm.**
- **Wet oxidation step:** during t=9h 10 min at T=1100°C, under a mixture of (H_2+O_2)(5+3.5) slm.
- **Dry oxidation step:** during t=10 min at T=1100 °C, with an O_2 flow of 6000 sccm.
- **Furnace unload step** : from T=1100 °C to 800 °C, with a rate of 5 °C/min, under an O_2 gas flow of 500 sccm and a N_2 flow of 6000 sccm.

The temperature cycle is presented in (Fig 1.a) and the SEM micrograph of the obtained 2 µm-SiO_2 film was shown in (Fig 1.b).

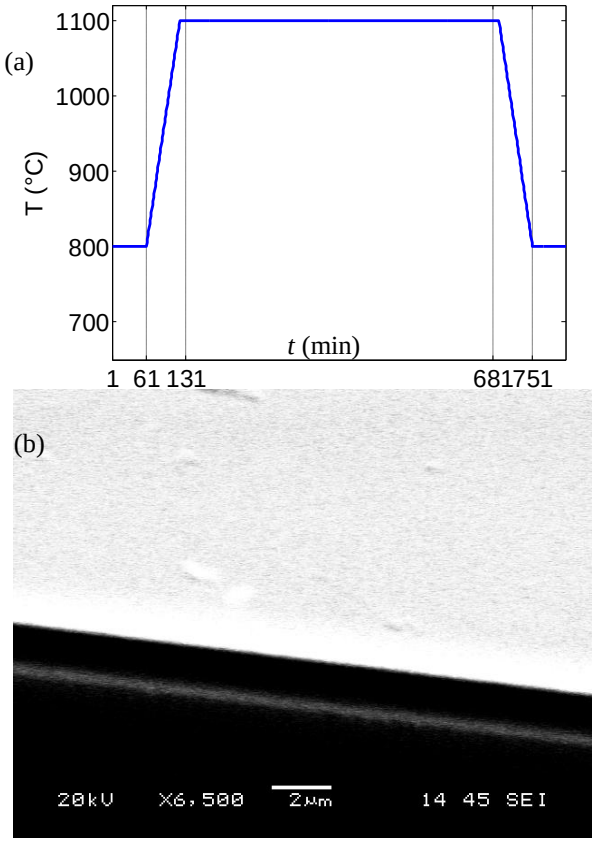

Fig. 1: (a)-Oxidation cycle, (b)- SEM characterization of the SiO_2 film obtained by the thermal oxidation.

2.2. . Deposition of the Al electrode on SiO_2 by EBE technique

The Al buffer layer, which serves as a bottom electrode for the piezoelectric characterization, has been deposited by the Electron Beam Evaporation (EBE) technique on the SiO_2 layer. The deposition is realized during 35 min at a pressure of 1.6 10^{-6} mbar with a current intensity of 0.486 A and a voltage of 6.17 kV. The deposition rate is estimated to be 1.2 Å/s.

2.2.1. Surface morphology and cristallinity of the Al thin film

The surface morphology of the Al grown films (Fig.2.a) is analyzed by a SEM (SEM-JEOL 6400) and the Al films microstructure (Fig 2.b) is determined with a Bruker D8 X-ray diffractometer (Advance (θ,2θ), Cu Kα and λ_α=1.5406 Å) in a grazing incidence. Figure 2.a shows that the Al thin film is uniformly deposited on the SiO_2 surface, its surface is smooth and no cracks are observed. The X-Ray Diffraction (XRD) patterns of Al thin films grown on a SiO_2/Si substrate (Fig 2.b) showed that the Al has different crystalline orientations ([111], [200], [220] and [311]), but if, in addition, we take into account the K_β X-ray radiation, the [111] direction becomes the most predominant orientation.

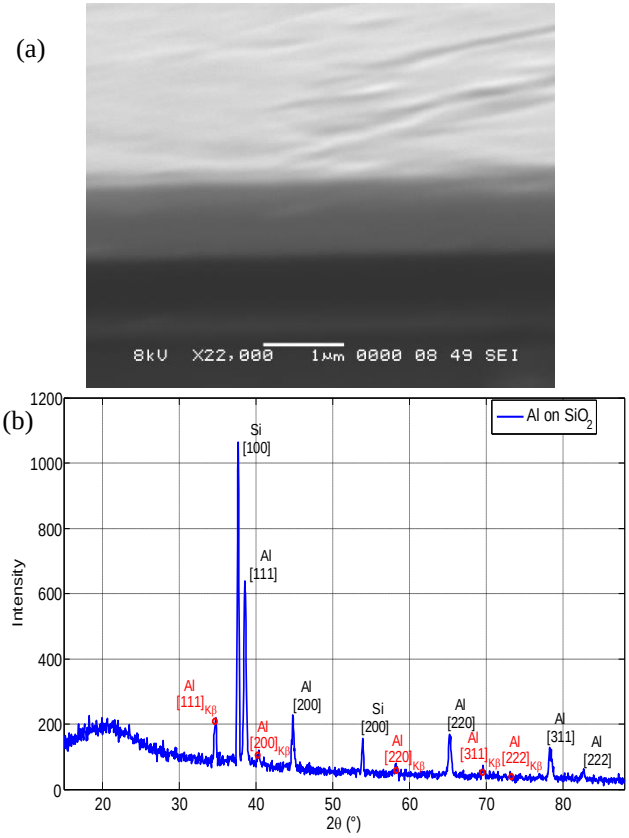

Fig. 2: Characterization of the Al thin film deposited on the SiO_2/Si substrate, (a)-SEM image of the Al layer and (b)- XRD patterns obtained at a grazing incidence.

2.3. Elaboration of the ZnO thin films by PLD

The Al/SiO_2/Si substrate of 0.25µm/2µm/350µm thickness respectively is mechanically attached to a heating block in a PLD chamber at vacuum of 10^{-6} mbar. A power generator monitors the temperature of the substrate. The ZnO target is fixed on the rotated holder located at 4 cm

far from the substrate holder. The pulsed KrF laser beam, (f=10 Hz, λ=248 nm and τ=25 ns), is directed at 45° with respect to its normal and focused on the target surface at a fluence of 2 J/cm^2. The vacuum chamber is, then, filled with Oxygen until obtaining the pressure of 10^{-2} mbar [15]. The deposition of ZnO is performed during 1h30min at the substrate temperatures of 100, 200, 300, 400 and 500°C.

3. Results and discussion

3.1. ZnO this film characterization

3.1.1. Crystallinity of the ZnO thin films

Fig. 3.a shows the XRD patterns of the ZnO thin films deposited on Al at different substrate temperatures (T), the ZnO polycrystalline film of Wurtzite structure grows in a preferred (002) orientation (located at 2θ=34.48°) corresponding to the $P6_3mc$ space group [16]. We notice that the ZnO thin film structure is sensitive to the deposition substrate temperature. Indeed, for all the obtained diffractograms, from 100 to 500 °C, the film realized at 300 °C exhibits the strongest intensity of the (002) peak of diffraction.

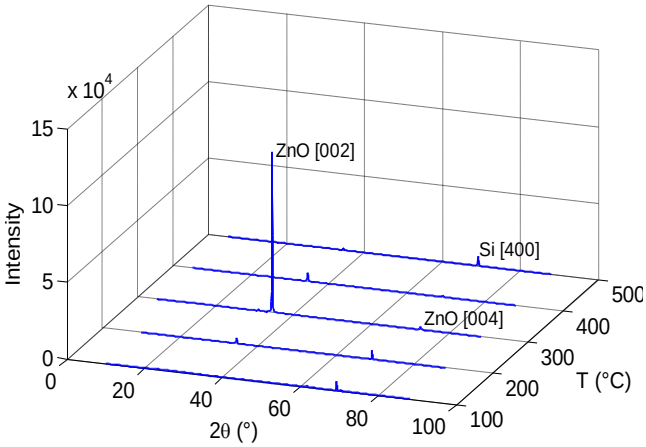

Fig. 3: a)- XRD patterns of the elaborated ZnO at different substrate temperatures

To assess the crystallite grain size D (coherence length) of the ZnO films, the line breadth β is calculated by fitting the (002) ZnO peak at 34.48° (observed in Fig.3.a) with the pseudo-Voigt function and taking the corresponding full width at half maximum. The line breadth β is related to the grain size D according to Scherrer formula [17, 18]:

$$D=\frac{0.9\lambda_0}{\beta.\cos(\theta_0)}, \quad (1)$$

where λ_0=1.5406 Å is the Cu-K_α radiation wavelength and θ_0 the Bragg angle corresponding to the (002) ZnO peak. The line breadth value is around 0.18° for the ZnO at 300 °C. The grain size is evaluated to 47 nm, which means a high quality of the ZnO films elaborated by PLD [19]. The c_0 lattice constant of the ZnO hexagonal unit cell is calculated from the Bragg relationship using $1/d_{hkl}^2=4(h^2+hk+k^2)/3a_0^2+l^2/c_0^2$ [20] (h=0, k=0, l=2), where c_0 is close to 5.207 Å [21].

3.1.2. Surface morphology characterization of the ZnO thin film

Fig. (4) shows the SEM images of the ZnO thin film deposited on Al/SiO_2/Si at 300°C. The surface morphology of the ZnO film on Al (Fig. 4.a) presents some roughness and shows a macroporous structure of a honeycomb-type morphology. The SEM cross-section image (see Figure (4.b)) shows a compact structure of the ZnO thin film and a columnar grain growth along the c-axis. The crystallized grains are perpendicular to the substrate surface, and this is a consequence of the high growth rate (~1.24 Å/pulse) of ZnO along the c-axis [22] which also promotes the growth of (002) polar planes with the lowest surface free energy [23]. This plane is formed by the creation of an electronegative surface caused by the Oxygen plane, the polar plane increases the flux of incident species by attracting the Zn^+ species and depositing an electropositive Zinc plane, and so on. This mechanism leads to the formation of alternate planes of Zn atoms and O atoms [24], forming a hexagonal (Wurtzite) structure.

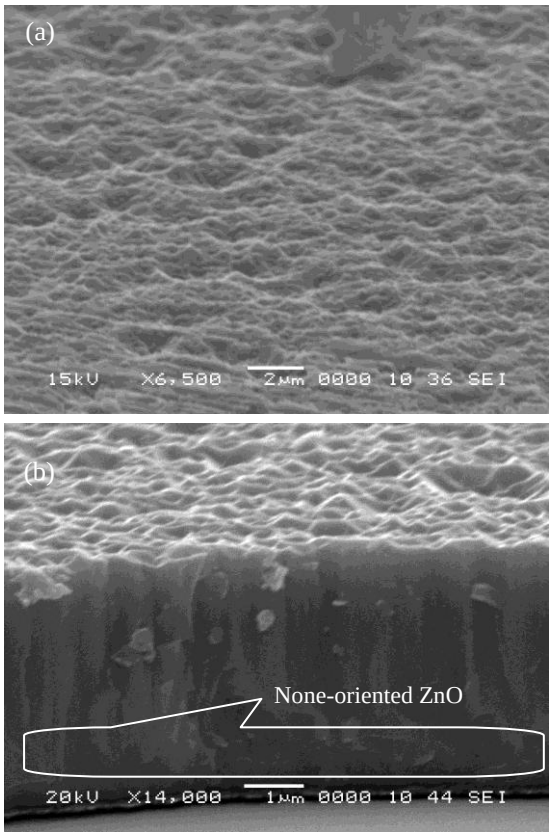

Fig.4: Characterization of the ZnO thin films deposited on Al/SiO_2/Si substrate; (a)- SEM surface morphology of sample realized at 300°C and (b)- SEM cross-section.

The ZnO film presents a stratified structure with continuous transitions between each other. A first layer is constituted of an amorphous phase of ZnO, followed by a non-oriented layer, and finally comes the oriented layer of ZnO (see Fig. 4.b). The amorphous phase of ZnO is due to an amorphous Aluminum oxide layer, which is formed on the Aluminum electrode surface by injecting Oxygen in the PLD chamber. This oxidation occurs during the time in which the Oxygen pressure is stabilized and the substrate is heated at 300 °C (roughly 10 to 15min before the ablation process).

In order to study the evolution of (002) ZnO peak in function of the thickness (grown on Al/SiO_2/Si substrate), we have done a set of XRD measurements on samples realized at different deposition times (7, 15, 30 and 45 min) corresponding to different thicknesses (~0.26, 0.56, 1.12 and 1.68 µm, respectively). These XRD data are presented in the figure (5.a), where the well-oriented (002) ZnO becomes clearly visible beyond 30 min of deposition time, and this corresponds approximately to 1µm thickness. For the first 7 minutes of deposition, no orientation of ZnO is observed; so, we assume that at this stage, the ZnO has an amorphous phase, and then, at 15 min, some phases become weakly apparent. At 30 min and beyond, the (002) peak is the predominant phase.

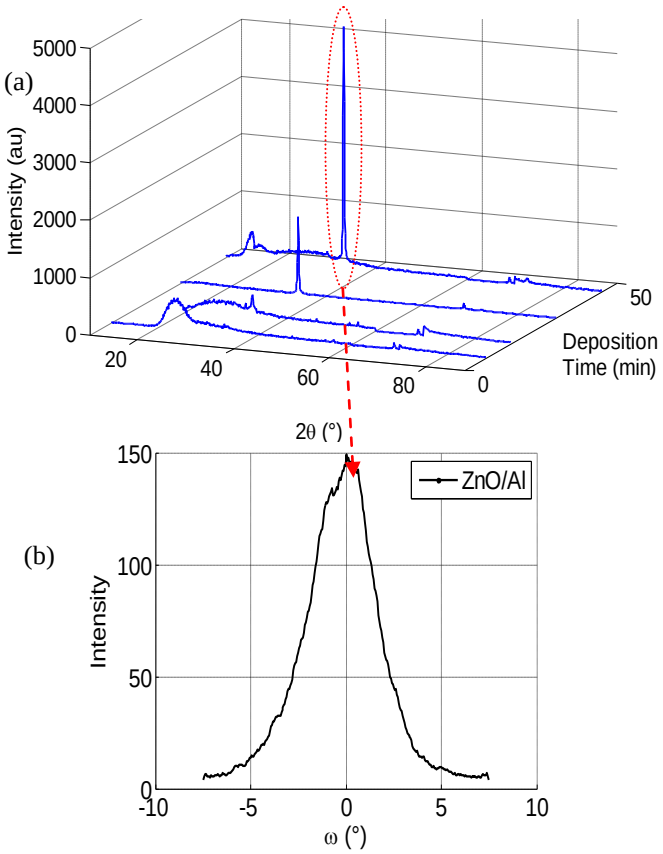

Fig. 5: (a)- XRD characterization of ZnO on Al for different deposition times (7, 15, 30 and 45 minutes) and (b)- XRD rocking curve of (002) c-axis of ZnO/Al deposited at 300°C.

The crystalline quality (mosaicity) of the elaborated ZnO thin film is evaluated by the rocking curve measurements [25] on the (002) diffraction peaks (Fig. 5.b), carried out for the sample of ZnO deposited at 300 °C during 90 minutes. This measurement permits to evaluate the degree of the *c*-axis alignment with respect to the normal of the substrate. The FWHM (Full Width at Half Maximum) value of this rocking curve is 3.75°, which means a good crystalline quality of the ZnO deposited on Al.

3.2. Deposition of the Al top electrode by thermal evaporation

In order to evaluate the piezoelectric effect of the considered BAW transducer (Al/ZnO/Al/SiO_2/Si structure), a circular top electrode (with a radius of 1.8 mm) is made on the ZnO surface by a thermal evaporation of Aluminum through a mask. The piezoelectric properties of the BAW transducer are deduced from the electrical input impedance measured by a HP8753ES Network Analyzer in the harmonic regime.

4. Piezoelectric characterization of the device

The representation of the electrical input impedance in Fig.6 shows some resonance peaks located at frequencies which are multiples of the fundamental mode frequency. It shows also some parasitic modes (denoted by PM). The fundamental resonance in thickness mode vibration is observed at f_r=157.4 MHz and the anti-resonance frequency appears at f_a=159.5 MHz. The electrical resistance at resonance is 10.5 Ω, whereas, at the anti-resonance, it becomes equal to 186.2 Ω. For each mode taken separately, the phase representation (dashed line) shows that the resonator behaves like a capacitance (*Phase(Z)=-π/2*) just before resonance. It switches to an inductive behavior between the resonance and the anti-resonance. Then, it becomes again capacitive after the anti-resonance frequency [26].

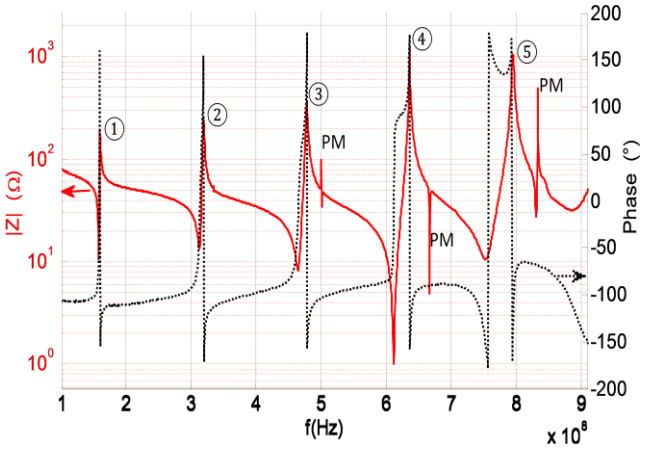

Fig. 6: Electrical input impedance (magnitude and phase) of the BAW device.

The effective electromechanical coupling coefficient [27], K_{eff}, is related to the resonance and the anti-resonance frequencies by the equation (3):

$$K_{eff}^2 = \frac{\pi f_r}{2 f_a} \cdot \tan^{-1}\left(\frac{\pi f_r}{2 f_a}\right) \quad (2)$$

The previous values of f_r and f_a corresponding to the first mode (fundamental mode) lead to K_{eff}^2=3.21 %. The table(1) shows the results for the fundamental mode and for the higher order harmonics.

Table 1 : Characteristics of the resonance peaks.

Mode	f_r (MHz)	f_a (MHz)	R_r(Ω)	R_a(Ω)	K_{eff}^2(%)
1st mode (fundamental)	157.4	159.5	10.5	186.2	3.21
2nd mode	312.5	318.8	13.4	260.3	4.78
3rd mode	464.4	478.1	8.3	370.7	6.87
4th mode	611.86	636.26	1	1258	9.10

The best electromechanical coupling coefficient is obtained for the fourth (4th) mode, with K_{eff}^2=9.10 %, where the electrical resistance at the resonance frequency shows the smallest value (R_r=1 Ω), and the resistance at the anti-resonance frequency exhibits the largest value (R_a=1.26 kΩ).

5. Conclusion

The piezoelectric ZnO layer was prepared by the PLD technique at different substrate temperatures, from 100 to 500°C. The XRD measurements showed that the deposited ZnO films were *c*-axis (002) oriented, corresponding to the wurtzite structure, and indicated that 300°C was the optimal substrate temperature to obtain the well crystallized ZnO on Al buffer layer. The SEM characterization showed the evidence of a columnar structure on the cross-section, which was perpendicular to the substrate surface, it also showed an evidence of compact grains on the surface forming a honeycomb-like structure. The good crystallinity and mosaicity of the ZnO film are confirmed by the low value of the rocking curve FWHM measurement.

The elaborated ZnO layer is used in Al/ZnO/Al/SiO_2/Si BAW resonator, the device can work at a frequency which is a multiple of the fundamental mode frequency (157.4 MHz), but the best working frequency corresponds to the fourth harmonic and is located at 611.86 MHz. Indeed, at this frequency, the device presents simultaneously the highest piezoelectric performances with the largest piezoelectric coupling coefficient (K_{eff}^2=9.1%), the smallest electrical resistance at the resonance frequency and the largest electrical resistance at the anti-resonance frequency.

Acknowledgment

The authors wish to express their gratitude to Mr. F. Metehri for his help in the clean room. They would like to acknowledge all the MEMS team of the CDTA center, especially Mr. H. Khales and Mr. W. Aouimeur for their help in the electrical characterization.

References

[1] J.C. Fan, K.M. Sreekanth, Z. Xie, S.L. Chang and K.V. Rao, p-Type ZnO materials: Theory, growth, properties and devices, Progress in Materials Science, 58 (2013) 874–985.

[2] H.S. Al-Salman and M. J. Abdullah, Hydrogen Sensing Based on ZnO Nanostructures Prepared by RF-Sputtering on Thermally Oxidized Porous Silicon, Sensor Letters, 01/2015; 13(1).

[3] M. Benhaliliba, Y.S. Ocak, H. Mokhtari, C.E. Benouis, M.S. Aida. The microelectronic parameters of Al /ZnO/p-Si/Al Schottky diode for solar cell applications, DUFED 4(1) (2015) 1-3).

[4] T. Gryba, J. Carlier, S. Wang, X.Z. Zhao, S. Guo and J.-E. Lefebvre, One port contour-mode ZnO piezoelectric MEMS resonator, Microelectronic Engineering, 88 (2011) 3003–3010.

[5] B.P. Nabar1, Z. Çelik-Butlern and D.P. Butler, Piezoelectric ZnO nanorod carpet as a NEMS vibrational energy harvester, Nano Energy, 10 (2014) 71-82.

[6] S. Joshi, M. Parmar and K. Rajanna, A novel gas flow sensing application using piezoelectric ZnO thin films deposited on Phynox alloy, Sens. and Actuators A, 187 (2012) 194–200.

[7] A.J. Festschrift, J. Luo, Y.Q. Fu, L. Garcia-Gancedo, X.Y. Du, J.R. Lu, X. B. Zhao, E. Iborra, M. Ramos, and W. Milne, *ZnO based SAW and FBAR devices for bio-sensing applications.* Journal of Non-Newtonian Fluid Mechanics, 222 (2015) 209-216.

[8] X. Bian, H. Jin, X. Wang, S. Dong, G. Chen, J.K. Luo, M. Jamal Deen, and B. Qi, UV sensing using film bulk acoustic resonators based on Au/n-ZnO/piezoelectric-ZnO/Al structure, Sci Rep., 5 (2015) 9123.

[9] H.L. Ma, Z.W. Liu, D.C. Zeng, M.L. Zhong, H.Y. Yu, and E. Mikmekova, Nanostructured ZnO films with various morphologies prepared by ultrasonic spray pyrolysis and its growing process, Applied Surface Science, 283 (2013) 1006-1011.

[10] L.W. Wang, F. Wu, D.X. Tian, W.J. Li, L. Fang, C.Y. Kong and M. Zhou, Effect of Na content on structural and optical properties of Na-doped ZnO thin films prepared by sol-gel method, J. Alloys Comp., 623 (2015) 367-373.

[11] H.S. Al-Salman and M.J. Abdullah, Preparation of ZnO nanostructure by RF-magnetron sputtering on thermally oxidized porous silicon substrate for VOC sensing application, Measurement, 59 (2015) 248-257.

[12] M. Acuautla, S. Bernardini, L. Gallais, T. Fiorido, L. Patout, M. Bendahan,Ozone flexible sensors fabricated by photolithography and laser ablation

processes based on ZnO nanoparticales, Sens. Actuators B 203 (2014) 602-611.
[13] S.S. Xiao, L. Zhao, Y.H. Liu and J.S. Lian, Nanocrystalline ZnO films prepared by pulsed laser deposition and their abnormal optical properties, Applied Surface Science 283 (2013) 781– 787
[14] K. Bdikin, J. Gracio, R. Ayouchi, R. Schwarz and A.L. Kholkin, Local piezoelectric properties of ZnO thin films prepared by RF-Plasma-assisted pulsed-laser deposition method, Nanotechnology 21 (2010) 235703 (6pp).
[15] R. Serhane, S. Abdelli-Messaci, S. Lafane, H. Khales, W. Aouimeur, A. Hassein-Bey and T. Boutkedjirt, Pulsed Laser Deposition of Piezoelectric ZnO Thin Films Bulk Acoustic Wave Devices, Applied Surface Science, 288 (2014) 572-578.
[16] J. Goulon, N. Jaouen, A. Rogalev, F. Wilhelm, C. Goulon-Ginet, C. Brouder, Y. Joly, E.N Ovchinnikova, and V.E Dmitrienko, Vector part of optical activity probed with x-rays in hexagonal ZnO, J. Phys. Condens. Matter. 19 (2007) 156201.
[17] B.D. Cullity, Element of X-ray Diffraction, 2nd ed., Addison-Wesley Pub Co, Boston, MA, 1978.
[18] S.L. King, J.G.E. Gardeniers and I.W. Boyd, Pulsed-laser deposited ZnO for device applications, Applied Surface Science, 96-98 (1996) 811-818.
[19] Y. Yoshino, M. Takeuchi, K. Inoue, T. Makino, S. Arai and T. Hata, Control of temperature coefficient of frequency in zinc oxide thin film bulk acoustic wave resonators at various frequency ranges, Vacuum, 66 (2002) 467-472.
[20] E. A. Irene, Electronic Materials Science, Wiley, New Jersey, 2005, p.22.
[21] E.H. Kisi and M.M. Elcombe, u parameters for the wurtzite structure of ZnS and ZnO using powder neutron diffraction, Acta Cristallographica C, 45 (1989) 1867-1870.
[22] M. Nistor, N.B. Mandache, J. Perrière, C. Hebert, F. Gherendi and W. Seiler, Growth, structural and electrical properties of polar ZnO thin films on MgO (100) substrates, Thin Solid Films 519 (2011) 3959-3964.
[23] J. Perrière, E. Millon, and V. Craciun, ZnO and ZnO-Related Compounds, in : Robert Eason (Eds), Pulsed Laser Deposition of Thin Films: Application Led Growth of functional Materials, John Wiley & Sons, 2007. pp.261-289.
[24] S.J. Pearton, D.P. Norton, K. Ip, Y.W. Heo, and T. Steiner, Recent progress in processing and properties of ZnO, Prog. Mater. Sci., 50 (2005) 293-340.
[25] M.C. Tamargo, II-VI Semiconductor materials and their applications, Volume.12, Taylor & Francis (2001).
[26] R. Serhane, T. Boutkedjirt, and A. Hassein-Bey, in IEEE Explorer of the 24th International Conference on Microelectronics (Algiers, 2012).
[27] S.R. Naik, J.J. Lutsky, R. Reif and C.G. Sodini, Electromechanical Coupling Constant Extraction of Thin-Film Piezoelectric Materials using a Bulk Acoustic Wave Resonator, IEEE UFFC, N°.1, 45 (1998) 257-263.

Journal of New Technology and Materials
JNTM
Vol. 7 N°01 (2017)53-63

OEB Univ. Publish. Co.

The influence of obstacles and suspended matter on the distribution of turbulent flow velocities in a lamella separator

Farida Merrouchi[1], Ali Fourar[1], Fawaz Massouh[2], Djamel haddad[3] and Hanane Azoui[4]

[1] *University of Batna2, Hydraulics Department,Algéria*
[2] Laboratory Dyn-fluid E*NSAM, Paris- France*
[3] *University of Batna2,Mechanical Department,Algéria*
[4] PRIMALAB Laboratory, University of Batna 1, Algeria
Corresponding author: email: merrouchi.farida@yahoo.fr

Received date: September 22, 2016; revised date: May 20, 2017; accepted date: May 23, 2017

Abstract

Lamellar settlers are used for stormwater treatment in order to separate suspended matter form water. In these settlers, the effective decantation area is increased thanks to the presence of many successive inclined plates.

The problem of lamella settling tank is the inhomogeneous distribution of flow velocity between the inclined plates so this work focuses on the study of turbulent flow and its interaction with the successive plates.

In this perspective, we propose a coupling of Euler and Lagrange approaches in order to model flow and sediment transport. The numerical model has been implemented in the Fortrancode. The finite volume scheme (ADI) was adopted as it ensures good precision with reasonable computation time. The model introduces the Lagrangian time constant CL to determine the size and lifetime of the eddies where the particles move.

For testing our program we first studied the case of turbulent flow around a single plate and then two plates where we found satisfying results.

Then we enlarged our study to study several plates. The obtained results show that the lamellar elements are efficient to reduce flow velocity and increase the sedimentation rate comparatively to conventional tanks with vertical obstacles or without barriers.

Keywords: obstacles, numerical modelling, turbulence, secondary currents, walls law, finites volumes, scheme ADI,lamella separator

1. Introduction

The modeling of free surface flows are particularly situated at the level of the complexity of the met geometrical configurations, the variation of the shape of the bed, the inhomogeneous roughness of the bottom,hese flows are generally three-dimensional and unsteady.

The numerical difficulty increases with the presence of turbulence and the obstacles as for case example a lamellar decanter which is characterized by a significant number of obstacles

To understand the effect of one obstacle or several obstacles on the turbulent flow is a subject for a long time studied (e.g. Lamb (Lam1932)), Length (Lon1954). There is a particular large number of asymptotic analyses (Houghton and Kasahara [HK on 1968], Baines [Bai(Bay) on 1995], Dias and Vanden-Broeck [DV on 1989]) and digital (Lamb and Britter [LB on 1984], Lowery etLiapis [LL 1999]) who had for objective to determine asymptotic solutions of the shape of the free surfaces asymptotic solutions our study aims to be to know the local flow in the neighborhood of the obstacles in particular, when the free surface is far from these obstacles (big heights) and the influence of the obstacles on the inhomogeneous distribution of velocity

Inclined parallel plates are a classical subject with a long history, and Boycott [1] was the first who observed that the settling rate of suspension is better “if the tube is inclined than when it is vertical

The settling behavior in inclined vessel was modeled firstly by Ponder [2] and later by Nakamura and Kuroda [3] and for this reason is known as the PNK theory.

In a primary sedimentation tank, where the discrete settling prevails, Imam et al [4] applied a fixed settling velocity and used an averaged particle velocity; there are very few theoretical studies about lamellar settlers. Doroodchi et al. [5] investigated the influence of inclined plates on the expansion behavior of solids suspensions in liquid fluidized beds

So far, many researchers have used CFD simulations to study water flow and solids removal in settling tanks for sewage water treatment

However, there are not many works in the literature in CFD modeling of sedimentation tanks for potable water treatment.[11]

In Euler-Lagrange models, the Navier-Stokes equations are solved for the fluid phase while Newton's equation of motion isused to model the particle phase motion. The trajectory ofeach particle is calculated from a balance of the forces acting on it(Maxey & Riley, 1983).

The continuous phase (water) are governed by the equations of Navier-Stokes and the equation of continuity .The numerical methods of resolution of these equations are limited until our days because by one hand there is no reliable and fast standard numerical method, and on the other hand, the resolution of the equations of Navier-Stokes governing the problem in general is very widely out of reach, where from the necessity of making approximations and of neglecting certain phenomena.

In this work for the continuous phase we suggest beginning a numerical simulation of the unsteady, turbulent and viscous flow of an incompressible fluid in the presence of obstacles in a channel to complex geometry

For flows that are not heavily loaded, such as those encountered in the case of decanter water in drinking water treatment plants, we neglect the interactions between the particles and the dynamic forces of the fluid govern the transport of the particles . The influence of the particulate phase on the fluid phase is also neglected because of the low particle concentrations (Dufresne, 2008; Yan, 2013) [6].

For the discrete phase We have taken only the solid particles which have a density greater than the density of the water and a shape of a sphere

The main aim of the present paper is to study the hydrodynamics and flow behavior of sedimentation with a system of inclined parallel plates (lamellar settlers) using the coupling between a Lagrangian method (discrete phase model) and Eulerien method Continuous phase.

2. Nature and position of the problem

In the present paper the sedimentation tank for potable water treatment plant whitch is constructed in the city of Timgad wilayaBatna

The treatment process is a gravity separation between two juxtaposed blades and inclined relative to a horizontal plane. In this type of separator, the raw effluent enters horizontally one of the lamellar block flanks. The water flows between the blades while The denser particles than the water descends . The clear waters come out the other side of the lamellar structure .

The velocity rates usually used to calculate the number of blades in the decanters are very low (Chebbo 1992[6] Chocat 1997[7] , Ashley et al. 2004[8]). In practice, it means that it is necessary to implement very important surfaces of settling to be able to separate these very fine particles. Unfortunately, this does not facilitate the distribution of the water in all of the lamellar structure. But one of the assumptions used to calculate the number of blades is the homogeneous distribution of water among all lames.it is one of the keys to proper operation of a lamella separator This problem is also reported by Chocat (1997) [7] in his "Encyclopedia of urban hydrology and sanitation." the equal distribution of hydraulic flow problems on the slats are particularly difficult to solve and no really satisfactory solution on an industrial scale could be reached.[9]Then this article is to study the influence of obstacles on the repair of flow velocities in a lamella separator

3. Calculating assumptions

In this paper, we used the Euler–Lagrange multiphase approach with one-way coupled calculations where the movement of the particle is affected by the fluid phase but not the reverse.

In order to account for turbulent dispersion, the stochastic tracking of particles due to turbulence eddies was determined using the discrete “random walk model” in conjunction with RNG k – ε model.Dufresneand al. (2009)[10] andRoza and al (2014)[11]

In this model, the lifetime and size of vortices Characteristics of the turbulence are calculated from a time constant Lagrangian CL. Dufresneand al. (2009)[10] showed that the default value (0.15) did not make it possible to reproduce the deposits observed experimentally.

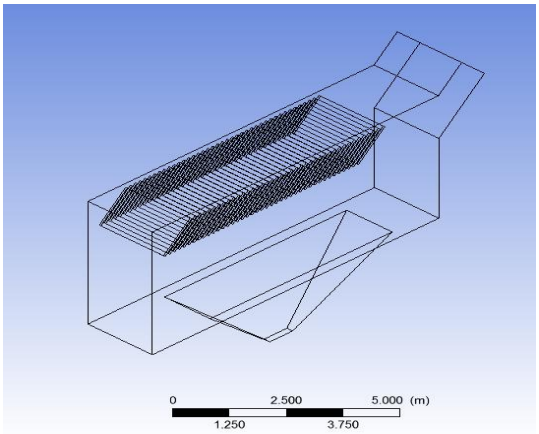

Figure 1: lamellar settler of water treatment plant

The decantation in the case studied is a decantation of the isolated particles but not flocculent particles (whose density and shape change during the decanting process), while the isolated particles are always present but with a low concentration [10],[11], For this reason and for the time which is very long with the coupling between the two approachesEulerian-Lagrangian especially for a 3D simulation, it has been assumed that the suspended materials are isolated particles which retain their density and which have a spherical shape.

The particle density used was 1080 kg/m 3 and the range of particle size was 30–890 μm and followed the Rosin–Rammler distribution [11].

4. Mathematical modelingof hydrodynamics and sediment transport in unsteady turbulent free-surface flow

The Euler-Lagrange approach for modeling of particle transport is used; this is for saying that the Navier-Stokes equations are solved for the fluid phase while the equations of Newton motion are solved for the particle phase in to determine particle trajectories.

4.1. Fluid phase

Fluid phase is treated as a continuum by solving the Navier–Stokes equations so the equations of conservation of mass (Eq. (1)) and momentum (Eq. (2)) in the case of incompressible, instationary turbulence can be written in Cartesian-tensor notation as:

$$\frac{\partial \overline{u_i}}{\partial t} + \overline{u_j}\frac{\partial \overline{u_i}}{\partial x_j} = -\frac{1}{\rho}\frac{\partial \overline{P}}{\partial x_i} + v\frac{\partial^2 \overline{u_i}}{\partial x_k \partial x_k} - \left(\frac{\partial \overline{\grave{u}_i \grave{u}_j}}{\partial x_j}\right) + g(1)_i$$

$$\frac{\partial \overline{u_i}}{\partial x_i} = 0 \qquad (2)$$

Where p is the static pressure, v is the kinematic viscosity, ui denotes the instantaneous velocity associated with the x i coordinate direction, while U i is the average, mean flow velocity and u i′ is the turbulent velocity fluctuation such that u i = U i + u i

4.2. Turbulence

The general transport equations for the turbulence kenetic energy k and the turbulence dissipation rate Ɛ of the $k-\text{Ɛ}\,RNG$ [10], [11] turbulence model, can be described by equation (3) and equation (4) respectively

$$\frac{\partial k}{\partial t} + \overline{\text{v}}_i.grad\ k = div.(grad\ k) + P - \varepsilon \qquad (3)$$

$$\frac{\partial \varepsilon}{\partial t}\overline{\text{v}}.grad\ \varepsilon = div\left(\frac{v_t}{\sigma_\varepsilon} grad\ \varepsilon\right) + \frac{\varepsilon}{k}(c_{\varepsilon_1} p - c_{\varepsilon_2} p) \qquad (4)$$

where k is turbulence kinetic energy due to mean velocity gradients, , μeff is the effective viscosity and c_{ε_1}, c_{ε_2} are turbulence model constants.

The dispersion of particles due to turbulence in the fluid phase is predicted using the discrete random walk (DRW) model that includes the effect of instantaneous turbulent velocity fluctuations on the particle trajectories through the use of stochastic methods this approach, predicts the turbulent particles' dispersion by integrating the trajectory equations for individual particles, using instantaneous fluid velocity along the particle path during the integration. By computing the trajectory in this manner for a sufficient number of representative particles, the random effects of turbulence on the particle dispersion is accounted for.

4.3. Equation of particle motion

The proposed model predicts the trajectory of a discrete phase particle by integrating the force balance on the particle, which is written in a Lagrangian reference frame. This force balance equates the particle inertia with the forces acting on the particle.

$$m_p \frac{d\overrightarrow{u_p}}{dt} = \overrightarrow{F_p}$$

$$\frac{dx_p}{dt} = u_p$$

Then our model of resolution is:

$$\rho = c(x,y,z,t)\rho_{water} + \big(1 - c(x,y,z,t)\big)\rho_{mes}$$

$C(x,y,z,t) = 0$ If the cell is filled the MES

$C(x,y,z,t) = 1$ If the cell is filled with water

If $\boldsymbol{C(x,y,z,t) = 1}$

$\overline{NVS} + k + \varepsilon$

If $\boldsymbol{C(x,y,z,t) = 0}$

$\rho = \rho_{mes}$ if we solve the system below

Where: c: volume fraction, ρ:Density of the fluid [kg / m3], MES: suspended matter

The equations of Newton's movement are resolved for the particulate phase

$$m_p \frac{d\overrightarrow{u_p}}{dt} = \overrightarrow{F_p} \qquad (5)$$

Knowing the sum of the forces acting on the particle $\overrightarrow{F_p}$the trajectory there of is calculated by integrating the velocity of the particle ,with the aim of determining the trajectories of particles. Trajectories are obtained by solving the following equation:

$$\frac{dx_p}{dt} = u_p \qquad (6)$$

The sum of forces acting on a particle moving in a viscous fluid is written

$$\overrightarrow{F_p} = m_p \frac{d\overrightarrow{u_p}}{dt} = \overrightarrow{F_D} + \overrightarrow{F_P} + \overrightarrow{F_g} + \overrightarrow{F_A} \qquad (7)$$

The drag force for spherical particles is calculated as follows:

$$\overrightarrow{F_D} = m_p \frac{18\mu}{\rho_p d_p^2} \frac{C_D Re_p}{24} \left(\vec{u} - \overrightarrow{u_p}\right) \quad (8)$$

Where m_p is the mass of the particle, dp is the diameter of the particle, ρp is the density of the particle, ρ is the density of the fluid, μ is the dynamic viscosity of the fluid and ν the kinematic viscosity of the fluid. CD drag coefficient is obtained from the following equation

$$C_D = \begin{cases} \frac{24}{Re_p} \; si \; Re_p < 1 \\ \frac{24}{Re_p}\left(1 + 0{,}15 Re_p^{0{,}687}\right) si \; 1 \leq Re_p \leq 1000 \\ 0{,}44 \; si \; Re_p > 1000 \end{cases} \quad (9)$$

$$\text{With} Re_p = \frac{d_p \|u - u_p\|}{\nu} (10)$$

For Re≥ 1000

$$\overrightarrow{F_D} = 3\frac{\rho}{\rho_p}\left(\vec{u} - \overrightarrow{u_p}\right)2 \quad (11)$$

Gravity and buoyancy give: $\overrightarrow{F_g} = m_p \vec{g}\left(1 - \frac{\rho}{\rho_p}\right)$ (12)

The force due to the pressure gradient is expressed as follows: $\overrightarrow{F_P} = \frac{1}{6}\pi d_p^3 \vec{\nabla} P$ (13)

Finally the added mass force:

$$\overrightarrow{F_A} = \frac{1}{12}\pi d_p^3 \rho_p \frac{d\overrightarrow{u_p}}{dt} \quad (14)$$

In addition to all these forces, one also takes into account the influence of the turbulent nature of the flow on the particle. The dispersion of the particles due to the turbulent fluctuations in the flow is modeled using a dispersion stochastic (random walk). instantaneous speed of the fluid is defined as: $u_i = \bar{u}_i + u_i'$.

$\bar{u}_i$ is the average flow velocity and u_i', is deducted from the local parameters of the turbulence, that is to say:

$$u_i' = \xi\sqrt{2k/3}$$

Or ξ is a random number according to a normal distribution and k is the turbulent intensity:

For 0≤ c≤1 we will solve the partial differential equation for the volume fraction

$$\frac{\partial c}{\partial t} + \vec{u}\nabla c = 0 \quad (15)$$

After one will overwrite the value of the volume fraction in the following equation

$$\rho = c_1\rho_{water} + c_2\rho_{MES} \quad (16)$$

Then we solve the system

$$\overline{NVS} + k + \varepsilon \quad (17)$$

So:

Continuity equation

$$\frac{\partial}{\partial t}(c_1\rho_{01}) + \frac{\partial}{\partial x_j}\left(c_1\rho_{01}U_j\right) = 0 \quad (18)$$

$$\frac{\partial}{\partial t}(c_2\rho_{02}) + \frac{\partial}{\partial x_j}\left(c_2\rho_{02}U_j\right) = 0 \quad (19)$$

Equation momentum

$$\frac{\partial}{\partial t}\left[(c_1\rho_{01} + c2\rho_{02})U_j\right] + \frac{\partial}{\partial x_j}\left[(c_1\rho_{01} + c_2\rho_{02}U_j)U_jU_i\right] = -\frac{\partial P^*}{\partial x_i} + [(c_1\rho_{01} + c2\rho02) - \rho0 * gi + \partial\partial xjc1\mu1 + c2\mu2 + c1\mu t1 + c2\mu t2\partial Ui\partial xj + \partial Uj\partial xi - 23\partial\partial xi[(c1\rho01 + c2\rho02)k] \quad (20)$$

Where c_1 :Volume fraction of water, c_2 : volume fraction of suspended matter (sand), ρ_{01}, ρ_{02} are respectively the density of water and suspended matter.

Variants of $\boldsymbol{k-\varepsilon}$ model adapted to sub viscous layer (models RNG)Chatelier P [12] to model the turbulence in the lamella separator is proposed using the version called "low Reynolds number model $k-\varepsilon$ in which c_u, c_{ε_1} and c_{ε_2} are algebraic functions of the Reynolds number turbulent R_{et} or near the wall in the computational domain toule.

5. Channel geometry and flow parameters

In this work we will study the turbulent free surface flows considering the presence of suspended matter and the influence of obstacles (one and two obstacles).This phase to test the program capacity.

Secondly, we will study the influence of several obstacles on the velocity of the flow in the channel complex geometry.

For the first case we consider a horizontal channel of 20 m long and 2 m height. Water flows from left to right at a Reynolds number of about 2.10^5. The obstacle is located at 5 m from the channel entrance and its height is 1m. The turbulent boundary layer is fully developed.

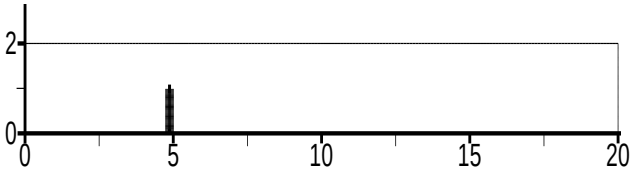

Figure2: channel with one obstacle

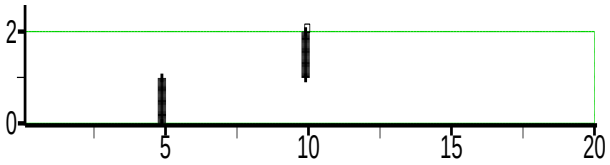

Figure3:channel with two obstacles

$$\underbrace{\frac{\partial(\rho\emptyset)}{\partial t}+\frac{\partial}{\partial x_j}(\rho\emptyset u_j)}_{1}=\underbrace{\frac{\partial}{\partial x_j}(\Gamma\frac{\partial\emptyset}{\partial x_j})}_{2}+\underbrace{S_\emptyset}_{3} \qquad (21)$$

For the second case we consider lamella separator which is characterized by a wave height 1.16 m;Cutter width: 2m; spaces between blades:0.08m ;blade thickness: 0.07m ;Number of blades: 50 ;Material plates: PVC ,Blade tilt angle: 55 °

Dimensions of the settling tank: 9.8m long x 2m wide x 4m high.

Dimensions input channel: 2m long x 2m wide x 1m high

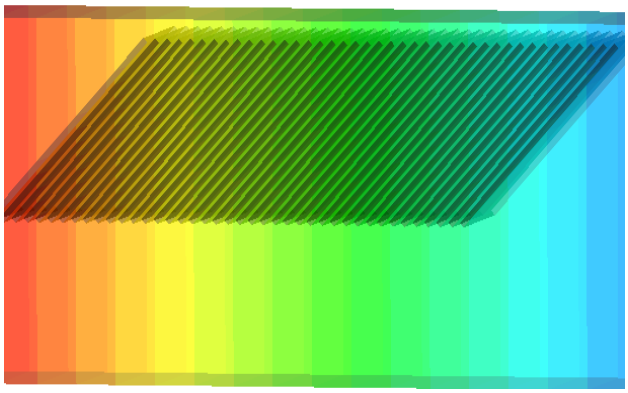

Figure4: The intermediate part (the lamellar part)

6. Numerical modeling with the method of finite volumes

All equations could be put in a general equation form of convection-diffusion for the variable ∅:

1-Convection term, 2- diffusion term, 3- source term

They will be resolved with initial and boundary conditions by finite volume method used by the code of the simulation.

6.2. *The solid phase*

Since the velocity of the fluid must be that at the position of the particle to calculate the drag force, a value $u_p$is interpolated from the values of the fluid velocity in the adjacent cells. The velocity of the particle is then calculated by discretizing the equation according to an implicit Euler scheme

$$\frac{u_p^n-u_p^0}{\Delta t}=-\frac{u_p^n-v_p^0}{\Delta t}+g(1-\frac{\rho}{\rho_p}) \qquad (22)$$

Where the exponent n refers to the values at time t + Δt and the exponent 0 to the values at the initial time

6.3. *Schematic implicit ADI*

The implicit methodis not restricted to the stability criterion, that is to say, it is stable for anyΔt ,and in other words it is unconditionally stable. One of these methods is the implicit method (ADI), it is very effective for solving the problems of transport phenomena.

6.7.*Adaptation of the time step*

The stability of the solution is ensured by adapting the time step. This oneIs adjusted at the beginning of the time iterationloop from the number of current)

$$C=\frac{u\,\Delta t}{\Delta x} \qquad (23)$$

Where c is the number of current ,Δt is the time step, **U**is the standard of the velocity through the cell and Δx is the size of the cell in the direction of the velocity .

6.8. *Boundary conditions*

For the discrete phase model the additional boundary conditions are: for the velocity inlet and pressure outlet an “escape” condition is prescribed.

Near the solid boundaries a “reflect” condition is prescribed

Finally, at the bottom of the tank a “trapped” condition is used.

For the continuous phase:

At the inlet of the decanter fixed value for velocity and ,turbulent kinetic energy,zero gradient for the pressure

Wall: fixed value for velocity=0 and ,turbulent kinetic energy,zero gradient for the pressure

Outlet:zero gradient for the velocity and turbulent kinetic energy ;zero gradient for the pressure

Finally we can conclude:

- A dynamic system sensitive.
- Use of ampirical laws.
- Boundary layer unmodelled.

7. Results

7.1.Case of one obstacle

As considered, the presence an obstacle changes significantly the characteristics of the flow near the surface. Indeed, in the centre of the section, there is a relatively velocity associated with a very low turbulence intensity. On the other hand, at the obstacle, the flow properties differ.

It is very clear that the time required to see a fixed stationary regime is very long because the flow is totally renewed each time, this is due to the fact that the eddies created on the free surface and above the obstacle emerge Very quickly and slow down, c to say: small circulations.

An example of the result is shown in the figure (5) where it is seen that, beyond T = 40 s, the flow has been completely renewed without seeing the stationary steady state. The knowledge of typical time and of the mean value of the velocity U gives an idea of the size of the largest vortices contained in the flow.

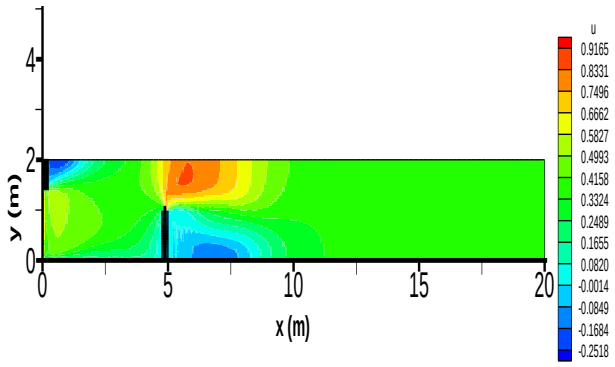

Figure5 - a: Temporal variation of the velocity field in m / s (T = 10 s)

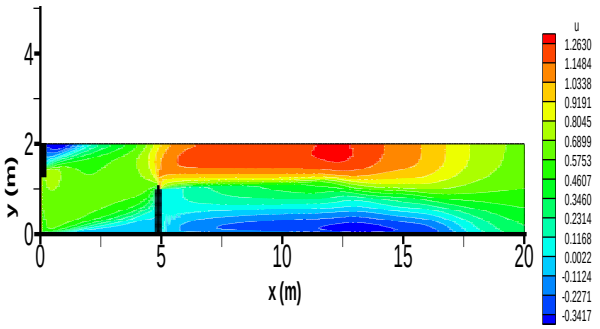

Figure5-b: Temporal variation of the velocity field in m / s (T = 25s)

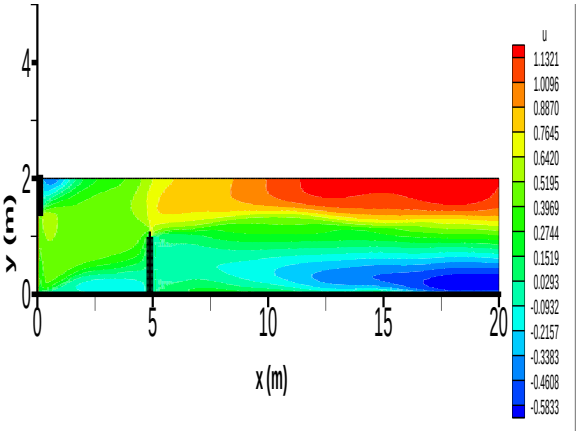

Figure5-C: Temporal variation of the velocity field in m / s (T = 35s)

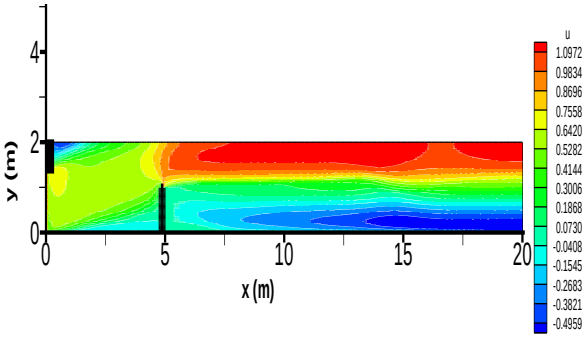

Figure5-d: Temporal variation of the velocity field in m / s (T = 40s)

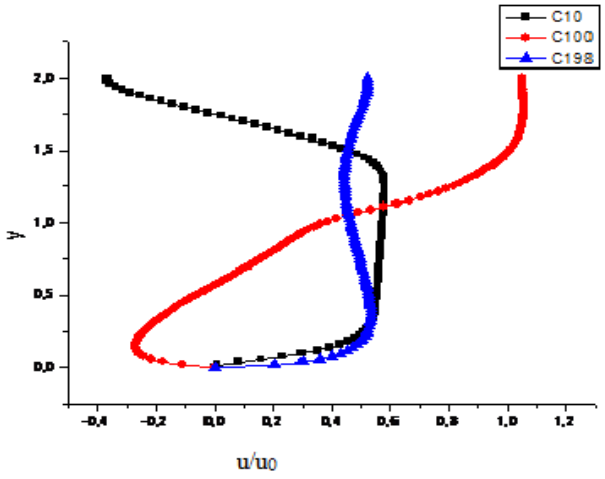

Figure 6: The velocity profiles in (m / s) calculated in a horizontal plane

In FIG. 6, the profiles of the speeds at the entrance before the obstacle c10 and after the obstacle c100 and far from the obstacle C198 can be seen, where the formation of the recirculation zones for the zone of l flow directly above the obstacle the penetration of the recirculation above the obstacle is respected, it can also be seen after the obstacle. The results obtained are in agreement with the specialized literature.

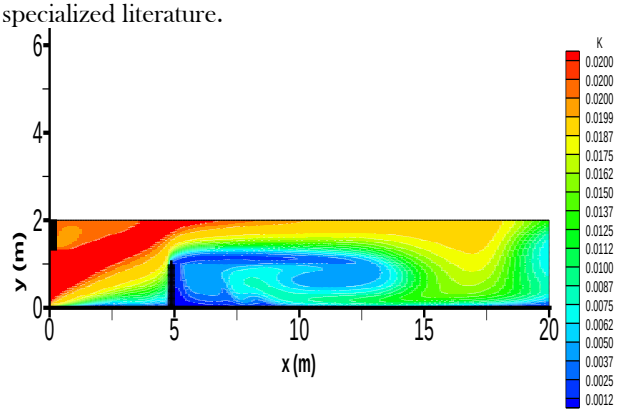

Figure7: Field of kinetic energy

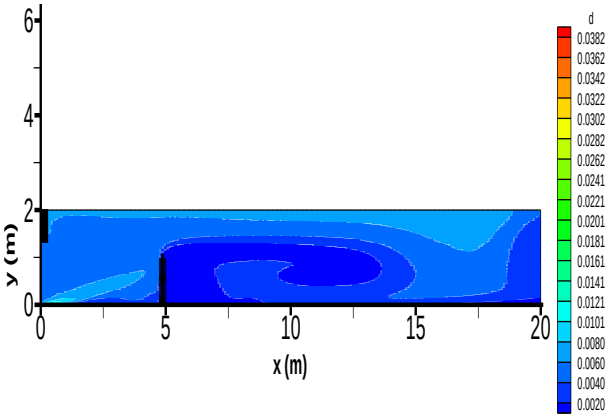

Figure 8: dissipation Field in (m^2/s^3)

The pressure profile in the presence of the obstacle is presented in the figure (9) where it can be seen that the pressure gradient is negative above the obstacle and downstream of the obstacle which corresponds to an acceleration Of the flow between the free surface and the obstacle created by the reduction in cross-section due to the presence of the obstacle .

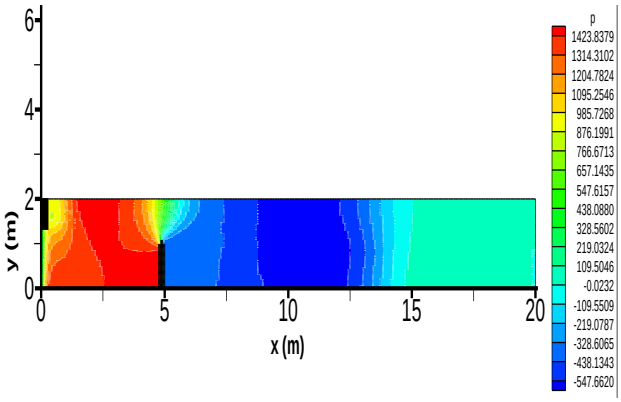

Figure9: Pressure field (pa) in a channel with one obstacle

For the area of the flow over the obstacle the intensity of the recirculation remains visible. With thek-εmodel we get an overestimation of the horizontal velocity component which leads to an increase of the turbulent kinetic energy.
This same type of result where we can see an increase in the turbulent mixing in the shear layers thus an increasing of the wake training rate was obtained by (Dragent, 1996) [13]
Despite the too diffuse nature of the model which is always underestimated the length of recirculation, but good results have been obtained (downstream of the obstacle), as the boundary conditions at the walls have been improved.

7.2.Case of two obstacles.

Interacting flows and turbulent flow processes, which are produced by the presence of the obstacle, cause energy losses;they are distributed downstream of the obstacle, and take place in shear layers, vortices, separation zones and turbulent decay in the wake [14]
The pressure profile in the presence of two obstacles is shown in Figure (10-a). We can say that we have a positive pressure gradient just the lover of the obstacle 1.
The positive gradient just greater prefers the barrier 2 is therefore two zones of overpressure (over short distances) and a slight negative pressure gradient in the area that lies between the two barriers and after the obstacle 2. Reflecting the slowdown front of the obstacle to the point

of stopping lover, which is consistent with the relationship Bernoulli, although it neglects viscous effects.

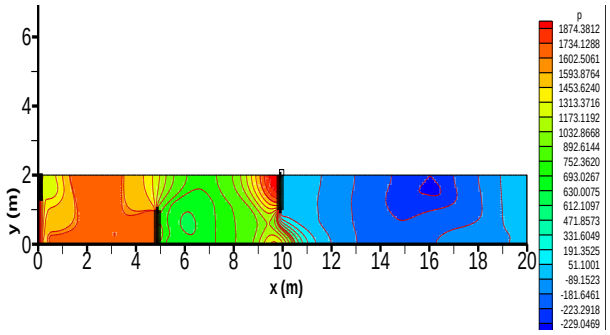

Figure 10-a: Pressure field (Pascal)

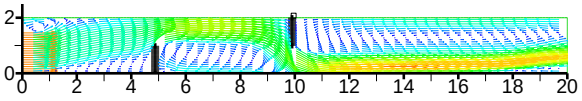

Figure 10-b:velocity vectors (m/s)

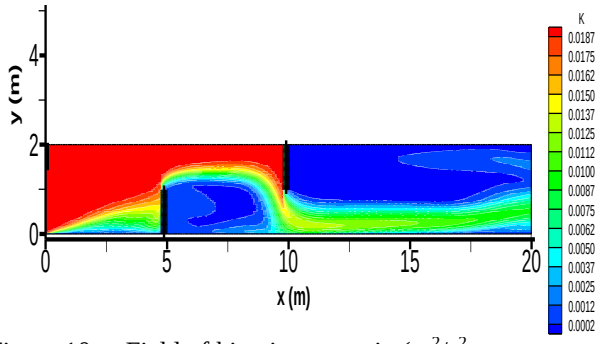

Figure 10-c: Field of kinetic energy in (m^2/s^2

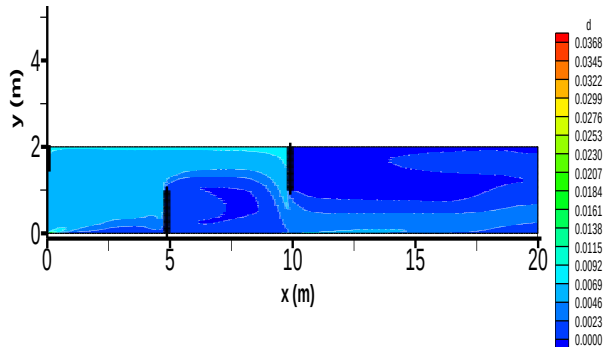

Figure 10-d:Dissipation Field in (m3/s3)

The presence of obstacles allows to obtain speeds of less important traffic. But with the model was an estimate of the horizontal component of the speed which leads to an increase of the turbulent kinetic energy and a better result for the length of recirculation.

7.3Case of lamella separator(case of suspended matter)

7.3. a.Hydrodynamic fields in a lamellar settling

7.3. a.1Macroscopic observations

The most important macroscopic observation drawn from this study is the influence of lamellar settlers on the flow field.;Examination of the simulations in a longitudinal and vertical median plane (Figures N. 11 and 12 and 13)

In the figure 11 At the initial injection (at t = 1 s), we observe an insignificant cloud of pollutant and the concentration increases in the vicinity of the entrance and the pollutant dispersed in both directions (horizontal and vertical) of the flow

At t = 2 s and t = 3 s, we can see that the position of the maximum concentration evolves in the longitudinal direction near the entrance and the pollutant continues its dispersion along the channel,which is in agreement with the specialized literature [14]

For the other figures : simulations show that it forms an important swirl in the vertical plane with lowering of the water lines to the back of channel, then lift water into the blades. They also show that water penetrates to the bottom

of the book, struck the rear compartment layered veil, then back in the opposite before recovering in the blades.

The formation of turbulence by the blades depends on the speed of water penetration. The main turbulence is approximately in the first half of the compartment. More work is, the more the turbulence lengthens. This turbulence seems to be causing the return movement of water in the opposite direction in the first blades.

If we observe the movement of water over the blade, the higher the compartment is, the more the area where the water flows against the direction is important. At the sludge storage area,slowly towards the bottom of the device without creating strong disturbances..

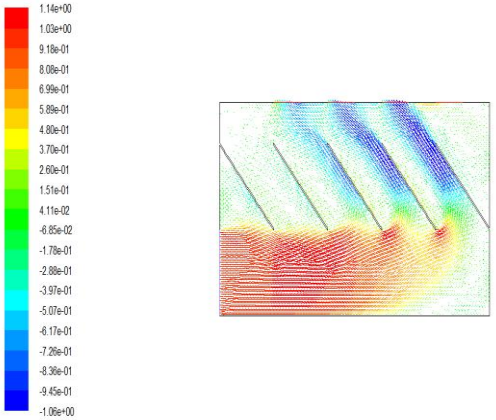

Figure11: velocity fields the particular phase in the first (five strips)

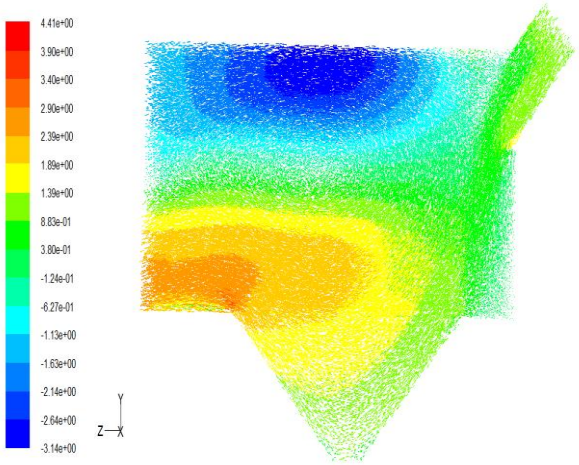

Figure12: velocity fields in the decanter along a longitudinal vertical plane YZ

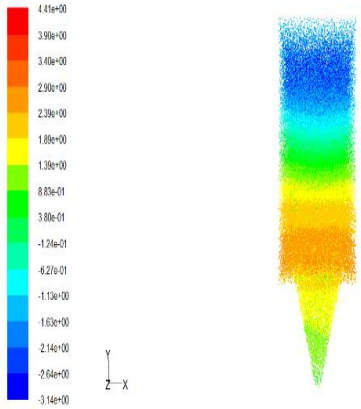

Figure 13 : velocity fields in the decanter in a vertical plane

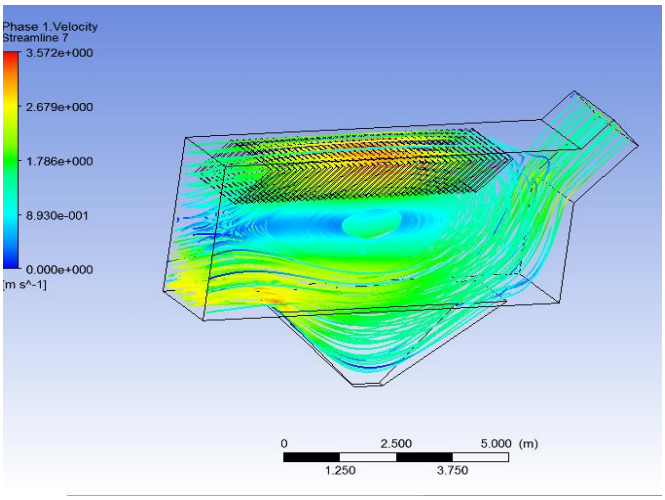

Figure 14: velocity streamline phase 1

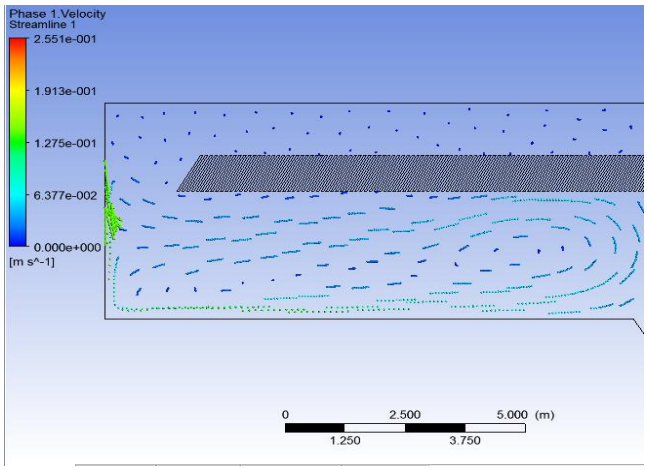

Figure 15: velocity streamline phase one and phase 2 (mes)

In Figures N. 14, 15 a representation of the flow in the three-dimensional blades. This figure confirms that the velocity distribution is not uniform throughout the lamellar structure. The flow rates are nevertheless low (a few centimeters / second). The closer the downstream threshold, the higher the flow velocity between the blades increases. The highest values of the speed (in red) are observed along the axis of the channel, and recirculation zones are observed singularities of the channel (the change of the section). The lowest values of the speed (blue) are noted along the walls, the blue area indicates a fluid recirculation following the roughness of the walls, the abrupt changes in section and the channel slope the raw effluent enters the feed channel with a speed of about 0.5 m / s. The flow strikes the veil placed down the hall, and then reverses direction, creating a large recirculation in the inlet channel. In this configuration, it will be difficult to have a uniform flow distribution in each group of slides

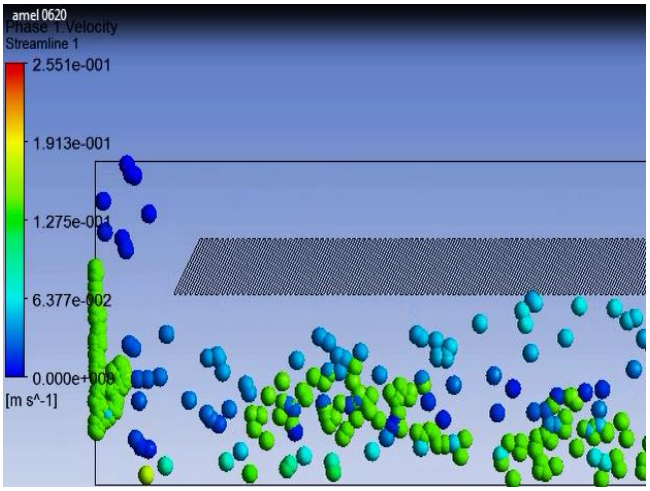

Figure 16: Velocity of deposit for different particle sizes

This figure (16) shows that a group of these particles is suspended in the flow (particles with a diameter 200 µm

with a very low deposition rate while another group of these sediments is deposited Below the obstacles (particles with a diameter380 µm . However, particles of very small size remain suspended in the flow and get to the exit of the sewer without any deposition rate. Thus, we conclude that by increasing the particle sizes, the deposition rates increase.

In this study, we conducted a simulation on a model complicated by its geometry and boundary conditions for turbulent multiphase flow model. a lamella separator treats 1.57 m3 / s, the lamellar structure is calculated on the basis of a drop in speed of 1 m / h and a height under blade is 1.70 m,

The results of this simulation are satisfactory, they describe the flow taking into account the elongation of the settler compartment, the dimensions of the channel (port) power remain constant, these results in an increase of the flow velocity under the blades. If the velocity of the water under the blades is high, for example greater than 20 cm / s, it generates whirlpools not conducive to the formation of a sludge blanket on the raft.

There is a part of the flow recirculation contraflow in the blades placed above the vortex, and the flow rates through the blades are not homogeneous. The flow is faster gradually as it approaches the outlet. At the level of the floor, in a horizontal plane water descends gradually to the bottom of the decanter. Arrival against the veil downstream compartment, the water returns to misinterpretation and then up in the blades. The flow rates are however low, of the order of 5 cm / s which reveals the instability of water bodies.

8. Conclusion

In many industrial situations in nature, it is necessary to transport mixtures of different fluids or fluids and solids under extremely varying proportions,

This study focused rightly on the coupling between turbulence and obstacles (blades) and suspended matter

The Euler-Lagrange approach is chosen to simulate the flow and the sediment transport .improved by new conditions taking the particle properties (différent diameter) .

for the turbulence , the decomposition of Reynolds equations makes the open system of equations and therefore to perform its closure it has been necessary to adopt a turbulence model able to handle turbulent flow in a lamella separator. It is interested focusing the attention on the models k-ε RNG. The RNG k-ε model seems the most appropriated for the flows with low Reynolds number (Hunze, 2008; Yan, 2013[4], [15], [16] ,[17]. This model takes account of the transport of turbulent quantities in their associating differential equations of transport

The three-dimensional modeling of the decanting structures allows us to understand the sedimentation process

It is common that part of the stream recirculated to misinterpretation in the blades placed on top of the vortex, and that the flow rates through the blades are not homogeneous.

The flow is faster gradually as it approaches the outlet. At the level of the floor, in a horizontal plane , water descends gradually to the bottom of the decanter. Arrival against the veil downstream compartment, the water returns to misinterpretation and then up in the blades. The flow rates are low, however, indicating the instability of the water bodies.

The flow is faster gradually as it approaches the outlet., which is in agreement with the specialized literature

The effective surface area for settlement is increased by the inclined plates giving a smaller footprint than in the conventional tank, and the installation of the lamellar settlers make the rectangular tank more efficient and more cost-effectiv

Finally, numerical simulations channels with barriers were used to test the concept of lamella separator. Numerical models manage to predict whether a work functions satisfactorily hydraulic viewpoint.

References

[1] A.E. Boycott, Sedimentation of blood corpuscles, Nature (.a guaranteed hydraulic operation and therefore treatment, prior to the execution of a work(1920) 104–532

[2] E. Ponder, On sedimentation and rouleaux formation, Q. J. Exp. Physiol. 15 (1925)235–252.

[3]N. Nakamura, K. Kuroda, La cause de l'acceleration de la vitesse de sedimentation desuspensions dans les recipients inclines, Keijo J. Med. 8 (1937) 256–296.

[4] E. Imam, J.A. McCorquodale, J.K. Bewtra, Numerical modeling of sedimentationtanks, J. Hydraul. Eng. ASCE 109 (1983) 1740–1754.

[5] E. Doroodchi, K.P. Galvin, D.F. Fletcher, The influence of inclined plates on expansion behaviour of solid suspensions in a liquid fluidised bed—acomputationalfluiddynamics study, Powder Technol. 156 (2005) 1–7.

[6] Chebbo G. Solides des rejets pluviaux urbains. Caractérisation et traitabilité. Thèse de doctorat, Ecole Nationale des Ponts et Chaussées,(1992). 413 p

[7] Chocat, B. (1997). Encyclopédie de l'hydrologie urbaine et de l'assainissement, Bassins de retenue p. 95, Eurydice 92, Ed Tec&Doc Lavoisier, Paris, 1997, 1121 p.

[8] Ashley R.M., Bertrand-Krajewski J.-L., Hvitved-Jacobsen T., Verbanck M., (editors) (Solids in Sewers. London (UK): IWA Publishing, (2004).

[9] José Vazquez*, Antoine Morin**, MatthieuDufresne*, JonathanWertel*A CFD approach for shape optimization of lamellarSettlers NOVATECH 2010

[10] Dufresne, M., Vazquez, J., Terfous, A., Ghenaim, A. & Poulet, J.B. . Experimental investigation and CFD

modelling of flow, sedimentation, and solids separation in a combined sewer detention tank. Computers & Fluids (2009)38(5), 042-1049.
[11] RozaTarpagkou.The influence of lamellar settler in sedimentation tanks for potable watertreatment– A computational fluid dynamic study Powder Technology 268 (2014) 139–149
[12] Chatelier P. « Simulation de l'hydrodynamique des chenaux d'oxydation par l'utilisation des équations de Navier -Stokes associées au modèle $k-\varepsilon$: évaluation de Technical Report n° 14, May 2004, 360 p. ISBN 1900222914.
[13]Dragent C. « Contribution à la modélisation de la dispersion de polluants : Etude de sillages autour d'obstacles de forme parallélépipédique ». Thèse de INP de Toulouse.5(1996).

[14] J.D. Fenton , Obstacles in streams and their roles as hydraulic structures, in: Proceedings of the 2nd [6] [6] International Junior Researcher and Engineer Workshop on Hydraulic Structures, Pisa, Italy, 2008, pp. 15–22 .

[15] Hunze M. (2008). Investigation of clarification tanks using 3-dimensional simulation studies- part 1 circular clarification tanks. Hannover, Germany, Flow Concept GmbH
[16] Yan, H., LipemeKouyi, G., Bertrand-Kraj
ewski, J-L. (2011). Modélisation numérique 3D des écoulements turbulents à surface libre chargés en polluants particulaires dans un bassin de retenue-décantation des eaux pluviales. La Houille Blanche n°5, 40-44.
[17] Yan H. (2013). Expérimentations et modélisations tridimensionnelles de l'hydrodynamique, du transport particulaire, de la décantation et de la remise en suspension
en régime transitoire dans un bassin de retenue d'eaux pluviales urbaines. Thèse de doctorat en hydrologie urbaine. Lyon. INSA de Lyon, 238 p.

Journal of New Technology and Materials
JNTM
Vol. 07, N°01 (2017)64-68

OEB Univ. Publish. Co.

Characterization of the sludge of Batna (Algeria) waste water treatment plant for its valorization

Issam Boudraa[a], Hassina Bougherara[b], Wassila Cheurfi[b] and Brahim Kebabi[b]

[a] *Unité de Recherche de Chimie de l'Environnement et Moléculaire Structurale, Faculté des Sciences Exactes, Université Mentouri Constantine, Algérie*

[b] *Laboratoire Pollution et Traitement des Eaux, Département de Chimie, Faculté des Sciences Exactes, Université Mentouri Constantine, Algérie*

Corresponding author: email: brahim.kebabi@umc.edu.dz
Received date: May 14, 2017; accepted date: June 9, 2017

Abstract

The treated waste waters of the city of Batna (Algeria) hold for about half of the needs of the land farmers in water in this area. The treatment of these waters generates a sludge which is rich in nitrogenous and phosphorous compounds and in organic matters. The purpose of this study is the characterization of this sludge in order to use it as a fertilizer. The X-ray fluorescence analysis allowed detecting the following element in this sludge : Mg, Al, Si, P, S, Cl, K, Ca, Ti, V, Cr, Mn, Fe, Ni, Cu, Zn, Ga, As, Se, Br, Rb, Sr, Y, Zr, Mo, Cd, Ba, Pb. The mass of the previous elements hold 38.52% of the dried sludge total mass. In this sludge, the X-ray diffraction analysis showed the existence of the following phases: $(Mg_{0.03}Ca_{0.97})CO_3$, SiO_2, ZnO, Cu_2O and $BaPbO_3$. The trace metals which are present in Batna waste water treatment plant, and the content of which is limited, are the following: Cd, Cr, Cu, Ni, Pb and Zn. Their contents are 40 mg/Kg, 240 mg/Kg, 70 mg/Kg, 830 mg/Kg and 3890 mg/Kg, respectively. An extraction in aqueous solution was used for determining the amount of dissolved ions nitrate, chemical oxygen demand (COD) and pH. The results obtained are 530 mg/Kg, 850 mg/Kg and 7.28, respectively.

Keywords: Batna, sludge, element trace, landspreading, sewage treatment plant.

1. Introduction

The climate of Northern Algeria is semi-arid. It is characterized by a strong rainfall irregularity. The water resources are insufficient and their exploitation has been intensified by the development of the Country [1-3]. Therefore the agricultural demand can be complied with only by using the storage of regular water [4] especially for the west of Algeria [5]. The search for other sources of water as the re-use of the treated waste waters as a supplement in irrigation is the ultimate solution [6]. The total amount of the used waste waters collected in Algeria is at the rate of 1.2 billion m^3/year [3]. Nearly 170 waste water treatment plants (most of which are mechanized) are used for treating 35% of this amount.

The city of Batna runs a mechanical and biological water treatment plant by activate sludge. It is designed for treating 28 000 m^3 (230 000 EH) of liquid discharge per day. The treated waste waters stand for approximately half the needs of the farmers in water in this area. The treatment of the waste waters generates a sludge rich in nitrogenous and phosphorous compounds and in organic matters. Therefore they are used as fertilizers. This sludge may consist of pathogenic microbes [7-11] and potentially dangerous chemical contaminants for human health and for the environment. Trace metals stand for the largest part of these compounds [12]. Above a certain concentration, the sludge from the water treatment plants is not recoverable anymore in agriculture. The organic matters contained in the sludge buried in the soil can be degraded [13]. The use of sludge contaminated by trace metals impairs the biodegradation of some organic compounds [14]. These trace metals are trapped in the sludge, dragged by lixiviation [15] or adsorbed by the plants [16, 17]. This adsorption incorporates them into the food chains. A very high concentration in trace metals as Pb, Zn and Cd prevents revegetation [18]. The continuous production of sludge in contaminated filtering plants will eventually end in landfills, incineration or composting. The cost of the disposal of the sludge from a filtering plant can reach 60% of the operation charge [19, 20].

The characterization of the sludge from the filtering plant is imperative before its valorization in agriculture. Many techniques can be used for the soil analysis. The obtained results depend on the technique used [21]. In our study, we used X-ray fluorescence and X-ray diffraction on powders for the metal analysis of the sludge from Batna waste water treatment plant. Carbon and nitrogen were chemically dosed after their extraction in aqueous solution.

2. Materials and methods

The sludge samples were collected in the drying beds of Batna waste water treatment plant. They were dried at 60°C. The entirely dried samples were crushed small

enough to guarantee a perfect homogeneity. This powder was used directly in the X-ray diffraction analysis. A pad of 30 mm diameter and 10 gram weight was realized under a 10-ton pressure to be used for the X-ray fluorescence analysis.

The X-ray fluorescence analysis was performed by a 9-watt power Panalytical Epsilon 3 spectrometer. The X-ray fluorescence range was recorded four times under different excitation conditions. The first range was performed with a 5.00-kV ddp and a 1000-µA current. It allows exploring the energy zone up to about 4 keV. The second range was performed with a silver filter with 100 µm thickness, a 30.00 kV ddp, and a 300 µA current. It shows high energy peaks. The peaks are highly mitigated under such conditions. The first range was recorded with a 50 µm thick aluminum filter with a 12.00 kV ddp and a 500 µA current. The fourth range was recorded with a 200 µm thick aluminum filter, 20.00 kV ddp and 450 µA current. The use of an aluminum filter allows exploring the spectrum zone ranging between 1 and 20 keV.

The diffractogram was achieved with an X'pert-PRO panalytical powder diffractometer. The data recording was carried out within an angle range from 5° to 120° with a 0.013° tread for a 560 s step time. The voltage and current of the tube were 45 kV and 40 mA, respectively. The device uses a 0.154056 nm wavelength radiation with a tube using a copper-made (Cu) anode. The diffraction data were analyzed with a PANalytical X'Pert HighScore Plus software program. The crystalline phases were determined compared to registered models of the PDF2 database.

The analysis of carbon and nitrogen by X-ray fluorescence is challenging. We measured their concentrations chemically after an extraction in aqueous solution. The nitric nitrogen was dosed by visible UV spectrometry, carbon by COD and acidity by pH-meter.

The extraction was performed by agitating 10 gram sludge in 100 ml UHQ water for an hour. The solution obtained after centrifugation served for determining the chemical oxygen demand (COD), ions nitrate concentration and pH.

The COD determination was carried out by oxidation of the organic matter in sulfochromic medium at 148°C. The decrease in the oxidant concentration (potassium dichromate) is proportional to the amount of organic matter contained in the sample. Such decrease is determined by spectrometric quantification at 345 nm of the initial and final concentration of the oxidant. It is proportional to the amount of oxygen necessary for oxidation of the organic matter present in the sample. The COD-meter is a Hach model 45600 brand. The spectrometer is a Hach DF/2000 brand.

The concentration in ions nitrate was determined after reaction with sodium salicylate. This reaction allows obtaining sodium paranitro-salicylate, yellow-colored and likely to have a spectrometric 420 nm measurement. The measurement of optic density was performed by JENWAY brand visible UV spectrometer.

The measurement of pH was performed with a JENWAY 3505 brand pH-meter.

3. Results

The X-ray fluorescence spectra under different conditions are presented in figure 1. The position of the peaks informs us on the metallic composition. The interpretation of the spectra indicates the presence in the analyzed sludge the following elements : Mg, Al, Si, P, S, Cl, K, Ca, Ti, V, Cr, Mn, Fe, Ni, Cu, Zn, Ga, As, Se, Br, Rb, Sr, Y, Zr, Mo, Cd, Ba, Pb. The total mass of the previous elements holds 38.52 % of the total mass of the dried sludge.

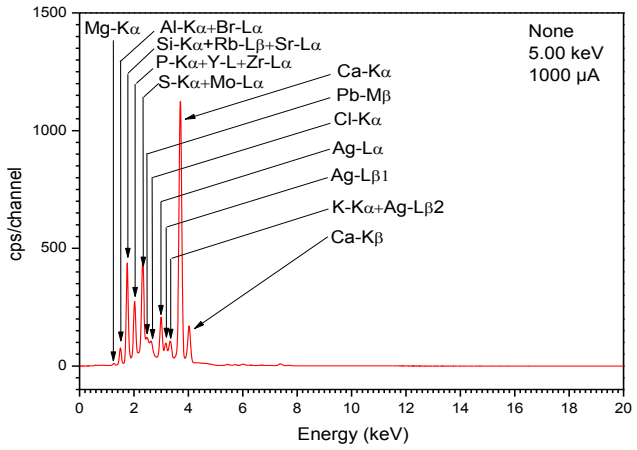

Figure 1a. *XRF spectrum of sludge of Batna waste water treatment plant achieved without a filter, 5.00 kV, 1000 µA*

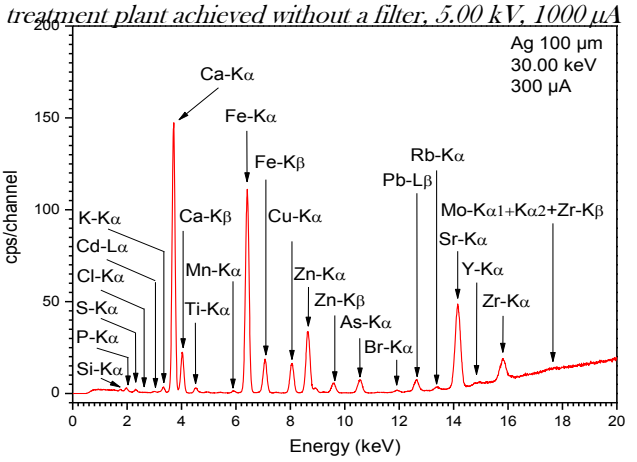

Figure 1b. *XRF spectrum of sludge of Batna waste water treatment plant achieved with a silver filter of 100 µm, 30.00 kV, 300 µA*

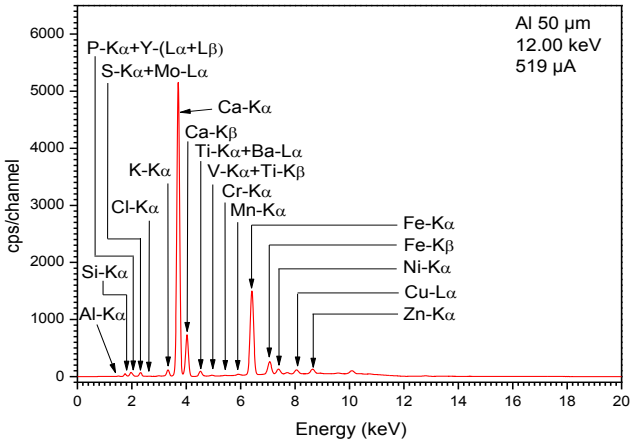

Figure 1c. *XRF spectrum of sludge of Batna waste water treatment plant achieved with an aluminum filter of 50 µm thickness, 12.00 kV, 519 µA*

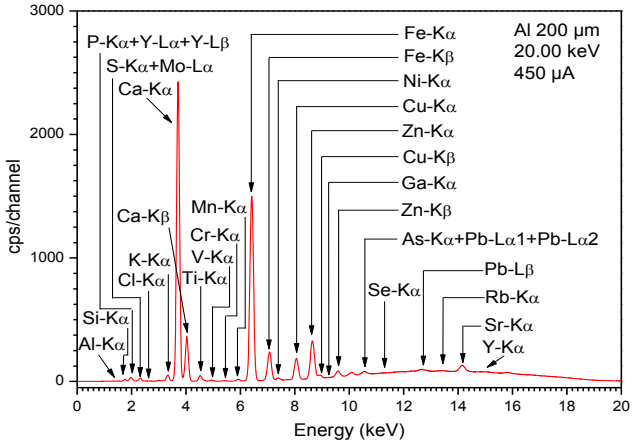

Figure 1d. *XRF spectrum of sludge of Batna waste water treatment plant achieved with an aluminum filter of 200 µm thickness, 20.00 kV, 450 µA*

The area of the X-ray fluorescence spectrum peak is proportional to the concentration of the element factor of the peak. The exploitation of this feature allowed us to quantify the concentration of the polluting elements in the sludge; table 1.

Table 1. *Trace elements present in the sludge from Batna waste water treatment plant and the quality limit of the sludge admitted in agricultural spreading ant the flow speed limits over 10 years of trace metals brought by the sludge* (French regulations; bylaw 08/01/98)

Compound	Cd	Cr	Cu	Hg	Ni	Pb	Zn	Cr+Cu+Ni+Zn
Concentration (mg/Kg MS)	40	240	2740	0	70	830	3890	2520
Content limit (mg/kg MS)	10	1000	1000	10	200	800	3000	4000
Limit flow limit (kg/ha/10 years)	0.15	15	15	0.15	3	15	45	

The X-ray diffraction analysis of the spectra (figure 2) of the sludge from Batna water treatment plant showed the existence of the following phases: magnesium calcium carbonate: $(Mg_{0.03}Ca_{0.97})CO_3$ (PDF number 01-089-1304), silicone oxide SiO_2 (PDF number 01-085-1054), zinc oxide ZnO (PDF number 03-065-0523), copper oxide Cu_2O (PDF number 00-001-1142), barium lead oxide $BaPbO_3$ (PDF number 01-081-0904).

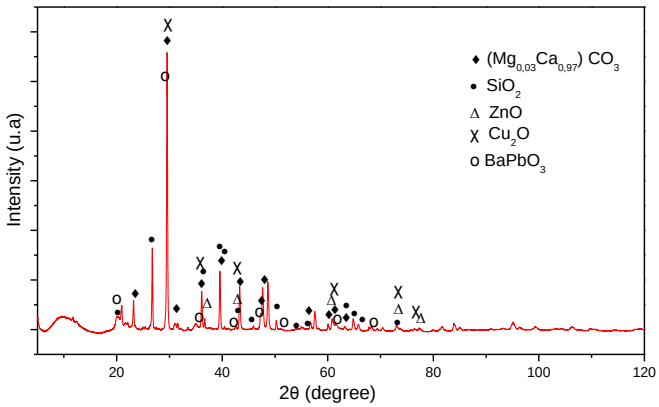

Figure 2. *XRD spectrum of the sludge from Batna waste water treatment plant*

The measurement of the concentration of dissolved ions nitrate gave us a value of 0.53 mg/g (0.53 Kg/ton)

The measurement of the COD in the sludge delivered a value of 0.85 mg/g (0.85 Kg/ton).

The measured pH of the sludge from Batna waste water treatment plant is 7.28.

The measured pH of the sludge from Batna waste water treatment plant is innocuous during its spreading. The concentration values of dissolved ions nitrate and that of the COD are very low. Therefore several hundreds of tons per hectare must be spread to cause a risk for the environment.

The X-ray fluorescence analysis showed the presence of a large number of metals in the sludge from Batna treatment plant. This large number of metals does not necessarily imply pollution. Certain trace metals in very low concentrations as iron, zinc, magnesium, copper, sodium, potassium, boron, molybdenum are indispensable to cellular biology [22]. The biological treatment cannot be done without them. These metals are mainly found in the drinking water [23] and the urban dust but at very small concentrations [24, 25].

The presence of cadmium, chromium, copper, mercury, nickel, lead and zinc at high concentrations, is on the other hand, synonymous with pollution. It is the consequence of their presence in the urban effluents [26]. The impact of the treatment was to make them concentrate in the sludge. The sludge contaminated by a high concentration of these elements cannot be spread over. The regulations also limit the flow of these elements over ten years; table 1. The concentrations of copper, lead and zinc present in the sludge from Batna waste water treatment go beyond the norms. This sludge must be subjected to treatment before being spread [27]. Without

an adequate treatment, the sludge from the water treatment of Batna must be incinerated or stored. The origin of pollution must be quickly determined in order for the future sludge to be valorized by agricultural spreading.

The origin of sludge pollution of Batna water treatment plant can be natural or entropic. The soil of the Batna region is known for its richness in copper, lead and zinc. This can account partly for the richness of the sludge of the Batna treatment plant in these metals. The automobile traffic is another major source of lead [28]. Lead tetraethyl is still used in Algeria as an anti-knock additive in gasoline-propelled car engines. The copper contained in the piping can be dragged by the water. This segment of the copper is in relation to the stagnation time in the water of the pipes, the dissolved oxygen concentration, pH, hardness and water temperature in the water. Cotitex-Batna textile industry uses chromium, copper, nickel, lead and zinc. This industry can be partly the cause of pollution of the waste waters of the city of Batna. [29].

A part of the pollutants trapped in the sludge is only mixed to it. The remaining part of these pollutants was processed by the bacteria [30]. The part which is not digested by bacteria is amorphous or crystalline. The one which is found in crystalline form can be characterized by XRD (X-ray diffraction). This identification of the phases of the pollutants can help track back the origins and propose techniques of treatment. The sludge of Batna waste water treatment plant contains the following crystals: magnesium calcium carbonate, silicon oxide, zinc oxide, copper oxide and barium lead oxide. These crystals can probably be collected by simple cleansing of the sludge.

4. Conclusion

The measured pH of the sludge from Batna waste water treatment is 7.28. It is harmless at land spreading. The concentration values of the dissolved ions nitrate and that of the COD are 0.53 mg/g and 0.85 mg/g, respectively. They are very low and show no risk for the Environment. This sludge consists of a large number of metals. Some of these do not necessarily imply pollution. At low concentration as iron, zinc, magnesium, copper, sodium, potassium, boron, molybdenum... are indispensable to cellular biology. These metals come from drinking water, city dust, etc. The presence of cadmium, chromium, copper, mercury, nickel, lead and zinc at high concentrations on the other hand means pollution. This is the consequence of their presence in the urban effluents. The impact of the treatment is to make them concentrate in the sludge of the waste water treatment plant. The concentrations of copper, lead and zinc present in the sludge from Batna waste water treatment plant exceed the norms. This sludge must be subjected to a treatment before being spread over. The cause of the pollution of the Batna treatment plant sludge can be natural or entropical. The soil of the Batna region is known for its richness in copper, lead and zinc. This can partly account for the richness of the sludge of Batna waste water treatment plant in these metals. The automobile traffic is another major source of lead. The copper contained in the piping can be dragged by the water. Cotitex-Batna textile industry uses chromium, copper, nickel, lead and zinc. This industry can be responsible, in part, for the pollution of the waste waters of the city of Batna. The sludge of Batna waste water treatment plant contains the following crystals: magnesium calcium carbonate, silicone oxide, zinc oxide, copper oxide and barium lead oxide. These crystals can probably be collected by a simple sludge cleansing.

Acknowledgements

The X-ray diffraction analysis was carried out with the aid of Mr. DEBBAH Younes, Plateforme Sciences et Technologie (PFT-ST).

References

[1] B. Aoun-Sebaiti, A. Hani, L. Djabri, H. Chaffai, I. Aichouri, N. Boughrira, J. Desalination and Water Treatment. 52 (2014) 12.
[2] A. Kadi, J. Hydrological Sciences Journal. 2 (1997) 42.
[3] A.M. Hamiche, A. Boudghene Stambouli, S. Flazi, J. Renewable and Sustainable Energy Reviews. 41 (2015) 261.
[4] A. Hannachi, R. Gharzouli, Y. Djellouli Tabet, A. Daoud. J. Fundamental and Applied Sciences. 8 (2016) 3.
[5] A. Hamlat, M. Errih, A. Guidoum, J. Arabian Journal of Geosciences. 6 (2013) 7.
[6] M. Irandoust, A.S. Tabriz, K.S. Tabriz, M.R. Forghani, J. Fundamental and Applied Sciences. 2S (2016) 8.
[7] R. Harder, G.M. Peters, S. Molander, N.J. Ashbolt, M. Svanstrom, J. Journal of life cycle assessment, 21 (2016) 1.
[8] K. Bibby, J. Peccia, J. Environmental science & technology. 47 (2013) 4.
[9] L. Sahlstrom, A. Aspan, E. Bagge, M.L. Danielsson-Tham, A. Albihn, J. water research. 38 (2004) 8.
[10] K.L. Nelson, B.J. Cisneros, G. Tchobanoglous, J.L. Darby, J. water research. 38 (2004) 1.
[11] R.D. Lumsden, J.A. Lewis, P.D. Millner, J. Phytopathology. 73 (1983) 11.
[12] S. Lahsaini, M. Chatoui, A. Aguelmous, L. El Fels, L. Idrissi, S. Souabi, M. Zamama, M. Hafidi,J. Scientific Study & Research Chemistry & Chemical Engineering, Biotechnology, Food Industry. 17 (2016) 2.
[13] M.A. AbdEl-Mongy, M.S. Shukor, S. Hussein, A.P.K. Ling, , N.A. Shamaan, M.Y. Shukor, J. Scientific Study & Research Chemistry & Chemical Engineering, Biotechnology, Food Industry. 16 (2015) 4.

[14] S. Lahsaini, L. Idrissi, S. Souabi, L. El Fels, A. Aguelmous, J. Scientific Study & Research Chemistry & Chemical Engineering, Biotechnology, Food Industry. 17 (2016) 1.
[15] P.S. Hooda, D. McNulty, B.J. Alloway, M. Aitken, J. Sc Food Agric. 73 (1997).
[16] H. Sahraoui, R. Attia, H. Hamrouni, M. Hachicha, J. Journal of Fundamental and Applied Sciences. 8 (2016) 1.
[17] O. Mokhtari, B. Nedjimi, M. Toumi, J. Roum. Chim. 61 (2016) 11-12.
[18] E. Paul, P.Camacho, M.Sperandio, P. Ginestet, J. Process Safety and Environmental Protection. (2006), B4.
[19] N. Benlkhoubi, S. Saber, A. Lebkiri, E.l Rifi, E. Fahime,J. Journal of Fundamental and Applied Sciences. 8 (2016) 2.
[20] S.M. Pyle, J.M. Nocerino, S.N. Deming, J.A. Palasota, J.M. Palasota, E.L. Miller, D.C. Hillman, C.A. Kuharic, W.H. Cole, P.M. Fitzpatrick, J. Environmental science & technology. 30 (1995) 1.
[21] W. Cheurfi, H. Bougherara, O. Bentabet, K. Batouche, B. Kebabi, J. Scientific Study & Research Chemistry & Chemical Engineering, Biotechnology, Food Industry. 10 (2009) 3.
[22] W. Cheurfi, H. Bougherara, B. Kebabi, J. Scientific Study & Research Chemistry & Chemical Engineering, Biotechnology, Food Industry. 17 (2016) 1.
[23] N.T. Hieu, B.K. Lee,J. Atmospheric Research. 98 (2010) 2-4.
[24] R. Fernández-Camacho, S. Rodríguez, J. De la Rosa, A.M. Sánchez de la Campa, A. Alastuey, X. Querol, Y. González-Castanedo, I. Garcia-Orellana, S. Nava, J. Atmospheric Environment. 61 (2012).
[25] A.S. Oliveira, A. Bocio, T.M. Beltramini Trevilato, A.M. Magosso Takayanagui, J.L. Domingo, S.I. Segura-Muñoz, J. Environmental Science and Pollution Research-International. 14 (2007) 7.
[26] M.E.A. Bendaha, B. Meddah, H.A. Belaouni, M. Mokhtar, A. Tirtouil, J. Journal of Fundamental and Applied Sciences. 8 (2016) 3.
[27] H.W. Mielke, J. Environmental geochemistry and health. 38 (2016) 4.
[28] L.J. Kristensen, J. Atmospheric environment, 111 (2015).
[29] S. Marref, J. Doctorat en sciences En Hygiène et Sécurité Industrielle Option: Gestion des Risques, Université Hadj Lakhdar de Batna. (2013).
[30] I.A. Stefanescu,J. Scientific Study & Research Chemistry & Chemical Engineering, Biotechnology, Food Industry, 16 (2015) 1.

Journal of New Technology and Materials
JNTM
Vol. 7 N°01 (2017)69-75

OEB Univ. Publish. Co.

Electrical characterization of passivation layers for p-type multi crystalline silicon EWT solar cells by numerical simulation

Batoul Benabadji, Abdellatif Zerga And Hanane Lachachi

Third Generation Solar Cells Team Materials and Renewable Energies Research Unit (URMER)
Faculty of Sciences, University of Tlemcen, PO Box 119, 13000, Tlemcen, Algeria

Corresponding author: email: b.benabadji@hotmail.fr,

Received date: October 15, 2016; revised date: June 04, 2017; accepted date: June 10, 2017

Abstract

In this study, the dielectric effects on solar cell efficiency were investigated. Different materials, such as Al_2O_3, HfO_2, TiO_2 and SiO_2, were deposited by various techniques on the front side of a p-type EWT (Emitter Wrap Through) multi crystalline silicon (mc-Si) solar cell. The passivated layer thickness was optimized using the software Matlab. The recombination velocities utilized in the simulation were taken from the literature. Using the software TCAD (2D) Silvaco/Atlas, the best results (for electrical parameters) were achieved with TiO_2 (refractive index n = 2.6 at λ = 620 nm) for a thickness of 5 nm; a solar cell efficiency around 20.5% was obtained

Keywords: p-type EWT mc-Si solar cell; passivation layers; reflectivity;, absorption; efficiency; simulation; Silvaco/Atlas.

1. Introduction

The energy conversion efficiency of a solar cell is limited by two factors: theoretical (which cannot be avoided) and technological (which can be improved). The technological factors are of three forms: optical, electrical (recombination) and resistive. The present work is part of a logic to increase the conversion efficiency of multi crystalline silicon solar cells by limiting the losses quoted above. Some of these limitations are:

-the shading rate that takes into account the partial coverage of the front surface of the cell by an opaque portion corresponding to the surface of the metal contacts

-the recombination of carriers in the volume and on the cell surface. The EWT (Emitter Wrap Through) structure was proposed for the first time by J.GEE [1] in which the shade rate is equal to zero (PV cells with rear contacts).

Today, and thanks to the excellent quality of the available silicon substrates, photovoltaic solar cells are limited by their surfaces (front and rear), knowing that with the progress of the crystallization techniques, recombination in the volume of the base is not a limiting factor anymore for the cell efficiency. A practical and proven means to improve the solar cell efficiency is through surface passivation. This consists in increasing the collection of the photogenerated carriers by improving their lifetime (or their diffusion length). This is possible, if the recombining action of the defects present on the surface is reduced (reduction of the recombination velocity on front and rear sides of the cell).

For that, thin layers of materials are deposited on the front and/or back sides of the cell to reduce the defects present on the silicon surface.

In addition to their passivation properties, thin films must have adequate optical properties, i.e. they must be non-absorbing and anti-reflective if deposited on the front; and on the other hand, they must have a high internal reflection rate on the rear face in order to limit the losses due to transmission. This work aims to show the effect of the passivation layer thickness deposited on the front side of a p-type EWT silicon solar cell, under Silvaco Atlas-2D TCAD, by using several oxides, like Al_2O_3, HfO_2, SiO_2 and TiO_2.

2. EWT cell simulation

"In the present work, all the simulations were carried out with (10×10) cm^2 EWT solar cells, under AM1.5G illumination, and were performed with the software TCAD (2D) Silvaco/Atlas.

EWT solar cells are developed using a p-type multi crystalline silicon substrate with a thickness of 200 µm. The front surface is covered with a SiNx :H antireflective coating to reduce light reflections. A

n^+p junction is created by diffusing a shallow (0.5 µm) n+ layer in the p-type silicon substrate. This diffusion is performed on the front face of the cell and into the holes within the substrate. It should be noted that these holes are made by means of a laser. The back surface field (BSF) is to create a potential barrier at the back of the cell to ensure the reflection of minority carriers. The metallic contacts are screen-printed on the back side of the structure. Aluminum and silver are used for p+ and n+ regions, respectively". [14].

The figure below illustrates the cross-section view of the investigated p-type EWT multi crystalline silicon solar cell.

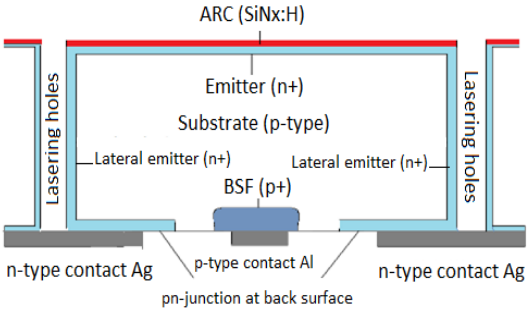

Figure 1: Schematic structure of p-type EWT mc-Si solar cell used during simulation

Base	Width = 200 µm Doping = 9E17 cm-3
Emitter	Junction depth =0.5 µm Doping = 1E20 cm-3 ERFC (complementary error function)
BSF (Back Surface Field)	Width = 5 µm Doping = 5E18 cm-3 Gaussian profile
Anti-reflective coating Si_xN_x :H	Thickness = 80 nm Refractive index = 2.05 (at λ = 0.632 µm)
Screen printed contacts	Thickness =10 µm Workfunction : W(Ag) =4.08 W(Al) = 5.2

Table 1: Parameters of the p-type EWT silicon solar cell used in simulation, without passivation layer.

With this parameters, simulation of the p-type EWT multi crystalline silicon solar cell under TCAD (2D) Silvaco/Atlas, gives the results reported in the table below:

Losses (%) by		I_{cc} (mA/cm²)	V_{oc} (V)	η (%)
reflection	absorption			
10.32	0.59	32.32	0.68	18.51

Table 2: Optical losses and electrical parameters of the simulated cell, without passivation layer (reference cell).

3. Program chart

In this paper, the simulation was used to determine the surface passivation effect (using several dielectrics) on the optical and electrical parameters of EWT cells.

We constructed simulation codes to evaluate optical losses (reflection, transmission and absorption) under the Matlab software. Indeed, the optical properties which govern the light propagation in a material are essentially its refractive index n and its absorption coefficient. It is necessary to seek the best configuration which allows having the minimum of reflection and the maximum of transmission according to the thickness d of the different layers.

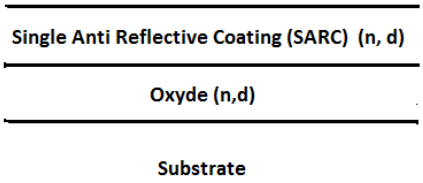

Figure2 : Parameters involved in the simulation under Matlab

Then, we injected the results into a Silvaco / Atlas program to determine the electrical parameters of the cell, namely: short circuit current, open-circuit voltage and efficiency. The procedure is as follows: after a judicious mesh of the device (the mesh must be done with the utmost attention to guarantee the reliability of the results), the structure is describe (the different regions, the electrodes and the doping) and the materials and models used are cited (contacts, materials, interfaces, models ...).

4. Passivation of p-type front side EWT cell

The surface recombination velocity has a significant effect on the change in the short-circuit current and the open circuit voltage. Surface recombination at the front can be reduced by decreasing the dangling bonds of silicon, using a passivation layer. These dangling bonds can be neutralized, using oxides such as Al_2O_3, HfO_2, SiO_2 and TiO_2. Due to the presence of oxide, they constitute good passivation layers for p-type silicon solar cells. This neutralization

operation allows decreasing the surface recombination rate and increasing the minority carrier lifetime. The optical properties of the films, deposited by plasma-assisted atomic layer deposition (ALD), are given in the table below.

Dielectric layer	Average refractive index (at 620 nm)	Band gap (eV)
Al_2O_3	1.65	8.8
HfO_2	2.10	5.6
SiO_2	1.47	9
TiO_2	2.60	3.1

Table 3: Optical properties of the thin films (dielectrics deposited by plasma-assisted ALD) used in the simulation [3].

By applying a thin coating, a few nanometers thick, the physical characteristics of the substrate are modified. Thin film deposition is a process that must be applied in a controlled manner. The deposition techniques used depend on the way the thin film is to be "created".

Different deposition methods exist and some of these are: the Atomic Layer Deposition (ALD) [3,4,5], Plasma Enhanced Chemical Vapor Deposition (PECVD) [5,6], Thermal Atomic Layer Deposition (T-ALD) [5] and Plasma Enhanced Atomic Layer Deposition (PE-ALD) [5].

Dielectic layer	thickness	Deposit technique	τ_{eff} (µs) at $\Delta n=5.10^{15}$	S_{eff} (cm/s)	S_{eff} (cm/s) reported by literature
SiO_2 [5]	20nm	T-ALD	324	31	10 - 70
SiO_2 [5]	20nm	PECVD	36	277	80-400
Al_2O_3 [5]	15nm	T-ALD	613	17	5 - 30
Al_2O_3 [5]	15nm	PE-ALD	3790	3	2 - 20
HfO_2 [7]	10nm	ALD	650	55	/
TiO_2 [13]	10nm	ALD	730	20	/

Table 4: τ_{eff} and S_{eff} values (kept from literature) used in the simulation for different dielectric materials

5. Results and discussion

To optimize the solar cell efficiency, we started by adjusting the single anti-reflective coating (SARC) thickness to the dielectric thickness. For that, a numerical simulation Matlab code (developed in our research team [8]) was used; the transfer-matrix method was applied to solve the optical equation. The solutions allowed plotting the optical reflectivity as a function of wavelengths and layer thicknesses. The optical refractive index and thicknesses of considered materials, which allowed us to have the lowest reflection, were used to simulate the electrical properties of the cell, using the TCAD (2D)/ Silvaco Atlas software.

The following figure represents the optical reflectivity of each material under consideration. The refractive index database of each material used in the simulation as a function of the wavelength was taken from references [9], [10], [11] and [12].

Using a passivation layer on the front side of the cell implies a compromise between reflection, absorption and surface passivation. Indeed, it can be seen that, the thicker the dielectric layer, the smaller the surface recombination. However, when the dielectric layer thickness increases, a large part of radiation is absorbed and therefore lost.

It is therefore required to determine the optimum thickness of the dielectric layer that can passivate the substrate correctly. So, a thin passivation layer must lead to the best compromise between the optical (absorption and reflection) and the electrical losses (recombination).

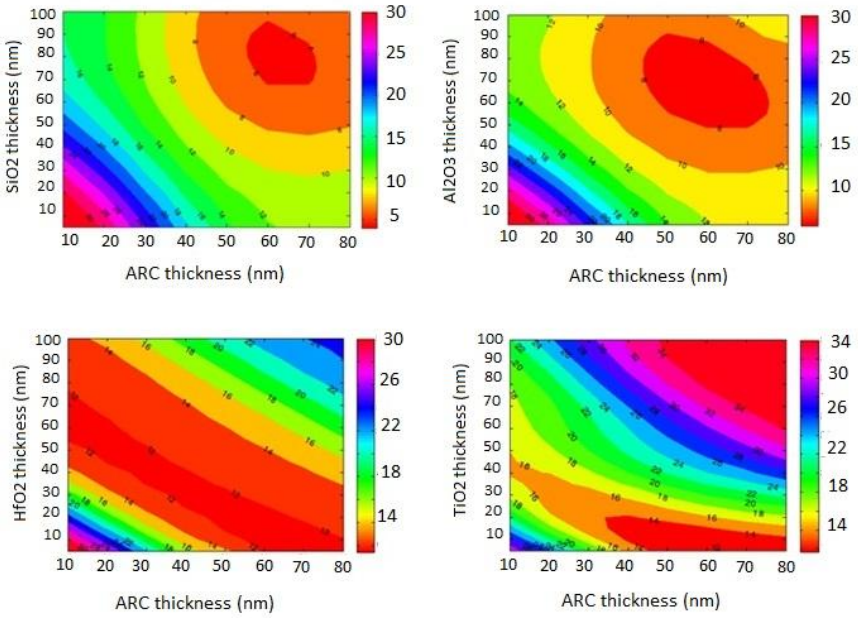

Figure 3: Reflectivity as a function of SARC thickness and dielectric thickness.

The optical losses due to reflection and absorption on the front side of the simulated mc-Si EWT solar cell, passivated with Al_2O_3, are evaluated and reported in the figure below.

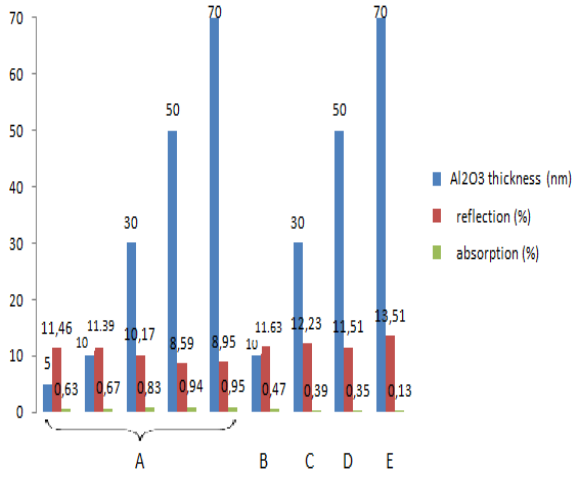

Figure 4: Optical losses of the simulated solar cell as a function of the variation of Al_2O_3 (dielectric layer) thickness and SiN_x (SARC) thickness (A: 80nm, B: 60nm C: 40nm D: 30nm and E: 10nm).

Then, the electrical parameters, such as the short-circuit current and the solar cell efficiency of the simulated solar cell, as a function of the variation of Al_2O_3 (dielectric layer) thickness and SiN_x (SARC) thickness are summarized in the figure below.

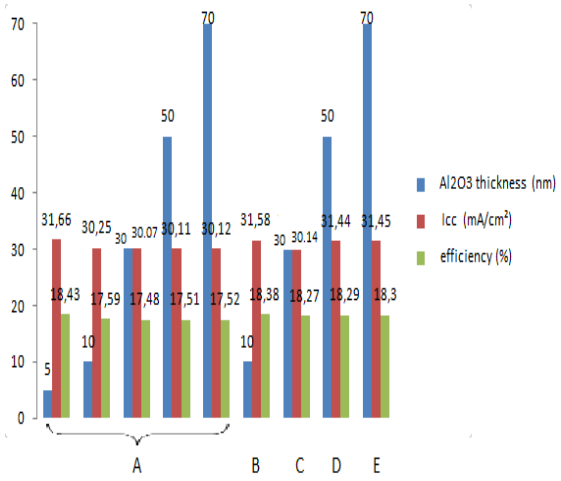

Figure 5: Electrical parameters of the simulated solar cell as a function of the variation of Al_2O_3 (dielectric layer) thickness and SiN_x (SARC) thickness (A: 80nm, B: 60nm C: 40nm D: 30nm and E: 10nm).

For Al_2O_3, the maximum efficiency obtained was 18.43 % (less than the efficiency of a p-type EWT multi crystalline silicon solar cell without front surface passivation). Figures 6, 7 and 8 show the variation of the optical losses (reflection and absorption) and the electrical parameters (short-circuit current and solar cell efficiency) of the simulated cell as a function of the thicknesses of different dielectrics (HfO_2, TiO_2 and SiO_2) and the thickness of SiN_x (SARC).

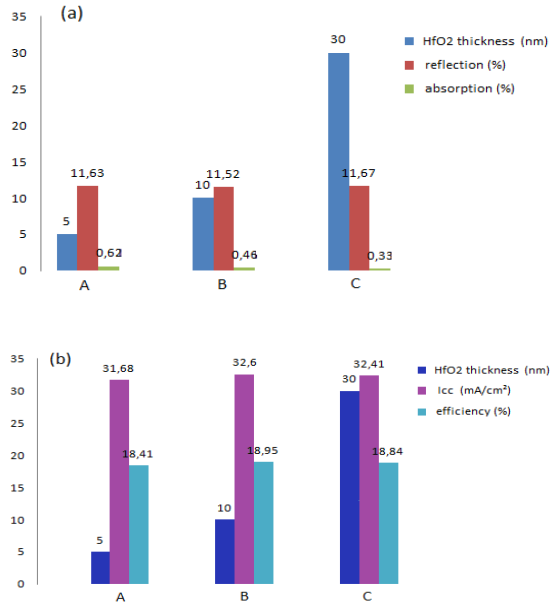

Figure 6: Variation of the optical losses (a) and electrical parameters (b) of the simulated cell with the variation of HfO_2 (dielectric layer) thickness and SiN_x(SARC) thickness(A: 80nm, B: 60nm and C: 40nm).

For HfO_2, good passivation properties were found. For a 10 nm thick dielectric layer and a 60 nm thick SARC, the short-circuit current achieved was about 32.6 mA/cm^2 and the energy conversion efficiency around 19%.

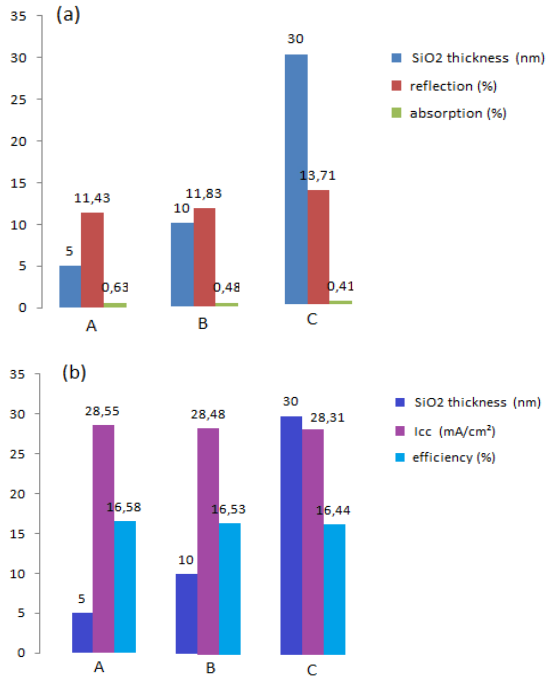

Figure 7: Variation of optical losses (a) and electrical parameters (b) of the simulated cell with the variation of SiO_2 (dielectric layer) thickness and SiN_x (SARC) thickness (A: 80nm, B: 60nm and C: 40nm).

For SiO_2 the electrical parameters degrade, especially the short-circuit current which decreases by about 6.75 mA/cm^2. This degradation is mainly caused by the diffusion of atomic hydrogen to the SiO_2-Si interface. From the simulation results, such degradation can only be explained by the increased recombination rate on the front.

.

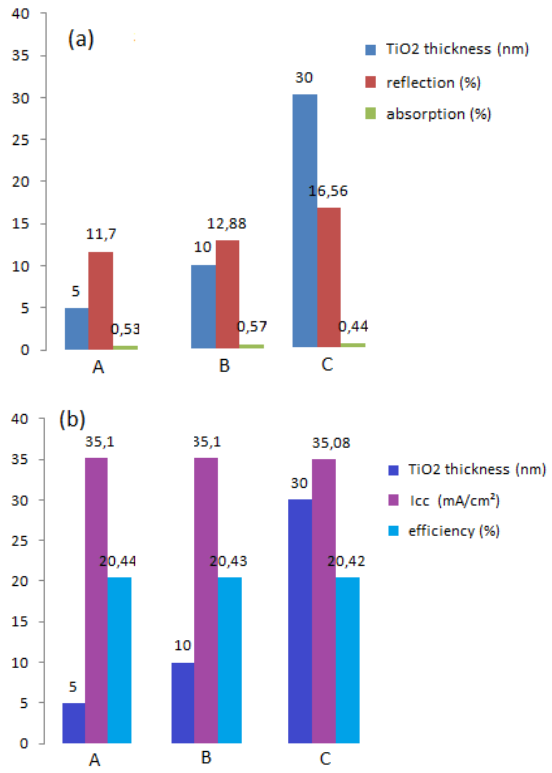

Figure 8: Variation of optical losses (a) and electrical parameters (b) of the simulated cell with the variation of TiO_2 (dielectric layer) thickness and SiN_x (A: 70nm, B: 70nm and C: 40nm).

For TiO_2, the implied open-circuit voltage approximated 0.7 V, the short circuit current obtained exceeded 35 mA/cm^2 and an energy conversion efficiency of 20.44% was reached. This efficiency improvement can be explained by the decreased recombination rate on the front of the cell.

The table below summarizes the optical losses (reflection and absorption) and the electrical parameters (short circuit current, open-circuit) voltage) and solar cell efficiency) of the considered EWT solar cell, for the four materials, with optimized thicknesses.

Dielectric oxide	Ref cell	Al_2O_3	HfO_2	SiO_2	TiO_2
oxide thickness (nm)	/	5	10	5	5
SiNx ARC thickness (nm)	80	80	60	80	70
Losses (%) by reflexion	10.32	11.46	11.52	11.43	11.70
Losses (%) by absorption	0.59	0.63	0.46	0.63	0.53
I_{cc} (mA/cm²)	32.32	31.66	32.60	28.55	35.10
V_{cc} (V)	0.680	0.697	0.696	0.694	0.699
η (%)	18.51	18.43	18.95	16.58	20.44

Table 5: Variation of the optical losses and electrical parameters of the simulated cell with the variation of dielectric materials and SiN_x (SARC) (best results).

Another way to confirm the above results is to plot the variation of the External Quantum Efficiency (EQE) for different dielectric materials, knowing that EQE is the ratio of the number of charge carriers collected by the cell to the number of incident photons (coming from the outside). The surface recombination velocity (SRV) affects the variation of EQE. Higher SRV means that the generation rate of charge carriers in the considered solar cell decreases.

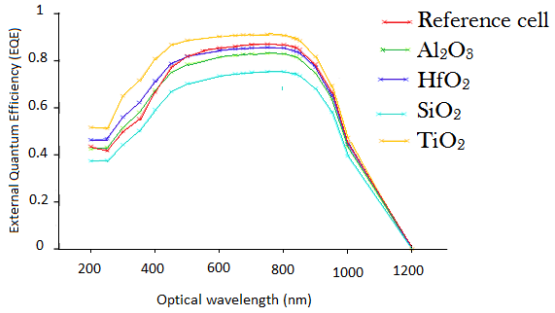

Figure 9: Variation of EQE with different dielectric materials (using TCAD Silvaco/Atlas software).

6. Conclusion

Surface passivation is an extremely important process for high-efficiency silicon solar cells, especially on the front surface where most of the light is collected. Significant differences were observed in the surface passivation of p-type EWT multi crystalline silicon solar cells when Al_2O_3, HfO_2, TiO_2 and SiO_2 were used.

A priori, thermal SiO_2 did not lead to a good performance of the EWT solar cell. The SiO_2 layer does not allow obtaining a good passivation. HfO_2 and Al_2O_3 show good front passivation properties.

To conclude, an average energy conversion efficiency of 20.5% was reached with a (10 x 10) cm² p-type multi crystalline silicon solar cell, with TiO_2 as a dielectric layer for surface passivation. An implied open-circuit voltage equal to 0.7 V was obtained. The high refractive index of TiO_2 ($n \approx 2.6$ at $\lambda = 620$ nm), which is extremely close to the optimal refractive index of a silicon solar cell under glass ($n = 2.43$ at $\lambda = 600$ nm) [15], is therefore interesting for increasing the cell efficiency.

Acknowledgements

This work was performed within the Research Unit Materials and Renewable Energy at the University of Tlemcen, we would like to thank the DGRSDT for their funding assistance during the research program PNR.

References:

[1] Gee, J.M., Schubert, W.K., Basore, P.A, "Emitter wrap-through solar cell", Proceedings of the 23rd IEEE Photovoltaic Specialists Conference, pp.265-270, Louisville, Kentucky, USA, 1993.

[2] Dirk-Holger Neuhaus, Adolf Münzer, (Review article), "Industrial Silicon Wafer Solar Cells", Advances in Opto Electronics, Volume 2007 (2007), Article ID 24521, 15 pages

[3] G. Dingemans, W.M.M. Kessels, "Aluminum oxide and other materials for Si surface passivation", ECS Transactions Vol 41 (2) 293-301 (2011)

[4] W.M.M. Kessels, J.A. Van Delft, G. Dingemans and M.M. Mandoc, "Review on the prospects for the use of Al2O3 for high-efficiency solar cells"

[5] R. Kotipalli, R. Delamare, O. Poncelet, X. Tang, L.A. Francis and D .Flandre, "Passivation effects of atomic-layer deposited aluminum oxide", EPJ Photovoltaics 4, 45107 (2013)

[6] J. Schmidt, F. Werner, B. Veith, D. Zielke, S. Steingrube, P.P. Altermatt, S. Gatz, T. Dullweber and R. Brendel , "Advances in the surface passivation of silicon solar cells", International Conference on materials for advanced technologies 2011 Symposium O, Energy Procedia 15 (2012) 30 – 39

[7] F. Lin, B. Hoex, Y.H.Koh, J.J.Lin and A.G.Aberle, "Low temperature Surface passivation of moderately doped crystalline silicon by atomic-layer deposited hafnium oxide films", International Conference on Materials for Advanced Technologies, Symposium O, Energy Procedia 15 (2012) 84 – 90

[8] N.SAhouane, A.Zerga "Optimization of Antireflection Multilayer for Industrial Crystalline

Silicon Solar Cells", Energy Procedia, Volume 44, 2014, Pages 118–125 Proceedings of E-MRS Spring Meeting 2013 Symposium D Advanced Inorganic Materials and Structures for Photovoltaics 27-31 May 2013, Strasbourg, France.

[9] P. Kumar, M. Wiedmann, C. Winter and I. Avrutsky, "Optical properties of Al2O3 thin films grown by atomic layer deposition", Applied Optics 48(28), pp. 5407–5412, 2009.

[10] D.L. Wood, K. Nassau, T.Y. Kometani and D.L. Nash, "Optical properties of cubic hafnia stabilized with yttria", Applied Optics 29(4), pp. 604–607, 1990.

[11] E. Palik, Handbook of Optical Constants of Solids Vol I, Academic Press, Orlando.

[12] B. Richards, "Single-material TiO2 double-layer antireflection coatings", Solar Energy Materials & Solar Cells 79, pp. 369–390, 2003.

[13] Benjamin G Lee, Jarmo Skarp , Ville Malinen, Shuo Li, Sukgeun Choi, HowardM.Branz, "Excellent Passivation and Low Reflectivity Al2O3/TiO2 Bilayer Coatings for n-Wafer" Silicon Solar Cells, IEEE Photovoltaic Specialists Conference Austin, Texas June 3–8, 2012.

[14] B.Benabadji, A.Zerga, "Optimal design of buried emitter of EWT silicon solar cells type by numerical simulation" Energy Procedia, Volume 44, Pages 126-131, 2014.

[15] Bryce S. Richards, Jeffrey E. Cotter, Christiana B. Honsberg, and Stuart R. Wenham, "Novel uses of TiO_2 in crystalline silicon solar cells", Presented at 28th IEEE PVSC, 15-22 September 2000, Anchorage, Alaska.

Journal of New Technology and Materials
JNTM
Vol. 07, N°01 (2017)76-82

OEB Univ. Publish. Co.

Simulation Study of Various Layers and Double δ-Doping Effect on Device Performance of InAlAs/InGaAs/InP HEMT

A. B. Khan[a*], S. G. Anjum[a] and M. J. Siddiqui[b]

[a]*Research Scholar, Department of Electronics Engineering, Z. H. College of Engineering & Technology AMU, Aligarh-202002*

[b]*Professor, Department of Electronics Engineering, Z. H. College of Engineering & Technology AMU, Aligarh- 202002*

Corresponding author: email: aboobakar.rs@amu.ac.in
Received date: November 11, 2016; revised date: June 13, 2017; accepted date: June 14, 2017

Abstract

The InAlAs/InGaAs/InP HEMT (High Electron Mobility Transistor) lattice matched to InP offers outstandinghigh frequency, low noise operation for low-noise amplifiers. In this work, efforts have been made to study and optimize the device performance of 0.5 µm gate length double δ-doped InP-based $In_{0.53}Ga_{0.47}As/In_{0.52}Al_{0.48}As$ HEMT with the help of the variation of various parameters like δ-doping, Schottky layer thickness, spacer layer thickness and gate length. To study the impact of various parameters we use Atlas Silvaco TCAD numerical simulation tool. We have performed characterization studies of two-dimensional electron gas (2DEG) in the channel layer, conduction band discontinuity (ΔE_C), transconductance (g_m), threshold voltage (V_{th})and cut-off frequency (f_T) to optimize the device performance. And hence optimize figure of merit such as transconductance and cut-off thefrequency of the device.

Keywords: mobility; δ-doping; 2DEG; transconductance; threshold voltage; cutoff frequency.

1. Introduction

InAlAs/InGaAs/GaAsIII-VUltrafasttechnology of MODFET (modulation doped field effect transistor) device is used in MMIC (monolithic microwave integrated circuits) forhigh-speed [1-3]. Today the GaN-based HEMT are used for power devices with low on-state resistance [4-7]. But in communication and various types of equipment's varying from electronic wafer systems to cell phones likes radio astronomy and radar InAlAs/InGaAs HEMT plays a key role.Numerous technologies are nowadays based on InGaAs/InAlAs quantum well HEMT devices[8-9]. These applications [10] are exposed to large sheet carrier density in the2DEG quantum well and higher transport properties of InGaAs which is formed near heterointerface [11-12]. But the limitation of the InP-based HEMT's impacts ionization effects, which occur in InGaAs narrow band gap channel layer. A number of negative consequences to improve the impact ionization effects likes decreased the breakdown voltage of on state and off state, therisein kink effects, output conductance and lasting device degradation. Due to higher impact ionization effects in the narrow band gap channel, conventional $In_{0.53}Ga_{0.47}As$ HEMT's bear low breakdown voltage.

The InAlAs/InGaAs/InP HEMT lattice matched to InP offers outstandinglow noise, high-frequency operation for low-noise amplifiers. In this article,works have been done to simulate and optimize the performance of 0.5 µm gate length double δ-doped InP-based$In_{0.53}Ga_{0.47}As/In_{0.52}Al_{0.48}As$ HEMT with the help of the variation of various parameters like δ-doping, Schottky layer thickness, spacer layer thickness and gate length. To get the effect of numerous parameters TCAD SilvacoAtlasnumerical simulationtool has been used. In this simulation, various important device parameters like the high electron density of two-dimensional electron gas (2DEG), conduction band discontinuity (ΔE_C), transconductance (g_m), threshold voltage (V_{th})and cutoff frequency (f_T) have been obtained. Further, the effect of parameter variation on the high electron density (2DEG), conduction band discontinuity and optimization of the performance of HEMT has been analyzed. These values, then used to optimize the figure of merit such as cutoff frequency and transconductance of the device.

2. Device Structure

The InAlAs/InGaAs HEMT device schematic cross-section view is Fig.1. The structure of this device has InGaAs cap layer which is heavily doped with Si at approximately $10^{18}/cm^3$, offers a good ohmic contact to the HEMT. The cap layer not only decreases the drain and source contact resistance of the device but also protect the surface depletion and oxidation of the Schottky layer. This device structure also consists a wide bandgap Schottky layer than the channel layer material. At the InAlAs/InGaAs heterointerface, a large conduction band discontinuity occurs due to this the free electrons diffuse from higher bandgapInAlAs material into lower bandgap InGaAs channel layer and form 2DEG. Due to this a high carrier concentration is obtained into the channel layer.

An InAlAs thinner Schottky layer makes thepossible small distance

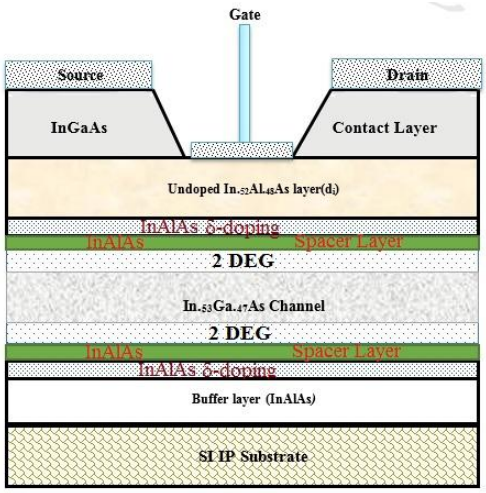

Figure 1:InP-based HEMT model

between the gate metal and the channel layer, which provide high transconductance but decreases the breakdown voltage of the device.

The spacer layer separates the ionized donors and 2-DEG at the heterointerface of donor layer and thechannel layer. It also decreases Coulomb scattering of the donor atoms due to this enhance the electron mobility of the device. The thickness of the doping layer is the order of 3 Å with a very high doping concentration of 2x1018/cm3, supply all the electrons into the channel layer and form 2DEG. This device consists two doping layer which serves as the source of electrons. Because the device consists two doping layers so it is called double δ-doped HEMT. Due to double doping electron transfer from both side and form 2DEG into the channel layer.

3. Physical Model of HEMT

The basic qualitatively description of HEMTs operation is based on one-dimensional charge control model and the direction of charge control model is perpendicular to the heterointerface. The electron wave function satisfies the Schrodinger equation while the electric potential (band diagram) and charge distribution follow the Poisson equation. Theoretically, by self-consistently solving the two equationsthe charge profile and the potential can be calculated. Based on the assumption that the carrier transfer from the supply layer is confined in the 2DEG, across hetero-interfacethe Fermi level is constant, and the potential well at the channel can be approximated by a triangular well, the electron charge (n_s) stored at the interface in a modulation doped structure is [13]

$$\boldsymbol{ns} = \frac{\varepsilon}{\boldsymbol{qd}} [\boldsymbol{Vg} - (\boldsymbol{\Phi b} - \boldsymbol{Vp2} + \frac{\boldsymbol{E_{fi}}}{\boldsymbol{q}} - \frac{\boldsymbol{\Delta E_C}}{\boldsymbol{q}})] \quad (1)$$

where Φ is barrier layer dielectric constant, q is electron static charge, d is thesum of the thickness of thedoped barrier $\boldsymbol{d_i}$ and Undoped barrier $\boldsymbol{d_d}$, Φ_b is the Schottky barrier height of the gatemetal deposited on the barrier layer,$\boldsymbol{V_g}$is the applied gate to source voltage, $\boldsymbol{V_{p2}} = \frac{\boldsymbol{qN_d d_i^2}}{\boldsymbol{2\varepsilon}}$ while $\boldsymbol{N_d}$ is the donor concentration in the barrier layer, $\boldsymbol{\Delta E_C}$ is the conduction band offset between the channel and barrier and$\boldsymbol{E_{fi}}$ is the Fermi level with respect to the conduction band edge in the channel layer.

The interface change in eqn-1 can be expressed in a more general form which can be used for theplanar doped structure as [14]:

$$\boldsymbol{n_s} = \frac{\varepsilon}{\boldsymbol{q}} \frac{\boldsymbol{V_g - V_{th}}}{\boldsymbol{d_B + d_s + \Delta d}} \quad (2)$$

where $\boldsymbol{d_B}$ and $\boldsymbol{d_s}$are the thickness of the barrier and spacer layer respectively, Δd is the average distance between 2DEG and interface. The threshold voltage is given as:

$$\boldsymbol{V_{th}} = \boldsymbol{\Phi_B} - \frac{\boldsymbol{\Delta E_C}}{\boldsymbol{q}} - \boldsymbol{V_{p2}} \frac{\boldsymbol{E_{fi}}}{\boldsymbol{q}} \quad (3)$$

for modulation doped structure

$$\boldsymbol{V_{th}} = \boldsymbol{\Phi_B} - \frac{\boldsymbol{\Delta E_C}}{\boldsymbol{q}} - \frac{\varepsilon}{\boldsymbol{q}} \boldsymbol{N_\delta d_B} \quad (4)$$

for δ doped structure.

$\boldsymbol{g_m}$, the transconductance is defined as the change in the drain to source current divided by the change in the gate to source voltage at certain drain to source voltage:

$$\boldsymbol{g_m} = \frac{\boldsymbol{dI_d}}{\boldsymbol{dV_g}} | \boldsymbol{V_{ds} = constant} \quad (5)$$

It is the most important dc figure of merit in field effect transistors as it demonstrates the current modulation efficiency of the gate.

The current cut-off frequency $\boldsymbol{f_T}$ is the defined as the frequency at which current gain of a two-port network goes to unity. It is the maximum frequency the device can work for current amplification. Under the assumption that feedback capacitance is negligible in HEMTs, $\boldsymbol{f_T}$ is given by:

$$\boldsymbol{f_T} = \frac{\boldsymbol{g_m}}{\boldsymbol{2\pi C_{gs}}} = \frac{\boldsymbol{v_{sat}}}{\boldsymbol{2\pi L_g}} \quad (6)$$

where C_{gs} is the gate to source capacitance, v_{sat} is the saturation carrier velocity in the channel and L_g is the gate length. The equation eqn-6 shows that improving saturation velocity and down-scaling gate length are the basic approaches to increase f_T [15].

4. Results and Discussion

4.1 Simulated Conduction Band Discontinuity (ΔEc) and 2DEG of InP-Based HEMT

Doubleδ-doped InP-basedInAlAs/InGaAs lattice matched HEMT structure model is shown in Fig. 1. The simulated band structure of the conduction band ofInP-basedInAlAs/InGaAs HEMT due to single δ-doping and double δ-doping are shown in Fig.2-a, Fig. 2-c respectively. The 2DEG or quantum well due to single δ-doping and double δ-doping are shown in Fig. 2-b and Fig. 2-d respectively, which is formed at the interface ofInGaAs and InAlAs due to their bandgap difference. From the simulation results, we observe that the carrier density is found to be very high at the wide band gap and narrower band gap material heterointerface. Also from simulation results very high carrier density is found at a distance of 55.3 nm to 105.3 nm. The electron density of this channel layer consists approximately *1.8 x 10^{18}/cm^3* due to 1stδ-doping, *2 x 10^{18}/cm^3* due to 2ndδ-doping.The electron transfer from both sides into the channel layer due to this channel layer consist the carrier density approximately *1.8 x 10^{18}/cm^3* and *2 x 10^{18}/cm^3* respectively due to double δ-doping which is quite high. A small amount (negligible) of theelectron is found across δ-doped layer because it is highly doped.

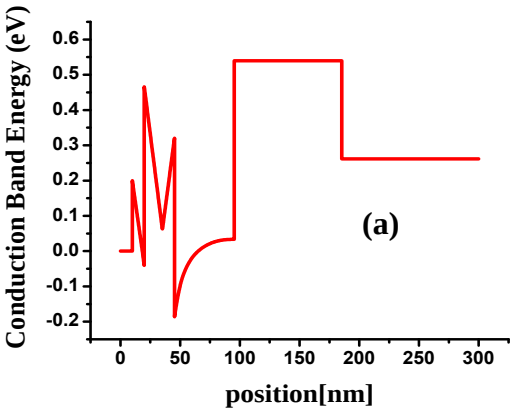

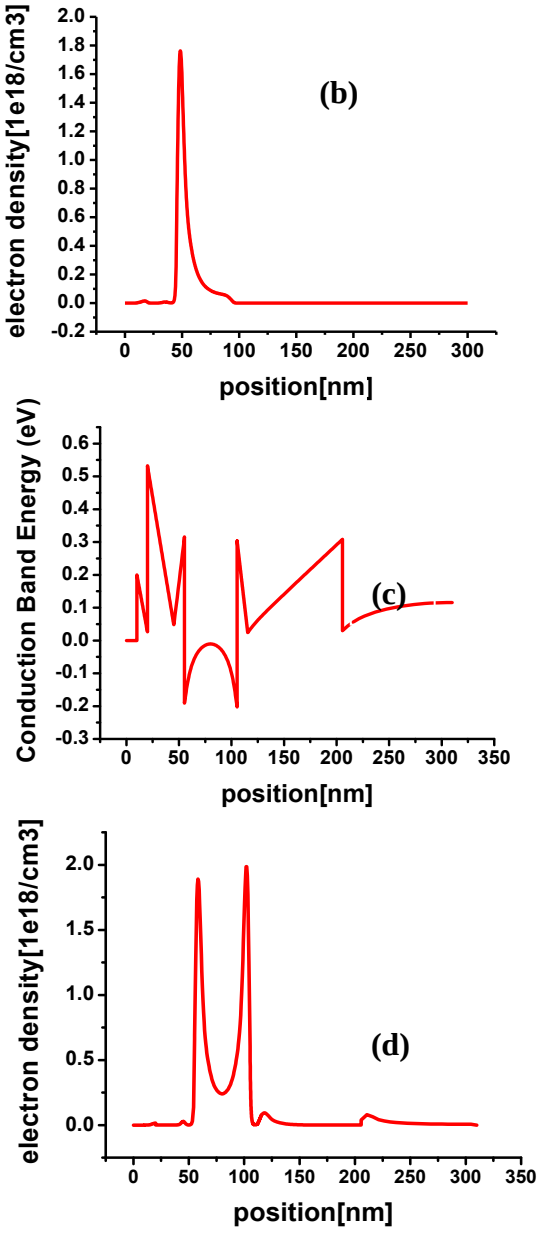

Figure 2:Conduction Band Energy, Carrier Concentration and band bending due to doping concentration. (a) Simulated Conduction Band Energy Diagram with position and Band Banding, ΔE_C=0.5eV due to 1stδ-doping. (b) Simulated Plot of Electron Density (2DEG) Vs position due to 1stδ-doping. (c) Simulated Conduction Band Energy Diagram with position and Band Banding, ΔE_C=0.5 eV due to 1st and 2ndδ-doping. (d) Simulated Plot of Electron Density Vs position due to 1st and 2ndδ-doping.

4.2 Effect of δ-Doping (N_D) Variation on device performance

From the simulation results it is found that as the electron concentration of δ-doped layer increases, the carrier concentration in the channel layer also increases.In this HEMT device, we add two silicon δ-doped layer. The simulation result of δ-doping with electron density is shown in Fig.4-a. Further, from simulation result, we observe that initially the carrier concentration (2DEG) in the channel layer is raised linearly up todelta doping concentration of*4.5x10*^{12} *cm*$^{-2}$, any further increase in delta doping concentration, the electron density in the channel remains almost constant. Fig.4-b shows the simulation result of the variation of double δ-doping concentration (N_D) with threshold voltage (V_{th}). However, from the simulation result it is found that threshold voltage of the device is shifted towards more negative as the 1st and 2ndδ-doping concentrationincreases. Furthermore, the simulation result ofδ-doping concentration (N_D) withtransconductance (g_m) is shown in Fig.4-c. From this simulation, it is found that the transconductance increases as the δ-doping concentration increases, because drain current is increases. Also from this simulation it is found that a high transconductance peak at high N_D. Also, the effect of δ-doping concentration (N_D) on cut-off frequency (f_T)is shown in Fig.4-d. The simulation result it is found that the Cut-off frequency is increases as the δ-doping concentration increases. In this analysis, the current gain cut-off frequency 61.7 GHz is found at *1x10*^{18}*/cm*^{3}δ-doping concentration.

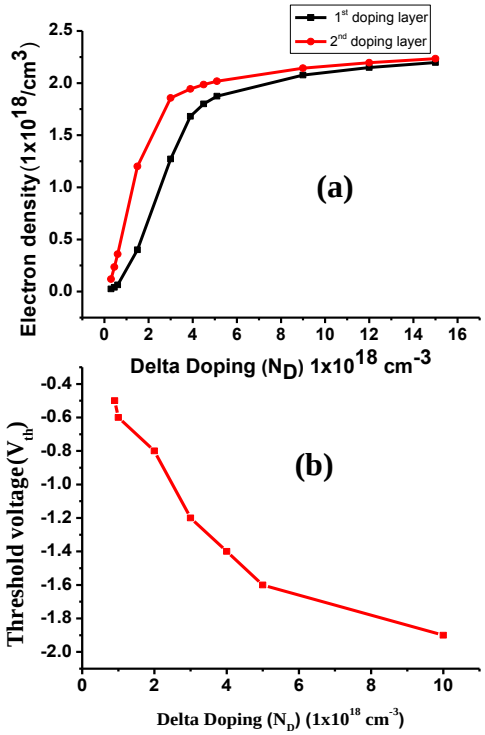

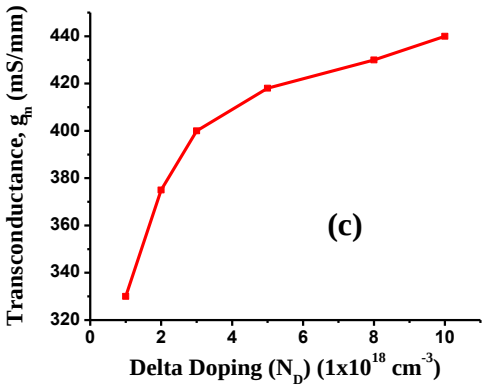

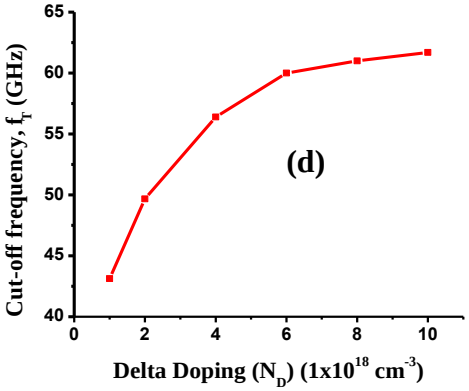

Figure 3: Effect of δ-doping (N_D) Variation. (a) Variation of 2DEG electron density with 1st and 2ndδ-doping (N_D). (b) Variation of threshold voltage (V_{th}) with double δ-doping (N_D). (c) Variation transconductance (g_m) with δ-doping (N_D). (d) Variation of cut-off frequency (f_T) with δ-doping (N_D)

4.3 Effect of Spacer Layer Thickness Variation on device performance

The spacer layer thickness playsanimportantrole on the device performance. A stripper spacer layer thickness rises the total sheet carrier concentration into the InGaAs channel layer. However, a wider spacer layer rises the electron mobility in the channel but, decreases the carrier transfer efficiency in the channel. Further, the spacer layer separates the ionized donor ions from 2DEG, decreasing the Coulomb scattering with the donor ions and raise the electron mobility.The variation of 2DEG electron density in HEMT with a spacer layer thickness d_s is shown in Fig. 4-a. In Fig. 4-a also shows that the effect of channel concentration due to 1st doping and 2nd doping with spacer layer variation. The variation of spacer layer thickness also affects the threshold voltage V_{th}. This variation of threshold

voltage due to the spacer layer thickness is shown in Fig. 4-b.

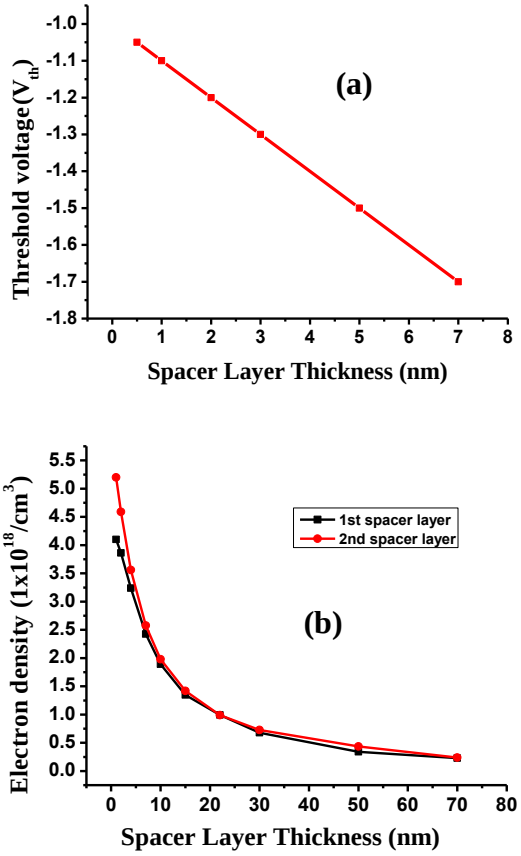

Figure 4: Spacer layer thickness variation. (a) Variation of 2DEG electron density with 1st and 2nd spacer layer thickness (d_s). (b) Variation of threshold voltage (V_{th}) with spacer layer thickness (d_s).

4.4 Effect of Schottky Layer Thickness Variation on device performance

In the HEMT device, the Schottky layer is a wide bandgap material where the channel layer a low bandgap material. Due to this high bandgap difference at the InAlAs/InGaAs heterointerface, where free carrier diffuses from higher bandgap InAlAs to lower bandgap InGaAs material to form 2DEG, which allows higher carrier sheet density and improve the carrier confinement into the channel. The effect of the variation of Schottky layer thickness on carrier concentration due to 1st δ-doping is shown in Fig. 5a. In the simulation analysis, it is found that as the Schottky layer thickness increases the carrier concentration into the channel also increases linearly up to a certain limit then sub-linearly and finally saturated. However, a stripper Schottky layer decreases the distance between the metal gate and channel, provide better gate control and improves the transconductance of the device but reduces the breakdown voltage. Also, the simulation result of Schottky layer thickness variation with a threshold voltage is shown in Fig. 5b. From this simulation result, it is observed that the threshold voltage of the device shifted towards more negative with increasing the Schottky layer thickness. Further, the effect of Schottky layer thickness variation on transconductance is shown in Fig. 5c. From this result, it is found that as the Schottky layer thickness decreases the transconductance of the device increases

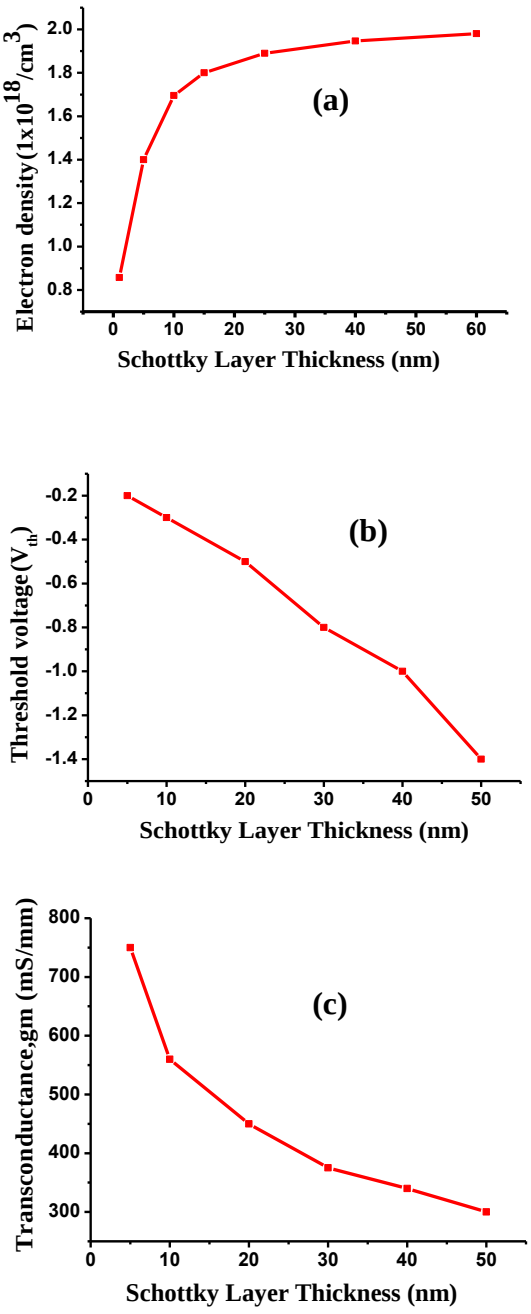

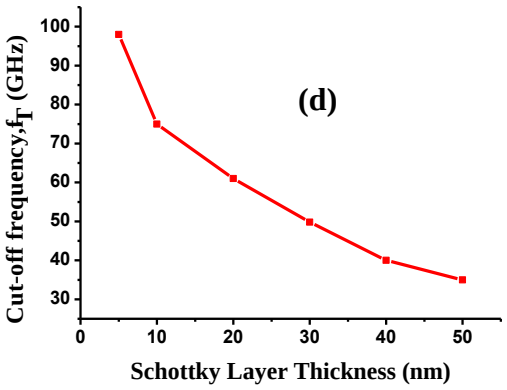

Figure 5:Schottky layer thickness (d_i) variation.(a)Variation of 2DEG electron density due to 1stδ-doping with Schottky layer thickness (d_i). (b) Variation of threshold voltage (V_{th}) with Schottky layer thickness (d_i). (c)Variation transconductance (g_m) with Schottky layer thickness (d_i). (d)Variation cut-off frequencies (f_T) with Schottky layer thickness (d_i)

because the threshold voltage decreases. Further, as the Schottky layer thickness decreases the current gain cut-off frequency is also rises. Effect of Schottky layer thickness variation on unity gain cut-off frequency is shown in Fig. 5d. In this simulation analysis, 98 GHz unity gain cut-off frequency is found at 5nm Schottky layer thickness.

4.5 Effect of Gate Length (Lg) Variation

The performance of HEMT enhancedwith decreases thedimensions, especially the gate length as we considerthe ballistic transport. Optimization of the device performance, like current gain cut-off frequency, can be done by varying the gate length [16]. The effect of the variation of threshold voltage with gate length is shown in Fig. 6a.The simulation result shows that as the gate length increases the threshold voltage of device decreases. However, as the gate length

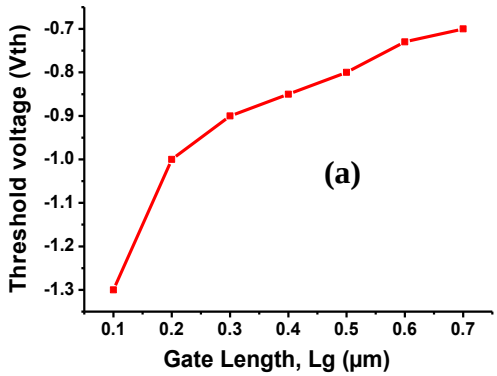

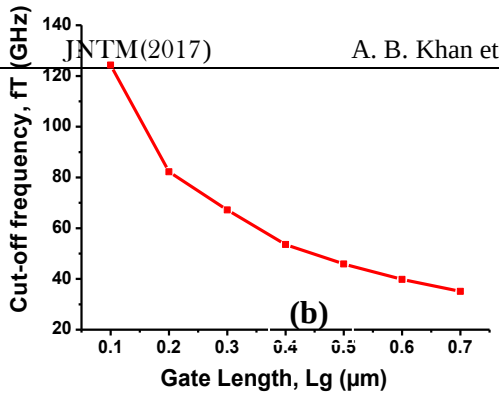

Figure 6: Effect of Gate length (L_g) variation.(a)Variation of threshold voltage (V_{th}) with gate length (L_g). (b)Variation of cut-off frequency (f_T) with gate length (L_g).

decreases thecurrent gain cut-off frequency is increased. The effect of gate length on thecurrent gain cut-off frequency of the device is shown in Fig. 6b.

5. Conclusion

The optimization of 0.5 μm gate length of InP-basedInAlAs/InGaAs HEMT is done after varying some parameters. These parameters are spacer layer thickness (d_s), δ-doping concentration(N_D), Schottky layer thickness (d_i) and gate length(L_g)which are used to optimize the deviceperformance. Spacer layer is used to improve in the mobility of the channel. With the variation of double δ-doping, the enhancement of device characteristics like channel concentration using δ- doped through numerous contours of sheet carrier density, threshold voltage has been studied. The double delta doped HEMT is providing higher 2DEG density and highertransconductancethan single doped HEMT. Further the device performance with Schottky layer thickness variation is also observed. When the Schottky layer thickness reduces, the threshold voltage becomes less negative due to this the transconductance and current gain cut-off frequency are increasing. Reduction on the device geometry like gate length, it is observing that the device performance is also affecting. Furthermore, the influenceof the gate length variationoncurrent thegain cut-off frequency and threshold voltage is alsoobserved. The maximum cut-off frequency125 GHz is observed at5nm Schottky layer thickness,0.1 μm gate length and 1nm, spacer layer thickness.

References

[1] L. D. Nguyen, L. E. Larson, and U. K. Mishra, in *IEEE Proceedings*, vol. 80, pp. 494–518, 1992.
[2] K. Joshin, T. Kikkawa, S. Masuda, and K. Watanabe,*Fujitsu Sci. Tech. J,* vol. 50, no. 1, pp. 138–143, 2014.

[3] Lepore A., Levy M., Lee H., Kohn E., Radulescu D., Tiberio R., Tasker P., Eastman L.,*Electron Devices, IEEE Transactions*, Vol. 35, No. 12, pp. 2441 – 2442, Dec 1988

[4] K. Shinohara, Y. Yamashita, A. Endoh, I.Watanabe, K. Hikosaka, T. Matsui, T. Mimura, and S. Hiyamizu, *IEEE Electron Device Lett.*, Vol. 25, No. 5, May 2004.

[5] S. Gupta, F. Rahman, M. J. Siddiqui, and P. A. Alvi, "Strain profile in nitride based multilayer nano-heterostructures," *Phys. B Phys. Condens. Matter*, vol. 411, pp. 40–47, 2013.

[6] P. A. Alvi, S. Gupta, M. J. Siddiqui, G. Sharma, and S. Dalela, "Modeling and simulation of GaN/$Al_{0.3}Ga_{0.7}N$ newmultilayer nano-heterostructure," *Phys. B Phys. Condens. Matter*, vol. 405, no. 10, pp. 2431–2435, 2010.

[7] P. A. Alvi, S. Gupta, P. Vijay, G. Sharma, and M. J. Siddiqui, "Affects of Al concentration on GaN/$Al_xGa_{1-x}N$ new modeled multilayer nano-heterostructure," *Phys. B Phys. Condens. Matter*, vol. 405, no. 17, pp. 3624–3629, 2010.

[8] D. Delagebeaudeuf and N. T. Linh, *Electron Devices, IEEE Transactions on*, vol. 29, no. 6, pp. 955–960, 1982.

[9] Farhan Aziz, M.J. Siddiqui, International Journal of Emerging Technologies in Computational and Applied Science, Vol. 4, No. 1, pp. 42-48, March-May, 2013.

[10] F. Aziz, M. Siddiqui, and M. Khan, in International Conference on Electronics Information and Communication Systems Engineering (ICEICE-2010).

[11] R. Gupta, S. K. Aggarwal, M. Gupta, and R. Gupta, *Journal of semiconductor Technology And Science*, vol. 4, no. 3, pp. 240–249, 2004.

[12] L. Aina, M. Burgess, M. Mattingly, J. M. O'Connor, A. Meerschaert, M. Tong, A. Ketterson, and I. Adesida, *Electron Device Letters*, IEEE, vol. 12, no. 9, pp. 483–485, 1991.

[13] S. N. Mohammad and H. Morkoc ,Compound Semiconductor Electronics: The Age of Maturity, p. 25, 1996.

[14] S. M. Sze, New York, Wiley-Interscience, 1990, 653 p. *No individual items are abstracted in this volume.*, vol. 1, 1990.

[15] N. Waldron, D.-H. Kim, J. del Alamo, et al., *Electron Devices, IEEE Transactions on*, vol. 57, no. 1, pp. 297–304, 2010

[16] A. B. Khan, M. Siddiqui, M. M. Singh, and C. Thaseena, in Multimedia, Signal Processing and Communication Technologies (IMPACT), 2013 International Conference on, pp. 264–267, IEEE, 2013.

Journal of New Technology and Materials
JNTM
Vol. 07, N°01 (2017)83-89

OEB Univ. Publish. Co.

Mathematical modelling and optimisation of a solar collector performances

M. Dahmani, B. Adouane, F. Z. Ferahta and Z. Aouachria

Energy Applied Physics Laboratory, Faculty of Physical Sciences University Batna 1

Corresponding author: email: zeroual.aouachria@univ-batna.dz
Received date: November 11, 2016; revised date: June 08, 2017; accepted date: June 14, 2017

Abstract

Although a lot of research work has been performed in the field of renewable energy, this domain of research has received, with the recent technological developments, a significant turnover both on the theoretical and experimental sides. At low temperatures, the solar collector plays the role of a converter of solar radiation into heat. Our work focuses on the study of the dynamics and thermal transport phenomena in the air gap of a solar collector in order to optimize its performance. The evolution of thermal and dynamic profiles in the air gap is presented in this paper, which allows us to quantify the convective energy losses. The impact of the interposition of partitions in the air gap was analyzed as well. The influence of this new model on convection losses turns out to be significant

Keywords: solar energy, solar collector, mathematical modelling, performance optimisation;

1. Introduction

Solar water heating is a promising technology to produce hot water, it is a technology that is simple and easy to adopt. The growing importance of solar thermal collectors has led to significant progress in their design characteristics (design features), this was performed, on one hand by improving the absorption capacity of heat by the solar collector by adding new features to the absorber plate, AlShamaileh (2010),[1], improving the hydraulic and geometric design, Tanaka (2011)[2] and the use of alternative materials, Carlson et al (2014)[3], on the other hand, investigations are focusing on the minimization of heat losses to the outside, Vestlund et al (2006), Subiantoro et al (2013)[4 - 5]. A good solar thermal converter requires effective control of the heat loss at the absorber to the environment. Designers seek economical alternatives to minimize losses by thermal conduction and especially the coupling between convection and radiation. The most significant thermal losses happen through the glass cover, Benkhalifa A. (1998), Ghoneim (2005)[6 – 7] . Researches, in this axis, focus on reducing to the maximum their effect. This can be achieved by inserting baffles (obstacles) in the air gap between the absorber and glazing. Youcef-Ali (2005). H. Buchberg et al (2008) [8 – 9] showed that the installation of a rectangular cell positioned above a solar absorber is an effective device for lowering losses by natural convection. The obstacle should be very thin and transparent to avoid interference with different radiations. Finally, this study is equivalent to a study of natural convection in a partitioned cavity having dimensions of the solar collector. Natural convection, in partitioned cavities, has been extensively studied both numerically and experimentally, because of its substantial interest. We can cite the work of Frederick (1989) [10] which is a numerical study of natural convection in an inclined square cavity filled with air and heated differentially with a single partition attached to its cold wall, Ra = (10^3-10^5). It has been proved that the partition leads to the suppression of convection, and reduces the heat transfer by 47% compared to the cavity without partitions, in the same conditions. E. Bilgen (2004) [11] studied natural convection in cavities with a thin fin on the hot wall, he concluded that normalized Nusselt number, Nu is an increasing function of Rayleigh, Ra, and a decreasing function of fin length. Hua-Shu Dou et al (2016) [12] present a numerically investigation of natural convection flow in a differentially heated cavity. The effects of fin number, fin position, and fin length on heat transfer in natural convection are analyzed ,when Ra is relatively small, the fin(s) blocks the heat transfer. The effect of the fin number on heat transfer is negligible when the fin number is larger, than one ,when Ra is relatively large, the fin(s) enhances heat transfer ,the effect of fin number on heat transfer is also negligible when the fin number exceeds one. However, the heat transfer rate decreases when the fin number exceeds one comparing to that when there is only one fin in the cavity Mohammed Jami (2006) [13] presented a numerical study of heat transfer by laminar natural convection in an inclined enclosure differentially heated, with inclined partitions attached to the hot wall. He concludes that the reduction in heat transfer increases with increasing the partition length when the partition is tilted. Mezrab et al (2006)[14] studied the effect of the number of partitions on heat transfer phenomena in a tilted square cavity where the partitions are fixed to the cold wall. He showed that in the case of several partitions, the reduction of the heat transfer is

considerably increased with the number of partitions up to a certain value it remains constant by the fact of the disappearance of the convection. Mr. Yousaf et al (2015) [15] A numerical algorithm was developed to analyze the role of the sinusoidal roughness elements on the thermal and hydrodynamic behavior of a fluid in laminar region. Two-dimensional studies were conducted in a square cavity ,the sinusoidal roughness elements were located on a hot, and both the hot and cold walls. He conclude that The maximum reduction in the average heat transfer was calculated to be 28% at Ra number equal to 10^5 when the sinusoidal roughness elements were located at both the hot and cold walls.. The remark drawn from this literature review is that for similar cavities with flat plate solar collectors, the conditions applied to the limits do not reflect the actual operating conditions of the solar collectors. The geometry dimensions in our study are real and are subject to a flow imposed on the absorber taking into account the losses by radiation and convection to the outer face of the solar flat plate collector. The partition conductivity is taken into account for a comprehensive study of the phenomenon. So the aim of this study is to identify the impacts of partitions on the dynamic and thermal phenomena in the air gap of a solar collector.

2. Generating of the problem

2.1. physical model

The studied geometry is a parallelepiped cavity with dimensions (L x D x e = 1m x 0.02m x em) with an aspect ratio A= L / D, formed by an absorber (lower face) of a glass cover (upper side) 4mm thickness and whose side walls are insulated. partitions are interposed in the interior of the cavity, attached to the inner face of the glass which is uniformly distributed; the study area is presented in Fig.1.

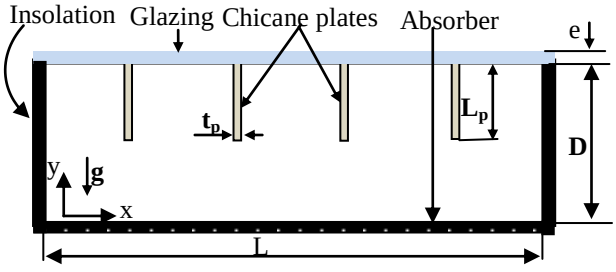

Fig. 1: Numerical model schema

A '2-D' simulation of the solar air gap spacing between plate and inner glasses equipped with obstacle is investigated. The following assumptions are imposed for the computational analysis: i- the flow is steady-state, laminar and two dimensional. ii- the thermal conductivity of the duct wall, absorber plate and roughness material are independent of temperature. iii- the duct wall, absorber plate and roughness material are homogeneous and isotropic, iv- In the cavity volume the Boussinesq approximation define the density as a constant, except for the buoyancy term in the momentum equation. The rest of fluid properties are also constant. In table 1 the air properties at the reference temperature, fixed at 300 k ,are defined, v- No-slip boundary conditions are assigned to the walls in contact with the fluid, vi- Negligible radiation heat transfer.

Table1: physical air properties: Boussinesq approximation

K (W/mK)	ρ (Kg/m^3)	C_p (J/Kg K)	μ (Kg/m.s)	β (1/K)
0.0263	Boussinesq Approximation	1007	$1.846.10^{-5}$	0.0033

2.2. boundary condition

The boundary conditions imposed in the numerical model are: i- the energy losses convection and radiation are taken into account at the outer side of the collector window. ii- an experimental correlation [16] is adopted to estimate the convective heat transfer coefficient for the flow above the glass $h_{ext} = 5.7 + 3.8V$ where V is the wind speed, it is taken as 1.13m/s. iii- To model irradiative losses, according to [17], the black sky radiation temperature was considered equal to the air temperature. iv- The side walls are defined as adiabatic walls. v- A constant heat flux is imposed on the absorber to simulate solar radiation where q=50w/m^2. vi - The non-slipping condition is imposed on the walls.

2.3. mathematical modelling

In the case of natural convection, it is necessary to take into account the value of the number of Raleigh that can be used as a criterion for laminar and turbulent flow in the system. The problem is governed by two dimensionless parameters Ra and Pr, defined by:

$$Ra = \frac{g\beta L^4 q}{\nu\alpha k}, \quad \Pr = \frac{\nu}{\alpha} \tag{1}$$

We present the system of conservation equations describing a stationary regime, 2D phenomenon in the air layer of the flat collector. These equations describe the transport of mass and heat inside the air gap, taking into account the above-mentioned assumptions.

$$\frac{\partial u}{\partial x} + \frac{\partial v}{\partial y} = 0 \tag{2}$$

$$u\frac{\partial u}{\partial x} + v\frac{\partial u}{\partial y} = -\frac{1}{\rho}\frac{\partial p}{\partial x} + \nu\left[\frac{\partial^2 u}{\partial x^2} + \frac{\partial^2 u}{\partial y^2}\right] \tag{3}$$

$$u\frac{\partial v}{\partial x} + v\frac{\partial v}{\partial y} = -\frac{1}{\rho}\frac{\partial p}{\partial y} + \nu\left[\frac{\partial^2 v}{\partial x^2} + \frac{\partial^2 v}{\partial y^2}\right] - g\beta(T - T_0) \tag{4}$$

$$u\frac{\partial T}{\partial x}+v\frac{\partial T}{\partial y}=\alpha\left[\frac{\partial^2 T}{\partial x^2}+\frac{\partial^2 T}{\partial y^2}\right] \quad (5)$$

3. Numerical simulation

Calculations reported hereafter have been performed with the commercial code Fluent based on the finite volume method, the pressure based solver, implicit formulation, Green-Gauss node based and absolute velocity formulation were used, therefore, the double precision was selected. The governing equations of mass, momentum and energy are solved by the finite volume method in the steady-state regime, The SIMPLE algorithm (Semi-Implicit Method for Pressure Linked Equations), was adopted for coupled pressure and velocity. The Body Force Weighted discretisation scheme was used for pressure, however the second-order upwind is chosen for all other equations. The convergence criteria of 10^{-6} for the residuals of the continuity equation, the velocity components and 10^{-6} for the residuals of the energy are assumed. All simulations are started with under-relaxation factors for pressure, momentum, energy of 0.3, 0.7, and 0.9 respectively. The above mentioned values, was fixed to achieve the convergence criteria.

3.1. grid independence test

The developed model was used to study the obstacle effect on the performance of the absorber and on the convection, which causes the heat losses. The mesh tool, GAMBIT 2.2.30 was used to create the geometry and generate the mesh. The mesh independence was studied using three different meshes illustrated in Fig.2 (217728 as a coarse mesh cells, 528504 cells to a fine mesh and 709 120 cells for a finer mesh). This figure shows the temperature profiles in the middle of the cavity, between the obstacles, 2 and 3 . There is a perfect agreement in the temperature profiles corresponding to the two latest meshes. Therefore, for the calculations reported in this study, the fine mesh was chosen to optimize the relationship between accuracy and computation time.

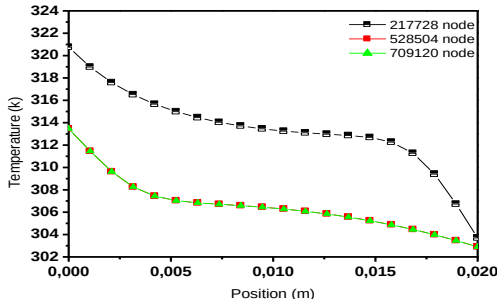

Fig.2 mesh independence for three different cases

3.2. heat transfert

4. The study of heat transfer requires a thorough knowledge of the local heat transfer coefficient (h) at the absorber. For the determining, choosing a distance between two obstacles that are divided into 100 to 200 elements to calculate their coefficient h. The desired distance reflects the phenomenon of periodicity observed in the sensor as illustrated in fig.3.

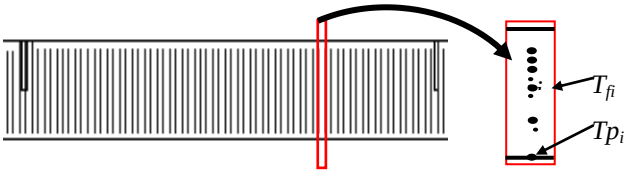

Fig.3 fragmentation pattern of an element of the absorber for calculating the local heat transfer coefficient.

Using the results of the simulations, for each elementary slice of the strip between two consecutives baffles, giving the wall temperature and the average temperature of the fluid above the point of the considered wall, one can calculate the local heat transfer coefficient by the expression.

$$h=\frac{q}{(T_p-T_{moy})} \quad (6)$$

Where T_p is the wall temperature and T_{moy} is the average temperature of fluid which is determinate by:

$$T_{moy}=\frac{\int_A \rho u T dA}{\int_A \rho u dA} \quad (7)$$

The local Nusselt numbers Nu_L were calculated using custom field function CFD code for both cases (with and without partitions). $Nu_L=h \cdot D/k$
where k is the air thermal conductivity.

4.1. validation

The model we have developed to solve the basic equations has been validated by comparison with results of studies [18], [19] and [20]. This comparison of results at different numbers of Ra, to those obtained by these different methods is illustrated in Table 2 and figs.4 and 5. Our model is applied to a cavity similar to that of [18], with the same conditions. The former table shows this good agreement for the Nusselt number to 1%. The figs.4 shows this good agreement through isotherms and the streamlines corresponding current lines at different Ra numbers in comparison with the above refs.. Concerning the computer code validation, the agreement obtained between our results and those available in the literature proved to be excellent.

Table 2. Comparison of Nusselt different values

Ra	Present study	Ref. [18]	Ref. [19]	Ref. [20]
10^3	**1.117**	1.118	1.118	1.115
10^4	**2.249**	2.252	2.243	2.250
10^5	**4.514**	4.545	4.523	4.569

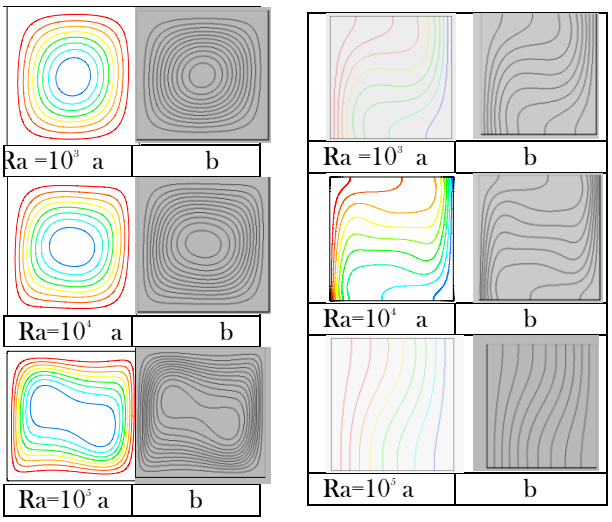

Fig.3 isothermes and streamlines for different Ra. a present study, b results of Ref.[18]

5. RESULTS

5.1. effect of the obstacles' length

The purpose of the present study was to analyze the effects of the partitions elements in the air gap cavity of solar collector by Changing their length and number. Figure 4 shows the influence of the length of the partitions on the iso-contours speeds in the air space of the solar collector. It is observed in this figure a formation of Rayleigh Benard rolls. The effect of the partitions length does not affect the number of cells of air masses fig 5. However, the strength of circulation is influenced by this length fig4. Indeed, the increase in length leads to weaker flow intensity due to the expected increased resistance of motion of the rotating convection cells. which will curb the phenomenon of convection and therefore energy losses are also reduced because in the central zone transfer is done primarily by conduction. Then, the convection phenomenon affects only the ends of the cell. Figures, 5 and 6, show the distribution of the temperature of the surface of the absorber of the solar collector, The first remark shows that the temperature increases with partitioned cavity with respect to the cavity without partition. It is clear that the temperature of the absorber grows below the partition with the increase of the length Lp, the variation of the temperature is not distinctive beyond Lp = 1.2cm, for Lp = 2cm the temperature at the side of the partitions diminished because of the conduction where the partition joins the absorber. The temperature distribution is not uniform on the surface of the absorber, recording a temperature gap of 9.5° C between the extreme values, the influenced length is manifested near the end of the partitions.

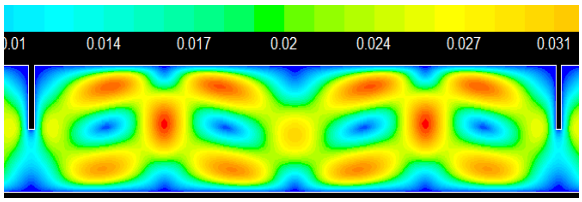

a- Lp =1cm

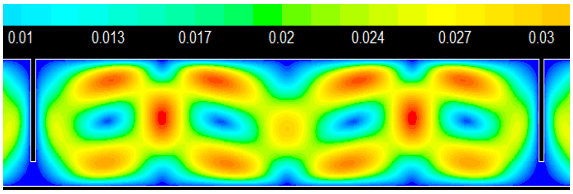

b- Lp= 1.6cm

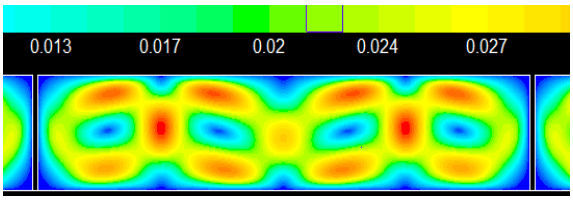

c- Lp =2cm

Fig.4 Velocity contours for different lengths of chicane

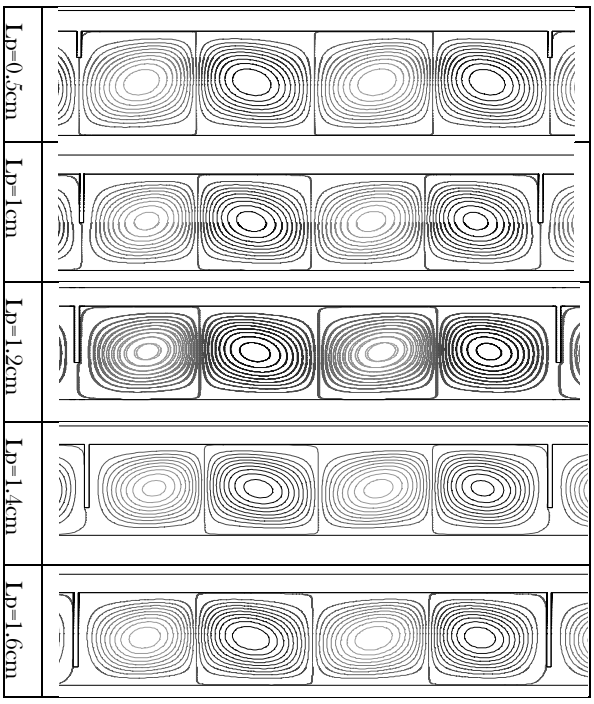

Fig.5: stream function for different value of Lp

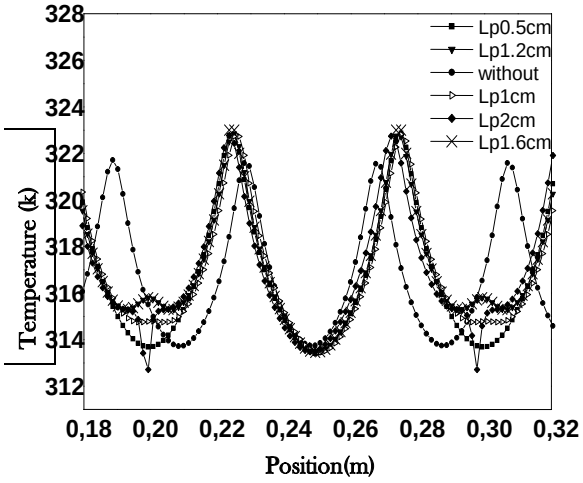

Fig.6: absorber temperature profile

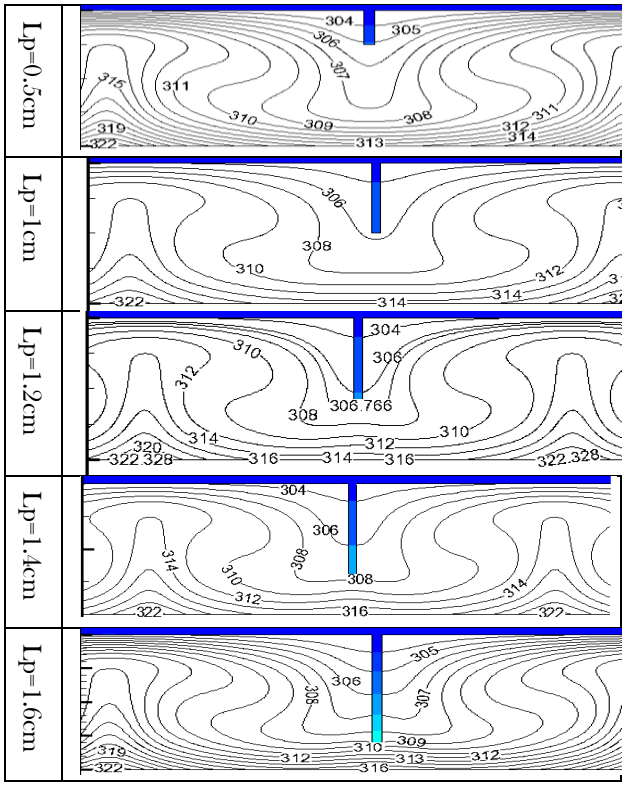

fig.7: isotherms for different value of Lp

fig.8 shows the variation of the average Nu with varying partitions length. It can be seen that the change in the average Nu was minimal for all cases, The maximum decrease in the average value of Nu as compared to the case without partitions, it was observed to be 7.56% at Ra number 10^4,

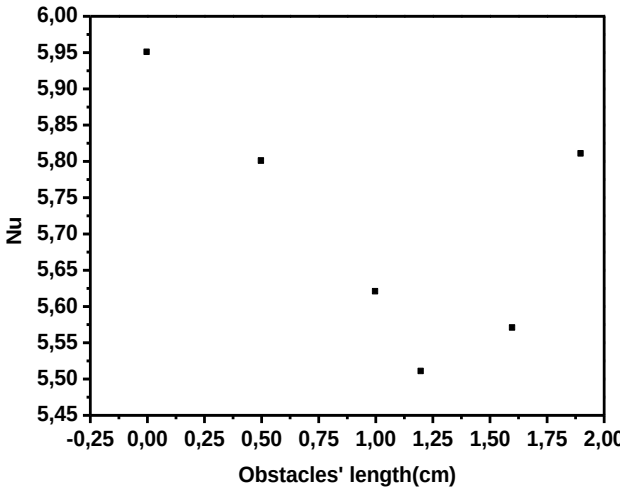

Fig. 8: Variation of the average Nusselt number on the hot wall with partitions length

5.2 EFFECT OF THE NUMBER OF PARTITIONS

Figure 9,10 illustrates the existence of longitudinal cells that develop in the air layer having the same structure of Fig.4,5, but here, the structure varies according to the obstacle number. Indeed, when the number of obstacles is increased, the number of cells decreases fig.10. Its variation is significant both on the velocity field and on the temperature see fig. 11 and 12. It is noted that the maximum temperature gap between the case with the number of partitions 4 and 20, passes from 11.5°C to 6.6°C. This means that the high number of obstacles enhances significantly the absorber temperature and decrease the heat losses mainly by convection. The largest intensity of flow instability occurs when there is no partitions, the fin(s) blocks heat transfer, the heat transfer rate decrease when the partitions number increases.

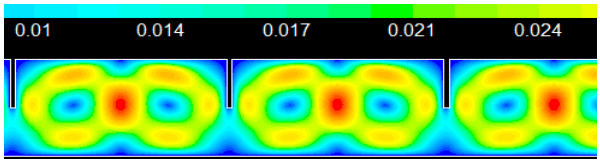

a-24 partition

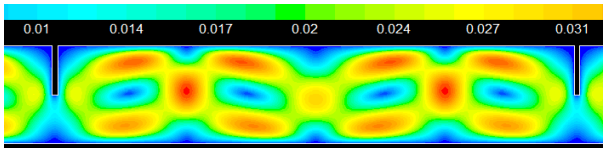

b-9 partition

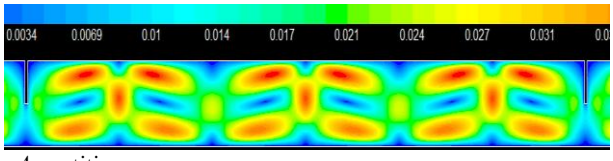

c-4 partition

Fig.9: Velocity contours for different numbers of partitions

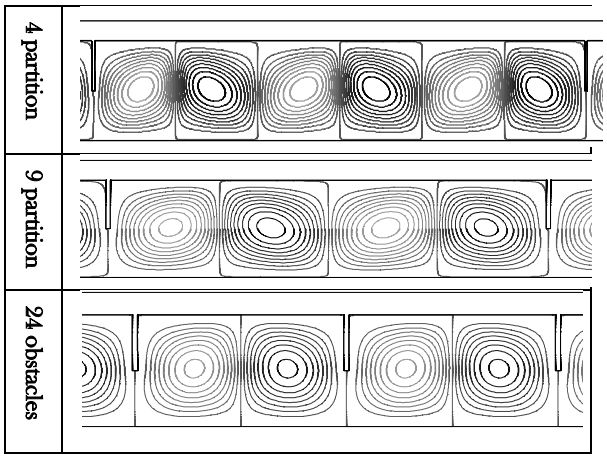

Fig.10: stream function for different partitions number

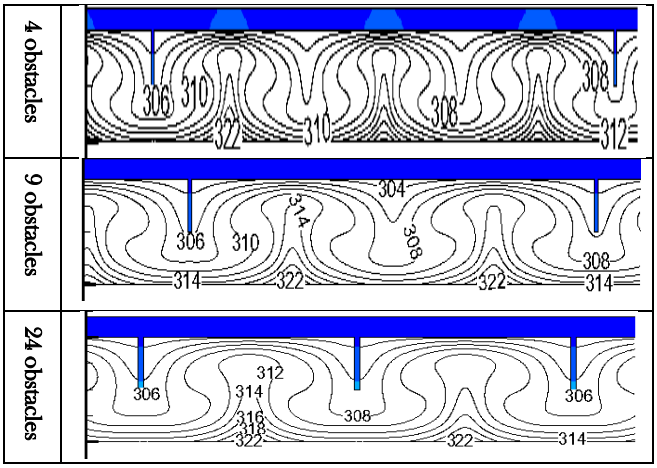

Fig.11: isotherms for different partitions number

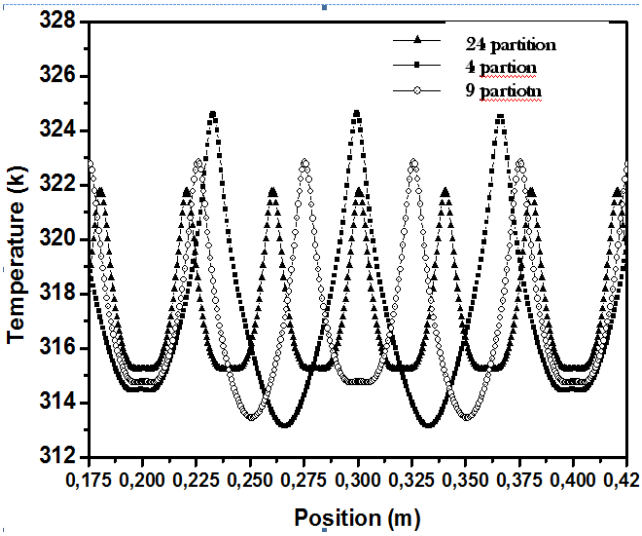

Fig.12: partitions number effect on the temperature

VI CONCLUSION

In this work, a 2D cavity, having the same dimensions of a solar collector has been studied, focusing on the presence of partitions and their effect on the collector inner flow when a heat flux is applied to the absorber. A comparative study was made between a cavity with and without partitions, whereas the length and the number of partitions were varied. In this study, the following conditions were assumed for Ra and Pr ($2.8 * 10^4$ and 0.71) respectively.

In general, increasing the number of partitions and their lengths contribute to the reduction of heat loss by convection and help to increase the temperature of the absorber. The optimal length of the partitions is close to 66.6% of the air gap.

REFERENCES

[1] AlShamaileh E., Testing of a new solar coating for solar water heating applications. Solar Energy 2010; 84(9):1637–43.

[2] Tanaka H. Solar thermal collector augmented by flat plate booster reflector optimum inclination of collector and reflector. Appl Energy 2011; 88 (4): 1395–404.

[3] Carlsson B, Persson H, Meir M, Rekstad J.A total cost perspective on use of polymeric materials in solar collectors–importance of environmental performance on suitability.Appl Energy 2014;125:10–20.

[4] Vestlund J, Rönneild M, Dalenbäck JO. Thermal performance of gas-filled in flat plate solar collectors. Solar Energy 2009; 83(6):896–904

[5] Subiantoro A, Ooi KT. Analytical models for the computation and optimization of single and double glazing flat plate solar collectors with normal and small air gap spacing. Appl Energy 2013; 104:392–9.

[6]Benkhalifa A. Optimisation d'un capteur solaire plan. Revue des Energies Renouvelables 1998; Volume spécial SIPE:13-18.

[7] Ghoneim A.A. Performance optimization of solar collector equipped with different arrangements of square-celled honeycomb, International Journal of Thermal Sciences (2005) pp.44, 95–105.

[8 Youcef-Ali. S: Study and optimization of the thermal performances of the offset rectangular plate fin absorber plates, with various glazing. Renewable Energy 30 (2005), 271– 280.

[9] Buchberg H. Catton I. Edwards D.K., Natural convection in enclosed spacer a review of application to solar energy .collection energy and kinetics department, school of engineering, university of California, los angels calf.

[10] Frederick R.L., Natural convection in an inclined square enclosure with a partition attached to its cold wall, Int J. Heat Mass Transfer 32 (1989) 87–94

[11] E. Bilgen Natural convection in cavities with a thin fin on the hot wall. Heat Mass Transfer 48 (2005) 3493–3505

[12]Hua-Shu Dou , Gang Jiang ., Numerical simulation of flow instability and heat transfer of natural convection in a differentially heated cavity. Heat Mass Transfer 103 (2016) 370–381.

[13] Mohammed Jamia, Ahmed Mezrhab A, Mohamed Bouzidib, Pierre Lallemandc. Lattice-Boltzmann computation of natural convection in a partitioned enclosure with inclined partitions attached to its hot wall. Physica A 368 (2006) 481–494.

[14] Mezrhab A., Jami M., Abid C., Bouzidi M., Lallemand P., LatticeBoltzmann modelling of natural convection in an inclined square Mathematical modelling and optimisation of a solar captor performances enclosure with partitions attached to its cold wall, Int. J. Heat Fluid Flow, 27 (2006) 456–465.

[15] Yousaf M., Natural convection heat transfer in a square cavity with sinusoidal roughness elements International Journal of Heat and Mass Transfer 90 (2015) 180–190.

[16] McAdams WH. Heat transmission,3rd ed .New York:McGraw Hill: 1954

[17]Duffie JA, Beckman WA. Solar engineering of thermal processes. 3rd end .Hoboken, New Jersey: Johan Wiley and Sons: 2006.

[18] Amraqui. S, "Modélisation des transferts thermiques couplés dans un capteur solaire thermique avec cellules anti-pertes". Thèse de doctorat en cotutelle de l'Université Mohammed premier- faculté des sciences-Oujda et université de Provence-institut universitaire des systèmes thermiques industriels – Aix-Marseille (2009).

[19] G. De Vahl Davis, Natural convection of air in a square cavity: a bench mark numerical solution. Int. J. for numerical methods in fluids, Vol. 3 (1983) 249-264.

[20]R. Kumar,M. A. Kalam, Laminar thermal convection between vertical coaxial isothermal cylinders. Int. J. Heat Mass Transfer, Vol. 34, N° 2 (1991) 513-524.

Journal of New Technology and Materials
JNTM
Vol. 07, N°01 (2017)90-96

OEB Univ. Publish. Co.

Optimization of the Raw Material Input Molar Ratio on the Carbothermal Production of Solar-Grade Silicon

Rabie Benioub[a,b,*], Mohamed Adnane[b], Abderahmane Boucetta[a], Amina Chahtou[a], Hidekazu Kobatake[a], Yasubumi Furuya[a] and Kenji Itaka[a]

[a]*North Japan Research Institute for Sustainable Energy, Hirosaki University, 2-1-3, Matsubara, Aomori, 030-0813, Japan*
[b]*Université des Sciences et de la Technologie d'Oran Mohamed Boudiaf, USTO-MB, BP 1505, El M'naouer, 31000 Oran* Algérie
*Corresponding authors, E-mail: dr_b_r@yahoo.fr
Received date: March 09, 2017; revised date: June 15, 2017; accepted date: June 17, 2017

Abstract

With the fast growth of solar cells market, it is strongly required to improve the fabrication process of solar-grade silicon, which is the base material for more than 93% of solar cells technology. Conventionally, solar-grade silicon is produced via the direct reduction of silica stone to metal-grade silicon by arc furnace followed by the Siemens method with chemical treatment and hydrogen. However, in this technique a low yield of solar-grade silicon is obtained with high energy cost due to its multiple complex processes. Meanwhile, it has been turned out that, the direct reduction process from silica sand to solar-grade silicon via induction furnace simplify the fabrication process with low energy and cost consumption with higher yield. In this study, the optimum partial pressure and temperature conditions of this process were based on the stability phase diagram for reduction reaction process. Using the simulation results, we succeeded to increase the reduction yield by ten times.

Keywords: Carbothermic silica reduction;Solar-grade silicon; Raw material ratio; Reduction yield.

1. Introduction

As the first material for solar cells fabrication, solar-grade silicon (SoG-Si, around 6N) has been produced via the carbothermic reduction process using an electric furnance [1]. Silica from gravel and stones and carbon from charcoal, wood chips, coal, and coke, were used as raw materials in the silicon production process which requires high temperatures and much energy [2]. Various route for silicon production have been investigated, including the Siemens as shown in Figure 1 (a), starting by a direct reduction in an arc furnace of silica stone by carbon to get metallurgical-grade silicon with a huge amount of CO_2 gas released, and followed by a reduction of $SiHCL_3$ gas using hydrogen gas[3-6]. In addition, other methods such as Union Carbide, Fluidized bed processes and electrolytic were used too[7,8]. However, some of these processes includes multiples processes which make the application of these methods complicated. Therefore, the high purity direct carbothermic reduction process which represents a new method of production of low-cost SoG-Si expresses less time and energy consumption as shown in Fig. 1(b). This method includes a two-step conversion processes, statring by extraction of pure silica (SiO_2) from silica sand with raw purity of 97% and 99.9% (3N) after purification[9], and followed by direct carbothermal reduction of this pure silica in an induction furance for production of silicon[10]. However, this method expressed a low reduction yield[11,12]. Therefore, the understanding of the phase diagram of the direct carbothermic silica reduction process, and the estimation of by-product such as SiO and CO gases partial pressure is inevitable for the improvement of the direct reduction. Moreover, previous report show a solid relationship between the raw material input such as silica and carbon and the final product such as Si and SiC [13-15]. However, the dependency on raw material input of the total mass balance of the reduction process which represent a total understanding of the different material conversion and total mass preservation related the solid-gas form conversion were not discussed before.

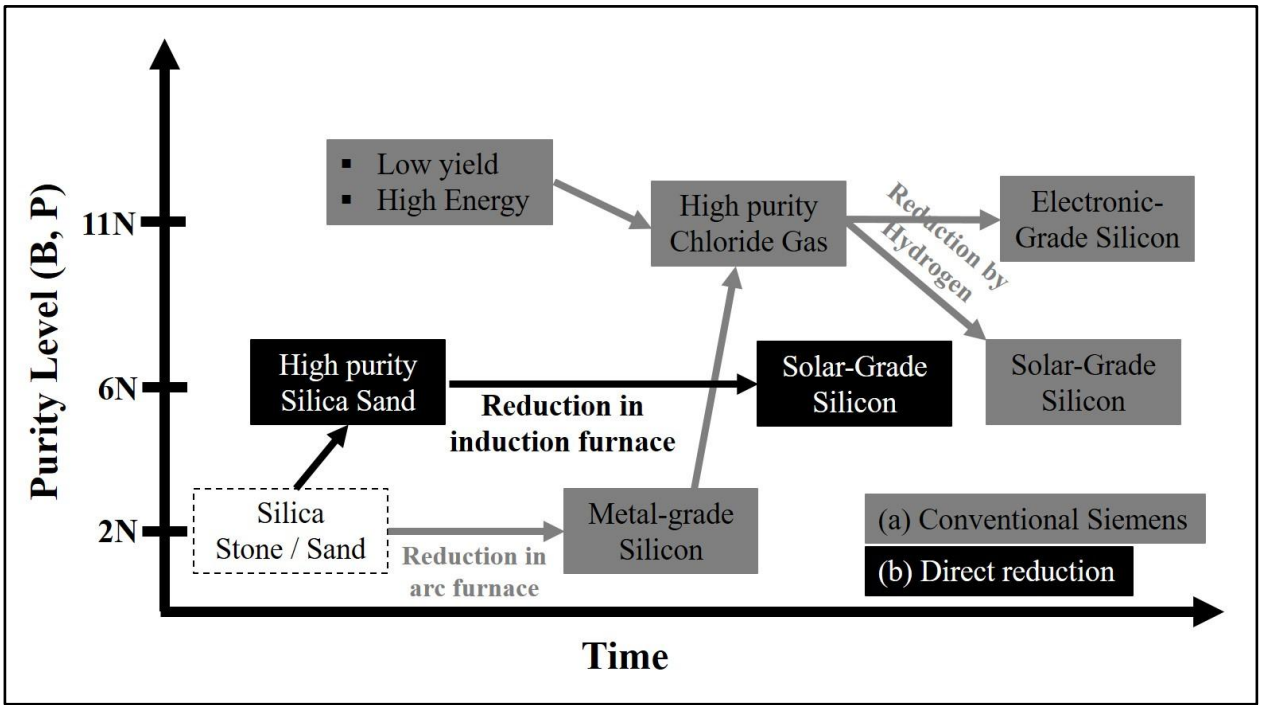

Fig. 1 Schematic comparison between conventional Siemens method through direct reduction process from silica stone to metal-grade silicon (a) and the main target of this research work which is the direct reduction process from silica sand (b).

In this research work, the phase diagrams of the direct carbothermal reduction possible reaction were simulated and discussed as a function of partial pressure of SiO to CO gasses using thermodynamic calculation of Gibbs free energy. The optimum temperature and partial pressure of SiO/CO were deduced from the simulation results and used in experimental work to confirm the effect of mole ratio variation between SiO_2 and Carbon raw material on the solid-gas conversion efficiency known as the reduction yield.

2. Simulation and Experimental Procedure

2.1. Si-O-C Phase Stability Diagram

The simplified overall reaction in the reduction process are shown below in equations (1-5) below, show the overall reaction in silicon production, which requires knowledge about the reaction at high-temperature zones of the furnace[16].

SiO_2 (s) + C (s) = SiO (g) + CO (g)..... .....(1)

$\Delta G^\circ = 668.07 - 0.3288T(\text{kJ})(1273\text{K} \le T \le 1993\text{K})$

$2SiO_2$ (s) + SiC (s) = 3SiO (g) + CO (g).....(2)

$\Delta G^\circ = 1415 - 0.6586T(\text{kJ})(1273\text{K} \le T \le 1993\text{K})$

SiO (g) + 2C (s) = SiC (s) + CO (g).....(3)

$\Delta G^\circ = -78.89 + 0.0010T(\text{kJ})(1273\text{K} \le T \le 2273\text{K})$

SiO (g) + SiC (s) = 2Si (s) + CO (g)..... .....(4)

$\Delta G^\circ = 165.56 - 0.0751T(\text{kJ})(1673\text{K} \le T \le 2273\text{K})$

SiO_2 (l) + Si (l) = 2SiO (g)..... ....(5)

$\Delta G^\circ = 616.37 - 0.2875T(\text{kJ})(1673\text{K} \le T \le 2273\text{K})$

where, ΔG° represents the standard Gibbs energy of each reaction. (s), (l) and (g) referred to solid, liquid and gas phases.

In this process to produce silicon, a reaction temperature higher than 1500℃ (1773K) to produce enough SiO gas through reaction (1) and (2). Phase stability diagrams for the reactions in Eqs. (1-5) were calculated as illustrated in Figure 2 (a-d) with the standard Gibbs energy of the reactions taken from MALT2[17].Our main target was focused on the partial pressure ratio of SiO gas to CO gas because of its possible experimental occurrece as shown in Figs. 2 (a-d) with black dashed horizontal lines. In the carbothermic process of silicon, silica will start to react with carbon at a temperature over 1054°C(1327K) as increasing temperature with generation SiO gas Eq. (1) which is shown as the first gray color in Fig. 2 (a). While silicon carbide starts to react with carbon in Eq. (2) at 1070℃ (1343K) to generate SiO corresponding to the first gray color in Fig. 2 (b). As for the reactions in Eqs. (3), (4) and (5), silicon carbide is generated via Eq. (3) with the interaction between SiO gas and carbon, and thermodynamically the reaction proceeds even at low temperature but experimentally it is difficult because its required rich SiO gas pressure generated from the previous reactions[18]. Si is produced by the reaction of silicon carbide with SiO gas at the temperature of 1500℃ (1773K) via Eq. (4)[19]. While si production from SiO2 releasing of SiO gas Eq. (5) could be occurred at very low temperature below 1400°C(1673K) due to requirment of the presence of liquid silica and silicon forms at lower temperature. Colorless area below at lower temperature corresponds to no reaction in Figs. 2 (a-d) due to the negligible partial pressure of SiO(g) and CO(g) due to the presence of solid silica and carbon[20, 21].

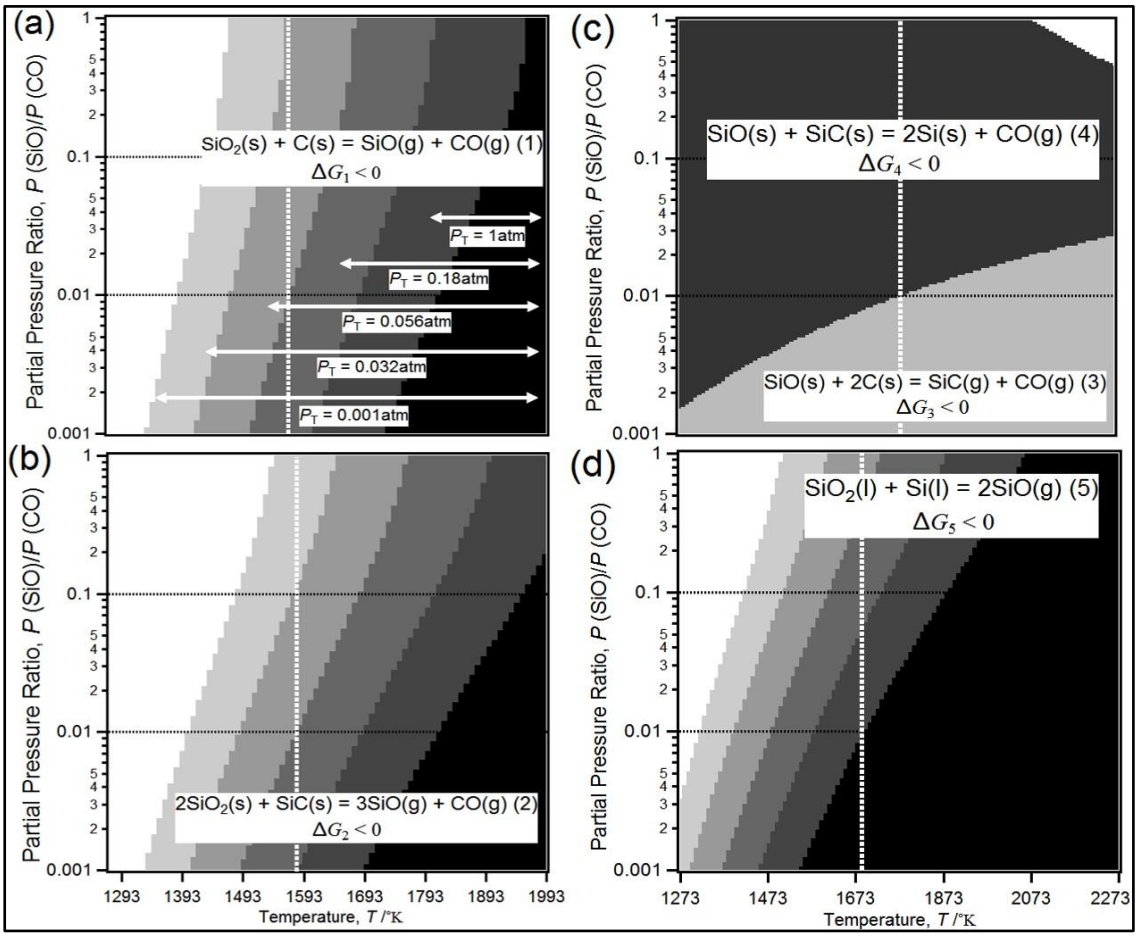

Fig. 2 Si-O-C Phase stability diagram for the ratio of SiO/CO gas phases: (a), (b), (c), and (d) for reactions in Eqs. (1), (2), (3), (4) and (5). This diagram shows the variation of the partial pressure ratio SiO/CO and temperature impact on the reduction of silica to silicon based on calculated data from MALT2.

Therefore, our system, the partial pressure ratio of SiO and CO range is between 0.01 to 0.1. The change in the Gibbs energy of the reaction in Eqs. (1) and (2) suggests that most likely, SiO gas is generated through a solid-solid reaction in the presence of direct contact between silica and carbon and between silica and silicon carbide[22]. While silicon is produced via solid-gas reaction in the contact between SiO and SiC. The optimum reduction temperature for silicon production is in a range from 1500℃ (1773K) to 1800℃ (2073K).

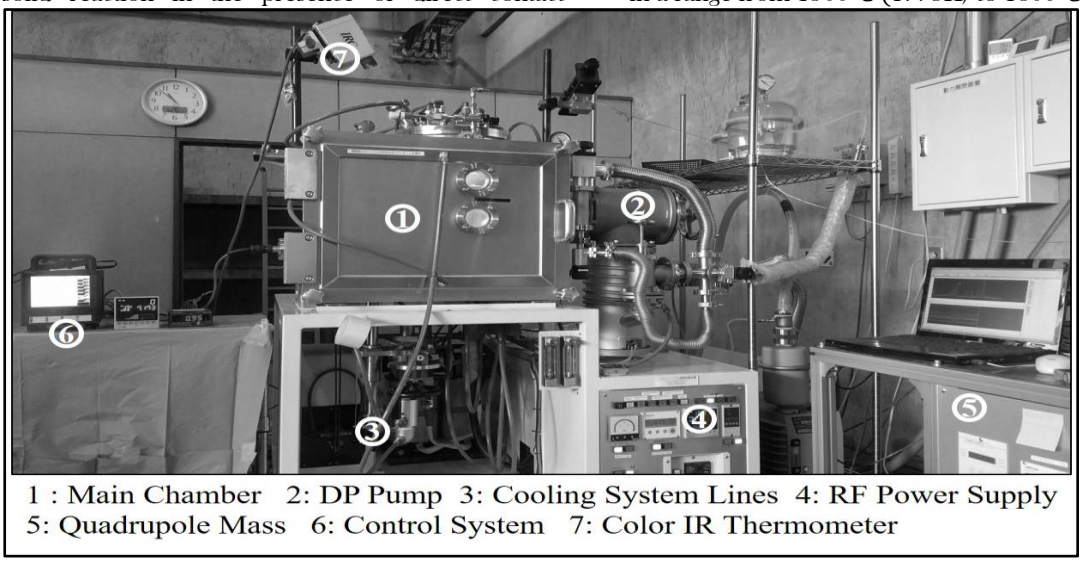

Fig. 3 Image of the induction heating furnace for the reduction process in this study.

2.2. Experimental Setup

Figure 3 shows the induction heating furnace of 30 kW power (Toei Scientific Industrial CO,. Ltd) used for carbothemal processioning. In the carbothermal reduction experiment, the gas species generating during the measurment were also investigated using quadrupole mass spectrometry (Q-mass) with direct connection to the induction furnace. Figure 4 shows a schematic illustration of the crucible setup in the present reseach. A high-purity graphite crucible with inner diameter of 40 mm and height of 70 mm was used for this study. Four mixture of silica (diameter 20~100um, Taiheiyo Cement Corporation Japan) and glassy carbon (diameter 20 um, Tokai Carbon, Ltd), were installed to the crucible with changing the molar ratio of siluca, graphite and silicon carbide as listed in table 1. The sample in the crucible was placed a the center of the induction furnance [16].

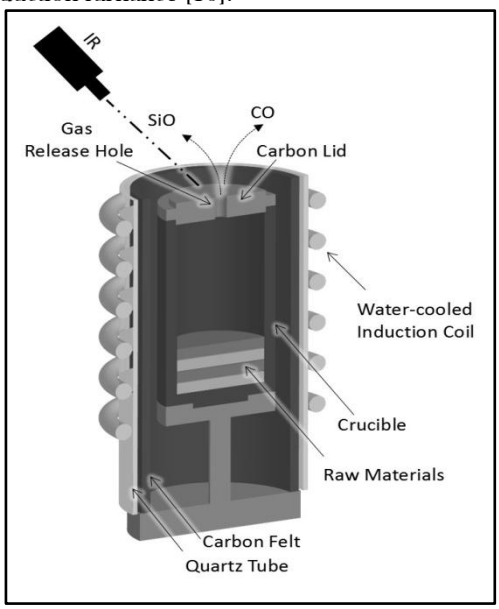

Fig. 4 Schematic figure of the crucible configuration.

The crucible was covered with carbon felt and surrounded by a quartz tube as insulation. The crucible temperature measured from the crucible top via infrared thermometer. The evacuation system of this appartus is composed of a rotary and diffusion pumps, which can reach to 10^{-3} Pa in a vacuum. During the heating experiment, the top temperature of the crucible was monitored by a high sensitive single color type infrared thermometer with a temperature range from 650℃ (923K) to 3500℃ (3773K) through the top glass window of the chamber. The induction coil heated the crucible with a frquency of 30 kHz under an open-loop control, and a quartz tube was placed in between the crucble and the coil for the protection of the crucible. The atmosphere during the heating process was pure argon gas (99.999%) with a pressure of 0.07 MPa to avoid the leak of the lethal carbon monoxide gas. The evacuation of the chamber to a higher vacuum order is required before the filing of the argon gas because the mass peaks between nitrogen and carbon monoxide are overlapped completely. The total pressure inside the chamber was recorded manually from the Bourdon gauge connected to the chamber.

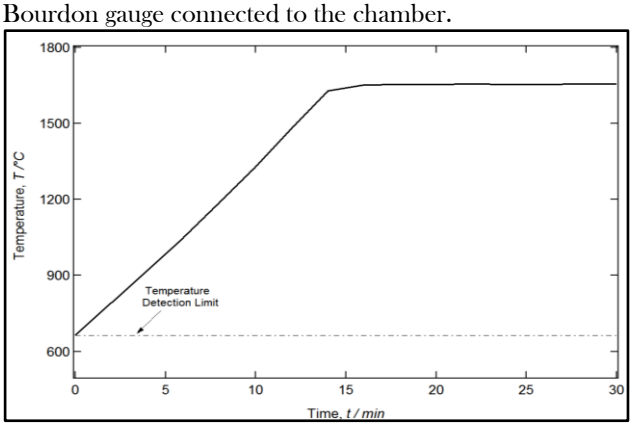

Fig. 5. The optimum used temperature was around 1650°C (1923K) recorded by the infrared thermometer during the reduction process. The detection range of the infrared thermometer is from 650°C to 3500°C.

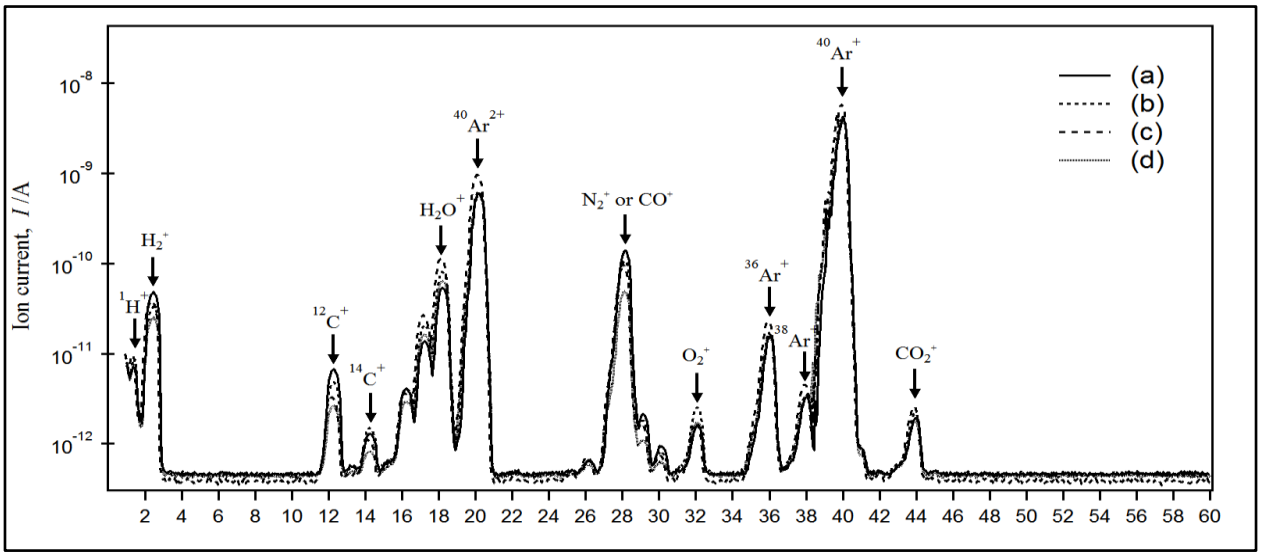

Fig. 6. Mass spectra of the chamber gases during the heating in case of four different silica to carbon ratios. A higher amounts of H_2O and O_2 were released when increasing the ratio of silica due to the presence of oxygen.

2.3. Method of Analysis

The analysis of x-ray diffraction (XRD) with a Cu-$K\alpha$ (λ = 1.5405 Å) radiation source over the angular range of $20° \leq 2\theta \leq 80°$ and a scan rate of 10°/min was employed by an x-ray diffractometer (SmartLab, Rigaku Corporation) to examine the phase composition. The system is equipated with a quadrupole mass spectrimeter (Q-mass) to analyze the chamber gas spectrometer and it can detect only CO gas because of the analysis in this study were performed at room temperature which is an impossible condition to detect SiO gas phase due to its low stability below 1300℃(1573K). The gas phase of SiO cannot reach the Q-mass analyzer because the Q-mass analyzer and the chamber are connected through a long metallic tube (inner diameter 0.711 mm) with an orifice. Therefore, the ratio of SiO gas to CO was calculated using the following equations:

$$M(\mathrm{CO})_{\mathrm{mol}} = P_{\mathrm{chamber}} * k * V_{\mathrm{chamber}} / R * T \quad \text{.....(6)}$$

where k is the maximum quadrupole intensity ratio between CO and Ar and it is plotted in Figure 7.

$$M(\mathrm{SiO})_{\mathrm{mol}} = (W_{\mathrm{Loss}} - M(\mathrm{CO})_{\mathrm{mol}} * 28)/44 \quad \text{.....(7)}$$

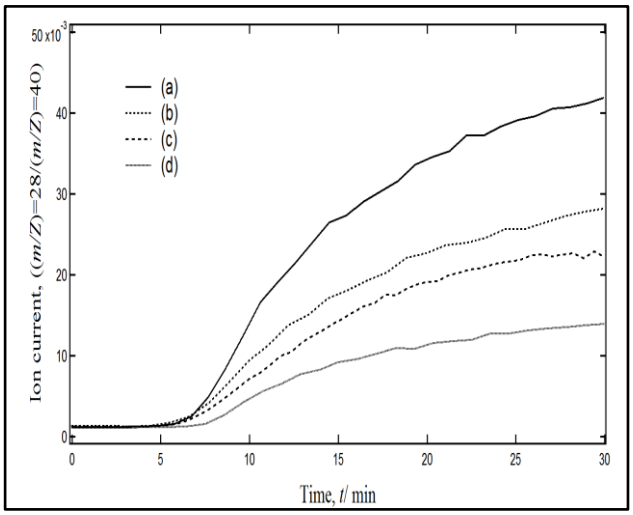

Fig. 7 (a, b, c and d) graphs representing the variation of released CO gas during the reduction process analyzed by quadrupole mass spectrometry, the highest released amount occurs in the case of (1.5, 1) ratio of silica to carbon as shown in (a).

3. Results and Discussion

3.1. Chamber Gas analysis

Figure 5 shows the temperature profile curves of the blank test as a typical temperatuere profile chosen and measured by the infrared thermometer in the pressent research work. For all the heating experiments the heating time was 30 minutes and the maxium temperature of the crucible was around 1650°C(1923K). The voltage and current of the induction coil, the temperature of the crucible were recorded by a data loger.

		a		b		c		d	
		(g)	(Si mol)	(g)	(Si mol)	(g)	(Si mol)	(g)	(Si mol)
SiO_2		6.160	0.103	6.360	0.106	6.560	0.109	6.660	0.111
C		0.840		0.640		0.440		0.340	
Total Mixture		7.000	0.103	7.000	0.106	7.000	0.109	7.000	0.111
SiC		1.300	0.033	1.300	0.033	1.300	0.033	1.300	0.033
Total Input		8.300	0.135	8.300	0.139	8.300	0.142	8.300	0.144
Total Product		2.729		1.918		1.590		1.205	
	Si	0.783	0.028	0.400	0.014	0.257	0.009	0.100	0.004
	SiC	1.940	0.049	1.500	0.038	1.330	0.033	1.100	0.028
Lost Gas		5.571		6.382		6.710		7.095	
	SiO	2.576	0.059	3.791	0.086	4.370	0.099	4.939	0.112
	CO	2.995		2.591		2.340		2.156	
Total Output		8.300	0.135	8.300	0.139	8.300	0.142	8.300	0.144
Si Yield (%)			20.7		10.3		6.5		2.8
SiC Yield (%)			35.9		27.0		23.5		19.1

Table 1 The mass balance of comparison between different ratios of SiO_2 to Carbon shows that the lower SiO gas loss, the more will be the amount of Si produced. The highest Silicon yield was achieved using the ratio of SiO_2 to carbon of (1.5, 1) as shown in the mass balance (a).

Figure 6 shows a compariosn of the quadrupole mass spectra between different molar ratios of silica to carbon. These results show that increasing the molar ratio of silica to carbon from 1.5 to 4 leaded to a release of a sginficant amount of H_2O and O_2 which is due to the additional O_2 gas contained on the solid form of SiO_2. While Figure 7 illustrates the temporal change of the relative mass peaks (m/Z = 28) which represents N_2/CO gasses and occurs mainly by the carbothermic reduction of silica. The intensity between the different molar ratio of silcia to carbon has a siginificant difference due to highe reactivity between silica and carbon in case of lower molar ratio (a), while in higher molar ratios (d) lack of carbon quantity leaded to less CO emission.

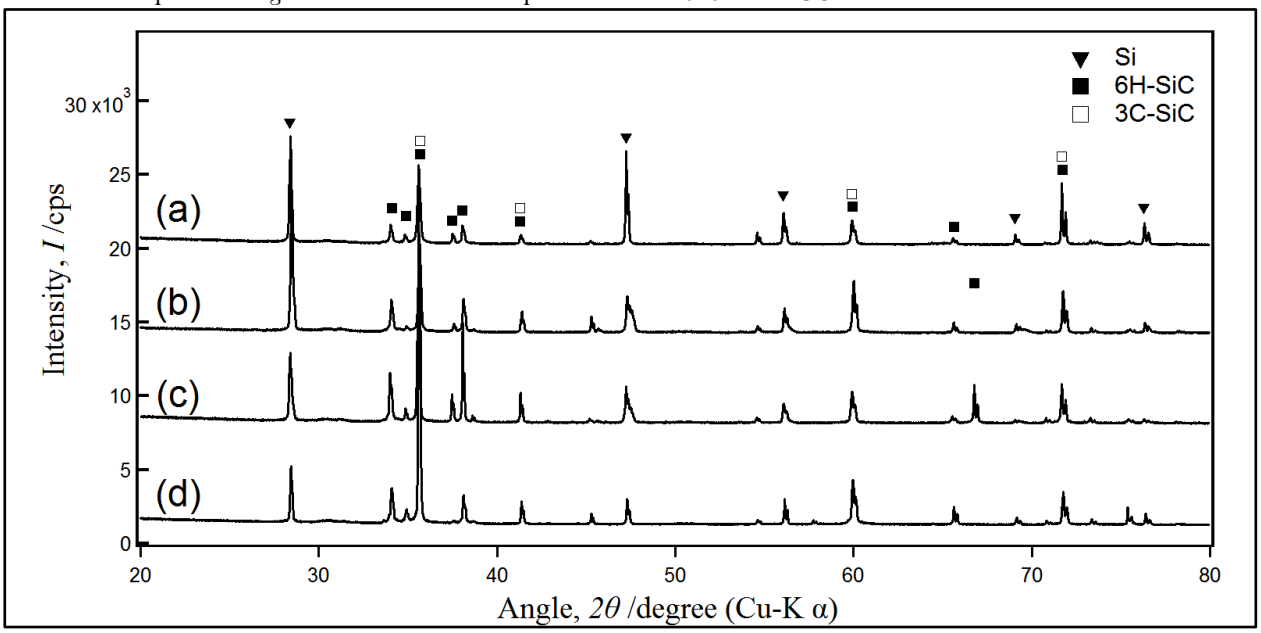

Fig. 8 X-ray diffraction patterns of obtained products for different raw material ratios.

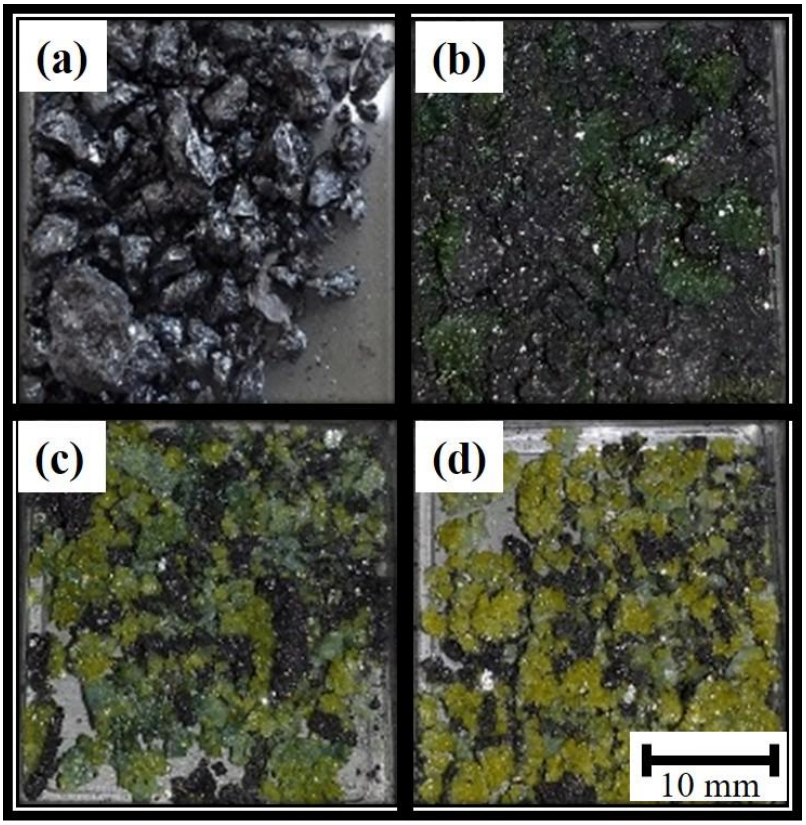

Fig. 9 Photos of the reduction product with four (SiO_2 : C) mixture ratios: (a) with (1.5, 1) showing solidified grey rocks of silicon mixed with silicon carbide, (b) with (2, 1) showing less solid form with obvious dark green colored material from silicon carbide, (c) with (3, 1) showing yellowish green product mixed with grey as proof of less amount of silicon, and (d) with (4, 1) showing mostly yellow colored product with almost no silicon

3.2. Product Analysis

Table 1 represents the mass balance, including the amount of input raw material, the product output and the weight loss as a gas phase in the case of each molar ratios. The Si product yield is defined as molar ratio of Si element in the product by the molar ratio of Si element in the input. The molar ratio 1.5 (a) between silica and carbon shows the highest Si yield of 20.7% compared to molar ratios (b), (c) of 10.3% and 6.5% while the lowest yield was observed when using the moalr ratio 4 represented by (d) and estimated by the powder diffraction patterns by the x-ray mille product as shown in Figure 8 which shown that the product included two phases of silicon carbide which are 6H-SiC and 3C-SiC with no peak mapped to silica or carbon in all XRD patterns which is consistent with the Si-C-O phase diagram discussed previously that the total consumption of silica and carbon was achieved in a temperature range from 1300K to 1900K. and proved by the different product obtained as illsutrated in Figure 9 which shows an image of the products in the case of the four different molar ratios, respectively. A grey solid rock image in case of (a) which represents the molar ratio of 1.5 can be explain by total reaction between silica and carbon raw material showing a higher yield of silicon (20.7%) and pure phase of silicon carbide (35.9%). In the case of (b), (c) and (d) molar ratio of 2, 3 and 4, respectively, the insuffisane of carbon was obvious leading to uncomplished reaction and illustrated by green and yellow colored material in the product which is different phase of silicon carbide, with less presence of silicon which agree with XRD results.

The decrease of Si yield in case of higher molar ratio between silica and carbon seems to be related to insufisance of carbon due to its exhaustion in the different redcution reactions as show in the phase diagram stability.

4. Conclusion

The phase stability diagram simulation of different reactions in the carbothermal reduction showed to be a powerful method for the estimation of the optimized reaction conditions such as temperature and partial pressure of the by-product gasses SiO and CO. Silicon was successfully obtained in a small-scale carbon crucible using an induction heating furnace with raw material powder form. Silicon production yield was improved by ten times via the optimization of the raw material input molar ratio between silica and carbon.

References

[1] H. C. Lee, S. Dhage, M. S. Akhtar, D. H. Kwak, W. J. Lee, C. Y. Kim and O. B. Yang: Curr. Appl. Phys. **10** (2010) S218–S221.

[2] E. Myrhaug and H. Tveit: El. Furnace Conf. **58** (2000).

[3] M. Stephen: PCT International Patent (1996) WO1996/041036.

[4] S. K. Iya, R. N. Flagella and F. S. Dipaolo: J. Electrochem. Soc. **129** (1982) 1531–1535.

[5] S. Wakamatsu and H. Oda: PCT International Patent (2001) WO2001/085613.

[6] H. S. N. Setty, C. L. Yaws, B. R. Martin and D. J. Wangler: U.S. Patent (1976) US 3,963,838.

[7] T. Homma, N. Matsuo, X. Yang, K. Yasuda, Y. Fukunaka and T. Nohira: Electrochim. Acta **179** (2015) 512–518.

[8] R. N. Andrews and S. J. Clarson: Silicon **7** (2015) 303–305.

[9] Y. Sakaguchi, M. Ishizaki, T. Kawahara,M. Fukai,M. Yoshiyagawa andF. Aratani: ISIJ Int. **32** (1992) 643–649.

[10] K. Itaka,T. Ogasawara,A. Boucetta,R. Benioub,M. Sumiya, T. Hashimoto,H. KoinumaandY. Furuya: J. Phys.: Conf. Ser. **596** (2015) 012015.

[11] R. K. Eckhoff: J. Loss Prev. Process Ind. **25** (2012) 448–459.

[12] R. K. Eckhoff: J. Loss Prev. Process Ind. **22** (2009) 105–116.

[13] S. V. Komarov, D. V. Kuznetsov, V. V. Levina and M. Hirasawa: Mater. Trans. **46** (2005) 827–834.

[14] E. Dal martello, G. Tranell, S. Gaal, O. S. Raaness, K. Tang, and I. Arnberg: Metall. Mater. Trans. **B42B** (2011) 939–950.

[15] L. P. Hunt, J. P. Dismukes and J. A. Amick: J. Electrochem. Soc. **131** (1982) 5–8.

[16] R. Benioub, A. Boucetta, A. Chahtou, S. M. Heddadj, M. Adnane, Y. Furuya and K. Itaka: Mater. Tran, JIM. 57 (2016) 1930-1935.

[17] H. Yokokawa, S. Yamauchi S and T. Matsumoto: Acta. Thermo.**245** (1994)45-55.

[18] S. V. Komarov, D. V. Kuznetsov, V. V. Levina and M. Hirasawa: Mater. Tran, JIM. **46** (2005) 827-834.

[19] M. Tada and M. Hirasawa: High Temp. Mater. Proc. **19** (2000) 281-297.

[20] A. W. Weimer, K. J. Nilson, G. A. Cochran and R. P. Roach: J. AIChE. **39** (1993) 493-503.

[21] T. Kikuchi, T. Kurosawa and T. Yagihashi: Mater. Tran, JIM. **32** (1968) 866-872.

[22] D. H. Filsinger and D. B. Bourrie: J. Am. Ceram. Soc. **73** (1990) 1726–1732.